Minimal instances for $\mathbb{Z}_2$ lattice gauge theories and spin pumps

Christian Schweizer

SIGILL · UNIVERSITAT · LUDOVIC · MAXIM

München 2019

Minimal instances for $\mathbb{Z}_2$ lattice gauge theories and spin pumps

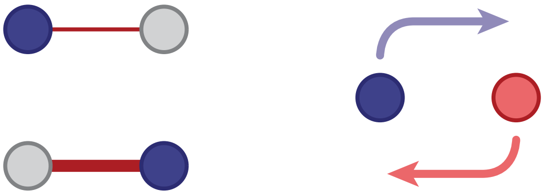

Dissertation an der Fakultät für Physik
Ludwig-Maximilians-Universität München

vorgelegt von
Christian Schweizer
aus Nürtingen

München, den 24. Mai 2019

Tag der mündlichen Prüfung: 3. Juli 2019
Erstgutachter: Prof. Immanuel Bloch
Zweitgutachter: Prof. Michael Knap
Weitere Prüfungskommissionsmitglieder: Prof. Alexander Högele, Prof. Dieter Braun

Zusammenfassung

Die Implementierung und Charakterisierung minimaler Bausteine von komplexen Vielteilchensystemen hat eine grundlegende Bedeutung für die Entwicklung von Quantensimulatoren. In dieser Doktorarbeit werden die Implementierungen zweier minimaler Bausteine präsentiert: Ein minimaler Baustein für $\mathbb{Z}_2$-Gittereichtheorien gekoppelt an Materie und ein minimaler Baustein für Spinpumpen.

$\mathbb{Z}_2$-Gittereichtheorien sind durch einen $\mathbb{Z}_2$-Eichfreiheitsgrad auf jeder Gitterkante charakterisiert. Wenn Materieteilchen sich über diese Kanten bewegen, sammeln sie eine Phase ein, die vom Eichfeld der überquerten Kante abhängt. Um die lokale Eichsymmetrie auch während dieser Bewegung zu erhalten, ändert sich das Eichfeld selbst. Ein entsprechender minimaler Baustein besteht aus einem Materieteilchen auf zwei Gitterplätzen, die durch eine Kante verknüpft sind. Die hier vorgestellte Implementierung des minimalen Bausteins basiert auf ultrakalten Rubidiumatomen mit zwei Komponenten in einem periodisch getriebenen, optischen Doppeltopfpotential, welches einen komponentenabhängigen Energieunterschied zwischen benachbarten Gitterplätzen aufweist. In dieser Implementierung stellt eine Komponente die Materie und die andere Komponente das Eichfeld dar. Der entsprechende effektive Floquet-Hamiltonoperator ist $\mathbb{Z}_2$-symmetrisch für spezifische Modulationsparameter, wenn die periodische Modulation resonant mit der Wechselwirkungsenergie auf einem Gitterplatz ist. Die Dynamik für verschiedene Anfangszustände wurde untersucht und mit einer numerischen Analyse verglichen. Diese numerische Analyse stimmt mit den Messungen überein und zeigt, dass die Messungen einer nicht-triviale Dynamik folgen wie es von einer $\mathbb{Z}_2$-Gittereichtheorie gekoppelt an Materie erwartet wird. Zudem werden eichsymmetriebrechende Terme identifiziert und Wege aufgezeigt diese Beschränkungen zu umgehen. Schießlich wird eine Möglichkeit vorgeschlagen wie aus minimalen Bausteinen ein eindimensionales erweitertes System entstehen kann. Diese Ergebnisse stellen einen ersten Schritt zur Quantensimulation von Eichtheorien dar und ermöglichen wichtige Einblicke für zukünftige Studien mit Floquet-basierten Techniken.

Eine Quantenspinpumpe generiert einen Spintransport als Antwort auf eine zyklische und adiabatische Änderung eines eindimensionalen Hamiltonoperators. Dabei werden die Spins in entgegengesetzte Richtungen transportiert ohne dass Ladungstransport auftritt.

In einem System mit Spinerhaltung und homogen gefüllten Bändern ist der Spintransport pro Pumpzyklus quantisiert und mit der Topologie des Pumpzykluses verknüpft. Im Experiment wurde ein minimaler Baustein für solch eine Spinpumpe mit ultrakalten Rubidiumatomen in optischen Doppeltopfpotentialen implementiert. Im Fall von während des Pumpzykluses abschnittsweise isolierten Bausteinen, die sich jeden halben Pumpzyklus um einen Gitterplatz verschieben, wird eine eindimensionale Spinpumpe realisiert. Um das Verhalten der Pumpe zu charakterisieren, werden die Spinauftrennung und die auftretenden Spinströme gemessen. Die Spinauftrennung wird aus den Schwerpunktspositionen der beiden Spinkomponenten in in-situ Absorptionsbildern bestimmt. Für die Detektion der Spinströme wurde eine neue Methode entwickelt, die die Superaustauschoszillationen nach einer Projektion auf statische Doppeltöpfe mit dem unmittelbaren Spinstrom verbindet. Diese neu entwickelte Methode kann auf allgemeine Systeme angewendet werden und in Kombination mit Einzelplatzauflösung sogar unmittelbare Spinströme lokal bestimmen. Diese Ergebnisse legen den Grundstein für die Implementierung von Spinpumpen, die dann beispielsweise durch das Hinzufügen von zeitumkehrerhaltenden Spin–Orbit-Wechselwirkungen oder das Brechen der Zeitumkehrsymmetrie erweitert werden können. Dadurch entsteht dann entweder ein System mit einer mit nicht-trivialen $\mathbb{Z}_2$-Erhaltungsgröße oder ein nicht-triviales Quanten-Spin-Hall-System, welches durch eine Spin-Chernzahl beschrieben wird.

Summary

The implementation and characterization of minimal instances of complex many-body systems have fundamental importance for the development of quantum simulators. This thesis reports on the implementation of two such minimal instances: a minimal instance for $\mathbb{Z}_2$ lattice gauge theories coupled to matter and a minimal instance for spin pumping.

$\mathbb{Z}_2$ lattice gauge theories are characterized by a $\mathbb{Z}_2$ gauge degree-of-freedom on every lattice link. Matter particles moving across these links pick up a phase depending on the traversed link's gauge field. To conserve the local gauge symmetry during this motion, also the gauge field itself changes. A corresponding minimal instance consists of a single matter particle on two lattice sites, which are connected by a link. The presented implementation of this minimal instance is based on two-component ultracold rubidium atoms in a periodically-driven optical double-well potential with a state-dependent energy offset between neighboring sites. In this implementation, one component represents the matter, while the other component represents the gauge field. The resulting effective Floquet Hamiltonian exhibits $\mathbb{Z}_2$ symmetry for specific modulation parameters, if the periodic driving is resonant with the on-site interaction energy. The dynamics was investigated for different initial states and compared to a numerical analysis. This numerical analysis is in agreement with the measurements and reveals nontrivial dynamics as expected from a $\mathbb{Z}_2$ lattice gauge theory coupled to matter. Furthermore, symmetry-breaking terms are identified and routes to overcome these limitations are discussed. Finally, a way to couple minimal instances to a one-dimensional extended system is proposed. The results constitute a first step towards quantum simulation of gauge theories and provide important insights for future studies using Floquet-based techniques.

A quantum spin pump generates a spin transport in response to a cyclic and adiabatic variation of a one-dimensional Hamiltonian. The spins are transported in opposite directions and thereby exhibit a vanishing charge transport. In a spin-conserving system with homogeneously filled bands, the spin transport per pump cycle is quantized and deeply connected to the pump cycle's topology. Therefore, such a spin pump can be interpreted as a dynamical version of a two-dimensional time-reversal symmetric quantum spin Hall system. In the experiment, a minimal instance of such a spin pump was implemented with ultracold rubidium atoms in an optical double-well potential. In the limit of piecewise isolated instances throughout the pump cycle, where each instance shifts by one lattice site per half pump cycle, a one-dimensional spin pump is realized. To characterize the response of the pump, the spin separation and the occurring spin currents are measured. For the detection of the spin separation, the center-of-mass positions of both spin components are analyzed in in-situ absorption images. For the detection of spin currents, a novel detection method was developed, which connects the superexchange oscillations after a projection onto static double wells to the instantaneous spin current. This newly developed method can be applied to a general class of systems and in combination with single-site detection, it also allows for a local detection of instantaneous spin currents. The results demonstrate a corner stone for the implementation of a spin pump, which can be extended, e.g. by adding time-reversal-invariant spin–orbit interactions or by breaking time-reversal symmetry. This extension then results either in a system described by a nontrivial $\mathbb{Z}_2$ invariant or a quantum spin Hall system described by a spin-Chern number.

Publications

- **Christian Schweizer**, Fabian Grusdt, Moritz Berngruber, Luca Barbiero, Eugene Demler, Nathan Goldman, Immanuel Bloch, Monika Aidelsburger. "Floquet approach to $\mathbb{Z}_2$ lattice gauge theories with ultracold atoms in optical lattices". *Nat. Phys.* (2019).
- Luca Barbiero, **Christian Schweizer**, Monika Aidelsburger, Eugene Demler, Nathan Goldman, Fabian Grusdt. "Coupling ultracold matter to dynamical gauge fields in optical lattices: From flux-attachment to $\mathbb{Z}_2$ lattice gauge theories". *arXiv* 1810.02777 (2018).
- Andrew Hayward, **Christian Schweizer**, Michael Lohse, Monika Aidelsburger, Fabian Heidrich-Meisner. "Topological charge pumping in the interacting bosonic Rice-Mele model". *Phys. Rev. B* 98 (2018), p. 245148.
- Michael Lohse, **Christian Schweizer**, Hannah M. Price, Oded Zilberberg, Immanuel Bloch. "Exploring 4D quantum Hall physics with a 2D topological charge pump". *Nature* 553 (2018), pp. 55–58.
- **Christian Schweizer**, Michael Lohse, Roberta Citro, Immanuel Bloch. "Spin pumping and measurement of spin currents in optical superlattices". *Phys. Rev. Lett.* 117 (2016), p. 170405.
- Michael Lohse, **Christian Schweizer**, Oded Zilberberg, Monika Aidelsburger, Immanuel Bloch. "A Thouless quantum pump with ultracold bosonic atoms in an optical superlattice". *Nat. Phys.* 12 (2016), pp. 350–354.
- Monika Aidelsburger, Michael Lohse, **Christian Schweizer**, Marcos Atala, Julio T. Barreiro, Sylvain Nascimbène, Nigel R. Cooper, Immanuel Bloch, Nathan Goldman. "Measuring the Chern number of Hofstadter bands with ultracold bosonic atoms". *Nat. Phys.* 11 (2015), p. 162–166.

Contents

Preface 1

I. Floquet approach to $\mathbb{Z}_2$ lattice gauge theories 3

1. Introduction to gauge theories 5
- 1.1. Gauge theories in physics 5
- 1.2. From classical electrodynamics to dynamical gauge fields 7
  - 1.2.1. Gauge theories in classical electrodynamics 7
  - 1.2.2. Static homogeneous magnetic fields on a lattice 10
  - 1.2.3. Quantum simulation of the Harper-Hofstadter model 13
  - 1.2.4. Backaction requires gauge degree-of-freedom 14
- 1.3. From $U(1)$ to $\mathbb{Z}_2$ lattice gauge theories 15
  - 1.3.1. Global and local gauge symmetry for matter tunneling 15
  - 1.3.2. $U(1)$ lattice gauge theories 16
  - 1.3.3. $\mathbb{Z}_N$ lattice gauge theories 18
  - 1.3.4. $\mathbb{Z}_2$ lattice gauge theories 19

2. Minimal instance for $\mathbb{Z}_2$ LGTs coupled to matter 23
- 2.1. $\mathbb{Z}_2$ lattice gauge theories coupled to matter 23
  - 2.1.1. Elementary ingredients 23
  - 2.1.2. Basic dynamics in 1D 25
  - 2.1.3. Minimal instance 25
- 2.2. Floquet implementation 28
  - 2.2.1. Field-particle species representing the link degree-of-freedom 28
  - 2.2.2. Multiphoton processes in a periodically-driven two-site potential 28
  - 2.2.3. Matter–gauge coupling 30
  - 2.2.4. Gauge field dynamics 31
  - 2.2.5. Time-dependent and effective Hamiltonian 33

3. Experimental realization and measurements 35
- 3.1. Experimental realization and calibrations 35
  - 3.1.1. Setup with modulation lattice 35

3.1.2. Detection and inhomogeneous tilt distribution 36
3.1.3. Multiphoton processes 38
3.1.4. Tight-binding description 40
3.1.5. Parameter calibrations 42
3.1.6. Sequence and initial state preparation 46
3.2. Dynamics in the $\mathbb{Z}_2$ double well 48
3.2.1. Probing a single sector with the $\hat{\tau}_x$ initial state 48
3.2.2. Probing two sectors with the $\hat{\tau}_z$ initial state 52

4. Discussion of symmetry breaking 55
4.1. Symmetry-breaking terms in the minimal instance 55
4.2. Effect of finite-frequency corrections on the effective model 57
4.3. Effect of the corrections from the Bose-Hubbard model 61

5. Towards extended $\mathbb{Z}_2$ LGTs 65
5.1. One-dimensional LGT with super-sites 65
5.1.1. Super-sites model 65
5.1.2. More than one matter particle 68
5.1.3. Floquet implementation of the super-site 68
5.2. Proposal for an experimental implementation of the super-site model . . . 69
5.3. Ladder model features a global $\mathbb{Z}_2$ symmetry 71
5.4. Conclusions 72

II. Spin pumping and measurement of spin currents in optical superlattices 73

6. Introduction to spin pumping 75
6.1. Quantum spin Hall effect 75
6.2. Topological charge pumping 77
6.3. Spin pumping 79

7. Minimal instance for $\mathbb{Z}_2$ spin pumps 81
7.1. Spin pumps in a spin-dependent Rice-Mele model 81
7.2. Limit of isolated double wells 83

8. Spin-current measurement technique 87
8.1. Charge and spin currents 87
8.1.1. Continuity equation 87
8.1.2. Probability current 88
8.1.3. Definition of a spin current 88

8.2. Spin currents in the minimal instance 89
    8.2.1. Two-site extended Bose-Hubbard model 89
    8.2.2. Spin-current operator 90
    8.2.3. Spin-currents during pumping 91
8.3. Measurement method 92

9. Experimental setup and calibrations **95**
9.1. Setup 95
9.2. Experimental sequence 95
9.3. Calibrations 97

10. Measurements and numerical analysis **101**
10.1. Measurements of spin separation 101
10.2. Measurements of spin currents 103
10.3. Conclusions 108

III. Appendix **109**

A. Effective Hamiltonian of the $\mathbb{Z}_2$ double well **111**
A.1. Floquet expansion 111
A.2. Floquet model in the infinite-frequency limit 112
A.3. Floquet model including first-order correction for finite-frequency drive . 113

B. Spin currents **115**
B.1. Derivation of the coefficients for the temporary wave function 115
B.2. Operator expectation value after stop of the adiabatic evolution 116

Acronyms **117**

Bibliography **119**

List of Figures

1.1. Aharonov-Bohm effect on a lattice 10
1.2. Homogeneous flux patterns 11
1.3. Electrodynamics on a lattice 14

2.1. Basic ingredients of $\mathbb{Z}_2$ lattice gauge theories coupled to matter 23
2.2. Basic dynamics of the 1D $\mathbb{Z}_2$ LGT 26
2.3. Ideal dynamics of the minimal instance 27
2.4. Illustration of multiphoton processes in a periodically-driven double well 30
2.5. Implementation of the matter–gauge coupling 32
2.6. Implementation of the gauge-field dynamics 33

3.1. Modulation lattice and gradient 36
3.2. Inhomogeneous tilt distribution 37
3.3. Measured renormalization of the tunneling of a driven double well 40
3.4. Tight-binding parameter dependence on the modulation lattice depth . . 42
3.5. Superlattice calibration 43
3.6. Calibration of the interaction energy 44
3.7. Calibration of the modulation lattice 45
3.8. Experimental sequence 47
3.9. Dynamics of the $\mathbb{Z}_2$ double well starting from an eigenstate of the electric field operator 50
3.10. Overview over single numeric traces 51
3.11. Dynamics of the $\mathbb{Z}_2$ double well starting from an eigenstate of the gauge field operator 53

4.1. Coefficients of the first-order corrections to the effective model 59
4.2. Finite-frequency corrections to the zeroth-order Floquet Hamiltonian . . . 59
4.3. Symmetry-breaking terms from first-order corrections to the Floquet model 60
4.4. Suppression of symmetry-breaking towards the high-frequency limit . . . 61
4.5. Symmetry-breaking in the extended Bose-Hubbard model 62

5.1. Extending the $\mathbb{Z}_2$ double well to a 1D model with super-sites 66
5.2. Numeric analysis of the dynamics in the super-site model 67

5.3. Implementation of super-site processes 70
5.4. Proposal for a super-site model implementation 70

7.1. Spin pump cycle and pumping in the minimal instance 84
7.2. Comparison of the energy spectrum for staggered and gradient model . . 85

8.1. Energy spectrum and admixture-coefficients of the minimal instance . . . 91
8.2. Spin current measurement method 93

9.1. Illustration of the experimental sequences 96
9.2. Calibrations of the magnetic gradient 99

10.1. Spin separation 102
10.2. Static spin imbalance $\mathcal{I}$ during the pump cycle 103
10.3. Spin-current measurement 104
10.4. Comparison of models for the spin current measurement 106
10.5. Spin imbalance oscillation amplitude A at $\Delta_s = 0$ as a function of J_{ex} . . . 107

Preface

Quantum simulation has the potential to investigate complex many-body systems, which are challenging to analyze both analytically and numerically. A promising platform for analog quantum simulations are ultracold atoms in optical potentials [1, 2]. However, before implementing a certain many-body Hamiltonian in a quantum simulator, it is of great interest to test fundamental building blocks of these extended systems. Testing these building blocks is a successful strategy to understand basic physical concepts and especially also to develop technology to control and manipulate atomic many-body samples. Furthermore, the building blocks might even be coherently connected to generate the extended system of interest in a controlled fashion. Intriguingly, it was experimentally found that certain quantities of few-body systems converge fast to the many-body limit with increasing particle number, e.g. the normalized interaction energy in a quasi one-dimensional system [3]. This suggests that few-body systems – maybe already a minimal instance or a small collection of these instances – might open the route to observe complex properties or even to discover new phenomena.

In recent years, a variety of minimal instances have been implemented, which greatly enriched the tool box to study many-body quantum phenomena with atomic quantum simulators. These fundamental building blocks include for instance the observation of superexchange oscillations between two distinguishable interacting bosons in an optical superlattice [4, 5]. This second-order process is a corner stone for many proposals, e.g. for quantum simulations of lattice gauge theories (LGT) and resonating valence-bond (RVB) states. RVB states describe a topological spin liquid relevant for high-temperaturee superconductivity. Similar to superexchange oscillations, also second-order pair tunneling constitutes a minimal instance. For certain parameters, it acts as a single atom switch and allows to efficiently create entanglement over different lattice sites in extended systems [6]. Later, such two-particle minimal instances have been implemented in optical tweezers with bosonic atoms, where their quantum statistics was observed in an interferrometric experiment [7], and with fermions, constituting a key component of the Fermi-Hubbard model [8, 9]. In this fermionic system, an analog of the Mott–metal transition as well as a charge density regime was directly observed. Both realizations are candidates to achieve larger systems by a bottom-up approach. Moreover, minimal instances with four particles on a four-site plaquette have been realized, for example RVB states [10] and ring-exchange interactions [11]. A RVB state on a plaquette is a minimum version of a topological liquid and can directly correspond to a Laughlin state [12] for two particles [13]. The ring exchange interaction is a main ingredient for $\mathbb{Z}_2$ LGTs and the toric-code Hamiltonian. It can also serve as a minimum version of a string-net-condensate state [13]. Another class of building blocks uses Floquet-based methods to engineer new types of interactions. This route was also followed in Part I in this thesis. A prominent example for the use of Floquet-based methods is the demonstration of strong magnetic fields on a plaquette as a minimum version of the Harper-Hofstadter model [14]. In an alternative approach using Rydberg atoms, the basic instances of exotic quantum phases and collective excitations were realized, e.g. in self-ordered crystals [15] and a two-site boson sampling experiment using the Hong-Ou-Mandel effect [16].

This thesis comprises two parts, each describing the implementation and analysis of a minimal instance. Part I deals with a minimal instance for $\mathbb{Z}_2$ LGTs coupled to matter implemented through Floquet engineering and is based on Ref. [17]. After a general introduction to LGTs (Chap. 1), the working principle of the minimal instance is described (Chap. 2). In Chap. 3, the experiment is presented and compared to a full time-dependent numerical analysis. Then, symmetry-breaking terms (Chap. 4) and extensions of the minimal instance to 1D systems (Chap. 5) are discussed. Part II deals with a minimal instance for spin pumping based on Ref. [18]. This spin pump is a dynamical version of a quantum spin Hall system (QSH system), which is outlined in Chap. 6. The minimal instance in the limit of isolated double wells is described in Chap. 7. To complement spin-transport measurements on the spin pump, a novel detection method for spin currents is introduced, which connects the oscillation amplitude after projection on isolated double wells to the spin current (Chap. 8). Finally, the experimental setup and calibrations (Chap. 9) as well as the measurements and numerical analysis (Chap. 10) of the minimal instance for spin pumping are presented.

Part I.

Floquet approach to $\mathbb{Z}_2$ lattice gauge theories

1. Introduction to gauge theories

1.1. Gauge theories in physics

The world around us is extraordinarily complex and rich of astonishing phenomena, which follow fundamental principles. Uncovering and formulating these principles is the purpose of natural sciences and understanding the interplay of matter more specifically of physics. Physics is entirely based on observations made in nature. It is descriptive and ultimately an experimental science. The descriptions are formulated using mathematical language and together they form a physical theory. Such theory should predict all outcomes of experiments of similar nature covering a wide range of length and energy scales. However, a theory cannot be proven to be complete or generally valid; nature can only reject it by offering surprising and contradictory experimental results.

While developing more comprehensive theories in order to someday find a unified explanation of all phenomena in the universe, it was proven to be successful to divide things into smaller and smaller pieces. With this approach, simpler and more fundamental structures were identified over time [19]. First, it was found that matter is composed of a small number of different elements – atoms. Later, it was discovered that atoms themselves are composed of smaller particles – electrons, protons, and neutrons. Today, it is known that these particles as well have a substructure. To our current knowledge, the universe is built from photons, electrons, quarks, and a few other particles [19]. These particles interact by the four fundamental interactions of nature: gravitation, electromagnetic, weak, and strong interactions [20]. The latter three are combined in the $\mathrm{U}(1)\times\mathrm{SU}(2)\times\mathrm{SU}(3)$ Standard Model. This Standard Model is a field theory, which says that forces are mediated by the exchange of a gauge boson between the interacting partners [21]. This field theory has a local gauge structure and is invariant under local gauge transformations according to the name-giving symmetry groups. In the following we will find that gauge theories are a recurrent element in modern physical descriptions in various fields.

Physical theories built on this microscopic perspective were remarkably successful in predicting a variety of phenomena, thereby offering a deep understanding of nature's constituents. From this microscopic perspective, the description of phenomena with a large number of components, however, seems hopeless, as the interplay of all components needs to be considered. Therefore, an effective global standpoint provides a promising alternative. Thermodynamics is a classical example for such an effective description, where e.g. in the case of the ideal gas the microscopic observables position, momentum, and energy of the gas particles do not appear, while collective quantities like pressure, particle density and temperature are employed. In condensed matter physics, the situation is similar. In principle, the behavior of many quantum particles is known and governed by the Schrödinger equation. However, when many particles are involved, the equations are typically unsolvable. In consequence, the microscopic description does not allow for any predictions. In this situation, it is a good idea to zoom out and find an effective theory that connects experimental observations. In the last decades, theoretical approaches using gauge theories have proven useful to describe the essentials of a variety of systems, e.g. 2D quantum Ising [22] and XY magnets [23, 24] together with Boson vortex duality [25], from quantum antiferromagnets [26–28] and quantum dimer models [29, 30] to high T_c superconductors [31–34] and quantum spin liquids [35], as well as frustrated magnets [36–39], and fractional quantum Hall states [40–43]. All these descriptions have in common that their physics arises from low energy excitations, where new quasi-particles with their own physical rules emerge. Therefore, not only the particles themselves but also their physics laws are emergent [44].

The occurance of gauge theories in various different settings, from the *microscopic* to *macroscopic* perspective, vastly motivated the interest in their study. The emergence of new particles with their individual set of physical rules further raised the question, whether the pathway of dividing matter in smaller and smaller pieces is constructive. An alternative approach is to interpret literally everything, including the fundamental particles with their interactions, as an emergent phenomenon of the universe [19]. The basis for such theory can be a string-net condensate on a regular lattice. This gauge theory with collective modes and associated physics can already unify three fundamental ingredients of physics: identical particles, gauge interactions, and Fermi statistics [19]. However, a unification that also embeds chiral fermions and gravity is still lacking.

In addition to creating these effective models, the calculation of their phases also remains challenging. Although remarkable results have been achieved using numerical techniques, especially through Monte-Carlo methods [45], they face the computationally hard sign problem [46, 47] for systems with a finite chemical potential of fermions. For some models, a sign-problem free analysis can be performed for arbitrary fermion densities [48] or in certain limiting cases [49]. However, calculating quantum mechanical properties with classical computers is an immensely difficult task. A promising approach is to quantum simulate such models using general purpose, digital or analog quantum simulators [50]. Analog quantum simulators emulate a very specific quantum problem by directly implementing the problems' the degrees-of-freedom, e.g. the coupling and interaction terms of the model. This movement was triggered by the enormous progress made in laboratories to precisely control quantum systems, such as ultracold atoms in optical lattices [1, 2], trapped ions [51], photonic systems [52], Rydberg atoms [53], superconducting qubits [54, 55] and more. These experiments are promising candidates to quantum simulate certain quantum models and to observe phenomena, which may be otherwise inaccessible [56].

In this part of the thesis, foundational experiments for a possible realization of $\mathbb{Z}_2$ LGTs coupled to matter were conducted. This is one of the simplest theories with a gauge structure and expected to have many rich features [57], because already in the case of static matter, a phase transition [58] to a confining phase was found [59–61]. Based on a scheme proposed in [62], the implementation uses bosonic ultracold spinful ^{87}Rb atoms in an optical superlattice potential together with resonant periodic driving [14, 63–71] at the on-site interaction energy [17, 72–78]. The experiment demonstrates a minimal instance consisting of two particles on a double well that could be used to generate one- or two-dimensional realizations of $\mathbb{Z}_2$ LGTs. Before presenting the details of the scheme and the experimental and numerical results, an introduction to LGTs is given. The introduction is not intended to be comprehensive but rather reflect the author's personal view on the topic.

1.2. From classical electrodynamics to dynamical gauge fields

1.2.1. Gauge theories in classical electrodynamics

In classical electrodynamics, the interplay between charges, magnetic and electric fields is described by the Lorentz force

$$\mathbf{F} = q\left(\mathbf{E} + \mathbf{v} \times \mathbf{B}\right) \tag{1.1}$$

and the four Maxwell's equations

$$\nabla \cdot \mathbf{E} = \frac{\rho}{\epsilon_0}, \qquad \nabla \cdot \mathbf{B} = 0, \qquad (1.2, 1.3)$$

$$\nabla \times \mathbf{E} = -\frac{\partial \mathbf{B}}{\partial t}, \qquad \nabla \times \mathbf{B} = \mu_0 \left(\mathbf{j} + \epsilon_0 \frac{\partial \mathbf{E}}{\partial t}\right), \qquad (1.4, 1.5)$$

where $\mathbf{E}$ is the electric, $\mathbf{B}$ the magnetic field, q the charge, ρ the density, $\mathbf{j}$ the current density, $\mathbf{v}$ the velocity, ϵ_0 the vacuum permittivity, and μ_0 the vacuum permeability. These equations indicate that charges are the sources of electric fields [Gauss's law, Eq. (1.2)], that there are no sources of magnetic fields [Eq. (1.3)], i.e. no magnetic monopoles, that charge currents create magnetic fields [Ampère's law, first part in Eq. (1.5)], that changes of the magnetic field create a curly electric field [Faraday's law, Eq. (1.4)], and finally that changes of the electric field create a curly magnetic field [Eq. (1.5)]. The latter is the so called displacement current found by Maxwell himself [79]. This discovery was a remarkable step forward, not only because it led Maxwell to the conclusion that light is an electromagnetic wave but also because it promoted the power of field theoretical formulations to gain physical insights [80, 81].

The notion of fields is introduced to avoid the idea of action at a distance [82]. Imagine a charge at a certain position, which is influenced by many other charges in its proximity. Then, a *real* field captures the influence of all the surrounding charges only by the field value at the particle's position.

The commonly known formulation of Maxwell's equations as shown in Eqs. (1.2)–(1.5) differs from Maxwell's original representation. He originally used the vector potential $\mathbf{A}$, which he identified to be Faraday's electrotonic intensity. The vector potential itself was introduced by Thomson [80] as

$$\mathbf{B} = \boldsymbol{\nabla} \times \mathbf{A}. \tag{1.6}$$

In analogy to the vector potential for magnetic fields, a scalar potential Φ can be introduced for electric fields $\mathbf{E} = -\boldsymbol{\nabla}\Phi - \partial_t \mathbf{A}$. It is important to recognize that both the vector and the scalar potential are not uniquely defined, as Maxwell's equations are invariant under a transformation with the scalar function $f(r,t)$

$$\mathbf{A} \to \mathbf{A} + \boldsymbol{\nabla} f, \tag{1.7}$$

$$\Phi \to \Phi - \partial_t f. \tag{1.8}$$

Each set of $(\mathbf{A}, \Phi)$ is called a gauge and $f(r,t)$ a gauge function. Notably, Maxwell was fully aware of this fact and explicitly discussed this in his publication [80]. However, the vector potential with its gauge freedom was highly debated to be an adequate description as it did not seem to have any physical significance. In classical electrodynamics, the only effect of a magnetic field on a charged particle is the Lorentz force Eq. (1.1). This fundamentally changed when quantum mechanics came into play. With quantum mechanics, the notion of forces looses importance, while the concept of energy and momentum gains relevance. Quantum mechanical particles are described by wave functions with amplitudes and phases. The effect of a magnetic field – in fact the vector potential – on the wave function is an additional phase factor φ_B collected along a path γ

$$\varphi_B = \frac{q}{\hbar} \int_{\gamma} \mathbf{A}\, \mathrm{d}l\,. \tag{1.9}$$

For a closed path ∂S, the phase factor can be associated with the magnetic flux

$$\Phi_B = \frac{q}{\hbar} \oint_{\partial S} \mathbf{A}\, \mathrm{d}l = \frac{q}{\hbar} \iint_{S} \mathbf{B}\, \mathrm{d}\mathbf{S}\,. \tag{1.10}$$

Note that the gauge freedom in **A** is still present and φ_B is a gauge-dependent quantity. However, Φ_B is gauge invariant. Can we therefore conclude that **B**, instead of **A**, is the relevant field? The answer is no. The vector potential **A** is the *real* field when considering quantum mechanics. The reason is that a description by magnetic fields requires action at a distance. This became clear during the proposal of Aharonov and Bohm's famous interferrometric experiment [83].

It is interesting and instructive to continue the discussion on a discrete grid [84], as the focus of this thesis will be on lattice models of gauge theories. Such LGTs are in general advantageous compared to continuum models for both theoretical and experimental investigations. When the continuum result is needed, often the limit towards smaller lattice spacings is analyzed. To formulate electrodynamics on a lattice, the magnetic field needs to be discretized. Therefore, the Peierls substitution method is used to approximate an external magnetic vector potential **A** by phase factors θ_{ij} associated with each link in the lattice. These phase factors are the ones mentioned in Eq. (1.9) with the path being the link between two neighboring sites. As mentioned previously, the phase on a closed loop, e.g. on a plaquette, reflects the magnetic field through the surface included in the loop. With this knowledge, we can straightforwardly construct gauge patterns for certain magnetic field distributions. These gauge patterns are of course not unique because of the gauge freedom.

Back to the Aharonov-Bohm effect, where a closed path is considered through points in space with zero magnetic field strength. This loop, however, should include an area with a finite magnetic field. To this end, we assume a plaquette with non-zero magnetic flux Φ_B to be surrounded by plaquettes carrying zero flux. A possible gauge pattern is shown in Fig. 1.1 b. This pattern is constructed by adding a single phase $-\Phi_B$ to the upper bond of the plaquette such that the flux is Φ_B. The plaquette above, however, now carries a flux too. It is $-\Phi_B$ but can be compensated to zero by adding another phase to the plaquette, e.g. on the upper bond. This again results in a flux $-\Phi_B$ in a plaquette above. Iteratively adding phases to these plaquettes shifts them outwards to infinity. Therefore, independent of the path around the magnetic field region, the vector field locally "knows" about the magnetic field inside without ever traversing it. Thus, the vector potential is a field according to the previous definition [82].

Before discussing the interplay between charges (matter particles) and the electromagnetic field (gauge field) the case of static magnetic fields is presented.

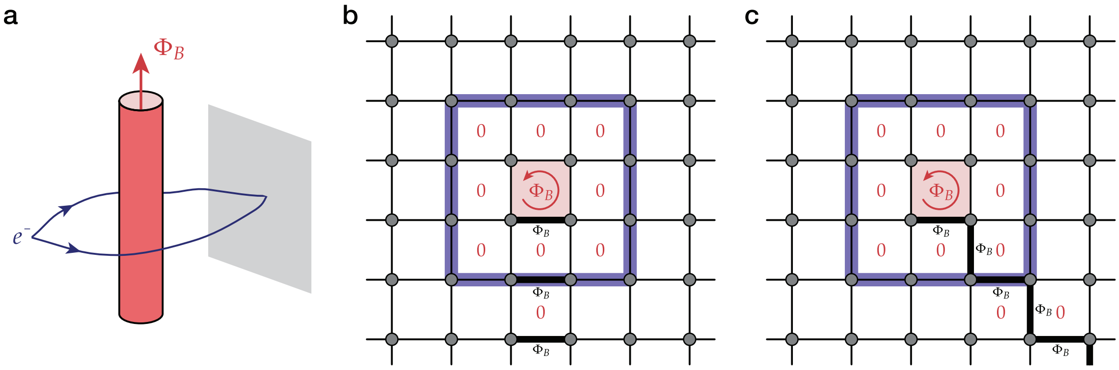

Figure 1.1.: Aharonov-Bohm effect on a lattice. **a** The Aharonov-Bohm effect describes an interferrometric experiment with an electron e^- that moves around an infinitely long coil. The electron remains thereby always outside of the coil, where the magnetic field is zero. However, the interference pattern depends on the strength of the magnetic field inside the coil. Therefore, the magnetic field acts at a distance, which is a property a field should not have. The vector potential, on the other hand, provides this local description. **b-c** A lattice version of the Aharonov-Bohm effect. A single, central plaquette is pierced by a flux Φ_B; the plaquettes around it carry zero flux. The blue square, shows an exemplary path of the particle around the magnetic field region. **b** and **c** represent two possible gauges of the vector potential. Here, it becomes visible how the knowledge of the magnetic field region propagates outwards and local knowledge for every path is reflected in the vector potential.

1.2.2. Static homogeneous magnetic fields on a lattice

A static and homogeneous magnetic field piercing a 2D lattice can be represented by a Peierls phase pattern, a discrete version of the vector potential. The Peierls phase pattern thus also has a gauge degree-of-freedom analog to the vector potential. To emulate a homogeneous magnetic field, each plaquette needs to carry the same magnetic flux. Figure 1.2 shows an illustration of a possible phase pattern. Every lattice structure is defined by a translational symmetry and therefore involves a unit cell from which the entire lattice can be generated by unit translations along the lattice vector. First, assume a single particle in a lattice without flux. The particle has a quantized single-particle energy spectrum of discrete Bloch bands. The associated length scale is the lattice spacing d and the unit cell is a square with area d^2, containing exactly one lattice site. If now a magnetic field is applied, a second length scale $l_B = \sqrt{\hbar/eB}$ appears, which is the magnetic length. This new length scale changes the translational symmetry. Instead of the lattice unit cell a new magnetic unit cell needs to be taken into consideration. The new magnetic unit cell also needs to satisfy the translational properties of the underlying lattice structure, while containing an integer number of magnetic flux quanta [85]. In terms of Peierls phases, the magnetic flux quantum corresponds to $\Phi_0 = 2\pi$. In consequence, for a rational flux

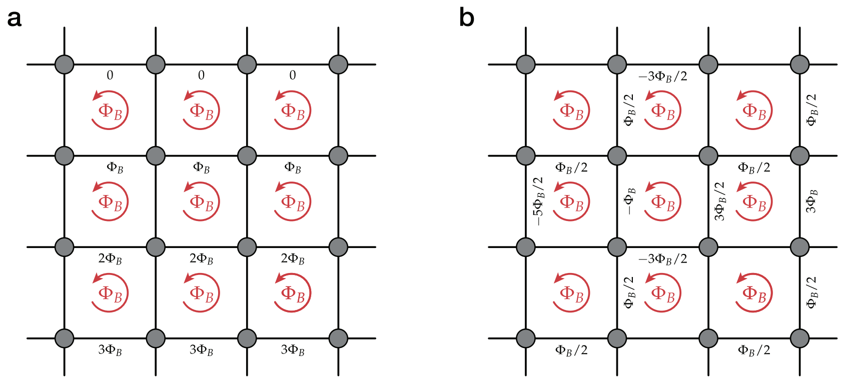

Figure 1.2.: Homogeneous flux patterns. a-b Two exemplary Peierls phase patterns that describe a homogeneous flux.

per lattice unit cell of $\Phi_B/\Phi_0 = p/q$, with p and q being integers, the magnetic unit cell has an area that is q times the area of a lattice unit cell, containing a flux of $2\pi\, p$. The number of sites in a unit cell is directly connected to the number of subbands. Therefore, a lattice pierced by a strong magnetic field on the order of a flux quantum per lattice unit cell, exhibits a fractal energy spectrum. For an underlying square lattice, the model is known as the Harper-Hofstadter model [86–88]. Its special fractal energy spectrum is called Hofstadter's butterfly [85].

The Harper-Hofstadter model obeys particular geometric and topological properties, which are intimately connected to the quantum Hall effect. In addition, the description in quasi-momentum space has close analogies to the formulation of electrodynamics [89]. Assuming the momentum representation of the Hamiltonian is $H_{\mathrm{HH}}(\mathbf{k})$, then an orthonormal basis can be introduced according to

$$H_{\mathrm{HH}}(\mathbf{k})\,|n(\mathbf{k})\rangle = \epsilon_n(\mathbf{k})\,|n(\mathbf{k})\rangle \tag{1.11}$$

except for a $\mathbf{k}$-dependent phase factor. This phase degree-of-freedom is equivalent to a gauge freedom: selecting an initial phase therefore corresponds to fixing the gauge. Consider the system in an eigenstate $|n(\mathbf{k}_0)\rangle$ and an adiabatic path Γ in the Brillouin zone from $\mathbf{k}_0$ to $\mathbf{k}_t$. During an adiabatic evolution, the system follows the instantaneous eigenstates according to the adiabatic theorem [90]. This determines the respective state at any point in time during the evolution independent of the evolution history. The respective phase, however, depends on this history and has two contributions: a dynamical part and a geometrical part. The dynamical part depends on the rate of change and energies along the path, while the geometric phase only depends on the specific path taken. The geometrical phase γ_n can be written as a path integral over a vector field and is

$$\gamma_n = \int_{\Gamma} \mathcal{A}_n(\mathbf{k})\,\mathrm{d}\mathbf{k} \tag{1.12}$$

with the vector field called Berry connection

$$\mathcal{A}_n(\mathbf{k}) = \mathrm{i} \, \langle n(\mathbf{k}) | \partial_{\mathbf{k}} | n(\mathbf{k}) \rangle \, . \tag{1.13}$$

The definition of the geometrical phase collected on a path through the Berry connection reminds us of the phase a particle acquires when moving through the vector potential in electrodynamics. The Aharonov-Bohm phase is indeed a specific example of a geometric phase. As discussed before, in electrodynamics the phase on closed paths is gauge-invariant and connected to the magnetic flux through the surface enclosed by the path. The same holds true for the geometric phases: the phase for open paths is gauge-variant, while the phase for closed loops, the Berry phase, is gauge-invariant [91]. The analogy can be continued by defining an equivalent quantity to the magnetic field as the curl of the Berry connection

$$\mathbf{\Omega}^n = \mathbf{\nabla} \times \mathcal{A}_n. \tag{1.14}$$

This quantity is the Berry curvature Ω^n_{xy}, which reduces to a scalar function for 2D systems

$$\Omega^n_{xy} = \mathrm{i} \left[\left\langle \partial_{k_x} n(\mathbf{k}) \middle| \partial_{k_y} n(\mathbf{k}) \right\rangle - \left\langle \partial_{k_y} n(\mathbf{k}) \middle| \partial_{k_x} n(\mathbf{k}) \right\rangle \right] . \tag{1.15}$$

Unlike the Berry connection, the Berry curvature is gauge-invariant [89] and therefore an observable quantity. It is important to emphasize that the presented concepts are independent of the model and the parameter space. The only requirement is a system represented by a Hamiltonian, which depends on time through a set of parameters [89]; here the exemplary set is $\mathbf{k} = (k_x, k_y)$.

In addition to geometric effects, the Harper-Hofstadter model also exhibits topologically nontrivial subbands, which arise due to broken time-reversal symmetry in the presence of a magnetic field. Formally, the topology of the subbands is characterized by the Chern number [92]. This topological invariant can be defined for every subband or connected group of subbands that is gapped. The Chern number ν_n is then given by the integral over the Berry curvature in the entire Brillouin zone

$$\nu_n = \oiint \Omega^n_{xy}(\mathbf{k}) \, \mathrm{d}^2\mathbf{k} \, . \tag{1.16}$$

Note that the Brillouin zone is a closed surface like the surface of an object. In mathematics, objects are characterized by the number of non-contactable points, or simply by their number of holes. Mathematically speaking, this can be expressed by the integral over the entire object's curvature. The result is an integer number – the genus [93, 94]. The equivalent to the genus in the topology of objects is the Chern number. Thus, the Chern number is also quantized, which has a far-reaching impact on the connected observables: namely robustness. The reason for this robustness is that a small deformation of the curvature will not influence the topology. In the picture of objects, this means that small deformations of the shape of the object will not change the number of holes. In the context of the quantum Hall effect, small deformations of the band structure therefore will not change an observable connected to the Chern number. Furthermore, it has been shown that this quantization remains robust even in the presence of many-body interactions and disorder [95–97].

1.2.3. Quantum simulation of the Harper-Hofstadter model

Entering the regime of the Harper-Hofstadter model experimentally in conventional solid state experiments is very challenging because for typical crystal lattice constants magnetic field strengths of several thousands Tesla would be required for a magnetic flux on the order of a flux quantum per lattice unit cell. A possible way to overcome this limitation is, for example, to artificially create a larger lattice spacing, or to implement the desired Peierls phases directly and create an artificial gauge field, rather than using a platform with charged particles and magnetic fields. A broad overview over different realizations can be found in [85] including e.g. photonics, phonons, and cold atoms. Here, only briefly a realization with cold atoms using Floquet engineering is mentioned as it serves as a seminal experiment for the experimental realization of the minimal instance for $\mathbb{Z}_2$ LGTs described in this thesis. This setting also allows to develop an intuition for implementing gauge fields in ultracold atomic quantum simulators by comparing it to the classical electrodynamics example.

The idea of creating effective magnetic fields in cold atoms goes back to Jaksch and Zoller [98], who proposed an implementation of tunneling processes between optical lattice sites, which are associated by a Peierls phase using a Raman coupling of two internal states. However, the first realizations of the Harper-Hofstadter model [65, 66] induced Peierls phases by laser-assisted tunneling [63]. In this approach, neighboring lattice sites are first energetically detuned such that atoms cannot tunnel between the sites. Then, tunneling is restored by periodically modulating the on-site energy with a frequency matched to the detuning. The resulting time-periodic Hamiltonian can be expressed in a series of time-independent components using Floquet expansion [99, 100]. The phase of the periodic modulation is thereby imprinted on the tunneling in the high-frequency limit [69, 101, 102]. Such a periodically-driven system is discussed in more detail in Sec. 2.2 in the context of the implementation of the $\mathbb{Z}_2$ minimal instance. It is important to recognize that this implementation does not only realize a magnetic field with any gauge description but instead realizes a very specific, fixed gauge pattern (Fig. 1.2). Moreover, these specific gauge patterns can in fact be observed in time-of-flight experiments.

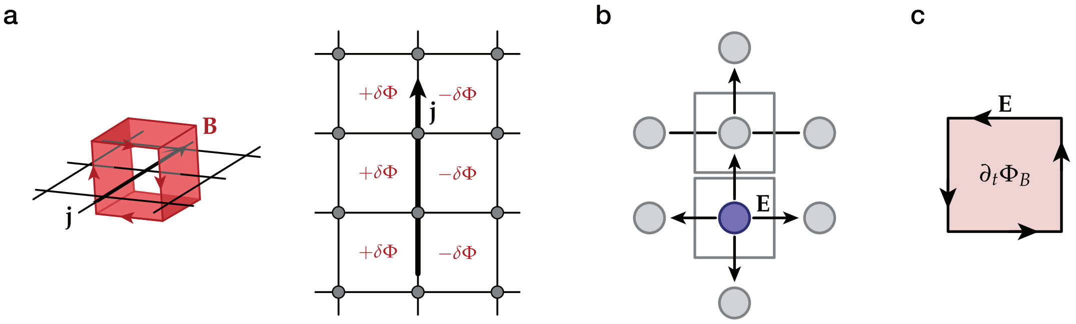

Figure 1.3.: Electrodynamics on a lattice. **a** Particles that flow along a path through the lattice create a current **j**. The current induces a magnetic field **B** according to Ampère's law, which changes the plaquette flux on the left and right side of the current by $\pm\delta\Phi_B$. **b** Illustration of Gauss's law. Gray circles describe empty, blue circles occupied lattice sites, and the black arrows the electric field lines **E**. The gray squares describe closed surfaces around lattice sites (a closed surface corresponds to a closed line in two dimensions). The surface enclosing an empty side has the same amount of electric field going inside and outside of the surface, while for the surface that does enclose a charge, the sum of the electric field lines through the surface is non-zero. Hence, charges are the sources of electric field lines. **c** According to Faraday's law, changes in the magnetic flux $\partial_t\Phi_B$ induce curly electric field lines.

1.2.4. Backaction requires gauge degree-of-freedom

The discoveries associated with particles in strong magnetic fields are remarkable and most prominently underlined by the detection of the celebrated integer [103] and fractional quantum Hall effects [104]. The implementation of artificial gauge fields, e.g. with ultracold atoms, serves as a playground to study the topological effects of particles in strong and static background fields. It has already led to the measurement of topological bulk transport of particles filling the lowest subbands of the Hofstadter model and with it the determination of the lowest band's Chern number [105]. If the Harper-Hofstadter model is realized in a single-site-resolving quantum gas experiment [70], where strongly interacting particles can be combined with local manipulation techniques, signatures of fractional quantum-Hall states might be observable [106–109]. Note that there is no effect of the particles, representing in fact charges, on the gauge field, as the gauge field is static by construction. To facilitate this kind of back effect as implicated by Maxwell's equations, the gauge field needs to obtain a gauge degree-of-freedom. On the lattice, this effectively corresponds to variable Peierls phases, which are represented as a degree-of-freedom on each link. However, not all degrees-of-freedom are independent but instead they are constrained by a local gauge symmetry, which is defined by local gauge generators. The gauge symmetry restricts the accessible physical states to a subset of the Hilbert space and is therefore sometimes also referred to as a gauge structure [44].

For the matter–gauge coupling given by electrodynamics, the local gauge symmetry operators need to satisfy Ampère's, Gauss's, and Faraday's law. The associated phenomenology is illustrated in Fig. 1.3. A matter current needs to induce a curly magnetic field and thereby the flux through the plaquetts on the left and right side of the current change in opposite directions. Furthermore, the matter particles carry a charge and should therefore be the sources of electric fields. Moreover, positive and negative charges should attract each other and an electric field line should connect them. In addition, a change in the magnetic field should induce a curly electric field. The resulting LGT would then be an Abelian $U(1)$ LGT coupled to matter.

Quantum simulations of gauge theories have been proposed for a variety of platforms [50], including superconductiong qubits [110, 111], Rydberg atoms [112–114], trapped ions [115], and ultracold atoms in optical lattices [116–122]. Furthermore, minimal implementations, e.g. of the Schwinger model with quantum-classical algorithms [123] and with a digital quantum computer composed of four trapped ions [124], have been realized. One possibility to implement the gauge degree-of-freedom is to realize density-dependent Peierls phases [62, 125], which have been observed in experiments [78, 126] and will be used in the context of this thesis as well [17].

1.3. From $U(1)$ to $\mathbb{Z}_2$ lattice gauge theories

1.3.1. Global and local gauge symmetry for matter tunneling

For a more formal introduction to LGTs coupled to matter, a Hubbard-type Hamiltonian of interacting particles is considered

$$H = J \sum_{\langle i,j \rangle} \left(\hat{a}_i^\dagger \hat{a}_j + \text{h.c.} \right) + \sum_i \mu_i \, \hat{a}_i^\dagger \hat{a}_i \,, \tag{1.17}$$

where $\hat{a}_i^\dagger$ creates a matter particle on site i, $\sum_{\langle i,j \rangle}$ denotes the sum over neighboring sites J is hopping matrix element, and μ_i a local chemical potential. The Hamiltonian is invariant under a global unitary gauge transformation $\hat{\mathcal{V}} \in U(1)$ for spinless particles and in the case of spinfull particles with N spin components it is invariant under a transformation with $\hat{\mathcal{V}} \in SU(N)$

$$\hat{a}_i \to \hat{\mathcal{V}} \, \hat{a}_i \,, \qquad \hat{a}_i^\dagger \to \hat{a}_i^\dagger \, \hat{\mathcal{V}}^\dagger. \tag{1.18}$$

This symmetry corresponds to the conservation of the total matter particle number $N_{\text{tot}} = \sum_i \hat{a}_i^\dagger \hat{a}_i$ and underlines an important feature of the matter field. However, LGTs coupled to matter have a local gauge symmetry. Therefore, also local symmetry transformations

$\hat{\mathcal{V}}_i$ need to be considered, which are unitary elements of the gauge group [56]. The transformations of the matter field are then

$$\hat{a}_i \to \hat{\mathcal{V}}_i \, \hat{a}_i \,, \qquad \hat{a}_i^\dagger \to \hat{a}_i^\dagger \, \hat{\mathcal{V}}_i^\dagger . \tag{1.19}$$

The chemical potential term of the Hamiltonian (1.17) remains intact under this local transformation as the term is also purely local. The particle hopping process, however, changes to

$$\hat{a}_i^\dagger \hat{a}_j \to \hat{a}_i^\dagger \hat{\mathcal{V}}_i^\dagger \hat{\mathcal{V}}_j \, \hat{a}_j \, . \tag{1.20}$$

In conclusion, the pure hopping term cannot appear in a LGT coupled to matter. Each hopping process of a matter particle needs to be accompanied by an additional local coupling to the gauge field degree-of-freedom. Formally, this means that every link $\langle i,j \rangle$ needs to be associated with a local connection $\hat{\mathcal{U}}_{\langle i,j \rangle}$, which is an element of the gauge group and satisfies the property

$$\hat{\mathcal{U}}_{\langle i,j \rangle} \to \hat{\mathcal{V}}_i \, \hat{\mathcal{U}}_{\langle i,j \rangle} \hat{\mathcal{V}}_j^\dagger . \tag{1.21}$$

In conventional, Wilsonian minimally-coupled LGTs, the connection is chosen to be unitary. This has many advantages, but other choices are in general also possible [56]. Including the local connection results in a Hamiltonian with matter–gauge coupling

$$H = J \sum_{\langle i,j \rangle} \left(\hat{a}_i^\dagger \, \hat{\mathcal{U}}_{\langle i,j \rangle} \, \hat{a}_j \, + \text{h.c.} \right) + \sum_i \mu_i \, \hat{a}_i^\dagger \hat{a}_i \, . \tag{1.22}$$

We will continue by selecting explicit Abelian groups for the local gauge transformations. Starting with a LGT based on the group $U(1)$, although historically Wegner's Ising LGT was developed earlier [22]. The Ising LGT is based on the cyclic group $\mathbb{Z}_2$ and will be in the focus of this part of the thesis. The $U(1)$ LGT is a continuous generalization of the Ising LGT initially developed by Wilson and Polyakov [127–129] and later reformulated by Kogut and Susskind using a Hamiltonian formulation [130]. It describes compact quantum electrodynamics (cQED) and therefore provides many analogies to the classical electrodynamics.

1.3.2. $U(1)$ lattice gauge theories

The Peierls phases represent a discrete version of the vector potential. They serve as the group parameters θ_{ij} to generate elements of the circle group $U(1)$ together with the scalar group generator $\hat{T} = \mathbb{1}$. In general, the group parameter can be vector valued $\bar{\theta}_{ij}$ parameterizing a set of Hermitian group generators $\hat{T}$, e.g. the set of Pauli-matrices to generate the Lie algebra of $SU(2)$. The resulting gauge group elements can then be identified with the connection

$$\hat{\mathcal{U}}_{\langle i,j \rangle} = \mathrm{e}^{\mathrm{i}\bar{\theta}_{ij}\hat{T}} . \tag{1.23}$$

For the Abelian group $U(1)$, the connection is simply $\hat{\mathcal{U}}_{\langle i,j\rangle} = \mathrm{e}^{\mathrm{i}\theta_{ij}}$. The Peierls phase θ_{ij} therein represent the angular position on a circle [56]. Note that the Peierls phases are defined between neighboring sites with ordered indices, e.g. left to right. In analogy to the position and momentum operators x and p forming a canonical pair, a conjugate angular momentum to the Peierls phase can be defined [130]

$$\hat{L}_{\langle i,j\rangle} = -\mathrm{i}\hbar \, \frac{\partial}{\partial \theta_{ij}}. \tag{1.24}$$

It obeys the following commutation relation

$$\left[\theta_{ij}, \hat{L}_{\langle i',j'\rangle}\right] = \mathrm{i}\hbar \, \delta_{i,i'} \, \delta_{j,j'}. \tag{1.25}$$

As $\hat{L}_{\langle i,j\rangle}$ is a momentum operator, it is suggestive that the kinetic energy is

$$\hat{H}^{\mathrm{kin}}_{U(1)} \propto \sum_{\langle i,j\rangle} \hat{L}^2_{\langle i,j\rangle}. \tag{1.26}$$

This term reminds strongly of the electric field energy $\frac{1}{2}E^2$. Therefore, it seems natural to identify $\hat{L}_{ij}$ as an electric field. This connection can be underlined following Koguts argument [130] by comparing the commutation relation to continuum electrodynamics. First, the Peierls phases are associated back to the vector potential by the relation $\theta_{ij} = dgA_{ij}$, with d the lattice spacing and g^2 the electromagnetic coupling constant. Then the commutation relation Eq. (1.25) can be rewritten as

$$\frac{g}{d^2}\left[A_{ij}, \hat{L}_{\langle i',j'\rangle}\right] = \mathrm{i}\hbar \, \frac{\delta_{i,i'}}{d^3} \, \delta_{j,j'}, \tag{1.27}$$

where $\delta_{i,i'}/d^3$ is the discrete form of the Dirac delta function. A comparison to the continuum form of this commutation relation reveals that $E_{ij} = \frac{g}{d^2}\hat{L}_{\langle i,j\rangle}$ [56, 130].

With the notion of an electric field, it is further possible to more formally describe Gauss's law. The operator $\hat{Q}_i$ describes a dynamical charge on the ith lattice site and is connected to the matter field. This dynamical charge is the source of the electric field lines. Therefore, the charge and the field lines need to be locally connected. This local connection is provided by the gauge transformation generator

$$\hat{G}_i = \sum_{j\in +} \hat{L}_{\langle i,j\rangle} - \hat{Q}_i. \tag{1.28}$$

Note that $\hat{L}_{\langle i,j\rangle} = \hat{L}^{\dagger}_{\langle j,i\rangle} = -\hat{L}_{\langle j,i\rangle}$ and therefore the sum over all links connected to the site i, indicated by the symbol $\sum_{j\in +}$, resembles the discrete version of the divergence, leading to

$$\hat{G}_i = \boldsymbol{\nabla} \cdot \hat{L}_i - \hat{Q}_i \tag{1.29}$$

in the continuum limit [56]. Here, the connection to Gauss's law is obvious. Any LGT that follows Gauss's law will commute with $\hat{G}$ everywhere and vice versa, if a LGT commutes with $\hat{G}$ it fulfills Gauss's law.

The meaning of θ_{ij} and $\hat{L}_{ij}$ has now become apparent but what exactly is $\hat{\mathcal{U}}_{ij}$? The connection $\hat{\mathcal{U}}$ is a raising and $\hat{\mathcal{U}}^\dagger$ a lowering operator of the electric field on the link as $\left[\hat{L}, \hat{\mathcal{U}}\right] = \hat{\mathcal{U}}$. This can be seen by applying m-times the raising operator on a state $\hat{L}\left|0\right\rangle = 0$, which leads to

$$\left(\hat{\mathcal{U}}\right)^m \left|0\right\rangle = \mathrm{e}^{\mathrm{i}m\theta} \left|0\right\rangle = \left|m\right\rangle . \tag{1.30}$$

Testing this state with the electric field operator will reveal that the electric field was raised m-times as $\hat{L}\left|m\right\rangle = m\left|m\right\rangle$.

A representation of the electric field energy was already found above, but how can the magnetic energy be represented? To this end it is useful to define a plaquette term

$$B_\square = \sum_{\langle i,j\rangle \in \square} \theta_{ij}, \tag{1.31}$$

which we know should be gauge-invariant and belong to the magnetic field. The relevant field energy is then given by [130]

$$H^B_{U(1)} \propto \sum_r \mathrm{tr}\Big(\prod_{\langle i,j\rangle \in \square_r} \hat{\mathcal{U}}_{\langle i,j\rangle} \Big) + \mathrm{h.c.} = \sum_r \cos\left(B_{\square_r}\right). \tag{1.32}$$

In the classical continuum limit, the plaquette flux is small and the cosine can be approximated to second order

$$\cos\left(B_\square\right) \approx 1 - \frac{1}{2} B_\square^2 \tag{1.33}$$

and the well-known scaling of the magnetic field energy arises [130].

Combining the electric and magnetic part of the Hamiltonian leads to the Kogut-Susskind representation of cQED [56, 130]

$$H_{\mathrm{KS}} = \frac{g^2}{2} \sum_{\langle i,j\rangle} \hat{L}^2_{\langle i,j\rangle} - \frac{1}{g^2} \sum_r \cos\left(B_{\square_r}\right). \tag{1.34}$$

1.3.3. $\mathbb{Z}_N$ lattice gauge theories

The $U(1)$ LGT discussed above is a continuous Abelian LGT and has a countable but infinite number of local degrees-of-freedom. The LGT based on the cyclic group $\mathbb{Z}_N$ can be viewed as a discrete version of $U(1)$ and is therefore not a Yang-Mills theory [56]. It is a discrete version in the sense that in the limit $N \to \infty$ it can be formally related to a $U(1)$ LGT, e.g. cQED, which is an interesting aspect as cQED in (3+1) dimensions features a confining and a non-confining phase [60]. Furthermore, $\mathbb{Z}_N$ and especially $\mathbb{Z}_3$ LGTs play an important role in the description of confinement in quantum chromodynamics (QCD) [130–133].

The gauge theory is again based on a set of unitary link operators $\hat{Z}^\dagger \hat{Z} = \hat{X}^\dagger \hat{X} = \mathbb{1}$, which in this case satisfy the $\mathbb{Z}_N$ algebra [60]

$$\hat{X}^N = \hat{Z}^N = \mathbb{1}, \qquad \hat{X}^\dagger \hat{Z} \hat{X} = \mathrm{e}^{\mathrm{i}\alpha} \hat{Z}, \tag{1.35}$$

with $\alpha = 2\pi/N$ and N an integer. This group can be interpreted as the cyclic stepwise rotation on a circle reaching the initial state after N steps. The operators do not commute according to their definition (1.35) and mutually serve as ladder operators for the respective other operator's eigenstates. Assume the eigenstates of $\hat{X}$ are $|m\rangle$, such that

$$\hat{X} |m\rangle = \mathrm{e}^{\mathrm{i}m\alpha} |m\rangle \,, \tag{1.36}$$

then $\hat{Z}$ is a lowering operator

$$\hat{Z} |m\rangle = |m-1\rangle \,. \tag{1.37}$$

The $\mathbb{Z}_N$ algebra contains N states and the ladder operators connect them cyclically [56], e.g. $\hat{Z} |0\rangle = |N-1\rangle$.

1.3.4. $\mathbb{Z}_2$ lattice gauge theories

The $\mathbb{Z}_2$ or Ising LGT constitutes one of the simplest type of a LGTs. It appears in the description of a variety of strongly correlated systems [44, 134]. One way of writing an appropriate LGT for an interacting fermionic system is to transform it to the slave-boson representation. This representation includes auxiliary fermionic, and so-called slave-boson fields, as in a LGT coupled to fermionic matter [135]. In a $\mathbb{Z}_2$ slave-boson theory [35], the fermionic matter field then carries a $\mathbb{Z}_2$ charge. In order to obtain this spin–1/2 degrees-of-freedom of the fermion Hilbert space, it is projected onto the local $\mathbb{Z}_2$-charge-neutral subspace. The emerging low energy effective theories of such models can feature $SU(2)$, $U(1)$ or $\mathbb{Z}_2$ gauge fluctuations [34]. With this technique e.g. $\mathbb{Z}_2$ spin liquids with gapless spin-1/2 excitations were identified in the context of d-wave superconductivity [34, 35]. Moreover, for the description of Cooper pairing, such gauge theories are relevant because of their confinement-deconfinement transition in $(2+1)$D [34]. Furthermore, $\mathbb{Z}_2$ LGTs are applied in the analysis of spin liquids in frustrated magnetic systems [36, 37, 40]. It was shown that an exotic $\mathbb{Z}_2$ spin liquid indeed exists e.g. in the nearest-neighbor Heisenberg model on the kagome lattice. This conclusion was found by analyzing frustration effects on infinitely long cylinders with finite odd or even circumference [136]. A recent study of the 2D version of this model investigated the vision confinement transitions between the

$\mathbb{Z}_2$ gauge theory and valence bond solid states [137]. Here, visions are vertices carrying a $\mathbb{Z}_2$ magnetic flux. This was independently verified by a model based on a different $\mathbb{Z}_2$ gauge theory, using the quantum dimer model approximation of the original kagome Heisenberg-model [138]. Moreover, symmetry-breaking topological insulators [139] and Kitaev's toric code [140] are examples for applications of $\mathbb{Z}_2$ LGTs.

The pure $\mathbb{Z}_2$ LGT was studied extensively, starting with Wegner back in the 1970th [22]. $\mathbb{Z}_2$ LGTs coupled to matter, on the other hand, were studied comparably less [134]. For gapped matter degrees-of-freedom, phenomena at energies much below this energy gap can be solved perturbatively by reducing the LGT coupled to matter to a pure LGT, for which in many situations reliable results for the low-energy behavior can be calculated and also the phase diagrams are typically well-known [134]. For a coupling to gapless bosonic matter fields Fradkin und Shenker provided central insights into the phase diagram [141]. For a coupling to gapless fermionic matter fields, however, only little is known [134], even though recently great progress was made promising further advances [48].

A $\mathbb{Z}_2$ LGT is a special case of the $\mathbb{Z}_N$ LGT discussed in Sec. 1.3.3. The operators of the $\mathbb{Z}_2$ group have only two eigenvalues, which are connected by a rotation of π. A possible representation of the operators $\hat{X}$ and $\hat{Z}$ are the Pauli matrices $\hat{\tau}$

$$\hat{X} = \hat{\tau}^x, \qquad \hat{Z} = \hat{\tau}^z. \tag{1.38}$$

Each of them needs to be a ladder operator for the other operators' eigenstates. Let the eigenstates of $\hat{\tau}^z$ be $|\pm1\rangle$ such that $\hat{\tau}^z |\pm1\rangle = \pm|\pm1\rangle$. Then $\hat{\tau}^x$ is a cyclic (ladder) operator on these eigenstates with $\hat{\tau}^x |\pm1\rangle = |\mp1\rangle$. The eigenstates of $\hat{\tau}^x$ in this basis are $|\pm\rangle = (|+1\rangle \pm |-1\rangle)/\sqrt{2}$. Applying $\hat{\tau}^z$ to these eigenstates verifies that it is also a cyclic ladder operator as $\hat{\tau}^z |\pm\rangle = |\mp\rangle$.

The Peierls phases of the $\mathbb{Z}_2$ group are $\theta_{ij} = \{0, \pi\}$ with an additional global $U(1)$ gauge degree-of-freedom. The associated connection $\hat{U}_{\langle i,j\rangle} = \mathrm{e}^{\mathrm{i}\theta_{ij}}$ can be represented by the z-Pauli matrix $\hat{\tau}^z_{\langle i,j\rangle}$ on each link. Note that again the links are defined directional, i.e. from left to right and bottom to top, which means traversing a link in the opposite direction requires to take the link operator's conjugate transpose. Here in the $\mathbb{Z}_2$ case, this seems irrelevant as all operators can be chosen real. However, the global $U(1)$ gauge degree-of-freedom of the $\mathbb{Z}_2$ LGT appears only in this general formulation. As explained above, the ladder operator of the connection can be interpreted as the electric field. Here, $\hat{\tau}^x_{\langle i,j\rangle}$ is the ladder operator of the connection $\hat{\tau}^z_{\langle i,j\rangle}$ and therefore $\hat{\tau}^x_{\langle i,j\rangle}$ represents the $\mathbb{Z}_2$ electric field.

The pure $\mathbb{Z}_2$ LGT can then be constructed from magnetic and electric energy terms

$$\hat{H}_{\mathbb{Z}_2} = -J_B \sum_r \prod_{\langle i,j\rangle \in \square_r} \hat{\tau}^z_{\langle i,j\rangle} - J_f \sum_{\langle i,j\rangle} \hat{\tau}^x_{\langle i,j\rangle} \tag{1.39}$$

and a fermion field can be minimally coupled to this $\mathbb{Z}_2$ gauge field by associating the motion of the fermions with a change in the electric field

$$\hat{H}_m = -J_a \sum_{\langle i,j\rangle,\sigma} \hat{c}^{\dagger}_{i,\sigma} \hat{\tau}^{z}_{\langle i,j\rangle} \hat{c}_{j,\sigma} + \text{h.c.} - \mu \sum_{i,\sigma} \hat{c}^{\dagger}_{i,\sigma} \hat{c}_{i,\sigma}. \tag{1.40}$$

Here, $\square_r$ is a plaquette with lower left site r. $\langle i,j\rangle$ denotes a link and $\hat{c}^{\dagger}_{i,\sigma}$ is a fermionic creation operator at site i with spin σ. J_B and J_f are the magnetic and electric field energy, respectively, J_a is the matter hopping amplitude, and μ the chemical potential [48].

The Gauss's law for the $\mathbb{Z}_2$ LGT is

$$\hat{G}_j = (-1)^{\hat{n}^a_j} \prod_{i\in +_j} \hat{\tau}^{x}_{\langle i,j\rangle}, \tag{1.41}$$

where the product runs over all links connected to the site j, indicated by $+_j$, and $\hat{n}^a_i = \sum_\sigma \hat{c}^{\dagger}_{i,\sigma} \hat{c}_{i,\sigma}$. The Gauss's law restricts every state evolution to a physical subspace of the full Hilbert space. The operator $\hat{G}_j$ commutes on all sites with the Hamiltonian $\left[\hat{G}_j, \hat{H}_{\mathbb{Z}_2} + \hat{H}_m\right] = 0$. This leads to a set of locally conserved quantities $\{g_j\}$. These locally conserved set of quantities $\{g_j\}$ define each of the subspaces and can be interpreted as background charges at the site where $g_j = -1$. Typically, the physical subspace is chosen to be the set without any background charges $g_j = +1$ for all j. For this even sector a sign-problem free analysis can be performed [48]. In the odd sector, where $g_j = -1$ for all j, such an analysis can only be performed for half-filling, due to an exact mapping between the odd and the even sector [48].

2. Minimal instance for $\mathbb{Z}_2$ LGTs coupled to matter

2.1. $\mathbb{Z}_2$ lattice gauge theories coupled to matter

2.1.1. Elementary ingredients

In this chapter, the focus lies on an intuitive understanding of the basic ingredients relevant for a $\mathbb{Z}_2$ LGT as well as a possible implementation of these ingredients. It is instructive to restrict the discussion to a simple 1D system. However, 1D LGTs do not provide a magnetic plaquette term. An illustration of the elementary ingredients is shown in Fig. 2.1. The considered extended one-dimensional model is captured by the following

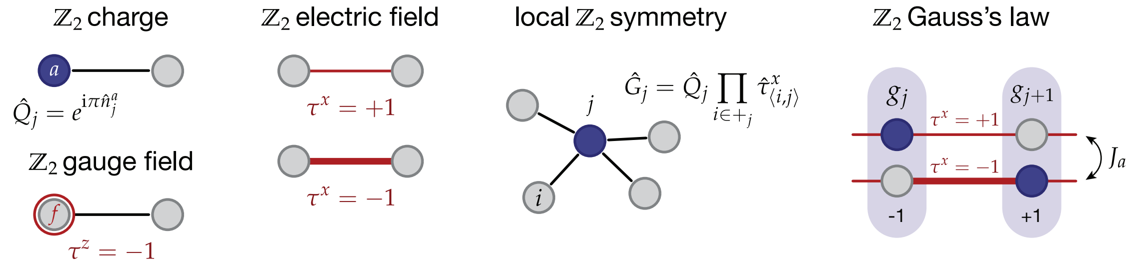

$\mathbb{Z}_2$ charge
a
$\hat{Q}_j = e^{i\pi\hat{n}^a_j}$
$\mathbb{Z}_2$ gauge field
f
$\tau^z = -1$
$\mathbb{Z}_2$ electric field
$\tau^x = +1$
$\tau^x = -1$
local $\mathbb{Z}_2$ symmetry
$\hat{G}_j = \hat{Q}_j \prod_{i \in +_j} \hat{\tau}^x_{\langle i,j \rangle}$
j
i
$\mathbb{Z}_2$ Gauss's law
g_j
g_{j+1}
$\tau^x = +1$
$\tau^x = -1$
J_a
-1
+1

Figure 2.1.: Basic ingredients of $\mathbb{Z}_2$ lattice gauge theories coupled to matter. Gray circles describe empty lattice sites and blue circles the lattice sites occupied by a $\mathbb{Z}_2$ charge; the lines between the circles illustrate the links. The matter is encoded by a species, named a, that moves freely in the lattice. The $\mathbb{Z}_2$ charge $\hat{Q}_j = \mathrm{e}^{i\pi\hat{n}^a_j}$ (blue) is the parity of the site occupation of the matter species. The $\mathbb{Z}_2$ gauge field $\hat{\tau}^z_{\langle j,j+1 \rangle}$ is a two-valued degree-of-freedom on each link, which is illustrated by a red circle around the right and left site corresponding to $\tau^z = \pm 1$, respectively. This is illustrated by the red circle either around the left or right site. The coupling of these two states of the gauge field then describes the $\mathbb{Z}_2$ electric field energy $\hat{\tau}^x_{\langle j,j+1 \rangle}$, which has two eigenvalues $\tau^x = \pm 1$ (thin and thick red lines). The local symmetry operator $\hat{G}_j$ connects the local charge with the local electric-field environment. According to Gauss's law the eigenvalues of $\hat{G}_j$ are conserved quantities g_j. The matter–gauge coupling occurs with strength J_a.

Hamiltonian

$$\hat{H}_{\mathbb{Z}_2} = -\sum_j \left(J_a \, \hat{\tau}^z_{\langle j,j+1\rangle} \hat{a}^\dagger_j \hat{a}_{j+1} + \text{h.c.} \right) - \sum_j J_f \, \hat{\tau}^x_{\langle j,j+1\rangle}, \tag{2.1}$$

where $\hat{a}^\dagger_j$ creates a matter particle on lattice site j. The matter particle tunnels along the chain with a tunneling rate J_a, while coupling to the local gauge-field degrees-of-freedom. For $\mathbb{Z}_2$ LGTs, these local gauge-field degrees-of-freedom have two possible states and are represented by Pauli operators $\hat{\tau}_{\langle j,j+1\rangle}$, which are defined on the links between neighboring lattice sites. Figuratively speaking, this means that a spin-1/2 is on each link, which represents the gauge field degree-of-freedom that interacts with the matter. Depending on the state $\hat{\tau}^z_{\langle j,j+1\rangle}$ of this $\mathbb{Z}_2$ gauge field – up or down in the spin picture – the tunnel process of the matter acquires a phase of $\{0, \pi\}$. Furthermore, a $\mathbb{Z}_2$ charge

$$\hat{Q}_j = \mathrm{e}^{i\pi \hat{n}^a_j} \tag{2.2}$$

is associated with the matter field at every site j; it is given by the parity of the site occupation $\hat{n}^a_j = \hat{a}^\dagger_j \hat{a}_j$. In addition to the matter dynamics, which is locally coupled to the gauge field, the second term in Eq. (2.1) introduces dynamics of the gauge field itself and couples the two states with strength J_f. In analogy to electrodynamics, this term $J_f \hat{\tau}^x$ is referred to as $\mathbb{Z}_2$ electric field (Sec. 1.3).

A special characteristic of LGTs is that they do not only fulfill global symmetries but are also invariant under local gauge transformations. A local gauge transformation generator for a $\mathbb{Z}_2$ LGTs is given by

$$\hat{G}_j = \hat{Q}_j \prod_{i \in +_j} \hat{\tau}^x_{\langle i,j\rangle}, \tag{2.3}$$

where $\prod_{i\in +_j}$ denotes the product over all links connected to the lattice site j. A Hamiltonian $\hat{H}$ preserves the gauge symmetry when it commutes with the gauge transformation generator

$$\left[\hat{H}, \hat{G}_j\right] = 0 \quad \forall j. \tag{2.4}$$

In our model Hamiltonian Eq. (2.1), both terms commute with the gauge transformation separately. For the matter–gauge interaction [first term in Eq. (2.1)], this becomes clear as the term factorizes in the two anticommuting contributions $\hat{\tau}^x_{\langle j,j+1\rangle} \hat{\tau}^z_{\langle j,j+1\rangle} = -\hat{\tau}^z_{\langle j,j+1\rangle} \hat{\tau}^x_{\langle j,j+1\rangle}$ and $\hat{Q}_j \hat{a}^\dagger_j \hat{a}_{j+1} = -\hat{a}^\dagger_j \hat{a}_{j+1} \hat{Q}_j$; for the electric field energy, it is apparent because it only contains the operator $\hat{\tau}^x$. The fact that the Hamiltonian stays intact under these local gauge transformations leads to locally conserved quantities. Therefore, the physical Hilbert space $\mathfrak{H}$ inherits the gauge invariance and separates into isolated sectors

$$\mathfrak{H} = \bigotimes_{\{g_j\}} \mathfrak{H}\left(\{g_j\}\right). \tag{2.5}$$

Each sector is characterized by a set of eigenvalues $\{g_j\}$ of the gauge transformation generator $\hat{G}_j$ [56]. These different sets of eigenvalues can be interpreted as different configurations of static background charges placed on all sites with $g_j = -1$. Note that the dynamics cannot change these static charges and any physical state $|\psi(\{g_j\})\rangle \in \mathfrak{H}(\{g_j\})$ remains in sector $\mathfrak{H}(\{g_j\})$. This is summarized by the generalized Gauss's law

$$\hat{G}_i \left|\psi\left(\{g_j\}\right)\right\rangle = g_i \left|\psi\left(\{g_j\}\right)\right\rangle, \tag{2.6}$$

which is at the heart of LGTs. The microscopic manifestation of Gauss's law and the consequences on the matter–gauge dynamics is discussed for the 1D model in the next section.

2.1.2. Basic dynamics in 1D

Let the 1D model (2.1) be initially prepared in the eigenstate of the electric field operator with $\tau^x = +1$ on all links. Furthermore, a single matter particle is located on site $j = 0$. Therefore, the locally conserved quantities are $g_j = +1$ for all $j \neq 0$ and $g_0 = -1$ at the position of the matter particle. This initial state is illustrated in Fig. 2.2. When the matter particle moves along the 1D chain, the electric field value changes on all traversed links according to Gauss's law. In the limit of vanishing electric field energy $J_f \to 0$, these changes of the electric field value cost only a negligible amount of energy. Thus, the matter particle can tunnel freely along the 1D chain. However, in the limit of finite electric field energy $J_f \neq 0$, tunneling of the matter particle is detuned because changes of the electric field value have a finite energy cost. In consequence, the matter particle is confined to the location of the static background charge at $j = 0$ because the energy of the system increases linearly with the distance between the static charge and the matter particle in this regime [134].

2.1.3. Minimal instance

The extended 1D model can be perceived as a chain of minimal instances exhibiting $\mathbb{Z}_2$ symmetry. Each of these minimal instances is comprised of two sites connected by a $\mathbb{Z}_2$ link. In the next section, an implementation of this double well with $\mathbb{Z}_2$ symmetry is discussed; here the dynamics of the minimal instance is analyzed analytically. To this end, we restrict the Hamiltonian (2.1) to two sites and denote the two sites by left (L) and right (R). The Hamiltonian then reads

$$\hat{H}_{\mathbb{Z}_2\mathrm{DW}} = -J_a\, \hat{\tau}^z \left(\hat{a}_L^\dagger \hat{a}_R + \text{h.c.}\right) - J_f\, \hat{\tau}^x. \tag{2.7}$$

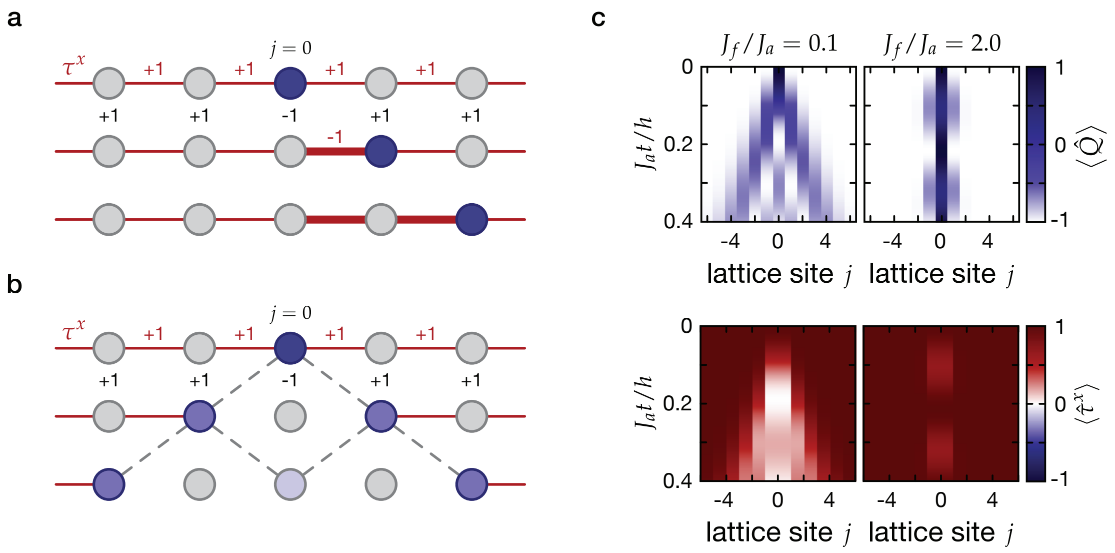

Figure 2.2.: Basic dynamics of a 1D $\mathbb{Z}_2$ LGT. The dynamics according to the 1D model captured by Hamiltonian (2.1) is illustrated and numerically analyzed using exact diagonalization on a system with 13 sites. Gray circles indicate empty lattice sites and blue circles the lattice sites occupied by a matter particle, here in fact the $\mathbb{Z}_2$ charge. The initial state for the dynamics is a single matter particle at site $j = 0$ and the gauge field in the eigenstate of the electric field operator $\hat{\tau}^x_{\langle j,j+1\rangle} = 1$ on all links $\langle j, j+1\rangle$. **a** Two possible consecutive tunneling processes of the matter particle starting from the initial state are shown. In each tunneling process, the matter particle tunnels a site to the right and according to Gauss's law the electric field value changes, here from $+1$ to -1 (thin and thick red lines). This is accompanied by an energy cost of $2J_f$. **b** A quantum tunneling process realizes a superposition of all tunneling processes possible. Therefore, the $\mathbb{Z}_2$ charge can be found with equal probability on either side of the cone (light blue circles). Furthermore, the expectation value of the traversed links $\langle\hat{\tau}^x\rangle$ is zero (links not displayed). The dashed lines indicate the possible tunneling path of the particles. **c** Numerical results for the time evolution of $\langle\hat{Q}\rangle$ and $\langle\hat{\tau}^x\rangle$ according to the 1D model for different values of J_f/J_a.

To capture the matter–gauge interaction, a single matter particle is placed on the minimal instance. The Hilbert space is four dimensional and can be represented by the basis states $|L,-1\rangle$, $|L,+1\rangle$, $|R,-1\rangle$, and $|R,+1\rangle$, which are simultaneous eigenstates of the charge and gauge-field operator $\hat{\tau}^z$. The label before the comma indicates the site occupied by the matter particle. The label after the comma shows the eigenvalue of the gauge-field operator $\hat{\tau}^z$. Note that in the case of a single matter particle, the $\mathbb{Z}_2$ charge is directly carried by the matter particle. Using these basis states in the order as listed above, the

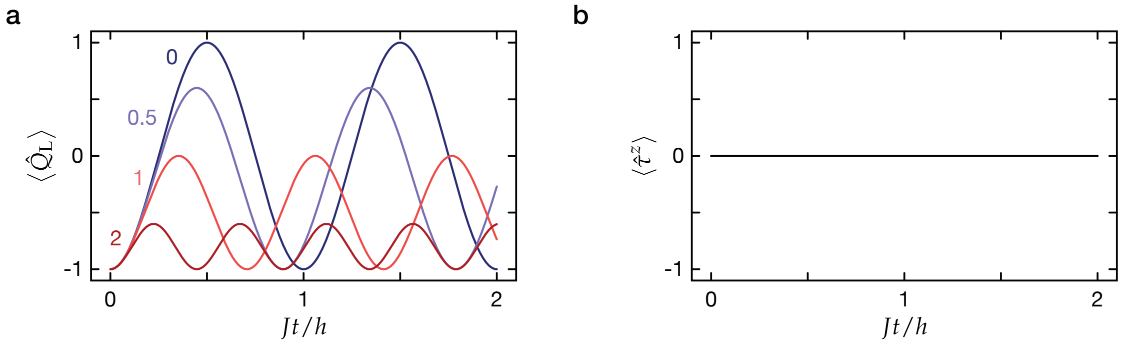

Figure 2.3.: Ideal dynamics of the minimal instance. a Time evolution of the expectation value of the $\mathbb{Z}_2$ charge $\langle \hat{Q}_\mathrm{L} \rangle$ according to Eq. (2.9) for different $J_f/J_a = 0, 0.2, 1, 2$. **b** Time evolution of the expectation value of the $\mathbb{Z}_2$ gauge field $\langle \hat{\tau}^z \rangle$ accoring to Eq. (2.10).

Hamiltonian in matrix form is

$$\bar{H}_{\mathbb{Z}_2\mathrm{DW}} = \begin{pmatrix} 0 & -J_f & +J_a & 0 \\ -J_f & 0 & 0 & -J_a \\ +J_a & 0 & 0 & -J_f \\ 0 & -J_a & -J_f & 0 \end{pmatrix}. \tag{2.8}$$

The time-evolution of the Hamiltonian is calculated by solving the time-independent Schrödinger equation $\bar{H}_{\mathbb{Z}_2\mathrm{DW}} |n\rangle = E_n |n\rangle$ and then applying the time-evolution operator to an initial state $|\psi_\mathrm{init}\rangle$. As already stated above, the initial state effectively defines the sector in which the time evolution occurs according to Gauss's law. In analogy to the 1D model, we choose an initial state where the matter particle is localized to one lattice site, the left site, and the gauge field is in an eigenstate of the electric-field operator $|\psi_\mathrm{init}\rangle = (|L,+1\rangle + |L,-1\rangle)/\sqrt{2}$. For this initial state, the locally conserved quantities are $g_\mathrm{L} = -1$ and $g_\mathrm{R} = +1$. The resulting expectation value of the $\mathbb{Z}_2$ charge is initially $\langle \hat{Q}_\mathrm{L} \rangle_\mathrm{init} = -1$ and oscillates according to

$$\langle \hat{Q}_\mathrm{L}(t) \rangle = -\frac{J_f^2 + J_a^2 \cos\left(2t\sqrt{J_f^2 + J_a^2}/\hbar\right)}{J_f^2 + J_a^2}, \tag{2.9}$$

while the expectation value of the $\mathbb{Z}_2$ gauge field is

$$\langle \hat{\tau}^z(t) \rangle = 0 \tag{2.10}$$

for all times (Fig. 2.3). This general property of the dynamics is per se not nontrivial; if the matter particle is not coupled to the gauge field, $-J_a\left(\hat{a}_L^\dagger \hat{a}_R + \hat{a}_R^\dagger \hat{a}_L\right) - J_f\,\hat{\tau}^x$, the expectation value of the charge will also oscillate $\langle \hat{Q}_\mathrm{L}(t) \rangle = -\cos(2J_a t/\hbar)$, while the expectation value of the gauge field is zero. However, the gauge–matter coupling has a strong influence on the oscillation amplitude and the oscillation frequency. The oscillation amplitude is $J_a^2/(J_a^2+J_f^2)$, i.e. it is 1 for $J_f=0$ and vanishes for $J_f\to\infty$. This behavior can be intuitively understood from the $\mathbb{Z}_2$ ingredients: Gauss's law forces a link, initially in the eigenstate of the electric field operator with eigenvalue $\tau^x=+1$, to change its state to the eigenstate with eigenvalue $\tau^x=-1$ when a matter particle traverses the link. According to Hamiltonian (2.7), this process has an energy cost of $2J_f$. Thus, the tunneling of the matter particle is detuned and is suppressed for large J_f. For the same reason, the oscillation frequency is initially $2J_a/h$ for $J_f=0$ and increases with J_f, analog to Rabi-oscillations.

2.2. Floquet implementation

2.2.1. Field-particle species representing the link degree-of-freedom

The minimal instance for $\mathbb{Z}_2$ LGTs consists of two sites connected by a link that has a $\mathbb{Z}_2$ degree-of-freedom (Sec. 2.1.3). Following the proposal [62], this gauge-field degree-of-freedom can be implemented using a particle that lives only on the sites that belong to the link. This field particle, referred to as f-particle, strongly interacts with the species representing the matter particle a. The gauge–matter coupling is then introduced by periodic modulation [69, 99, 101, 142] of the on-site energy at a frequency that matches the inter-species on-site interaction energy [72–78]. The resulting effective Floquet model realizes the minimal instance. Before presenting the implementation in detail, a short review of multiphoton processes in a periodically-driven two-site potential is presented, as it is the foundation of the implemented Floquet scheme.

2.2.2. Multiphoton processes in a periodically-driven two-site potential

The dynamics of time-periodic systems can be described by an effective Hamiltonian $\hat{H}_\mathrm{F}$ at stroboscopic time points, which are multiples of the system's driving period. This effective Floquet model can be described by a series expansion of time-independent terms in powers of $1/\omega$ [101, 142]. The series can be truncated to lowest order in the high frequency limit $\omega\to\infty$. Here, the effective Floquet Hamiltonian of a periodically-driven two-site potential occupied by a single particle is introduced. The renormalization of the tunnel coupling and the dependence of the tunnel phase on the modulation amplitude and phase as well as the sign of the energy offset between neighboring sites is derived to lowest order in the high-frequency expansion. This basic example provides a good intuition in order to understand the implementation of the $\mathbb{Z}_2$ minimal instance.

The Hamiltonian is written in the $|L\rangle$ and $|R\rangle$ basis indicating that the particle occupies the left or right site of the double well, respectively:

$$\hat{H}_{1\mathrm{P}}(t) = -J' \left(|L\rangle\langle R| + |R\rangle\langle L|\right) + \{\Delta + A\cos(\omega t + \phi)\} |L\rangle\langle L| . \tag{2.11}$$

Here, J' is the bare single-particle tunneling rate, Δ the energy offset between neighboring sites, A the modulation amplitude, ω the modulation frequency, and ϕ the modulation phase. Following references [69, 101], the infinite frequency limit of the effective Hamiltonian is calculated. This limit is equivalent to the lowest (zeroth) order of the Floquet expansion. To this end, a unitary transformation $|\psi\rangle \to |\psi'\rangle = \hat{R}(t)|\psi\rangle$ is chosen such that the new transformed Hamiltonian does not contain divergent terms in the high-frequency limit:

$$\hat{\mathcal{H}}(t) = \hat{R}\hat{H}(t)\hat{R}^\dagger - \mathrm{i}\hat{R}\partial_t\hat{R}^\dagger = \sum_{k\in\mathbb{Z}} \hat{\mathcal{H}}^{(k)} \mathrm{e}^{\mathrm{i}k\omega t}. \tag{2.12}$$

Furthermore, the transformed Hamiltonian is expressed in a series of time-independent components $\hat{\mathcal{H}}^{(k)}$. These components can be used to calculate the lowest orders of the Floquet Hamiltonian:

$$\hat{H}_\mathrm{F} = \hat{\mathcal{H}}^{(0)} + \frac{1}{\hbar\omega}\sum_{k>0}\frac{1}{k}\left[\hat{\mathcal{H}}^{(+k)}, \hat{\mathcal{H}}^{(-k)}\right] + \mathcal{O}\left(\frac{1}{\omega^2}\right). \tag{2.13}$$

A suitable transformation $\hat{R}$ for the time-dependent model (2.11) is

$$\hat{R} = \exp\left\{\mathrm{i}\Delta t\,|L\rangle\langle L| + \frac{iA}{\hbar\omega}\sin(\omega t + \phi)\,|L\rangle\langle L|\right\}. \tag{2.14}$$

In the high-frequency limit and for resonant driving $\Delta = \nu\hbar\omega$ with $\nu \in \mathbb{Z}$, the Fourier components of the Floquet expansion are

$$\hat{\mathcal{H}}^{(k)}_{1\mathrm{P}} = -J'\Big\{\mathcal{J}_{-k-\nu}(\chi)\,\mathrm{e}^{\mathrm{i}(k+\nu)\phi}\,|R\rangle\langle L| + \mathcal{J}_{+k-\nu}(\chi)\,\mathrm{e}^{\mathrm{i}(k-\nu)\phi}\,|L\rangle\langle R|\Big\} \tag{2.15}$$

using the expression in Eq. (2.12) and the transformation (2.14). The symbol $\mathcal{J}_\nu(\chi)$ refers to the νth order Bessel function of the first kind and $\chi = A/\hbar\omega$ is the dimensionless driving strength. The zeroth order ($k = 0$) of the Fourier components directly corresponds to the infinite-frequency Floquet Hamiltonian according to Eq. (2.13). The infinite-frequency Floquet Hamiltonian for the time-periodic model captured by Eq. (2.11) is then

$$\hat{H}_{\mathrm{F,1P}} = \tilde{J}_\nu\,\mathrm{e}^{\mathrm{i}\varphi}\,|R\rangle\langle L| + \mathrm{h.c.} \tag{2.16}$$

It is worth noting that the detuning Δ between neighboring sites vanishes in the effective model. However, the ratio of the detuning to the driving frequency $\nu = \Delta/\hbar\omega$ has a critical influence. The tunnel coupling is renormalized to $\tilde{J}_\nu = J'\,|\mathcal{J}_\nu(\chi)|$ and the tunneling process is associated with a tunneling phase[1] $\varphi = \nu\,\phi\,(+\pi$ for odd positive $\nu)$. The tunneling

---

[1] A formal representation would be $\varphi = [(\nu/|\nu|) - 1](-1)^\nu\pi/2 + \nu\,\phi$.

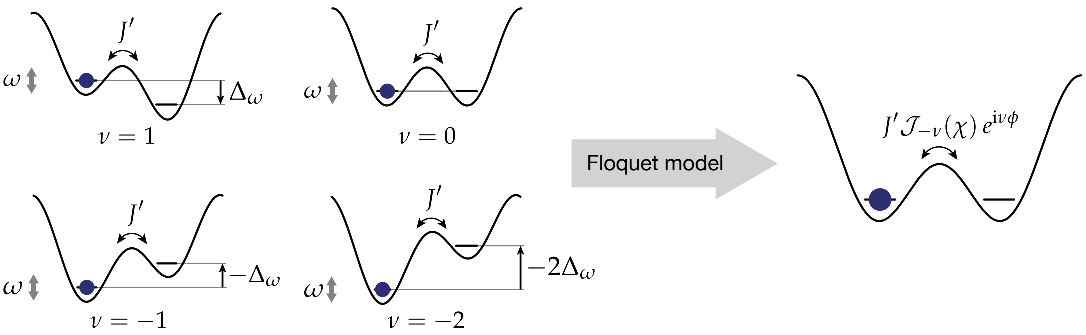

Figure 2.4.: Illustration of multiphoton processes in a periodically-driven double well. A double-well potential with energy offset $\Delta = \nu\,\Delta_\omega$, where $\Delta_\omega = \hbar\omega$, is periodically-driven at a frequency ω. The driving modulates the on-site energy of the left site $V_\mathrm{L} = A\,\cos(\omega t + \phi)$ with an amplitude A and a driving phase ϕ. The different illustrated processes can be interpreted such that the particle absorbs ν photons from the drive during a hopping process to conserve energy. In an effective Floquet picture, the energy difference between neighboring sites is therefore zero. However, the tunneling is renormalized by the νth order Bessel function of the first kind $\mathcal{J}_\nu(\chi)$ in dependence on the dimensionless driving strength $\chi = A/\hbar\omega$.

phase depends on the phase of the modulation and has a π-shift depending on the sign of the tilt Δ for odd ν. This π-shift has its origin in the anti-symmetry of the Bessel-function with odd order: $\mathcal{J}_{-\nu}(\chi) = (-1)^\nu \mathcal{J}_\nu(\chi)$. Fig. 2.4 illustrates the corresponding time-dependent and effective models. In Sec. 3.1.3, a measurement of the renormalization of the tunneling rate is presented for $\nu = \{0, 1, 2\}$.

2.2.3. Matter–gauge coupling

The multi-photon processes introduced in the previous section are the basis of the implementation of the minimal instance for $\mathbb{Z}_2$ LGTs. In this minimal instance, a matter particle is coupled to a $\mathbb{Z}_2$ gauge-field degree-of-freedom. In this implementation the gauge field is realized using exactly one additional particle f per link, which can occupy either the left or right site of the minimal instance. These two configurations directly represent the two values of the gauge-field τ^z. First, a static value of the gauge field or simply a localized f-particle is assumed. This is sufficient to understand the effective matter–gauge coupling. For the matter particles a, a lattice potential without an energy offset between neighboring sites is considered. The a- and f-particles interact via a strong on-site Hubbard interaction U. In addition, a periodic modulation of the left site's on-site energy is applied, which is experienced equally by both species. Then, the time-dependent

Hamiltonian is

$$\hat{H}^a(t) = -J\left(\hat{a}_\mathrm{R}^\dagger \hat{a}_\mathrm{L} + \hat{a}_\mathrm{L}^\dagger \hat{a}_\mathrm{R}\right) + U \sum_{j=\{\mathrm{L},\mathrm{R}\}} \hat{n}_j^a \hat{n}_j^f + A\cos(\omega t + \phi)\hat{n}_\mathrm{L}^a, \tag{2.17}$$

where J is the tunneling rate, $\hat{a}_j^\dagger$ creates an a-particle on site j, $\hat{n}_j^a$ is the number operator, A is the modulation amplitude, $\hbar\omega$ is the resonant driving frequency, and ϕ the modulation phase. Depending on the f-particle's position, the relative on-site energy difference between neighboring sites for the a-particles becomes either $\pm U$ (Fig. 2.5). This density-dependent sign change is the essential ingredient leading to the coupling between the matter and the gauge field. In the limit $U \gg J$ and $A = 0$, tunneling of the a-particles is suppressed. However, it can be restored by resonant driving with $\hbar\omega \approx U$. Analog to the multiphoton processes described above, the tunneling rate is renormalized in the effective Floquet Hamiltonian and gains a tunneling phase of φ. The zeroth order effective model is

$$\hat{H}_\mathrm{eff}^a = -\tilde{J}_a e^{\mathrm{i}\varphi} \hat{a}_\mathrm{R}^\dagger \hat{a}_\mathrm{L} + \mathrm{h.c.} \tag{2.18}$$

with the renormalized tunneling rate $\tilde{J}_a = J|\mathcal{J}_{\pm 1}(\chi)|$, which is independent of the f-particle's position. However, the phase φ depends explicitly on the f-particle's position and is

$$\varphi = \frac{\pi}{2} + \left(\hat{n}_L^f - \hat{n}_R^f\right)\left(\phi - \frac{\pi}{2}\right). \tag{2.19}$$

When defining the link variable $\hat{\tau}^z \equiv \hat{n}_\mathrm{R}^f - \hat{n}_\mathrm{L}^f$ and choosing the modulation phase $\phi = 0$, the gauge–matter coupling becomes explicit:

$$\hat{H}_\mathrm{eff}^a = -J_a \hat{\tau}^z \hat{a}_\mathrm{R}^\dagger \hat{a}_\mathrm{L} + \mathrm{h.c.} \tag{2.20}$$

2.2.4. Gauge field dynamics

In order to analyze the gauge field dynamics, the matter particle a is first kept localized, while the f-particle is allowed to tunnel. If identical potentials for the a- and f-particles were chosen, for symmetry reasons the result would be the same effective Hamiltonian. However, to realize the minimal instance, it is required that no a-particle-dependent phase is associated with tunneling of the f-particle. Note that in general the motion of the f-particle should be fully independent of the position of the a-particles. It is therefore not possible to use the same potentials for a- and f-particles as the f-particle would acquire a π-phase depending on the a-particle's position. To break this symmetry, a

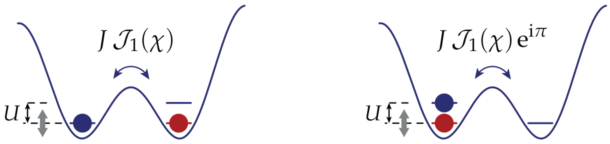

Figure 2.5.: Implementation of the matter–gauge coupling. The gauge field is implemented by a second particle species, the f-particles (red). The gauge field can have two possible values $\tau^z = \pm 1$. These values are encoded by the f-particle's position $\hat{\tau}^z = \hat{n}^f_{\mathrm{R}} - \hat{n}^f_{\mathrm{L}}$, where left and right correspond to $+1$ and -1, respectively. The matter–gauge coupling requires that the matter tunneling is associated with a phase of $\{0, \pi\}$ in dependence of the f-particle's position $\hat{\tau}^z\, \hat{a}^\dagger_{\mathrm{L}}\, \hat{a}_{\mathrm{R}} + \mathrm{h.c.}$ Thus, the tunnel couplings for the matter particle (a-particle, blue) are analyzed. The double well has no on-site energy shift between neighboring sites and a- and f-particles interact via strong on-site interactions. Therefore, the f-particle introduces an effective on-site energy difference between neighboring sites. Resonant driving with a frequency of $\hbar\omega = U$ leads to an effective Floquet model in the high-frequency limit realizing the matter–gauge coupling.

species-dependent energy-offset between the sites is introduced for the f-particles. The time-dependent Hamiltonian is then

$$\hat{H}^f(t) = -J'\left(\hat{f}^\dagger_{\mathrm{R}}\hat{f}_{\mathrm{L}} + \hat{f}^\dagger_{\mathrm{L}}\hat{f}_{\mathrm{R}}\right) + U \sum_{j=\{\mathrm{L},\mathrm{R}\}} \hat{n}^a_j \hat{n}^f_j + \Delta_f \hat{n}^f_{\mathrm{L}} + A\cos(\omega t + \phi)\hat{n}^f_{\mathrm{L}}, \tag{2.21}$$

where $f^\dagger_j$ creates an f-particle on site j. The relative on-site energy difference between neighboring sites for the f-particle becomes now $\Delta_f \pm U$ (Fig. 2.6). For $\Delta_f \equiv U$ both processes are resonant in the high-frequency limit for a driving with frequency ω. The tunnel coupling is renormalized by the zeroth- $\mathcal{J}_0(\chi)$ and second-order Bessel function $\mathcal{J}_2(\chi)$ according to the derived multiphoton processes because the energy offset is either zero or twice the driving frequency. It is important to recognize that the tunneling is not associated with a density-dependent π-shift because ν has the same sign and is even for both processes. Nevertheless, the two-photon process $\nu = 2$ inherits twice the modulation phase $\varphi = 2\phi$. Thus, a modulation phase of $\phi = 0$ or π is required and the effective model in the high-frequency limit reduces to

$$\hat{H}^f_{\mathrm{eff}} = -\hat{J}_f\left(\hat{f}^\dagger_{\mathrm{R}}\hat{f}_{\mathrm{L}} + \hat{f}^\dagger_{\mathrm{L}}\hat{f}_{\mathrm{R}}\right) = -\hat{J}_f\hat{\tau}^x, \tag{2.22}$$

where $\hat{J}_f$ is operator-valued and depends on the a-particle configuration

$$\hat{J}_f = J\mathcal{J}_0(\chi)\,\hat{n}^a_{\mathrm{L}} + J\mathcal{J}_2(\chi)\,\hat{n}^a_{\mathrm{R}}. \tag{2.23}$$

Simply combining the two processes described by $\hat{H}^a_{\mathrm{eff}}$ and $\hat{H}^f_{\mathrm{eff}}$, already constitutes a $\mathbb{Z}_2$-symmetric minimal instance. However, the f-particle tunneling rate depends in general on the position of the a-particle. This complication can be avoided by choosing the driving strength $\chi_0 \simeq 1.84$ such that $\mathcal{J}_0(\chi_0) = \mathcal{J}_2(\chi_0)$.

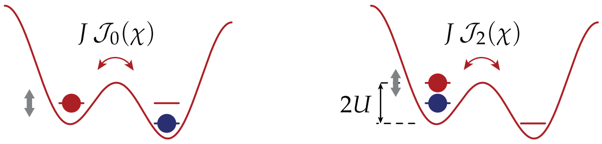

Figure 2.6.: Implementation of the gauge-field dynamics. The gauge-field particle dynamics (red) is presented for fixed positions of the matter particle (blue). In contrast to the configuration for the matter particle, an energy offset between neighboring sites of size U is introduced. This additional species-dependent tilt breaks the symmetry between the a- and the f-particles. Again looking at the effect of the energy offsets between neighboring sites taking the on-site interaction into account reveals two possible coupling processes: a zero and a two-photon transition. Here, the tunneling rate is renormalized differently depending on the two a-particle configurations but the tunneling phase is $\varphi = 0$ for $\phi = 0$ (Eq. 2.15).

2.2.5. Time-dependent and effective Hamiltonian

So far, the processes for a- and f-particles are treated separately. Here, the processes are combined and the time-dependent and effective Hamiltonian of the scheme for realizing a minimal instance of $\mathbb{Z}_2$ LGTs are summarized. A detailed derivation including higher order terms can be found in Sec. A. The assumptions are strong inter-species on-site interactions $U \gg J$ and a resonant periodic driving $\hbar\omega \approx U$. The resulting time-dependent Hamiltonian is

$$\begin{aligned}\hat{H}(t) = &-J\left(\hat{a}_{\mathrm{R}}^{\dagger}\hat{a}_{\mathrm{L}} + \hat{f}_{\mathrm{R}}^{\dagger}\hat{f}_{\mathrm{L}} + \text{h.c.}\right) + U\sum_{j=\{\mathrm{L,R}\}}\hat{n}_j^a\hat{n}_j^f + \Delta_f\hat{n}_{\mathrm{L}}^f \\ &+ A\cos(\omega t + \phi)\left(\hat{n}_{\mathrm{L}}^a + \hat{n}_{\mathrm{L}}^f\right).\end{aligned} \tag{2.24}$$

In the high-frequency limit $U/J \gg 1$ and for $\phi = 0$, the lowest order of the effective Floquet Hamiltonian takes the form

$$\hat{H}_{\text{eff}} = -J_a\hat{\tau}^z\left(\hat{a}_{\mathrm{R}}^{\dagger}\hat{a}_{\mathrm{L}} + \hat{a}_{\mathrm{L}}^{\dagger}\hat{a}_{\mathrm{R}}\right) - J_f\hat{\tau}^x, \tag{2.25}$$

where the a-particle position dependence vanishes for a specific driving strength, e.g. $\chi_0 = 1.84$. In conclusion, this scheme realizes a minimal instance for $\mathbb{Z}_2$ LGTs.

3. Experimental realization and measurements

3.1. Experimental realization and calibrations

3.1.1. Setup with modulation lattice

To realize the two-site model with $\mathbb{Z}_2$-symmetry, ultracold ^{87}Rb atoms are employed in a 3D optical lattice. The lattice consists of three mutually orthogonal standing waves with wavelength $\lambda_\mathrm{s} = 767\,\mathrm{nm}$. To create the superlattice along the x-direction, an additional long period lattice with $\lambda_\mathrm{l} = 2\lambda_\mathrm{s}$ is superimposed. The resulting potential is

$$V_\mathrm{SL}(x) = V_{x,\mathrm{s}} \cos^2(k_\mathrm{s} x) + V_{x,\mathrm{l}} \cos^2(k_\mathrm{l} x + \varphi_\mathrm{SL}), \tag{3.1}$$

where $V_{x,\mu}$ denotes the lattice depth and $k_\mu = 2\pi/\lambda_\mu$ the wave number with $\mu \in \{\mathrm{s,l}\}$. A description of the experimental apparatus can be found in Refs. [143–146]. As required by the scheme for the implementation of the minimal instance, the on-site potential needs to be modulated at frequency $\hbar\omega \approx U$ in an amplitude- and especially phase-controlled fashion. Therefore, an additional modulation lattice with wavelength λ_l is overlaid with a relative phase such that the potential maxima affect only one of the double-well sites (Fig. 3.1 a). The combined potential is then

$$V(x) = V_\mathrm{SL}(x) + V_\mathrm{mod} \cos^2(k_l x - \pi/4), \tag{3.2}$$

with V_mod the lattice depth of the modulation lattice. The time-dependent modulation of the on-site potential can then be introduced by modulating the amplitude of the modulation lattice $V_\mathrm{mod} = V_\mathrm{mod}^{(0)} + A_\mathrm{mod} \cos(\omega t + \phi)$ around a mean value $V_\mathrm{mod}^{(0)}$. However, this lattice introduces only a positive energy-offset and therefore generates a mean tilt $\Delta(V_\mathrm{mod}^{(0)})$. This mean tilt can be compensated by applying a suitable static superlattice phase φ_SL.

Moreover, the implementation requires two species and an additional species-dependent energy offset $\Delta_f = U$. In the experiment, these two species are realized by ^{87}Rb atoms in the hyperfine states $|F = 1, m_F = \pm 1\rangle$. They represent the f- and a-particles, respectively. These states have opposite magnetic moments and experience opposite energy offsets Δ_M

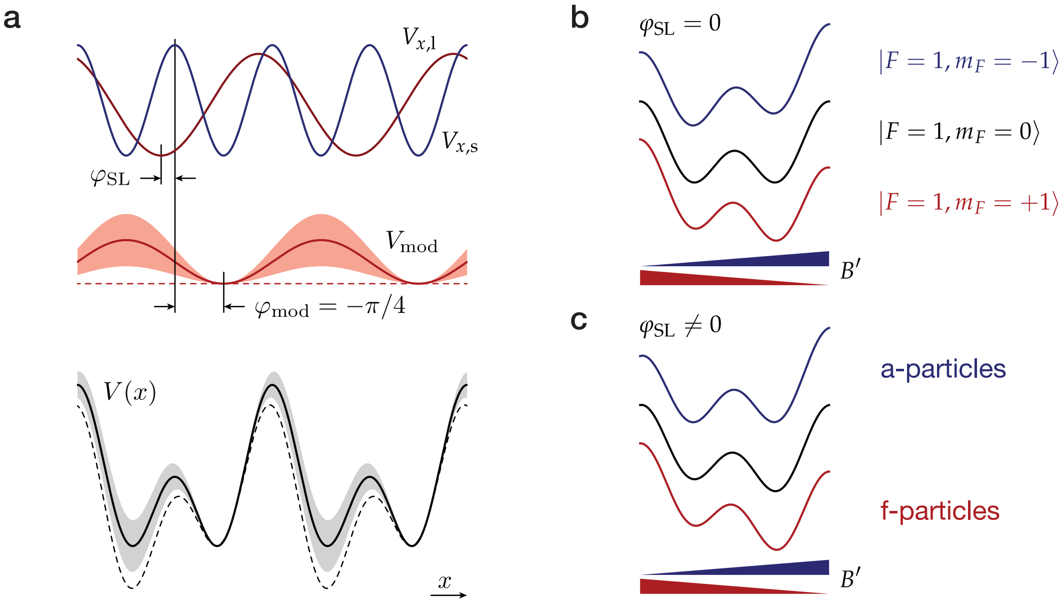

Figure 3.1.: Modulation lattice and gradient. **a** Superimposing a short- (blue) and a long- (red) period lattice with wavelengths λ_{s} and $\lambda_{\mathrm{l}} = 2\lambda_{\mathrm{s}}$ forms a superlattice potential (black). Depending on the relative phase φ_{SL}, an energy offset between neighboring sites can be introduced (black dashed line). In addition, a second lattice with wavelength λ_{l} is superimposed with a relative phase of $\varphi_{\mathrm{mod}} = -\pi/4$ such that the on-site energy of the left double-well site can be modified by a change in the modulation lattice depth V_{mod} [Eq. (3.2)]. This is illustrated by the red and gray shadings. **b** Illustration of the potentials in presence of a magnetic gradient for atoms in the $F = 1$ manifold. **c** Combining the magnetic gradient with a static superlattice tilt allows for a symmetric potential, e.g. for the a-particles.

in response to a magnetic gradient, thus $\Delta_M^a = -\Delta_M^f$ (Fig. 3.1 b). The implementation requires a zero tilt for a-particles. This can be achieved by an additional species-independent tilt Δ_{SL} from the superlattice, such that it compensates the tilt $\Delta_M^a = -\Delta_{\mathrm{SL}}$ for the a-particles. The energy offset between neighboring sites for the f-particle is therefore the sum of both contributions $\Delta_f = \Delta_M^f + \Delta_{\mathrm{SL}}$ (Fig. 3.1 c).

3.1.2. Detection and inhomogeneous tilt distribution

For the detection of the average local site occupation, site-resolved band mapping is used [6, 147]. Atoms on the left (right) site of each double well are thereby transferred to the first (third) energy level of the long-period lattice. The atom numbers $N_{\mathrm{L(R)}}$ on the left (right) site are determined after a band-mapping sequence from absorption images. Thereafter the average site imbalance $I = (N_{\mathrm{R}} - N_{\mathrm{L}}) \,/\, (N_{\mathrm{L}} + N_{\mathrm{R}})$ can be calculated based

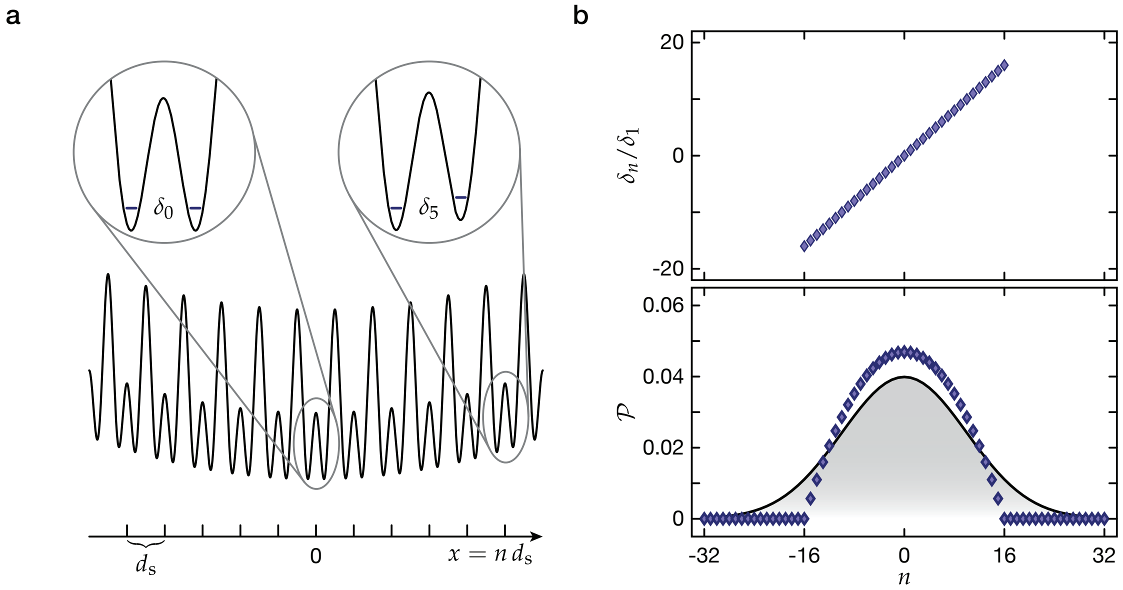

Figure 3.2.: Inhomogeneous tilt distribution. **a** Illustration of a superlattice potential on top of a harmonic trapping potential. The magnitude of the tilts δ_n between neighboring sites on the double wells linearly increases from the center towards at the edge of the cloud. In the experiment, a 3D cloud of atoms is trapped and the illustrated 1D superlattice represents a single instance out of the full 3D array. Due to the typically ellipsoidal shape of the cloud, each 1D system contains a different number of atoms. Therefore, each tilt δ_n appears with a different probability of occurrence. **b** A simple model assumes a spherical cloud with a radius of 16 double wells. The tilts then increase linearly as a function of the lattice site position (top). The probability of occurrence with which each tilt occurs is shown below. This model makes a number of assumptions especially on the cloud shape and allows only 39 different tilt values, which is experimentally unsubstantiated. Thus, the tilt distribution is modeled by a simple normal distribution, which only depends on a single parameter, i.e. the standard deviation Δ_σ (solid line).

on these atom numbers [6, 147]. By combining this technique with a Stern-Gerlach experiment, atoms in hyperfine-states with different magnetic moments can be distinguished [4]. Hence, the imbalance of a- and f-particles can be determined separately.

This measurement method only characterizes ensemble quantities; an average over all realization of double wells. As already explained, the atoms are loaded into a 3D optical lattice. For deep transverse lattices and suitable superlattice parameters, a 3D array of isolated double wells can thereby be generated. This array should ideally consist of many replicas of the same double well. However, the harmonic trapping potential and beam intensity variations alter the double wells significantly. The main contributions are varying energy offsets between the two double-well sites. The energy offsets introduced by a harmonic confinement can be directly modeled because the value of the energy offset linearly increases with the distance of the double well from the trap center projected onto the superlattice axis. To apply this model, accurate knowledge of the density distribution of the atoms is required and all other effects besides the harmonic trapping potential, e.g. through misalignment of the lattice beams and mismatched beam wastes, are ignored. In the experimental apparatus, neither the density distribution nor the individual tilts can be determined accurately. Therefore, an a priori model for the tilt distribution is chosen, which assumes that the energy offsets δ_n are normally distributed according to

$$\mathcal{G}_\Delta(\delta) = \frac{1}{\sqrt{2\pi\Delta_\sigma^2}} e^{-\frac{\delta^2}{2\Delta_\sigma^2}} \tag{3.3}$$

with a standard deviation Δ_σ. Figure 3.2 shows a comparison of the models for a spherical density distribution.

3.1.3. Multiphoton processes

The measurement of the tunneling dynamics and renormalization of the tunnel coupling of a single particle in a periodically-driven double-well potential was a first test of the modulation–lattice setup. Furthermore, it was used to characterize the modulation amplitude. Similar measurements have been performed in other experiments on a variety of platforms [74, 148–153].

The experimental sequence starts by loading atoms in the $|F = 1, m_F = -1\rangle$ state into the 3D optical lattice by performing an exponentially increasing ramp. Along the x-direction, only the long-period lattice is switched on. Then, a filtering sequence is used to remove atoms on doubly-occupied sites by light-assisted collisions [154–156] during temporal transfer to the $|F = 2, m_F = -1\rangle$ state. Now, the static part of the modulation lattice is turned on. Simultaneously, the superlattice phase ϕ_{SL} is set to a value such that, together with the modulation lattice, a tilt $\Delta \gg J'$ would be present. The particle then localizes to the low-energy site in the subsequent splitting of the long-period with the short-period lattice. The tilt of the double wells is then non-adiabatically changed to the final energy offset Δ_ν between the two sites. This energy offset is set to be resonant with the multiphoton processes for driving with a constant frequency ω. Now the time-evolution is initialized by rapidly coupling the double-well sites and the modulation is started with a frequency $\omega = 2\pi \times 4122\,\mathrm{Hz}$. The lattice parameters during time evolution are $V_{x,\mathrm{l}} = 35\,E_{r,\mathrm{l}}$, $V_{x,\mathrm{s}} = 9.5\,E_{r,\mathrm{s}}$, and $V_{\mathrm{mod}}^{(0)} = 15\,E_{r,\mathrm{l}}$. The sequence was repeated for different evolution times as well as a set of modulation amplitudes for $\nu = \{0, 1, 2\}$. For detection, the motion of the atoms was frozen by increasing the short lattice depth $V_{x,\mathrm{s}} = 40\,E_{r,\mathrm{s}}$. Then, the site imbalance was determined from site-resolved band mapping images [6, 147].

The measurements are conducted for resonant driving at constant driving frequencies for all ν-values. The value of the driving frequency is not deep in the high-frequency limit, which means J is not negligible compared to $\hbar\omega$. Therefore, a correction to the resonance condition for $\nu \neq 0$ occurs and the resonant tilt is

$$\Delta_\nu = \sqrt{(\nu\hbar\omega)^2 - 4J^2}. \tag{3.4}$$

To experimentally account for this correction, Δ_ν was determined by a spectroscopic measurement by varying the energy offset at constant driving frequency.

Finally, the oscillation frequency of each imbalance time trace was determined to extract the tunneling rate. To determine this oscillation frequency accurately, the inhomogeneous tilt distribution of the 3D array of double wells needs to be taken into account. As introduced before, the tilts δ_n are assumed to be normally distributed according to Eq. (3.3). Taking this into account, the renormalized tunneling rates $\tilde{J}_\nu$ are extracted by fitting an average of $S = 10$ sinusoidal functions

$$I_\nu(t) = \frac{I_A}{S} \sum_{n=1}^{S} \sin\left(\sqrt{\delta_n^2 + 4\tilde{J}_\nu^2}\, t/\hbar + \zeta\right) + I_0 \tag{3.5}$$

to the data. Here, δ_n is a random sample of the tilt distribution, $\tilde{J}_\nu = J'_\nu \mathcal{J}_\nu(\chi)$ is the renormalized tunneling coupling, ζ is an initial phase due to the finite initialization ramp time, I_A is the oscillation amplitude, and I_0 the imbalance offset of the oscillation. For these fits, the five parameters $\tilde{J}_\nu$, Δ_σ, ζ, I_A, and I_0 are kept free and the confidence intervals are estimated by a bootstrap of 1000 repetitions. These repetitions use different sets of $\{\delta_n\}$, a Gaussian error in the imbalance detection with standard deviation of 0.05 and randomly-guessed fit start values for $\tilde{J}_\nu$. In the right panel of Fig. 3.3 exemplary time traces for the dimensionless driving amplitude $\chi_P = 1.28$ are shown.

To extract the renormalization coefficient $\tilde{J}_\nu / \tilde{J}'_\nu$, the respective bare tunnel coupling strength J'_ν needs to be known. J'_ν is calculated from the respective double-well Wannier functions on the calibrated lattice parameters. The results $J'_0/h = 490\,\mathrm{Hz}$, $J'_1/h = 520\,\mathrm{Hz}$, and $J'_2/h = 563\,\mathrm{Hz}$ slightly differ for the three data sets $\nu = \{0, 1, 2\}$. With these values, the renormalizations are calculated and illustrated in Fig. 3.3. The data points and error bars show the median and the 1σ-confidence interval from the bootstrap analysis.

The dimensionless diving strength $\chi = A/\hbar\omega$ can be calculated by converting the modulation lattice amplitude V_{mod} into an on-site potential amplitude A_{mod}. This method leads to systematically too small driving amplitudes compared to the detected results. To this end, a conversion factor α for the driving amplitude $A = \alpha A_{\mathrm{mod}}$ was calibrated by a fit of the zeroth-order Bessel function $\mathcal{J}_0(\alpha_{\mathrm{fit}} A_{\mathrm{mod}}/\hbar\omega)$ to the experimental results for $\nu = 0$. The fitted conversion factor is $\alpha_{\mathrm{fit}} = 1.09(2)$. It is consistent over independent measurements.

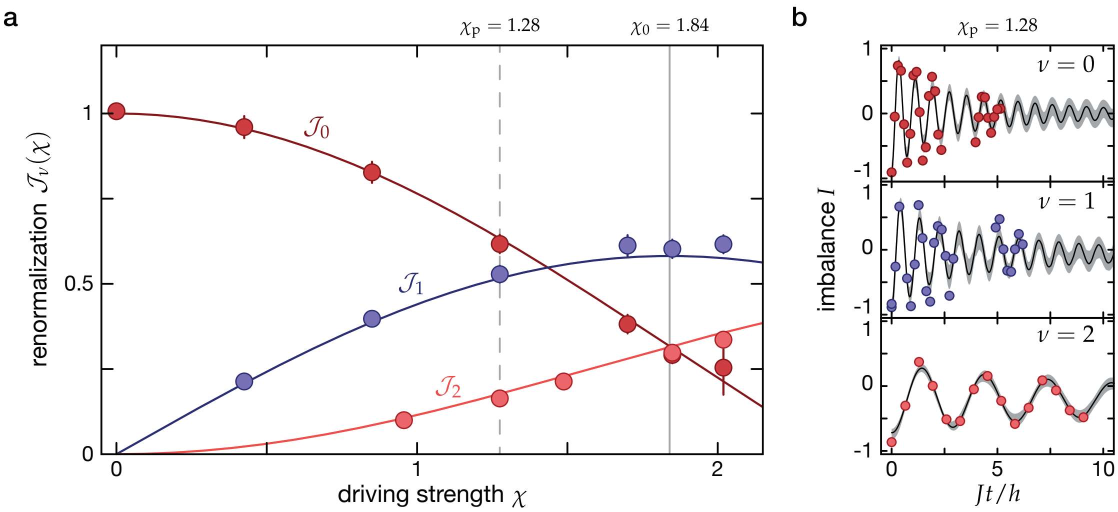

Figure 3.3.: Measured renormalization of the tunneling of a driven double well. **a** The tunnel coupling for ν-photon processes, $\nu = \{0, 1, 2\}$, with a driving frequency $\omega = 2\pi \times 4122\,\text{Hz}$ was measured by detecting the oscillation frequency of imbalance oscillations for various driving strengths χ. The measured scaling of the tunneling rate matches well with the expected Bessel-type behavior $\mathcal{J}_\nu(\chi)$ (solid lines) after calibrating the driving strength and including the respective bare tunneling rates $J'_0/h = 490\,\text{Hz}$, $J'_1/h = 520\,\text{Hz}$, and $J'_2/h = 563\,\text{Hz}$. The driving strength was calibrated by a fit of $\mathcal{J}_0(\chi)$ to the data, as the zero-photon process is insensitive to inaccuracies in the driving frequency. **b** Imbalance time traces $I(t)$ are fitted with averaged sinusoidal functions taking into account different tilts from the inhomogeneous tilt distributions (solid black lines). Exemplary traces are shown for $\chi_P = 1.28$ (dashed vertical line, **a**). The error bars and the gray shading are the 1σ-confidence interval obtained from a bootstrap analysis of 1000 repetitions. The point, where $\mathcal{J}_0(\chi_0) = \mathcal{J}_2(\chi_0)$ was identified and marked by a solid gray vertical line.

This deviation is most likely attributed to the non-linear behavior of $\Delta(V_{\text{mod}})$ [Fig. 3.4]. In addition, the value of the bare tunnel coupling $J'_\nu(V_{\text{mod}})$ depends on the modulation lattice depth during one driving period and may contribute to these corrections. The described effects are especially important for large values of the modulation lattice $V_{\text{mod}} \sim V_{x,l}$, as it changes not only the on-site potential but also the overall shape of the potential.

3.1.4. Tight-binding description

In the experiment, a superlattice potential of the form (3.1) is realized. The dynamics in such a potential is implicitly assumed to be captured by simple tight-binding models. These models typically include nearest neighbor tunneling J and on-site interactions U. For bosons, this results in the well-known Bose-Hubbard model [157]. However, for interacting particles in lattice potentials, additional processes can become relevant leading to the so-called extended Bose-Hubbard model [158]. Here, the full tight-binding description for the parameters used to realize the minimal instance is presented including the relevant terms of the extended Bose-Hubbard model.

To define a tight-binding lattice model, localized wave functions need to be defined on each lattice site. Such maximally localized wave functions are called Wannier functions $w(r)$. These functions can be calculated e.g. according to [159] and the tight-binding parameters can then be defined with these Wannier functions. The tunnel coupling between neighboring sites scales as the overlap of the Wannier functions on the two sites $J' = -\int w_{\mathrm{L}}^{*}(r)H(r)w_{\mathrm{R}}(r)\,\mathrm{d}r^3$ and the on-site interaction energy scales as the overlap of the on-site particle densities $U = g\int |w(r)|^4\,\mathrm{d}r^3$. Here, the effective interaction strength is $g = 4\pi\hbar^2 a_{\mathrm{s}}/m$, with a_{s} being the s-wave scattering length and m the mass. The extended Bose-Hubbard model additionally takes into account that densities from neighboring lattice sites overlap as well. This overlap leads to nearest-neighbor interactions $u_{\mathrm{LR}} = g\int |w_{\mathrm{L}}(r)|^2|w_{\mathrm{R}}(r)|^2\,\mathrm{d}r^3$ and density-assisted tunneling $\delta j = g\int w_{\mathrm{L}}^{*2}(r)w_{\mathrm{L}}(r)w_{\mathrm{R}}(r)\,\mathrm{d}r^3$, which modifies the tunnel matrix element $J = J' + \delta_j$. Furthermore, two-particle hopping processes arise with a strength u_{LR}, where either two particles on the same site simultaneously tunnel to the neighboring site, or two particles on neighboring lattice sites exchange their positions.

Now, a tight-binding model can be formulated for the minimal instance for $\mathbb{Z}_2$ LGTs. The realization of the minimal instance consists of two particles with opposite magnetic moment in an optical superlattice overlapped with an additional modulation lattice. The modulation lattice generates the time-dependent on-site energies. In addition, a magnetic field gradient is applied to break the symmetry between a- and f-particles. Taking into account the extended Bose-Hubbard parameters, the time-dependent, tight-binding model is

$$
\begin{aligned}
H(t) = &- J\big(|\mathrm{RL}\rangle\langle\mathrm{LL}| + |\mathrm{RR}\rangle\langle\mathrm{LR}| + |\mathrm{RR}\rangle\langle\mathrm{RL}| + |\mathrm{LR}\rangle\langle\mathrm{LL}| + \mathrm{h.c.}\big)\\
&+ U\big(|\mathrm{LL}\rangle\langle\mathrm{LL}| + |\mathrm{RR}\rangle\langle\mathrm{RR}|\big)\\
&+ A\cos(\omega t + \phi)\big(2\,|\mathrm{LL}\rangle\langle\mathrm{LL}| + |\mathrm{LR}\rangle\langle\mathrm{LR}| + |\mathrm{RL}\rangle\langle\mathrm{RL}|\big)\\
&+ \Delta_{\mathrm{SL}}\big(2\,|\mathrm{LL}\rangle\langle\mathrm{LL}| + |\mathrm{LR}\rangle\langle\mathrm{LR}| + |\mathrm{RL}\rangle\langle\mathrm{RL}|\big)\\
&+ \Delta_{\mathrm{M}}\big(-|\mathrm{LR}\rangle\langle\mathrm{LR}| + |\mathrm{RL}\rangle\langle\mathrm{RL}|\big)\\
&+ u_{\mathrm{LR}}\big(|\mathrm{LL}\rangle\langle\mathrm{RR}| + |\mathrm{LR}\rangle\langle\mathrm{RL}| + |\mathrm{RR}\rangle\langle\mathrm{LL}| + |\mathrm{RL}\rangle\langle\mathrm{LR}|\\
&\qquad + |\mathrm{LR}\rangle\langle\mathrm{LR}| + |\mathrm{RL}\rangle\langle\mathrm{RL}|\big).
\end{aligned}
\tag{3.6}
$$

Here, the states are labeled by the site the matter particle-a occupies followed by the site the gauge field particle-f occupies. For simplicity, all parameters are assumed to be independent of the modulation lattice depth during periodic driving with $A\cos(\omega t + \phi)$. which greatly simplifies the model. This is a reasonable assumption as the dependence has only little impact on the dynamics compared to other processes e.g. induced by inhomogeneities, which was confirmed by a numerical analysis. In Fig. 3.4, the dependence of

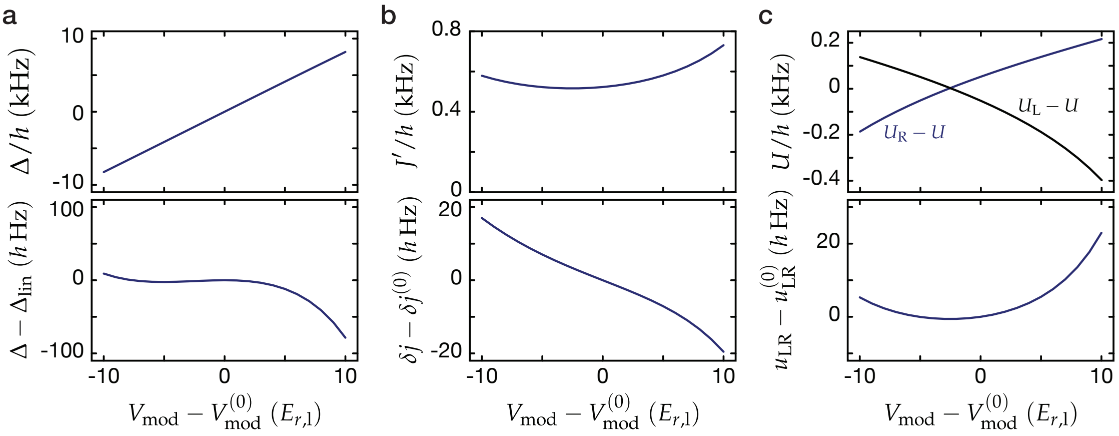

Figure 3.4.: Tight-binding parameter dependence on the modulation lattice depth. Numeric calculation of the tight-binding parameters for $V_{x,\mathrm{s}} = 9.5\,E_{r,\mathrm{s}}$, $V_{x,\mathrm{l}} = 35\,E_{r,\mathrm{l}}$, $\varphi_{\mathrm{SL}} = -0.364\pi$, and $V_{\mathrm{mod}}^{(0)} = 15\,E_{r,\mathrm{l}}$. **a** The energy offset between neighboring sites Δ and its deviation between from a linear expansion around $V_{\mathrm{mod}} = V_{\mathrm{mod}}^{(0)}$. **b** Nearest-neighbor tunneling rate J' and the deviation of the density-assisted tunneling δj to $\delta_j^{(0)}/h = \delta_j(V_{\mathrm{mod}}^{(0)})/h = 66\,\mathrm{Hz}$. **c** Deviation of the on-site interaction energy on the left and right site to the mean interaction energy at $V_{\mathrm{mod}}^{(0)}$ as well as the deviation of the extended Bose-Hubbard parameter u_{LR} to $u_{\mathrm{LR}}^{(0)}/h = u_{\mathrm{LR}}(V_{\mathrm{mod}}^{(0)})/h = 19\,\mathrm{Hz}$.

the parameters on the modulation depth are summarized. The tight-binding model (3.6) only realizes the $\mathbb{Z}_2$ minimal instance for very specific sets of parameters. Therefore, the parameters need to be calibrated accurately to fulfill the desired criteria. This calibration procedure is discussed in the next section.

3.1.5. Parameter calibrations

The calibration procedure starts with the verification of the superlattice-potential depths. To this end, the bare tunneling rate in a symmetric double-well potential is measured. A single particle is loaded in each double well and localized to one site, e.g. the left site. The loading sequence is analog to the loading sequence to determine the multiphoton processes (Sec. 3.1.3). Then, the energy offset between neighboring sites is removed non-adiabatically by tuning $\varphi_{\mathrm{SL}} = 0$. The new eigenstates of this symmetric double well are now $|\pm\rangle = (|\mathrm{L}\rangle \pm |\mathrm{R}\rangle)/\sqrt{2}$. The two sites are coupled with tunneling rate J' by rapidly decreasing the short lattice depth. Then, the site imbalance starts to oscillate. The oscillation frequency is given by the eigenenergy difference $\Delta E_{\pm} = 2J'$. Thus, J' can be extracted from a frequency fit to the imbalance oscillation (Fig. 3.5).

The averaging effect introduced by the inhomogeneous tilt distribution in the 3D array

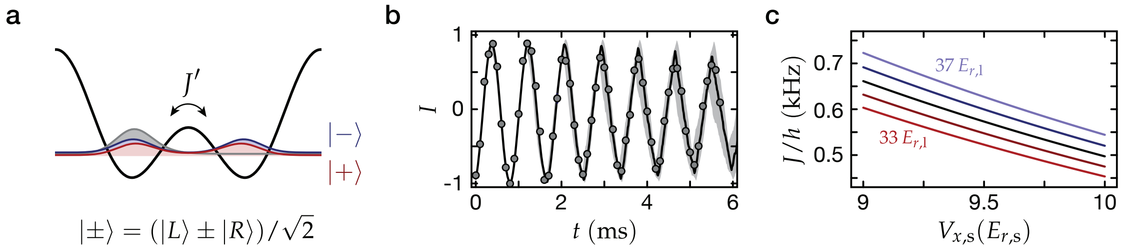

Figure 3.5.: Superlattice calibration. The lattice depth of the short- and long-period lattice creating the superlattice potential are individually calibrated using parametric lattice modulation spectroscopy. To further test this calibration, the frequency of imbalance oscillations is measured for the experimental parameters $V_{x,\mathrm{s}} = 9.5\,E_{r,\mathrm{s}}$ and $V_{x,\mathrm{l}} = 35\,E_{r,\mathrm{l}}$. **a** Illustration of the eigenfunctions $|\pm\rangle$ (red, blue) on a symmetric double well. On the left side in gray, a localized Wannier function is illustrated. It is the initial state for the bare tunneling oscillations. **b** Measured imbalance oscillation $I = (N_\mathrm{L} - N_\mathrm{R})/(N_\mathrm{L} + N_\mathrm{R})$, where N_L and N_R are the site occupations on the left and right site, respectively. **c** Calculation of the tunneling rate on the short- and long-period lattice depth. The method is sensitive to changes in both parameters. The measurement in **b** leads to $V_{x,\mathrm{s}} = 9.50(1)\,E_{r,\mathrm{s}}$ for the assumption that $V_{x,\mathrm{l}} = 35\,E_{r,\mathrm{l}}$.

of double wells leads to an increase of the detected frequency as the energy difference between neighboring sites scales with $\Delta E_\pm(\delta) = \sqrt{\delta^2 + 4J'^2} > 2J'$. Therefore, it is essential to take this effect into account by modeling average time traces including a distribution of energy offsets between neighboring sites. The average time trace consist of 256 double wells with randomly sampled tilts δ_n according to the Gaussian distribution Eq. (3.3). The median values of these imbalance time traces are fitted by a least-square method to the measured data. The fit result reproduces exactly the tunneling rate expected from the corresponding lattice depth calculated via the Wannier functions, or inversely leads to $V_x = 9.50(1)E_{r,\mathrm{s}}$. Moreover, this fit leads to an estimate for the standard deviation of the Gaussian-assumed tilt distribution of $\Delta_\sigma/h = 0.44(4)$ kHz.

The next step in the calibration procedure is to determine the value of the interaction strength U. The interaction strength is very sensitive to the exact shape of the lattice potential. Thus, it is important to measure U in a lattice configuration as similar as possible to the final lattice configuration. An adequate technique to measure U is the determination of the superexchange oscillation frequency of two distinguishable particles on the double well. It is clear that directly using the final a- and f-particle configuration for the $\mathbb{Z}_2$ minimal instance will not work, as only the a-particle experiences a zero-energy offset between neighboring sites, while the f-particle experiences a tilt Δ_f. The resulting superexchange oscillations would therefore be strongly detuned because of the opposite magnetic moment of a- and f-particles. Using a microwave-driven adiabatic passage transferring the f-particles from $|F = 1, m_F = +1\rangle$ state to f'-particles in the $|F = 2, m_F = +1\rangle$ state in the $F = 2$ manifold reverses the magnetic moment and makes it

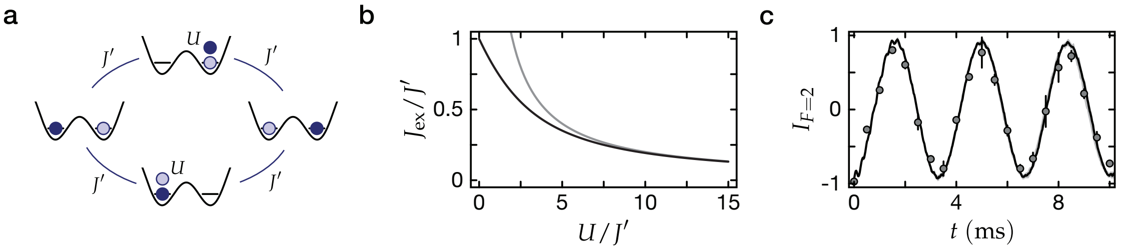

Figure 3.6.: Calibration of the interaction energy. a The superexchange is a second-order process, where two distinguishable particles exchange their position. The two required tunneling processes J' connect the initial and final configuration via an intermediate state, where both particles occupy the same lattice site. During this intermediate state, the particles interact with each other. The coupling between the initial and final state therefore depends on the interaction energy U. **b** Numerical calculation of the coupling strength as a function of U/J'. The energy gap between the first and second eigenstate, which in fact defines the exchange coupling, is shown in black. The gray line shows the scaling $2J'^2/U$, which is accurate for large U/J'. **c** Measurement of the superexchange oscillations for atoms in the $|F=1, m_\mathrm{F}=-1\rangle$ and $|F=2, m_\mathrm{F}=+1\rangle$ states. Only atoms in the $F=2$ manifold are imaged using F-state selective imaging. The resulting interaction energy is $U/h = 3.85(7)$ kHz.

equal to the magnetic moment of the a-particle. Now, both tilts are equal. This allows for a measurement using superexchange oscillations (Fig. 3.6). To this end, a- and f'-particles are localized to the left and right site of the double well, respectively, and the dynamics is started by coupling the two sites. Then, the f'-particle imbalance is detected by F-selective imaging. By numerically calculating the time evolution of the imbalance from the two-site, two-particle extended Bose-Hubbard model for a known tunneling-rate J' in this lattice configuration, the oscillation can be matched by fitting the interaction energy U. The tunneling J' in this configuration can be simply measured by observing bare single-particle oscillations of a single a-particle. The resulting interaction energy for the superlattice parameters $V_{x,\mathrm{l}} = 35\,E_{r,\mathrm{l}}$, $V_{x,\mathrm{s}} = 9.5\,E_{r,\mathrm{s}}$ and $V^{(0)}_{\mathrm{mod}} = 15\,E_{r,\mathrm{l}}$ is $U = 3.85(7)$ kHz.

After calibrating of the interaction energy, the species-dependent tilt Δ_f needs to be matched. In this context, also the sequence for determining the symmetric double well for the a-particles is introduced. As described above, the effective tilt for f- and a-particles $\Delta_{f,a} = \Delta_{SL} \pm \Delta_M$ are composed of the superlattice tilt and the contribution of the magnetic gradient. For the f-particle, both contributions add to $\Delta_f = \Delta_{SL} + \Delta_M$, while they subtract $\Delta_a = \Delta_{SL} - \Delta_M$ for the a-particles. The scheme requires $\Delta_a = 0$ and thus $\Delta_{SL} = \Delta_M$. This condition can be realized by performing an adiabatic splitting experiment for a single a-particle. To this end, the ground state of the double well is prepared, the tunnel coupling between the sites is adiabatically lowered, and the site imbalance is detected. A symmetric site-imbalance indicates zero tilt $\Delta_a = 0$. The tilt Δ_f now needs to be matched with the interaction energy U. Therefore, a modulation spectroscopy is performed with a single

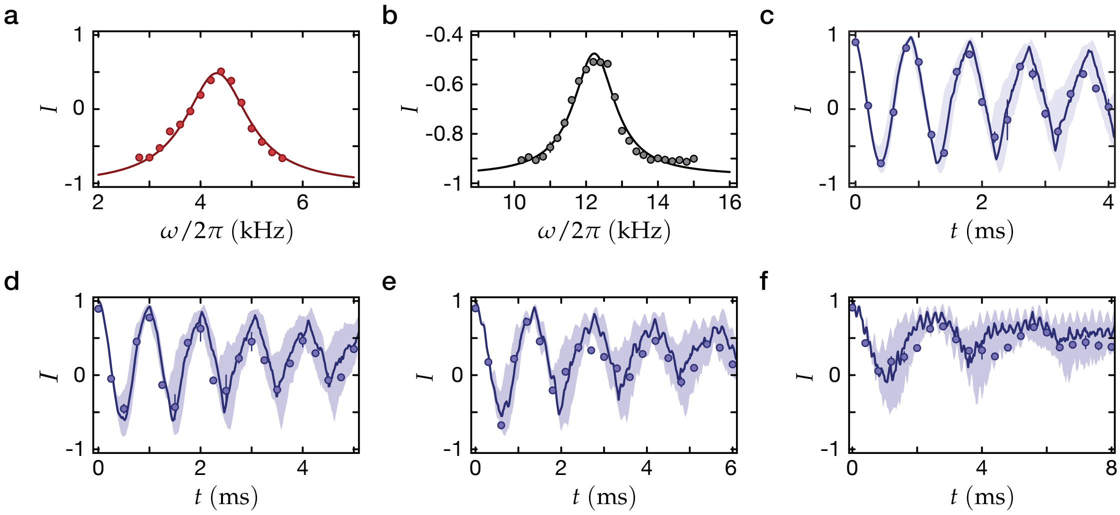

Figure 3.7.: Calibration of the modulation lattice. The superlattice parameters for all measurements are $V_{\mathrm{x,s}} = 9.50(1)\,E_{\mathrm{r,s}}$ and $V_{\mathrm{x,l}} = 35(1)\,E_{\mathrm{r,l}}$. **a** Spectroscopic measurement of the species-dependent tilt $\Delta_f = \Delta_{\mathrm{SL}} + \Delta_M$. The resonance is found at $\omega = 2\pi \times 4.32(2)$ kHz with a single f-particle. **b** On top of the otherwise symmetrically chosen double well with $\varphi_{\mathrm{SL}} = 0$, the mean modulation lattice depth $V_{\mathrm{mod}}^{(0)} = 15.0(2)\,E_{\mathrm{r,l}}$ induces a tilt. A resonance can be found at $\omega_{\mathrm{mod}} = 2\pi \times 12.23(2)$ kHz with a spectroscopic measurement by modulating the modulation lattice depth, allowing for a calibration of the mean modulation lattice depth. **c** In addition to the superlattice, the modulation lattice $V_{\mathrm{mod}}^{(0)} = 15.0(2)\,E_{\mathrm{r,l}}$ and the magnetic gradient were applied, exactly as in the final lattice configuration for the measurement of the $\mathbb{Z}_2$ minimal instance. This includes that the superlattice phase was adjusted to compensate the tilt for the a-particles. The tunnel oscillations are detected with a single a-particle. The resulting tunneling rate is $J'/h = 523(3)$ Hz and a tilt distribution with standard deviation of $\sigma_\Delta/h = 0.62(6)$ kHz. **d–f** Tunnel oscillations on a driven double well were measured for various driving strengths to calibrate the modulation amplitude. **d** $\chi \approx 0.61$, **e** $\chi \approx 1.23$, **f** $\chi = 1.84$.

f-particle between the ground and the excited state $\Delta E = \sqrt{\Delta_f^2 + 4J^2}$, from which Δ_f can be inferred (Fig. 3.7 a). $\Delta_f = U$ is matched by iteratively repeating this procedure until the condition is fulfilled.

Next in the calibration sequence, the modulation lattice depth and the modulation amplitude are calibrated. First, a lattice modulation spectroscopy is performed with a single particle in a double well. Here, the tilt of the double well is exclusively induced by the modulation lattice, meaning $\Delta_{SL} = \Delta_M = 0$. From the resulting resonance, the modulation lattice depth V_{mod} is inferred (Fig. 3.7 b). The modulation amplitude is further calibrated by analyzing the renormalized tunnel coupling by measurements of driven single-particle oscillations at various modulation amplitudes. Here again, it is relevant to perform the calibrations in the final lattice configuration. For this configuration, a single a-particle per double well is used because the final configuration for this particle has no energy offset between neighboring sites. In this case, the tunneling rate is renormalized according to the zeroth-order Bessel function. This has the advantage that the driving is always resonant and the observable depends strongly on the driving strength around χ_0. First, a measurement with zero driving $A_{\mathrm{mod}} = 0$ is performed in order to verify that the oscillation frequency in the combined potential agrees with the theoretical expectations (Fig. 3.7 c). Then, a set of driven tunnel oscillations at $A_{\mathrm{mod}} \neq 0$ is measured (Fig. 3.7 d-f). The driving amplitude is then fitted to match the measured oscillation frequencies. In this analysis also the inhomogeneous energy offsets between neighboring sites are taken into account and modeled to be Gaussian distributed [Eq. (3.3)].

3.1.6. Sequence and initial state preparation

In order to measure the dynamics of the Floquet model realizing the $\mathbb{Z}_2$ minimal instance, two different initial states are prepared. Both initial states have a localized matter particle, e.g. an a-particle on the left site, but differ in the state of the gauge field: for the first initial state, the gauge field is an eigenstate of the electric field operator $\hat{\tau}^x$; for the second initial state, it is in an eigenstate of the gauge-field operator $\hat{\tau}^z$. In the first case, the f-particle is delocalized over the two sites, e.g. in the positive superposition of being on the left and right double-well site. In the second case, the f-particle is localized to one of the sites. The experimental sequences for both initial states are very similar, thus the sequence is discussed based on the conceptually and experimentally more challenging initial state with a delocalized f-particle in a positive superposition state.

The experimental sequence starts with the preparation of two particles in the hyperfine states $|F = 1, m_F = \pm 1\rangle$ per double well. As the preparation of doubly-occupied sites cannot be done with high fidelity also double wells with other occupation numbers arise. These are mainly double wells occupied by a single particle. In order to distinguish the resulting signal of doubly- and singly-occupied double wells, it is desirable to prepare the particles in singly-occupied double wells in a different hyperfine state $|F = 1, m_F = 0\rangle$. To this end, a Bose-Einstein condensate (BEC) of bosonic ^{87}Rb atoms in the $|F = 1, m_F = -1\rangle$ state is loaded in a 3D optical lattice with lattice depth $V_{x,l} = 30(1)\,E_{r,l}$, $V_y = 35(1)\,E_{r,s}$, and $V_z = 50(2)\,E_{r,s}$. These loading ramps are exponentially shaped with a $1/e$-time of $\tau = 5\,\mathrm{ms}$ for the horizontal lattices (x, y) and $\tau_z = 1.5\,\mathrm{ms}$ for the vertical lattice during a time segment of 50 ms.

Initially, all atoms are in the state $|F = 1, m_F = -1\rangle$ (Fig. 3.8 a). The loading procedure is optimized to maximize the amount of doubly-occupied long-period lattice sites along the x-direction with respect to singly- and triply-occupied lattice sites. Then, they are transferred to the $|F = 1, m_F = 0\rangle$ state by a series of mircowave-driven adiabatic passages via the

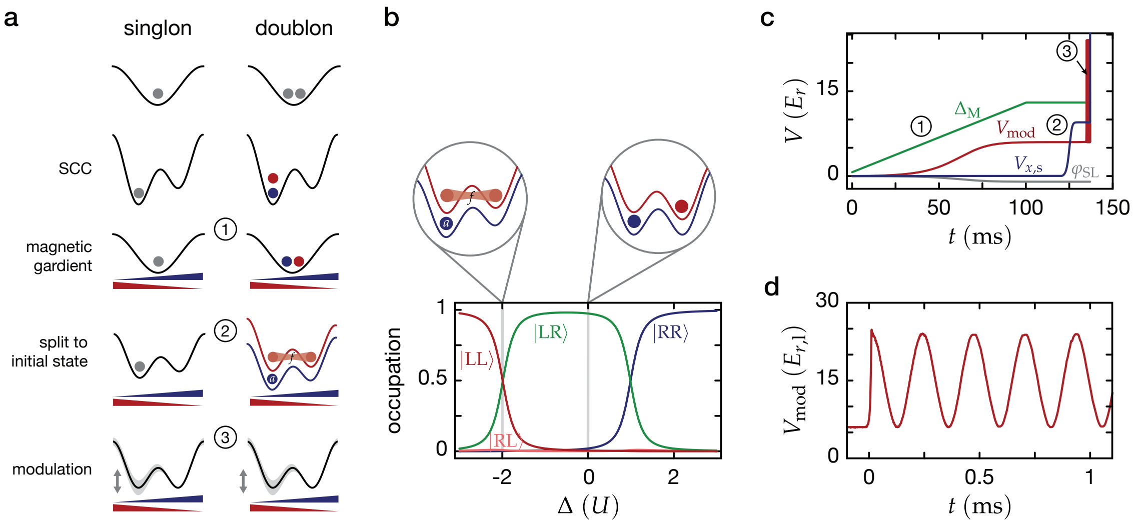

Figure 3.8.: Experimental sequence. a Illustrations of the individual steps during the experimental sequence for singly- and doubly-occupied double wells. Atoms are depicted as circles colored occurring to their hyper-fine state in the ^{87}Rb $F = 1$ manifold: $m_\mathrm{F} = -1$ (blue), $m_\mathrm{F} = 0$ (gray), and $m_\mathrm{F} = +1$ (red). The red and blue triangles represent the potential induced by the magnetic gradient. **b** Calculation of the state occupation for different modulation lattice depth during splitting with the short-period lattice potential. Zooms show illustrations of the two resulting initial states used for the experiment. **c** Experimental ramps of the parameters for the numbered steps in **a**. **d** Measured modulation intensity with sudden jump at $t = 0$.

$|F = 2, m_F = -1\rangle$ state. Afterwards, the atoms are more strongly confined to increase the on-site interactions by ramping up the short-period lattice with a superlattice phase φ_SL such that both particles are localized to the energetically lower-lying lattice site in 15 ms. During the same time, the orthogonal lattices are increased to $V_y = 100(5)\,E_{r,s}$ and $V_z = 120(6)\,E_{r,s}$ to further increase the on-site interaction energy. Finally, atom pairs are transferred to a pair of $|F = 1, m_F = \pm 1\rangle$ atoms by an adiabatic passage of microwave-mediated spin-changing collisions (SCC) [154]. Note that only pairs change their hyperfine state, while single atoms remain in the $|F = 1, m_F = 0\rangle$ state. The atoms are now correctly labeled and are merged again in a long lattice site by adiabatically switching off the short-period lattice $V_{x,s} = 0$ in 15 ms.

A magentic gradient of $B'/h \approx 5.93\mathrm{kHz}/\lambda_s$ is applied within 120 ms together with the calibrated superlattice phase φ_{SL} such that $\Delta_a = 0$. Then, the modulation lattice is turned on to $V_\mathrm{mod} = 6.0(1)\,E_{r,l}$ (Fig. 3.8 b). This value is chosen such that after subsequent adiabatic splitting with the short-period lattice $V_{x,s} = 9.50(1)\,E_{r,s}$ in 10 ms, the f-particle is delocalized between the two sites and the a-particle is localized. The smaller value of V_mod compared to $V_\mathrm{mod}^{(0)}$ thereby reduces the left site's on-site energy by approximately $2U$, which localizes the a-particle to the left site. The potential for the f-particle is also higher on the right site by exactly the interaction energy U. In the presence of the a-particle on the left site, however, the energy difference is compensated. Thus, the f-particle effectively experiences no tilt between neighboring lattice sites and adiabatically enters the positive superposition state after the splitting (Fig. 3.8 c). After this adiabatic initial state preparation, the dynamics is enabled by a quench to the effective model by switching on the modulation with a phase $\phi = 0$. The associated sudden jump of the modulation lattice is performed in 50 µs (Fig. 3.8 d). The modulation is performed with an amplitude $t_{\text{mod}} = 9.0(1)\, E_{r,\text{l}}$ and a frequency of $\omega = 2\pi \times 4320\text{Hz}$. After a variable hold time t, the dynamics was inhibited by rapidly decoupling the sites $V_{x,s} = 40\, E_{r,s}$ in 50 µs. Then, the site occupations are detected for a- and f-particles by site-resolved band-mapping detection together with a Stern-Gerlach species separation [4, 6, 147].

To prepare the second initial state, an eigenstate of the gauge-field operator $\hat{\tau}^z$, the sequence is only slightly modified. The change involves only the initial value of the modulation lattice ramp, which is set to $V_{\text{mod}} = V_{\text{mod}}^{(0)} = 15.0(1)\, E_{r,\text{l}}$. After the splitting, the f-particle localizes to the right lattice site. The a-particle is thereby repelled to the left site by the on-site interaction.

Both initial states are only approximations of the exact eigenstates of the parameters $\hat{\tau}^x$ and $\hat{\tau}^z$ and can be numerically calculated as the ground state of the static preparation Hamiltonians. For the experimental lattice parameters this leads to

$$|\Psi_{\text{init}}^x\rangle \approx 0.70\,|\text{LL}\rangle + 0.71\,|\text{LR}\rangle + 0.087\,|\text{RL}\rangle + 0.036\,|\text{RR}\rangle \tag{3.7}$$

for the initial state that corresponds to the eigenstate of the electric field operator $\hat{\tau}^x$. The experimental initial state that corresponds to the eigenstate of the gauge field operator $\hat{\tau}^z$ is

$$|\Psi_{\text{init}}^z\rangle \approx 0.071\,|\text{LL}\rangle + 0.98\,|\text{LR}\rangle + 0.025\,|\text{RL}\rangle + 0.15\,|\text{RR}\rangle\,. \tag{3.8}$$

3.2. Dynamics in the $\mathbb{Z}_2$ double well

3.2.1. Probing a single sector with the $\hat{\tau}_x$ initial state

The experiment is performed according to the sequence described above for two different initial states (Fig. 3.8). First, the initial state resembling an eigenstate of the electric-field operator $\hat{\tau}_x$ in the minimal instance is prepared $|\psi_{\text{init}}^x\rangle \simeq |\text{L}\rangle_a \otimes (\,|\text{L}\rangle_f + |\text{R}\rangle_f)/\sqrt{2}$ and the dynamics of the a- and f-particle occupation numbers are measured. The occupation numbers directly reveal the expectation value of the charge $\hat{Q} = e^{\text{i}\pi\hat{n}_{\text{L}}^a}$ and the gauge-field operator $\hat{\tau}^z = \hat{n}_{\text{R}}^f - \hat{n}_{\text{L}}^f$. In Sec. 2.1.3, the analytic result for the dynamics of the expectation value for both, the charge and the gauge-field operator, are presented for the minimal instance. The result is an oscillatory behavior of $\langle \hat{Q}_{\mathrm{L}}(t) \rangle$, while $\langle \hat{\tau}^z(t) \rangle = 0$ for all times. Furthermore, the oscillation amplitude is sensitive to the relative electric field strength $J_f / J_a = \mathcal{J}_0(\chi_0) / \mathcal{J}_1(\chi_0) \approx 0.54$ for $\chi_0 \simeq 1.84$. This ratio corresponds to an intermediate regime with an expected maximum value of $\langle \hat{Q}_{\mathrm{L}} \rangle_{\max} = (J_a^2 - J_f^2) / (J_a^2 + J_f^2) \approx 0.54$. Note that the oscillation frequency also depends on J_f / J_a and scales as $\sqrt{J_f^2 + J_a^2}$. On the level of the minimal instance, the limiting cases as well as this intermediate case can be understood by looking at the local gauge symmetries. The initial state occupies a single sector with $g_{\mathrm{L}} = -g_{\mathrm{R}} = -1$. According to Gauss's law, the local symmetries are conserved and therefore tunneling of the matter particle is accompanied by a change of the electric field on the traversed link. Changing the electric field involves the energy cost $2\,J_f$, which detunes the oscillations. In a weak electric field regime ($J_f / J_a \ll 1$), the energy cost is small and the matter particle tunnels freely between the two sites. In the limit of a strong electric field ($J_f / J_a \gg 1$), the energy cost for tunneling is high and therefore the particle remains localized. In the intermediate regime, the tunneling is hence neither fully free nor localized.

In Fig. 3.9 the measured results are presented. They consist of time traces of the expectation value of the charge (a-particles) and gauge-field (f-particle) operator for $U/J \simeq 6.6$ and $\Phi = 0$. As expected, the charge oscillates and the f-particle dynamics is strongly suppressed. However, a detailed comparison with the expected results reveals deviations (gray lines in Fig. 3.9). Especially a larger characteristic oscillation frequency for the charge compared to the prediction Eq. (2.9) is observed. This deviation and the damped oscillations can be mainly attributed to the averaging during the measurement over the 3D array of the double wells exposed to the intrinsic inhomogeneous tilt distribution (Sec. 3.1.2). To support this statement and additionally take the effects of the time-dependent implementation of the minimal instance into account, a numerical analysis of the tight-binding model (3.6) is performed. The simulation is based on independently calibrated parameters and does not include any fit free parameter. The results of this time-dependent exact diagonalization are the blue and red sold lines in Fig. 3.9. They are in good agreement with the experimental results. Note that the fast oscillations in both, the data and the numerics, can be attributed to the micromotion at non-stroboscopic times [101].

The numerical analysis is performed using a Trotter method. This means that the wave function evolves according to a sequence of quasi-static time-evolution operators $\hat{U}_n = \exp\{-\mathrm{i}\hat{H}(t_n)\,\Delta t/\hbar\}$ each at a time point $t_n = n\,\Delta t$ with $n \in \mathbb{N}$. The time step needs to be short compared to the highest frequency in the system $\Delta t = 2\pi / (s\omega)$ and is therefore chosen to subsample the driving frequency ω by $s \sim 50$. Regarding the parameters, the experimentally calibrated values for J', Δ_{M}, Δ_{SL}, and ω are used together with the calculated extended Bose-Hubbard parameters δ_j and u_{LR} from the lattice depths. For the

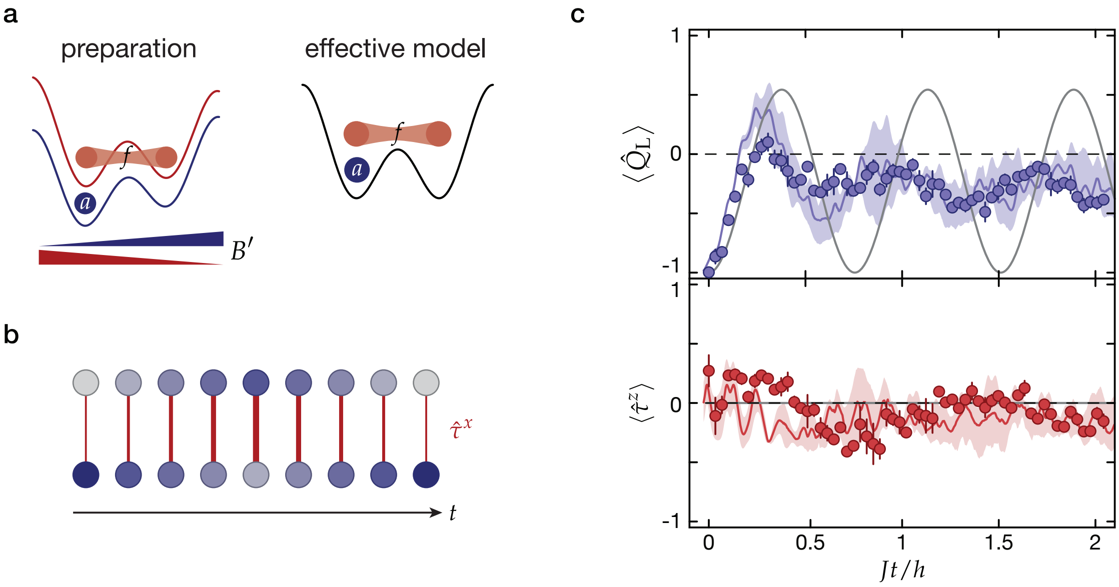

Figure 3.9.: Dynamics of the $\mathbb{Z}_2$ double well starting from an eigenstate of the electric field operator. a Illustration of the initial state $|\psi^x_\mathrm{init}\rangle = |\mathrm{L}\rangle_a \otimes (|\mathrm{L}\rangle_f + |\mathrm{R}\rangle_f)/\sqrt{2} = (|\mathrm{LL}\rangle + |\mathrm{LR}\rangle)/\sqrt{2}$ and its preparation. The species-dependent potentials in the experimental realization (left) and effective potentials during the dynamics in the Floquet model (right) are shown. **b** Pictogram of the dynamics showing how the charge and electric field dynamics are coupled. **c** Experimentally-measured dynamics of the expectation values of the $\mathbb{Z}_2$ charge $\langle \hat{Q}_\mathrm{L} \rangle$ and the $\mathbb{Z}_2$ gauge field $\langle \hat{\tau}^z \rangle$. The data points and error bars are the mean and the standard deviation of at least three independent measurements. The blue and red lines show a numerical calculation using a time-dependent exact-diagonalization method. The numerics include averaging of the observables in the presence of an inhomogeneous tilt distribution (Sec. 3.1.2). The tilt distribution is modeled by a normal distribution with a standard deviation of $\Delta_\sigma/h = 0.44(2)$ kHz, which was calibrated from bare tunneling oscillations (Fig. 3.5). A bootstrap for 1000 randomly sampled tilt values was performed. The solid line represents the median and the shading the 1σ-confidence interval. The calculations are preformed with the experimentally-calibrated parameters $J/h = 587(3)$ kHz, $\Delta_f/h = 4.19(3)$ kHz, and $U/h = 3.85(7)$ kHz and additionally calculated corrections from the extended Bose-Hubbard model. The gray solid lines are the ideal dynamics of the minimal instance according to Eqs. (2.9) and (2.10).

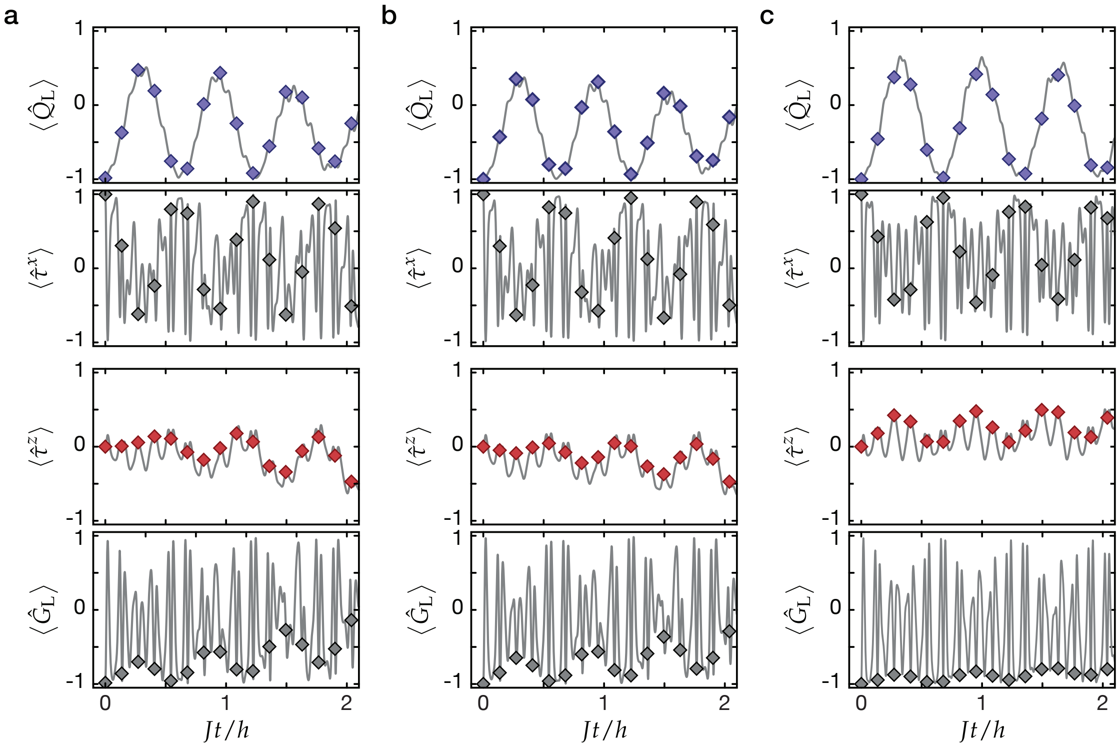

Figure 3.10.: Overview over single numeric traces. The solid lines show the expectation values of the $\mathbb{Z}_2$ charge $\langle\hat{Q}_\mathrm{L}\rangle$, the $\mathbb{Z}_2$ electric field $\langle\hat{\tau}^x\rangle$, the $\mathbb{Z}_2$ gauge field $\langle\hat{\tau}^z\rangle$, and the $\mathbb{Z}_2$ symmetry operator $\langle\hat{G}_\mathrm{L}\rangle$ according to a full numeric time evolution of the time-dependent Hamiltonian neglecting terms from the extended Bose-Hubbard model with $u_\mathrm{LR} = 0$. The diamonds indicate stroboscopic time points. **a** Traces for the central double well with the experimental parameters, $\delta_n = 0$, and the experimental $\hat{\tau}_x$ initial state. **b** Same parameters as in **a** but with the perfect initial state. **c** Perfectly matched parameters $\hbar\omega = U = \Delta_f$ and perfect initial state.

initial state, the ground state at the end of the preparation sequence is inserted [Eq. (3.7)]. The time traces for a single two-site model are presented in Fig. 3.10 and show a strong oscillatory behavior. The stroboscopic time points (diamonds in Fig. 3.10) reveal that these strong oscillations are present only within a driving period and correspond to the micromotion. In a next step, the averaging of the measured observables over the inhomogeneous tilt distribution is taken into account. To this end, an additional state-independent tilt δ_n is added to Δ_SL in the Hamiltonian, which is randomly drawn from a Gaussian distribution [Eq. (3.3)] with a standard deviation of Δ_σ extracted from the measurement of the tunnel oscillations (Sec. 3.1.5). For the analysis, 1000 different traces are averaged and the mean (blue and red solid lines) and the 1σ-confidence interval (blue and red shading) are calculated and illustrated in Fig. 3.9. In conclusion, the full time dynamics of the 3D system is well understood and describes the measurements without fit free parameters. Furthermore, the measurement constitutes a nontrivial result: an oscillation of the charge while the gauge field shows suppressed dynamics. This dynamics directly supports the realization of a minimal instance for $\mathbb{Z}_2$ symmetry LGTs. In contrast, a resonantly-driven double-well system with $\Delta_f = 0$, which does not exhibit $\mathbb{Z}_2$ symmetry, would show dynamics with equal oscillation amplitudes for a- and f-particles.

3.2.2. Probing two sectors with the $\hat{\tau}_z$ initial state

Instead of measuring the particle dynamics of an initial state occupying a single sector of the Hilbert space, a second experiment is performed. In this experiment the gauge field particle is initially in an eigenstate of the gauge field operator $\hat{\tau}^z$ and the matter particle still localizes to the left site of the double well $|\psi^z_{\mathrm{init}}\rangle = |\mathrm{L}\rangle_a \otimes |\mathrm{R}\rangle_f$. This initial state coherently occupies both sectors with $g_\mathrm{L} = -g_\mathrm{R} = \pm 1$. The expectation values of both local symmetry operators are $\langle \hat{G}_\mathrm{L} \rangle = \langle \hat{G}_\mathrm{R} \rangle = 0$. As stated above, Gauss's law Eq. (2.6) conserves the local symmetry, g_L and g_R, and therefore the sectors in the minimal instance do not couple Eq. (2.5). Here, the dynamics can be also understood discussing the limiting cases. For weak electric field strength ($J_f/J_a \ll 1$), the system is dominated by the gauge field $\hat{\tau}^z$ and remains in the eigenstate τ^z because the Hamiltonian (2.7) commutes with $\hat{\tau}^z$ for $J_f = 0$. In the limit, where the electric field dominates, the expectation value of the gauge field $\langle \hat{\tau}^z \rangle$ oscillates between the eigenvalues $\tau^z = \pm 1$. The analytic expression for the dynamics of the gauge field is

$$\langle \hat{\tau}^z \rangle = \frac{J_a^2 + J_f^2 \cos\left(2t\sqrt{J_f^2 + J_a^2}/\hbar\right)}{J_f^2 + J_a^2}, \tag{3.9}$$

which reverses the role of J_f and J_a compared to the expectation value of the $\mathbb{Z}_2$ charge. The dynamics of the $\mathbb{Z}_2$ charge Eq. (2.9), however, is identical to the dynamics expected for the $\hat{\tau}^x$ initial state. Experimentally, the intermediate regime is already probed at $J_f/J_a \approx 0.54$ for $U/J = 6.7$ and $\phi = \pi$. The resulting measurement is presented in Fig. 3.11 together with the ideal time evolution (gray lines). For short times, the dynamics agrees, while for longer observation times, it deviates due to the averaging over the inhomogeneous tilt distribution. Analog to the measurement before, a full time-dependent numerical analysis is performed by taking into account the inhomogeneous tilt distribution. The mean and the 1σ-confidence interval are shown as colored solid lines accompanied by a shading, here as well. The measured data is reasonably well captured by this numeric analysis. Noteworthy, the expectation value of $\hat{\tau}^z$ always exhibits a positive non-zero value in contrast to the previous measurement.

After the presentation of the implementation and the measurement results, the applicability for extending the $\mathbb{Z}_2$ double well to more general LGTs will be discussed. To this

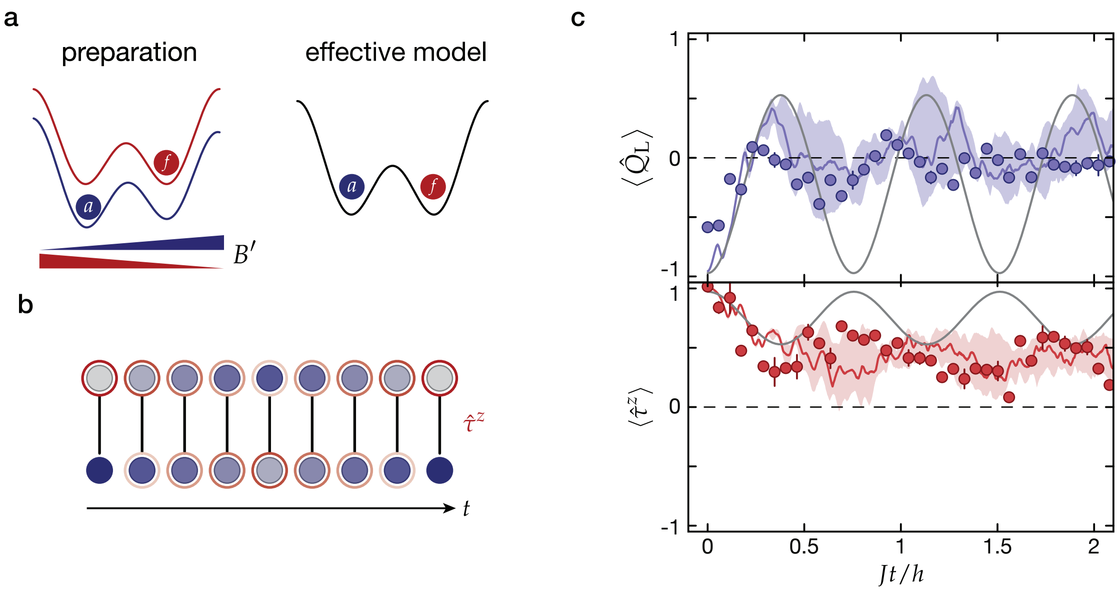

Figure 3.11.: Dynamics of the $\mathbb{Z}_2$ double well starting from an eigenstate of the gauge field operator. **a** Illustration of the initial state $|\psi^z_\mathrm{init}\rangle = |\mathrm{L}\rangle_a \otimes |\mathrm{R}\rangle_f = |\mathrm{LR}\rangle$ and its preparation. Species-dependent potential in the experimental realization (left) and in the effective Floquet potential (right). Note that the initial state has equal contributions in both sectors of the minimal instance. **b** Pictogram showing how the charge and the gauge field dynamics are coupled. **c** Experimentally-measured dynamics of the expectation value of the $\mathbb{Z}_2$ charge and the $\mathbb{Z}_2$ gauge field. The data points and error bars are the mean and the standard deviation of at least three individual experiments. The blue and red lines as well as the shadings show a numerical analysis analog to the one used for Fig. 3.9 with the experimental parameters $J/h = 578(3)$ kHz, $\Delta_f/h = 4.19(3)$ kHz, $U/h = 3.85(7)$ kHz, and $\Delta_\sigma/h = 0.46(2)$ kHz. The gray solid lines are the ideal dynamics of the minimal instance according to Eqs. (2.9) and (3.9).

end, first a detailed discussion of symmetry-breaking terms and sources is presented in the next chapter, before in Chap. 5 possibilities for extended $\mathbb{Z}_2$ LGTs are introduced.

4. Discussion of symmetry breaking

4.1. Symmetry-breaking terms in the minimal instance

Quantum simulations of gauge theories require an accurate implementation of the local symmetry constraints as these constraints ensure that Gauss's law is fulfilled and therefore ensure that the local static charges are conserved during the experiment. Such accurate implementation of local symmetry constraints sets high requirements on experimental realizations of LGTs to sufficiently suppress all symmetry-breaking terms. In the following, the terms breaking the local symmetry in the two-site two-particle model are summarized and possible sources of symmetry breaking are outlined. Furthermore, possible pathways how to suppress these symmetry-breaking sources are discussed.

The presented realization suffers from a variety of different symmetry-breaking sources. The dominant contribution stems from the inhomogeneous tilt distribution and prevents the realization from fulfilling the resonant-driving condition for all double wells simultaneously. Thus, for most of the instances, an additional energy offset between neighboring sites is present, which breaks the symmetry. However, this additional tilt can be avoided in future experimental realizations by generating a homogeneous box potential [160, 161]. In addition to this technical problem, fundamental symmetry-breaking terms of the realization can be identified. This type of gauge-variant terms directly violate the constraints of Gauss's law. They involve correlated two-particle tunneling and nearest-neighbor interactions. These processes are known to exist in interacting lattice models as a first order correction to the Bose-Hubbard model [158]. Moreover, they also arise as finite-frequency corrections to the zeroth-order effective Floquet Hamiltonian.

The zeroth-order effective Floquet model of the realization Eq. (2.25) can be expressed in matrix form using the set of basis states $|\mathrm{LL}\rangle$, $|\mathrm{LR}\rangle$, $|\mathrm{RL}\rangle$, and $|\mathrm{RR}\rangle$ as before. Here, the first and second letter describe the positions of the a- and f-particle, respectively. The effective model depends on the dimensionless driving strength χ, and the driving phase ϕ

(Sec. 2.2) and is

$$\overline{H}_{\mathrm{DW}}(\chi,\phi) = -J \begin{pmatrix} 0 & \mathcal{J}_2(\chi)\, e^{-2\mathrm{i}\phi} & \mathcal{J}_{-1}(\chi)\, e^{-\mathrm{i}\phi} & 0 \\ \mathcal{J}_2(\chi)\, e^{2\mathrm{i}\phi} & 0 & 0 & \mathcal{J}_1(\chi)\, e^{\mathrm{i}\phi} \\ \mathcal{J}_{-1}(\chi)\, e^{\mathrm{i}\phi} & 0 & 0 & \mathcal{J}_0(\chi) \\ 0 & \mathcal{J}_1(\chi)\, e^{-\mathrm{i}\phi} & \mathcal{J}_0(\chi) & 0 \end{pmatrix}. \tag{4.1}$$

A Hamiltonian fulfills the gauge symmetry, if it commutes with the local symmetry operator $\hat{G}_j$ on all sites. In the case of the minimal instance with exactly one matter particle, it is sufficient to show that the Hamiltonian commutes with the symmetry operator at one of the sites, e.g. $\hat{G}_{\mathrm{L}}$, because $\hat{Q}_{\mathrm{L}} = -\hat{Q}_{\mathrm{R}}$. This relation stems from the fact that the matter particle can be either on the left or on the right site of the double well and therefore also $\hat{G}_{\mathrm{L}} = \hat{Q}_{\mathrm{L}}\, \tau^x = -\hat{G}_{\mathrm{R}}$. Hence, $[\hat{G}_{\mathrm{L}}, \hat{H}] = -[\hat{G}_{\mathrm{R}}, \hat{H}]$ and $\hat{G}_{\mathrm{L}}$ and $\hat{G}_{\mathrm{R}}$ simultaneously commute with $\hat{H}$. Note that this symmetry leads also to $g_{\mathrm{L}} = -g_{\mathrm{R}}$, constraining the eigenvalues of $\hat{G}$ on the two sites together. Without loss of generality, the discussion is therefore restricted to $\hat{G}_{\mathrm{L}}$. In matrix form $\hat{G}_{\mathrm{L}}$ is

$$\overline{G}_{\mathrm{L}} = |\mathrm{LR}\rangle\langle\mathrm{LL}| - |\mathrm{RL}\rangle\langle\mathrm{RR}| + \mathrm{h.c.} \tag{4.2}$$

The Hamiltonian $\overline{H}_{\mathrm{DW}}(\chi,\phi)$ commutes with the symmetry operator $\hat{G}_{\mathrm{L}}$ for all χ but only for modulation phases $\phi = \{0, \pi\}$. Variations in the driving amplitude only make the $\mathbb{Z}_2$ electric field dependent on the matter particle (Sec. 2.2.4) but do not break the gauge symmetry, while an inaccurate modulation phase ϕ on the other hand will directly break the symmetry. Note that the weak constraint for the dependence of the electric field energy on the matter particle occupation is only valid for the $\mathbb{Z}_2$ double well. For extended $\mathbb{Z}_2$ LGTs, the electric field energy must be independent of the matter particle occupation.

In addition to the terms in $\overline{H}_{\mathrm{DW}}$, other terms can arise in the realization of the two-site two-particle model. First, individual detuning terms $\delta H_{\mathrm{det},ij} = \delta_{ij}\, |ij\rangle\langle ij|$ do not commute with $\hat{G}_{\mathrm{L}}$ individually and thus directly break the gauge-symmetry. These terms typically arise together in combinations, e.g. in the superlattice tilt $\delta H_{\mathrm{SL}} = \delta_{\mathrm{SL}}\{2\,|\mathrm{LL}\rangle\langle\mathrm{LL}| + |\mathrm{LR}\rangle\langle\mathrm{LR}| + |\mathrm{RL}\rangle\langle\mathrm{RL}|\}$ or in form of a finite magnetic gradient $\delta H_{\mathrm{M}} = \delta_{\mathrm{M}}\{|\mathrm{RL}\rangle\langle\mathrm{RL}| - |\mathrm{LR}\rangle\langle\mathrm{LR}|\}$. and violate the gauge constraints. The only combination that does not break the symmetry is a global energy shift. In addition to the detunings, another diagonal contribution is the next-neighbor interaction $\delta H_{\mathrm{nn}} = u_{\mathrm{nn}}\{|\mathrm{RL}\rangle\langle\mathrm{RL}| + |\mathrm{LR}\rangle\langle\mathrm{LR}|\}$, which also breaks the symmetry. Furthermore, two different two-particle tunneling processes are possible, which both do not commute with $\hat{G}_{\mathrm{L}}$ and therefore break the gauge symmetry. The processes are a direct exchange coupling $\delta H_{\mathrm{ex}} = u_{\mathrm{ex}}\{|\mathrm{LR}\rangle\langle\mathrm{RL}| + \mathrm{h.c.}\}$ and a pair-hopping $\delta H_{\mathrm{pair}} = u_{\mathrm{pair}}\{|\mathrm{LL}\rangle\langle\mathrm{RR}| + \mathrm{h.c.}\}$.

In summary, all other terms than those in $\overline{H}_{\mathrm{DW}}$ are gauge-variant and directly violate Gauss's law constraints. The matrix representation of the two-site two-particle model including δ_{ij}, u_{nn}, u_{ex}, and u_{pair} is

$$\overline{H}_{\text{DW,corr}} = -J \begin{pmatrix} \delta_{\text{LL}} & \mathcal{J}_2(\chi) & -\mathcal{J}_1(\chi) & u_{\text{pair}} \\ \mathcal{J}_2(\chi) & \delta_{\text{LR}} + u_{\text{nn}} & u_{\text{ex}} & \mathcal{J}_1(\chi) \\ -\mathcal{J}_1(\chi) & u_{\text{ex}} & \delta_{\text{LR}} + u_{\text{nn}} & \mathcal{J}_0(\chi) \\ u_{\text{pair}} & \mathcal{J}_1(\chi) & \mathcal{J}_0(\chi) & \delta_{\text{RR}} \end{pmatrix} . \tag{4.3}$$

In the experimental realization, the dominant symmetry-breaking contributions are the detuning terms, which stem mainly from the residual inhomogeneous trapping potential and residual magnetic gradients. Suppressing these inhomogeneities is a rather technical problem and can be resolved in future experiments by implementing a box potential among others. The detuning terms together with pair and exchange hoppings do, however, also arise as corrections to the zeroth-order effective Floquet model in the finite-frequency limit (Sec. 4.2). Next-neighbor interactions as well as pair- and exchange-hopping terms are also found as additional terms in the extended Bose-Hubbard model (Sec. 4.3). In the following sections, these sources of symmetry-breaking are discussed and their effect on the dynamics is studied numerically.

4.2. Effect of finite-frequency corrections on the effective model

Reaching the high-frequency limit in experimental realizations, which use periodic driving of the on-site potential is generally challenging because both energy scales, the energy scale for the driving $\hbar\omega$ and the tunneling J, are given by the lattice parameters. Therefore, the energy scales are coupled and cannot be chosen orders of magnitude different as required in the high-frequency limit $\hbar\omega \gg J$. This is especially difficult in setups, in which the driving is matched to the interaction strength $\hbar\omega \sim U$ as in the presented implementation and in setups, in which the interaction energy cannot be tuned independently, e.g. via a Feshbach resonance.

In the experimental realization of the $\mathbb{Z}_2$ double well, the parameter ratio is $U/J \simeq 6.6$ and consequently higher-order terms are expected to become relevant. To study the impact of the corrections on the dynamics and analyze the symmetry-breaking terms, the first order-correction to the infinite-frequency Floquet model was calculated. In this derivation a small deviation ξU to the infinite-frequency driving condition $\hbar\omega = U$ is taken into account such that $\hbar\omega = (1+\xi)U$. This is motivated by the fact that the resonant-driving condition for a single particle on a double well with tilt Δ_1 is $\hbar\omega_1 = \sqrt{\Delta_1 + 4J^2} \approx (1+\xi_1)\,\Delta_1$, where $\xi_1 = 2J/\Delta_1$. For a driving phase of $\phi = 0$, the resulting effective model including the first-order corrections is then

$$\overline{H}_{\mathrm{F}} = -J \begin{pmatrix} 2\xi\frac{U}{J} - 1_{\xi}\frac{J}{U}c_{\mathrm{L}}(\chi) & \mathcal{J}_2(\chi) & -\mathcal{J}_1(\chi) & -1_{\xi}\frac{J}{U}c_{\mathrm{P}}(\chi) \\ \mathcal{J}_2(\chi) & 1_{\xi}\frac{J}{U}c_{\mathrm{L}}(\chi) & -1_{\xi}\frac{J}{U}c_{\mathrm{ex}}(\chi) & \mathcal{J}_1(\chi) \\ -\mathcal{J}_1(\chi) & -1_{\xi}\frac{J}{U}c_{\mathrm{ex}}(\chi) & \xi\frac{U}{J} + 1_{\xi}\frac{J}{U}c_{\mathrm{R}}(\chi) & \mathcal{J}_0(\chi) \\ -1_{\xi}\frac{J}{U}c_{\mathrm{P}}(\chi) & \mathcal{J}_1(\chi) & \mathcal{J}_0(\chi) & \xi\frac{U}{J} - 1_{\xi}\frac{J}{U}c_{\mathrm{R}}(\chi) \end{pmatrix} \tag{4.4}$$

with the short form $1_{\xi} = 1 + \xi$ and the correction coefficients $c_{\mathrm{L}}(\chi)$, $c_{\mathrm{R}}(\chi)$, $c_{\mathrm{ex}}(\chi)$, and $c_{\mathrm{P}}(\chi)$, which only depend on the driving strength χ. The correction coefficients themselves scale with J/U compared to the tunneling and vanish in the high-frequency limit. Note that in addition, detuning terms proportional to $\xi U/J$ appear in the Hamiltonian, which diverge in the high-frequency limit. Therefore, ξ needs to vanish in the high-frequency limit and the resonance frequency must be $\hbar\omega = U$. In Fig. 4.1 a the values of the correction coefficients for the diagonal terms are shown individually for all states in dependence on χ. It is visible that the correction coefficients obey the symmetry $c_{\mathrm{LR}} = -c_{\mathrm{LL}} \equiv c_{\mathrm{L}}$ and $c_{\mathrm{LR}} = -c_{\mathrm{RR}} \equiv c_{\mathrm{R}}$, where c_{ij} describe the diagonal correction term to the state $|ij\rangle$. This relation is used in Eq. (4.4) to simplify the presentation. The full diagonal elements δ_{ii} are shown in Fig. 4.1 b together with the differences of the elements involved in the one-particle hopping processes. It is clear that by varying ξ the overall detuning can be reduced. However, the diagonal elements cannot be made equal. Note that the optimum does not seem to be at $\xi = 0$. In Fig. 4.1 c, a measure of this overall detuning is shown. It is, however, not known if the optimum of this quantity is also the optimum value for minimizing symmetry-breaking contributions.

To verify that the Hamiltonian including the first-order correction well describes the realization for the experimental parameters and time scales and also that higher-order terms can be neglected, the dynamics of the model was compared to a full time-dependent numerical analysis. The time traces in Fig. 4.2 show a good agreement between the time-dependent and the effective model for the experimental time-scales. This supports that the first-order corrections to the Floquet model are sufficient to describe the time evolution. However, a comparison of these traces to the zeroth-order effective model reveals drastic modifications. Thus, the correction terms have significant contributions and are not negligible. As discussed before, all correction terms break the $\mathbb{Z}_2$ symmetry of the minimal instance.

The expectation value of the symmetry operator $\langle \hat{G}_{\mathrm{L}} \rangle$ is a good measure for symmetry breaking. The value is constant during the time evolution for a gauge-invariant system and the value changes if the system breaks the gauge symmetry. Measuring $\langle \hat{G}_{\mathrm{L}} \rangle$ in the experiment is difficult because correlations between the a- and the f-particle need to be determined. In the current setup, this was not possible. Therefore, a numerical analysis was performed. For $U/J = 7$, close to the experimental parameter, the expectation value

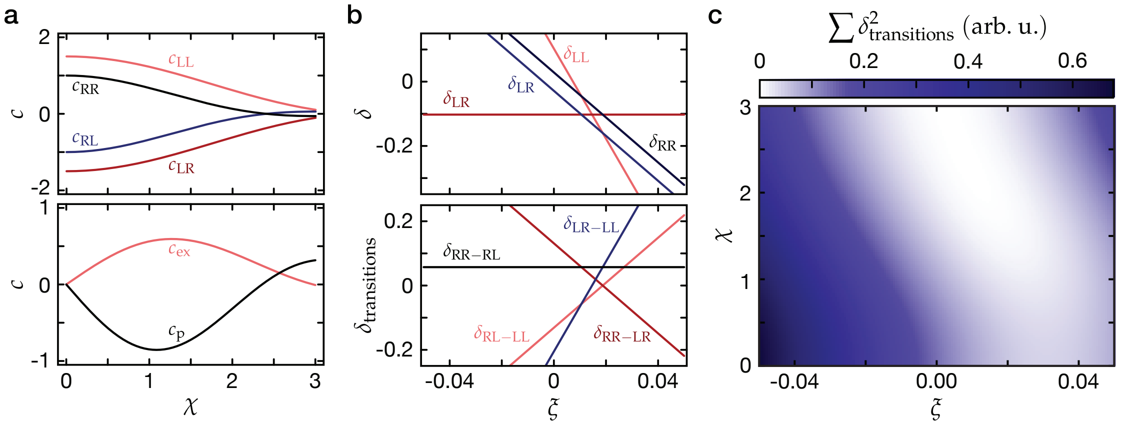

Figure 4.1.: Coefficients of the first-order corrections to the effective model. **a** Diagonal and off-diagonal coefficients of the first order-correction to the effective model in dependence of the dimensionless driving parameter. **b** Diagonal coefficients at $\chi = 1.84$ versus a detuning ξ from the ideal resonance condition $\hbar\omega = (1+\xi)\,U$ (top) and differences of the diagonal terms for the major transitions (bottom). **c** The geometric mean of the major transitions' detunings is used as a measure for the total detuning of the resonances versus χ and ξ.

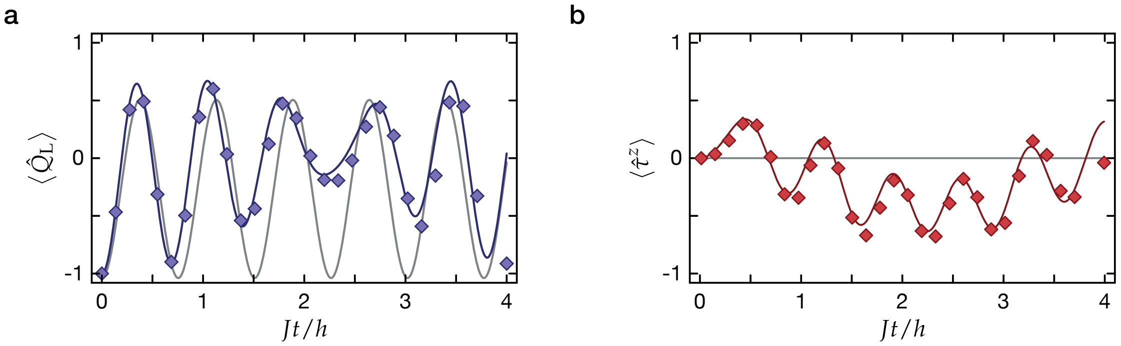

Figure 4.2.: Finite-frequency corrections to the zeroth-order Floquet Hamiltonian. The solid lines are the time evolution of the charge $\langle \hat{Q}_{\mathrm{L}} \rangle$ (blue, **a**) and gauge field $\langle \hat{\tau}^z \rangle$ (red, **b**) according to effective Floquet Hamiltonian (4.4), which includes the first-order correction. Diamonds show the stroboscopic dynamics of the full time-dependent Hamiltonian (2.24) neglecting terms from the extended Bose-Hubbard model. The parameters are chosen close to the experimental parameters $U/J = 7$. The driving is performed at single-particle resonant driving $\hbar\omega = \sqrt{U^2 + 4J^2} \approx 1.04\,U$. Gray lines show the ideal solution Eqs. (2.9) and (2.10) of the zeroth-order effective Hamiltonian (2.25) for $\phi = 0$.

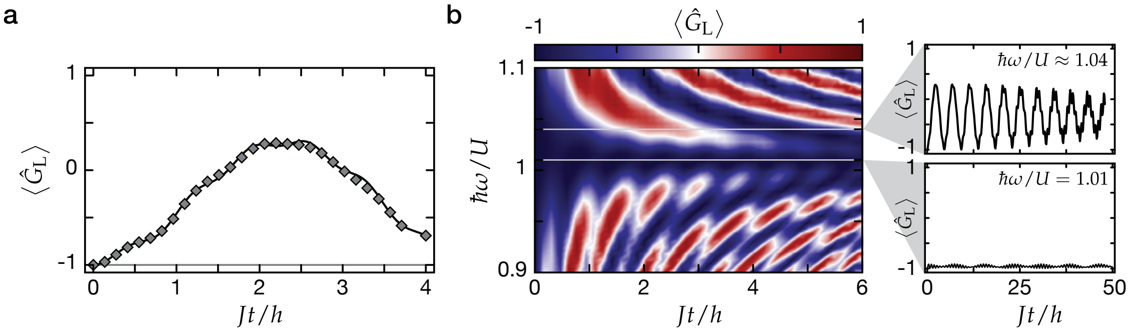

Figure 4.3.: Symmetry-breaking terms from first-order corrections to the Floquet model. **a** Time-evolution of the expectation value of the $\mathbb{Z}_2$ symmetry operator $\langle \hat{G}_\mathrm{L} \rangle$ of the effective Hamiltonian up to the first order for driving with $\hbar\omega = \sqrt{U^2 + 4J^2}$ and $U/J = 7$ close to the experimental parameters (solid line). The stroboscopic time points of the full time-dependent analysis according to Eq. (2.24) [diamonds]. The gray line shows the ideal solution. **b** Stroboscopic dynamics of the expectation value of the local $\mathbb{Z}_2$ symmetry operator $\langle \hat{G}_\mathrm{L} \rangle$ for different driving frequencies ω. The panels on the right show examples of the time traces for $\hbar\omega \approx 1.04\,U$ and $\hbar\omega = 1.01\,U$.

of the symmetry operator was calculated for the effective Hamiltonian including the first-order corrections Eq. (4.4) as well as for a full time-dependent numerical analysis. Note that terms from the extended Bose-Hubbard model are not included i n both calculations but their effect will be discussed separately in the next section. The results are shown in Fig. 4.3 a. The effective model agrees well with the full time-dependent numerics. However, after short times already large deviations from the initial condition $\langle \hat{G}_\mathrm{L} \rangle = -1$ are observed. This manifests a strong symmetry breaking due to finite-frequency corrections for the experimental parameters. In the experiment, a driving with $\xi \approx 0.04$ was chosen in agreement with the single-particle resonant-driving condition $\hbar\omega_1 = \sqrt{U^2 + 4J^2}$. Already the diagonal terms in the effective model including the first-order corrections (Fig. 4.1 b) suggest a lower resonance frequency. Thus, the expectation value of the symmetry operator is calculated for different $\hbar\omega/U$ in Fig. 4.3 b. In this calculation, the stroboscopic time points of the full time-dependent numerics are evaluated. It was found that the driving frequency can be fine-tuned to $\hbar\omega \approx 1.01U$ such that $\langle \hat{G}_\mathrm{L} \rangle$ only deviates by less than 10 % for long evolution times. This constitutes an interesting result as even in the finite-frequency limit driving parameters can be identified such that the symmetry breaking stays below a certain limit. Numerical studies suggest that some experimental observables are robust to such imperfections. Hence, relaxing experimental constraints regarding the precise implementation of the local gauge invariance might be possible [162, 163].

The finite-frequency corrections scale as J/U and can therefore be minimized by increasing the interaction energy relative to the tunneling U/J. A scaling of this quantity with the

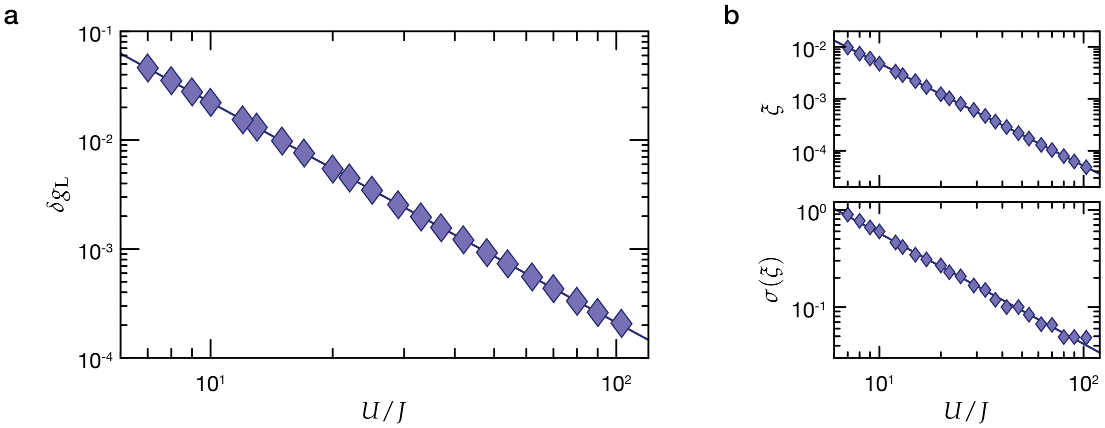

Figure 4.4.: Suppression of symmetry-breaking towards the high-frequency limit. Numerical simulation of the full-time dynamics of the minimal instance by numerically solving the time dependent Schrödinger equation. Terms from the extended-Bose Hubbared model are neglected $u_{\mathrm{LR}} = 0$. The driving frequency $\omega = (1+\xi)\, U/\hbar$ was sampled for 96 values of ξ in a range $\xi \in [0, 2\xi_{\text{guess}}]$. The time-trace with the smallest deviation in the expectation value of $\hat{G}_{\mathrm{L}}$ was selected. **a** The largest symmetry-breaking value $\delta g_{\mathrm{L}} = (1 + g_{\max})/2$ is shown versus U/J, where $g_{\max} = \max_t \langle \hat{G}_L \rangle (t)$ is the maximal value within 200 tunneling times. The initial value is $g_{\text{init}} = -1$. Note that this value belongs to the best matched driving frequency. **b** Scaling of the parameter ξ (top panel) and relative width of the resonance condition $\sigma(\xi) = |\xi_+ - \xi_-|/\xi$, where $\xi_\pm$ is such that $\delta g_{\mathrm{L}}(\xi_\pm) = 2\delta g_{\mathrm{L}}(\xi)$. This shows, that the accuracy necessary for the resonance condition increases rapidly with U/J.

lattice parameter $V_{x,s}$ is shown in the next section together with the scaling of the extended Bose-Hubbard parameters (Fig. 4.5). In real experiments, U/J cannot be increased arbitrarily. Therefore, symmetry-breaking contributions from the finite-frequency driving cannot be made arbitrarily small. To estimate the error and learn about the scaling of the corrections, a numerical analysis was performed solving the time-dependent Schrödinger equation. From the resulting wave functions, the evolution of the expectation value of $\langle \hat{G}_{\mathrm{L}} \rangle$ is considered and its maximum deviation from the initial value is calculated. The result is shown in Fig. 4.4. The symmetry-breaking is algebraically suppressed with U/J. However, the requirements for the precision of resonance frequency increases rapidly, which makes experimentally reaching higher values of U/J increasingly challenging.

4.3. Effect of the corrections from the Bose-Hubbard model

The tight-binding description of the realization was introduced in Sec. 3.1.4, in which additional processes to the regular Bose-Hubbard model [157] for interacting systems are introduced. These additional processes are nearest-neighbor interactions, direct exchange

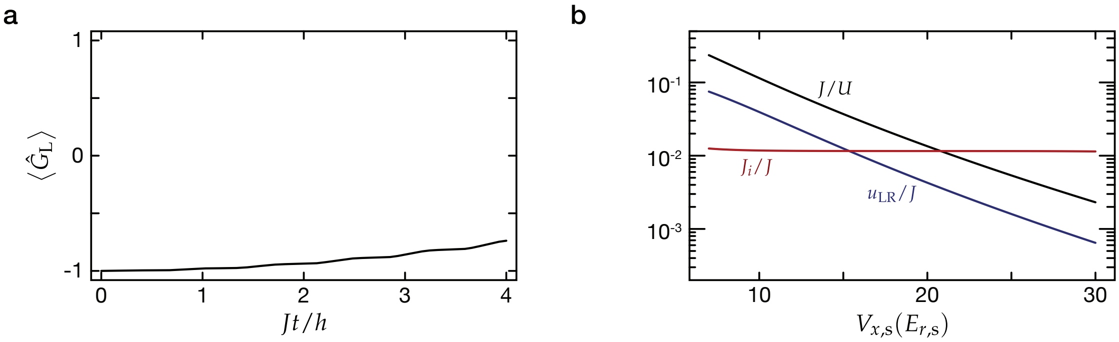

Figure 4.5.: Symmetry-breaking in the extended Bose-Hubbard model. a Time-evolution of the expectation value of the $\mathbb{Z}_2$ symmetry operator $\langle \hat{G}_\mathrm{L} \rangle$ of the zeroth-order effective Hamiltonian including $u_\mathrm{LR} = 0.03\,J$. **b** Scaling of the tight-binding parameters for an initial ratio of $V_{x,\mathrm{s}}/V_{x,\mathrm{l}} = 9.5/35$ with $V_{x,\mathrm{s}}$ and $V_{x,\mathrm{l}} \sim \sqrt{V_{x,\mathrm{s}}}$. This relative scaling keeps the ratio of the inter- to the intra-double-well tunneling constant. Shown are J/U, relevant for the finite-frequency corrections, u_LR/J for the extended Bose-Hubbard model, and the relative scaling of the inter-double-well tunneling rate J_i/J.

coupling, and correlated pair-hopping processes. The resulting model is known as extended Bose-Hubbard model [158]. All processes scale equally with u_LR (Sec. 3.1.4). Note that also the tunneling rates are modified. This, however, does not influence the gauge symmetry in the $\mathbb{Z}_2$ double well. For extended LGTs, on the other hand, the dependence of the tunneling rate on particles in the proximity is problematic and needs to be investigated in the future. Here, only symmetry-breaking terms on the level of the $\mathbb{Z}_2$ double-well are considered. To investigate the effect of these correction processes, the realization is assumed to be in the infinite-frequency limit and only the terms from the extended Bose-Hubbard model are added. In matrix representation the model is

$$\overline{H}_\mathrm{eBH} = \begin{pmatrix} 0 & -J_f & +J_a & u_\mathrm{LR} \\ -J_f & u_\mathrm{LR} & u_\mathrm{LR} & -J_a \\ +J_a & u_\mathrm{LR} & u_\mathrm{LR} & -J_f \\ u_\mathrm{LR} & -J_a & -J_f & 0 \end{pmatrix}. \tag{4.5}$$

Here, driving with $\chi_0 = 1.84$ is assumed so that the tunneling rates of the f-particles do not depend on the position of the a-particles. For the $\mathbb{Z}_2$ double well, the f-particle tunneling rate can in principle depend on the position of the a-particle without breaking the $\mathbb{Z}_2$ gauge symmetry. For extended systems this is not possible anymore.

Analog to Sec. 4.2, the expectation value of the symmetry operator is used to quantify the symmetry breaking of the corrections. To this end, the time-evolution according to Hamiltonian (4.5) is calculated numerically for the perfect initial state $|\psi^x_\mathrm{init}\rangle$. The result for $u_\mathrm{LR} = 0.03J$, similar to the experimental parameter, is shown in Fig. 4.5 a. For the experimental parameters, the resulting symmetry breaking is not as dramatic as for the finite-frequency corrections in Fig. 4.3 a. However, it is substantial with regard to extended LGTs. Therefore, it is important to also reduce the magnitude of these correction terms.

First, increasing the interaction energy via a Feshbach resonance to suppress the finite-frequency corrections will induce stronger extended Bose-Hubbard corrections because the strength of u_{LR} is proportional to the effective interaction strength $g = 4\pi\hbar^2 a_{\mathrm{s}}/m$. Therefore, a way to simultaneously suppress both corrections or at least independently suppress both contributions in necessary. Increasing the superlattice depth squeezes the wave function and thereby increases the on-site overlap. This enlarged on-site overlap increases the interaction energy and reduces the overlap between neighboring sites, which in turn reduces the extended Bose-Hubbard parameters. Simultaneously, however, the tunneling rate gets reduced; lighter atoms can help to compensate for the reduced tunneling rate in an experimental setting. In Fig. 4.5 b, the important parameters J/U and u_{LR}/J are calculated and shown in dependence of $V_{x,\mathrm{s}}$. The long lattice depth is scaled accordingly to keep the inter-double-well coupling constant.

5. Towards extended $\mathbb{Z}_2$ LGTs

5.1. One-dimensional LGT with super-sites

5.1.1. Super-sites model

In the previous sections, implementation and experimental setup for a double-well model with $\mathbb{Z}_2$ gauge symmetry were presented. The model was realized with ultracold ^{87}Rb atoms in a periodically-driven optical superlattice. The main result is the observation of the nontrivial time-dynamics of the expectation value of the $\mathbb{Z}_2$ charge and the $\mathbb{Z}_2$ gauge field. However, the experiment currently only captures the two-site model. Is it feasible to extend the scheme to a 1D $\mathbb{Z}_2$ LGT, a ladder system or even a LGT in two dimensions? And can the $\mathbb{Z}_2$ double well serve thereby as a minimal instance? In the following, a proposal for such an extension to a 1D model is presented [17] based on the work in [62].

The $\mathbb{Z}_2$ gauge field in the double-well model belongs to the link between the two sites. It is implemented by an f-particle occupying them. The gauge–matter coupling relies on the on-site interaction between a- and f-particles (Sec. 2.2). Therefore, connecting two $\mathbb{Z}_2$ double wells by simply introducing a joint site shared by both double wells is not applicable. The reason is that in this configuration, the right double-well sites would be the same as the left site of the right-neighboring double well. Consequently, the f-particles of neighboring links could both occupy the shared lattice site, which would lead to ambiguous tunneling phases for the a-particles. In this situation, the a-particle cannot distinguish to which link the f-particle belongs. Furthermore, the motion of f-particles cannot be restricted to the respective two sites of the link with a single f-particle species. In principle, both difficulties can be resolved using different species f and f' for the f-particles on alternating sites.

To practically circumvent the ambiguity caused by shared sites, a model where the double wells are stringed together is considered. The double wells are thereby connected by an additional tunnel coupling J_c. The resulting chain can then be interpreted as a 1D $\mathbb{Z}_2$ LGT of super-sites i with an a–b substructure (Fig. 5.1). The super-sites are connected by links with a gauge field $\hat{\tau}^z_{\langle i,i\pm1\rangle}$. Each super-site consists of two lattice sites, where matter

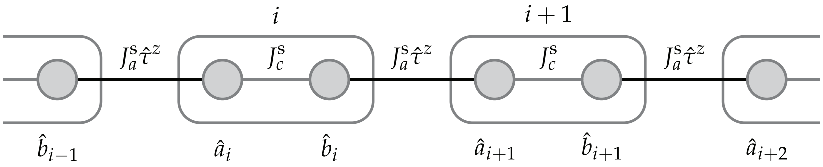

Figure 5.1.: Extending the $\mathbb{Z}_2$ double well to a 1D model with super-sites. Gray circles illustrate individual lattice sites. The box groups two lattice sites together to form a super-site i. Inside each super-site, the individual sites are coupled by J_c^{s}. The super-sites themselves are coupled by a link with a $\mathbb{Z}_2$ gauge field $J_a^{\mathrm{s}}\hat{\tau}^z$.

particles are created by the operators $\hat{a}^\dagger$ and $\hat{b}^\dagger$, respectively. The resulting Hamiltonian is

$$\hat{H}^{\mathrm{s}}_{\mathrm{1D}} = \sum_i \left[J_a^{\mathrm{s}}\, \hat{a}^\dagger_{i+1} \hat{\tau}^z_{\langle i,i+1\rangle} \hat{b}_i \, - J_c^{\mathrm{s}}\, \hat{a}^\dagger_i \hat{b}_i \, + \mathrm{h.c.} \right] - \sum_i J_f^{\mathrm{s}}\, \hat{\tau}^x_{\langle i,i+1\rangle}. \tag{5.1}$$

The interactions between matter particles are assumed to be hardcore and therefore the matter particle's creation and annihilation operators fulfill the anti-commutation relations $\{\hat{a}^\dagger_i, \hat{a}_j\} = \hbar\, \delta_{ij}$ and $\{\hat{b}^\dagger_i, \hat{b}_j\} = \hbar\, \delta_{ij}$. For the super-site model, a $\mathbb{Z}_2$ charge can be defined extending expression (2.2)

$$\hat{Q}^{\mathrm{s}}_i = \mathrm{e}^{\mathrm{i}\pi(\hat{n}^a_i + \hat{n}^b_i)}, \tag{5.2}$$

which depends on the matter-occupation number on the super-site, with $\hat{n}^a_i = \hat{a}^\dagger_i \hat{a}_i$ and $\hat{n}^b_i = \hat{b}^\dagger_i \hat{b}_i$. Then, the super-site's local gauge transformations can be defined using this charge definition

$$\hat{G}^{\mathrm{s}}_i = \hat{Q}^{\mathrm{s}}_i \hat{\tau}^x_{\langle i-1,i\rangle} \hat{\tau}^x_{\langle i,i+1\rangle}. \tag{5.3}$$

Hamiltonian $\hat{H}^{\mathrm{s}}_{\mathrm{1D}}$ is gauge-invariant with respect to the super-sites and commutes with the gauge transformation $[\hat{H}^{\mathrm{s}}_{\mathrm{1D}}, \hat{G}^{\mathrm{s}}_i] = 0$ for all sites. This strongly supports that the super-site model is a reasonable way to extend the $\mathbb{Z}_2$ double well to 1D systems. Thus, the $\mathbb{Z}_2$ double well can serve as a minimal instance. However, does the super-site model converge to the $\mathbb{Z}_2$ LGT in Eq. (2.1)?

In the limit $J_c^{\mathrm{s}} \gg J_a^{\mathrm{s}}$, each super-site hybridizes in two energetically separated states created by the operators $\hat{h}_{i,\pm} = (\hat{a}_i \pm \hat{b}_i)/\sqrt{2}$. These hybridized states have energies $\mp J_c^{\mathrm{s}}$. Therefore, there is only a negligible amount of coupling between the two hybridized states in this limit. Hence, Eq. (5.1) reduces to

$$\hat{H}^{\mathrm{s}}_{\mathrm{1D}} = J_a^{\mathrm{s}\star} \sum_i \sum_{\mu=\pm} \mu \left[\hat{h}^\dagger_{i+1,\mu} \hat{\tau}^z_{\langle i,i+1\rangle} \hat{h}_{i,\mu} + \mathrm{h.c.} \right] - J_c^{\mathrm{s}} \sum_{i,\mu=\pm} \mu\, \hat{n}^a_{i,\mu} - J_f^{\mathrm{s}} \sum_i \hat{\tau}^x_{\langle i,i+1\rangle}, \tag{5.4}$$

where the tunneling rate between states on neighboring super-sites is $J_a^{\mathrm{s}\star} = J_a^{\mathrm{s}}/2$. If initially only low energy states are occupied on the super-sites, then the higher bands

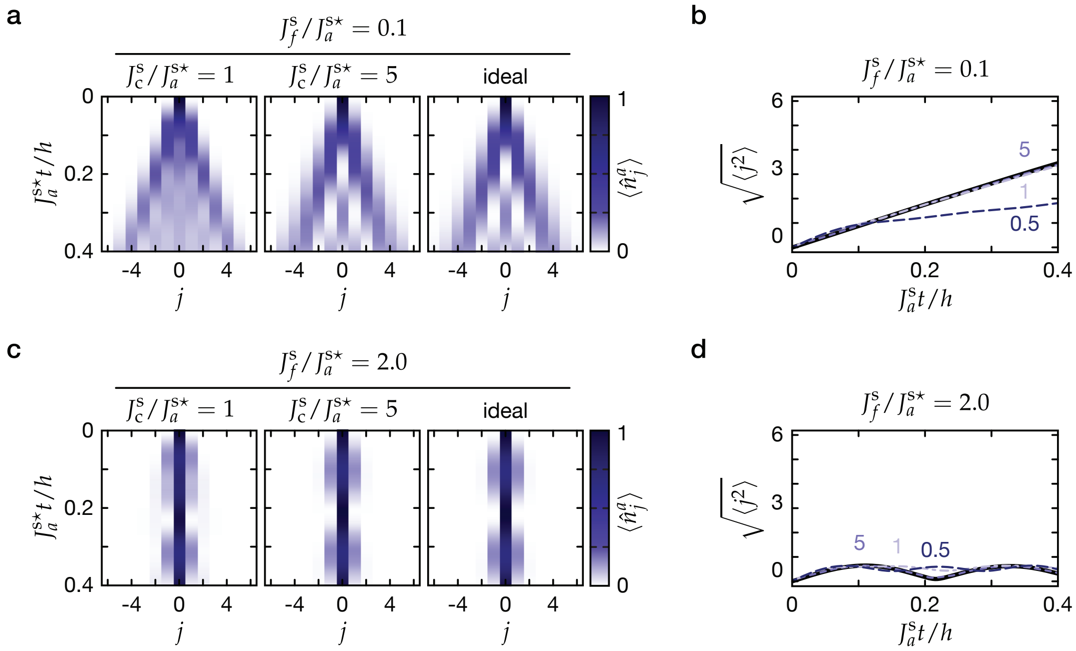

Figure 5.2.: Numeric analysis of the dynamics in the super-site model. Numerical results for the time evolution of the 1D super-site model captured by Hamiltonian (5.1) for different values of $J_f^{\mathrm{s}}/J_a^{\mathrm{s}\star}$ and different super-site couplings $J_f^{\mathrm{s}}/J_a^{\mathrm{s}\star}$. Note that $J_f^{\mathrm{s}}/J_a^{\mathrm{s}\star}$ should be directly compared to J_f/J_a in Fig. 2.2. The ideal data sets in **a** and **c** and the associated thick black lines in **b** and **d** are taken from this figure. **a** Expectation value of the $\mathbb{Z}_2$ charge in the regime with vanishing electric field $J_f^{\mathrm{s}}/J_a^{\mathrm{s}\star} = 0.1$. The cone shaped expansion of the matter particle is visible even for a super-site coupling on the order of the matter tunneling $J_c^{\mathrm{s}} \sim J_a^{\mathrm{s}\star}$. **b** Evolution of the root mean square position $\sqrt{\langle j^2 \rangle}$ for different $J_c^{\mathrm{s}}/J_a^{\mathrm{s}\star}$ labeled inside the plot. Already for $J_c^{\mathrm{s}} \sim J_a^{\mathrm{s}\star} = 1$ the expansion reproduces the ideal expansion captured by Hamiltonian (5.1) (thick black line). **c-d** The same calculations as in **a-b** for $J_f^{\mathrm{s}}/J_a^{\mathrm{s}\star} = 2.0$ in the electric field dominated regime are shown. The signatures of confinement are indeed also visible for $J_c^{\mathrm{s}} \sim J_a^{\mathrm{s}\star}$.

will remain unoccupied over time. Hence, $\hat{n}_{i,-}^a = 0$ can be assumed for all sites i. Then, Eq. (5.4) simplifies to the 1D LGT captured by Hamiltonian (2.1)

$$\hat{H}_{\mathrm{1D}}^{\mathrm{s}} = J_a^{\mathrm{s}\star} \sum_i \left[\hat{h}_{i+1,+}^{\dagger} \hat{\tau}_{\langle i,i+1 \rangle}^{z} \hat{h}_{i,+} + \mathrm{h.c.} \right] - J_c^{\mathrm{s}}\, \hat{n}_{i,+}^a - J_f^{\mathrm{s}} \sum_i \hat{\tau}_{\langle i,i+1 \rangle}^{x}. \tag{5.5}$$

In Figure 5.2, the results of a numerical analysis of the dynamics in the super-site model according to Hamiltonian (5.1) are presented. The 1D chain consists of 12 minimal instances. The features of the 1D model (2.1) is captured well by the super-site model (compare to Fig. 2.2) even for J_c^{s} on the order of $J_a^{\mathrm{s}\star}$. Already for $J_c^{\mathrm{s}}/J_a^{\mathrm{s}\star} \sim 5$, the root mean square position in Fig. 5.2b (blue) is only barely distinguishable form the ideal situation (black).

5.1.2. More than one matter particle

In an extended model with more than one matter particle, their occupation numbers on individual lattice sites can be larger than one. In this situation, more than one a-particle can interact with the f-particle and the resulting tunneling phase for the f-particle is modified. Thus, the scheme for the minimal instance breaks down. To resolve this issue, either a very low matter density or a very strong matter–matter interaction is required. The strong matter–matter interaction effectively suppresses the occurrence of multi-occupancy on each site.

In the super-site model, it is still enough to suppress multi-occupancy on individual lattice sites. The minimal instance stays functional and the gauge symmetry is fulfilled. However, the interaction has an interesting but peculiar structure as placing particles on empty site in the super-site is possible without any cost of on-site interaction energy. Therefore, placing two particles on a super-site is possible even for hardcore-interacting a-particles.

In the regime $J_c^{\mathrm{s}} \gg |J_a^{\mathrm{s}}|$, where the super-site occupation is better described by the hybridized states, an effective interaction for the second particle on the super-site arises. The Hubbard interactions on the two sites are $U_a\, \hat{n}_j^a(\hat{n}_j^a - 1)/2$ and $U_b\, \hat{n}_j^b(\hat{n}_j^b - 1)/2$. Assuming weak interactions compared to the super-site tunneling $U_a \ll J_c^{\mathrm{s}}$ and $U_b \ll J_c^{\mathrm{s}}$ ensures that the interactions do not mix the two hybridized states. A projection of the interaction on the energetically lower state results in the following interaction term of the Hamiltonian

$$\hat{H}_U^{\mathrm{s}} = \frac{1}{2} U^{\mathrm{s}\star} \sum_i \hat{n}_{i,+}^a (\hat{n}_{i,+}^a - 1) + \delta\mu \sum_i \hat{n}_{j,+}^a. \tag{5.6}$$

The first term is an effective Hubbard interaction $U^{\mathrm{s}\star} = (U_a + U_b)/4$ and the second term an additional chemical potential $\delta\mu = -(U_a + U_b)/8$. Thus, in the limit $|J_a^{\mathrm{s}}| \ll U^{\mathrm{s}\star} \ll |J_c^{\mathrm{s}}|$, the particles created by $\hat{h}_{j,+}$ can be treated as hardcore bosons [17].

5.1.3. Floquet implementation of the super-site

So far, only the effective couplings required for the extension of the minimal instance to an extended 1D system was introduced. However, a discussion of the microscopic implementation of the super-site couplings is missing. In this section, a Floquet scheme for the super-site coupling is discussed and a possible implementation with the minimal instance is proposed. The approach is closely related to the proposal [62].

There are four relevant super-site configurations for an a-particle hopping process. All of them need to have the same tunnel coupling and a tunneling phase of 0. They are defined by the gauge field values on the attached links, which are reflected by the respective

f-particle occupations on the sites. The configurations are shown in Fig. 5.3. The potential for the a-particles on the super-site has an energy-offset U between neighboring sites as in the implementation of the gauge-field dynamics (Sec. 2.2.4). The effective energy offsets between neighboring sites are 0, U, and $2U$ and have in particular always the same sign. Thus, the tunneling phase is zero for an appropriate driving phase choice. However, the three different multiphoton processes never have the same tunnel coupling for any single-frequency driving amplitude. To circumvent this limitation, a two-frequency drive is introduced [78]. The Hamiltonian for the super-site is

$$\begin{aligned}\hat{H}^{\mathrm{s}}_{c}(t) = &- J^{\mathrm{s}}_{c}\left(\hat{a}^{\dagger}\hat{b}\ +\mathrm{h.c.}\right) + \left(1 - \frac{\hat{\tau}^{z}_{\mathrm{L}} + \hat{\tau}^{z}_{\mathrm{R}}}{2}\right) U\,\hat{n}^{b} \\ &+ A^{c}_{\omega}\cos(\omega t)\,\hat{n}^{b} + A^{\mathrm{s}}_{2\omega}\cos(2\omega t)\,\hat{n}^{b}\end{aligned} \tag{5.7}$$

with $\hat{\tau}^{z}_{\mathrm{L}}$ and $\hat{\tau}^{z}_{\mathrm{R}}$ the gauge field on the left and right link, A^{c}_{ω} and A^{c}_{ω} the one- and two-frequency driving amplitude, and $\hat{n}^{b} = \hat{b}^{\dagger}\hat{b}$ the b-site occupation. An effective Floquet Hamiltonian can then be derived in the high-frequency limit similar to the minimal instance [62, 69]. Here, also the tunneling is renormalized. The renormalization factor is

$$\lambda_{n} = \sum_{l=-\infty}^{\infty} \mathcal{J}_{n-2l}(\chi^{\mathrm{s}}_{(1)})\mathcal{J}_{l}(\chi^{\mathrm{s}}_{(2)}/2) \tag{5.8}$$

for an n-photon process [78]. It depends on both dimensionless driving strengths

$$\chi^{\mathrm{s}}_{(1)} = A^{c}_{\omega}/\omega \approx 1.71, \tag{5.9}$$

$$\chi^{\mathrm{s}}_{(2)} = A^{c}_{2\omega}/\omega \approx 1.05, \tag{5.10}$$

which can be chosen such that all processes are renormalized to the same $\lambda_{0} = \lambda_{1} = \lambda_{2} \equiv \lambda^{c}$. All together, the effective Floquet Hamiltonian is

$$\hat{H}^{\mathrm{s}}_{\mathrm{F},c} = -J^{\mathrm{s}}_{c}\,\lambda^{c}\left(\hat{a}^{\dagger}\hat{b}\ +\mathrm{h.c.}\right). \tag{5.11}$$

In conclusion, the proposed super-site tunneling can be implemented such that the tunnel couplings are independent of the f-occupancy.

5.2. Proposal for an experimental implementation of the super-site model

The conceptual ingredients for an extended 1D LGT based on the experimentally demonstrated minimal instance have been established in the sections before. Here, the focus is on the experimental implementation of the presented Floquet scheme using ultracold atoms

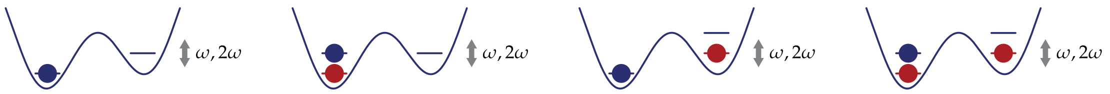

Figure 5.3.: Implementation of super-site processes. Four possible configurations of the f-particle (red circles) occupation on the super-site. The lattice potential for the a-particles (blue circles) has an energy offset of U between neighboring sites. The effective energy offset experienced by the a-particle has the same sign and is either 0, U, or $2U$. To generate the same tunnel coupling for all processes a two-frequency drive needs to be applied with the frequencies $\omega \approx U/\hbar$ and 2ω.

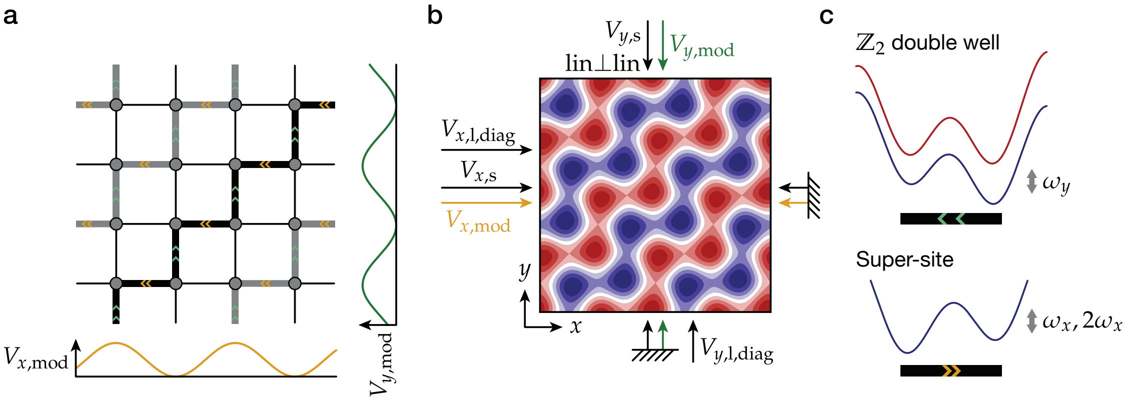

Figure 5.4.: Proposal for a super-site model implementation. **a** Square lattice with zig-zag chains. The thick lines are coupled links; the thin lines mark broken links. Links along the x-direction are the super-sites and links along the y-direction are $\mathbb{Z}_2$ double wells. The modulation lattices act on every second site illustrated by the modulation potentials (bottom and right). Note that the links are directional indicating the direction of the tilt. The modulation, however, alternately acts on the left and right side of the double wells along the chain. **b** Potential pattern realizing the zig-zag chain. It is created by a simple 2D short-period lattice ($V_{x,\mathrm{s}}$ and $V_{y,\mathrm{s}}$) and a 45° lattice created by the interference of two long-period lattice running wave beams ($V_{x,\mathrm{l,diag}}$ and $V_{y,\mathrm{l,diag}}$). In addition, the modulation lattice beams are required ($V_{x,\mathrm{mod}}$ and $V_{y,\mathrm{mod}}$). To create the energy offset for the $\mathbb{Z}_2$ double well, the short-period lattice along y is in an lin-angle-lin configuration [164]. The result is a phase shift of the lattice potential experienced by the two species. **c** Schematic of the minimal instance and the super-site associated with their directional link.

in optical lattices. Especially challenging are the different requirements for the $\mathbb{Z}_2$ double well and the super-site. The $\mathbb{Z}_2$ double well requires a species-dependent energy offset between neighboring sites and a periodic driving at $\hbar\omega = U$ with a dimensionless driving strength of $\chi_0 \approx 1.84$. The super-site on the other hand requires equal on-site energies for the a-particles, strong suppression of f-particle tunneling, and a two-frequency drive at $\hbar\omega = U$ and 2ω with dimensionless driving strengths $\chi^{\mathrm{s}}_{(1)} \approx 1.71$ and $\chi^{\mathrm{s}}_{(2)} \approx 1.05$. Hence, a separation of the two double wells into different degrees-of-freedom would be helpful.

This separation can be achieved by implementing a zig-zag 1D chain (Fig. 5.4). To this end, on top of a simple square lattice an additional lattice under 45° is overlapped with $2\sqrt{2}$ times the square-lattice spacing. The resulting lattice forms a zig-zag chain for an appropriate choice of the relative lattice phases. Now, the superlattice sites along one axes represent the $\mathbb{Z}_2$ double wells, e.g. vertical, and the double wells along the other axes the super-sites. For the $\mathbb{Z}_2$ direction a staggered species-dependent tilt is implemented, using a *lin-angle-lin* lattice configuration [164]. In this configuration, the inwards running and retro-reflected laser beams of an optical lattice are both linear polarized but with an angled polarization axis. In this setup, a relative phase shift between the potentials experienced by atoms in different atomic hyperfine states can be realized, which leads together with a long period lattice to a spin-dependent energy-offset between neighboring sites [11, 164]. The suppression of f-particle tunneling along the super-site can be achieved by a species-dependent short lattice or by a species-dependent gradient chosen off-resonant with the driving. The periodic driving can be implemented using the technique illustrated in Fig. 3.1. Thus, a modulation lattice is required on both of the axes. Note that the setup uses equal tilts but staggered driving, so that an alternating $\{0, \pi\}$-phase pattern is generated. The resulting effective Hamiltonian is

$$\hat{H}_{1\mathrm{D}}^{\mathrm{exp}} = \sum_i (-1)^i \left[J_a^{\mathrm{s}} \, \hat{a}_{i+1}^\dagger \hat{\tau}_{\langle i,i+1\rangle}^z \hat{b}_i \, - J_c^{\mathrm{s}} \, \hat{a}_i^\dagger \hat{b}_i \, + \mathrm{h.c.} \right] - \sum_i J_f^{\mathrm{s}} \, \hat{\tau}_{\langle i,i+1\rangle}^x, \tag{5.12}$$

which also fulfills the local symmetry constraints according to Eq. (5.3).

5.3. Ladder model features a global $\mathbb{Z}_2$ symmetry

The $\mathbb{Z}_2$ minimal instance can also be extended to a ladder model, which features a global $\mathbb{Z}_2$ symmetry. This model does not only obey an electric field but also $\mathbb{Z}_2$ magnetic field terms play a role. The minimal instances are thereby placed on the rungs of the ladder. Along the legs only the matter particles can tunnel. A detailed numerical analysis of this ladder using state-of-the-art density matrix renormalization group (DMRG) methods can be found in [62] together with an implementation scheme using Floquet engineering.

The numerical analysis conducted in [62] demonstrated a superfluid-to-Mott insulator transition in the charge sector for a comensurate filling with matter paricles. In the gauge sector, a transition from an ordered phase with broken global $\mathbb{Z}_2$ symmetry to a disordered regime was found. In the ordered phase, the $\mathbb{Z}_2$ magnetic field dominates and the vison excitations of the gauge field are gapped. In the disordered regime, the $\mathbb{Z}_2$ electric field dominates and the visons condense and strongly fluctuate. Such a behavior also occurs in higher-dimensional LGTs and indicates a confinement–deconfinement transitions [62].

5.4. Conclusions

In this part, a minimal instance for $\mathbb{Z}_2$ LGTs was demonstrated. The minimal instance is thereby realized by the effective Hamiltonian of a two-site, two-particles periodically-driven system. A measurement of its time dynamics was performed and the result is well described by a full time-dependent analysis of the 3D atomic system. Moreover, it was confirmed experimentally that the dynamics of the matter and gauge fields are nontrivial as predicted from the ideal $\mathbb{Z}_2$ LGT (Chap. 3).

A good understanding of the relevant symmetry-breaking contributions was gained by analyzing their sources and estimating their magnitude as well as their dependence on experimental parameters (Chap. 4). The sources in the experiment are an inhomogeneous on-site energy distribution, finite-frequency corrections to the Floquet model, and corrections to the Bose-Hubbard model [158]. The associated symmetry-breaking processes are energy offsets between neighboring sites and correlated two-particle tunneling terms. The inhomogeneous on-site energy distribution can be suppressed in future experiments by implementing a box potential. To reduce the symmetry-breaking contributions from finite-frequency corrections to the Floquet model, the high-frequency limit can be reached [99, 101, 142] or, in certain cases, the Floquet parameters can be fine-tuned. However, reaching the high-frequency limit requires highly accurate lattice and driving parameters. In experiments, this regime could be reached by increasing the inter-species scattering length using Feshbach resonances. At the same time, it enhances correlated tunneling processes. These correlated tunneling processes can be further reduced by localizing the Wannier functions more. This increased decoupling of the lattice sites is accompanied by a reduction of the tunneling rate, which suggests using a light atomic species.

In conclusion, improving the suppression of symmetry-breaking terms is possible and might enable studies of extended $\mathbb{Z}_2$ LGTs in future experiments. Future experimental realizations are especially promising because numerical studies indicate that certain experimental observables are robust to imperfections. Hence, experimental constraints regarding the precise implementation of the local gauge invariance [162, 163] could be relaxed. In summary, this study provides important insights into the applicability of Floquet schemes and underlines the relevance of considering symmetry-breaking terms in proposals for LGTs.

Moreover, the demonstrated double-well model is a key step for future experimental studies of $\mathbb{Z}_2$ LGTs coupled to matter. It serves as a minimal instance for extended models (Chap. 5) and can be assembled to 1D-chain or ladder models [62].

Part II.

Spin pumping and measurement of spin currents in optical superlattices

6. Introduction to spin pumping

6.1. Quantum spin Hall effect

In 1971, the occurrence of the spin Hall effect was predicted theoretically by Dyakonov and Perel [165, 166]. In the spin Hall effect, electrons with opposite spin accumulate on opposite surface boundaries in a sample carrying electric current. The effect is named after the classical Hall effect, which was already experimentally observed by Hall in 1879 [167]. Here instead of different spins, positive and negative charges accumulate at the surface boundary of a thin sample exposed to a magnetic field in response to an applied current. This charge accumulation leads to a Hall voltage between the boundaries, which, in the case of the ordinary Hall effect, is proportional to the applied external magnetic field. For the spin Hall effect, on the other hand, no external magnetic field is required. The spin separation is based on the spin-dependent scattering of the electrons at defects of the material via Mott-scattering [168, 169]. The scattering prefers opposite directions for the different spins and drives the diffusive spin separation process. This mechanism is called extrinsic spin Hall effect and was first detected inversely by a measurement of the transverse voltage induced by a spin current in 1984 [170].

In addition to the extrinsic spin Hall effect, there is also an intrinsic spin Hall effect, which has a close relation to the intrinsic contribution to the anomalous Hall effect in ferromagnetic metals [169, 171]. In such ferromagnetic materials, the anomalous Hall coefficient is experimentally found to be in general magnitudes larger than the ordinary Hall coefficient, which is not explainable by the material's magnetization [172, 173]. In this context, Karplus and Luttinger demonstrated that in response to an external electric field an additional contribution to the group velocity can arise, which solely depends on the eigenstates in the band structure and is vastly independent of scattering [174]. This additional contribution is called anomalous velocity and is perpendicular to the electric field. Hence, it can contribute to the Hall effect [171]. It was only much later recognized that the anomalous velocity is actually a geometric effect and given by the vector product of the electric field and the Berry curvature [89, 91, 171]. Note that the Berry curvature can be understood as magnetic field in momentum space (Sec. 1.2.2). In the case of ferromagnets, the contribution of the Berry curvature is non-zero because a strong spin-orbit interaction is present [171]. As already anticipated above, an intrinsic spin Hall effect was proposed for p- and n-type semiconductors [175, 176]. The induced spin current is dissipationless and can flow even in nonmagnetic materials [177]. The associated electron-spin polarization was first observed in electron-doped gallium arsenide near the edge of a semiconductor channel by Kerr rotation microscopy [178] and also in the hole-doped part of a p–n junction light-emitting diode by measuring the polarized light emision [179].

The dissipationless flow of spin currents in these systems and also their geometric description with the Berry curvature naturally raise the question, whether a quantized spin current can be generated under specific conditions, similar to the quantized charge transport in the quantum Hall effect (QHE) [92, 103]. In 2005, Fu and Kane predicted such a quantum spin Hall effect (QSHE) in graphene based on the Haldane model [180], which describes a 2D system on a hexagonal lattice with tunnel couplings that break time-reversal symmetry (TRS) but have no net magnetic flux. Such systems are now known as Chern insulators. The proposal effectively uses two copies of the Haldane model with opposite Berry curvature for the two electron spins. Therefore, each of the spin components independently realizes an integer QHE with inverse chirality so that a quantized spin current occurs without a net charge current. Note that the combined quantum spin Hall system does not break TRS. Soon after, Bernevig independently developed a model for a QSHE in a conventional semiconductor by spin-orbit coupling in the presence of a strain gradient [169]. Here, the spin-orbit coupling creates a momentum-dependent magnetic field coupling with opposite sign for the spins similar to the idea of Fu and Kane. In summary, the QSHE is characterized by symmetry-protected topological order with charge and spin S^z conservation and exhibits therefore a quantized spin current.

In real materials, spin-mixing terms are always present, which violate the spin S^z conservation and therefore destroy the QSHE and its quantized transport. However, it was shown that topologically nontrivial states survive in the presence of interactions and spin-mixing terms for systems that obey charge conservation and TRS [181, 182]. These systems are called topological insulators (TIs) and are characterized by the $\mathbb{Z}_2$ invariant [183]. In 2007, the proposal of Bernevig [169] led to the first observation of TIs in mercury telluride quantum wells [184]. Soon after, TIs [183, 185] have been also observed in bismuth antimony alloys [186, 187] and Bi_2Se_3 and Bi_2Te_3 bulk crystals [188–191]. TIs represent materials in a new class of symmetry protected topological states, which raised high interest in the field of spintronics [185, 192–195]. Often the QSHE and TIs are used interchangeably [183], however they have two very different foundations. The QSHE is based on spin S^z conservation [196, 197] while the TIs are based on TRS. Both systems have counterpropagating edge modes for the spins, for which scattering from one to the other edge mode is forbidden. However, the underlying reasons are different. In the case of the QSHE, back scattering is forbidden due to spin S^z conservation and for TIs due to TRS. This implicates, for example, that the QSHE is immune against spin-conserving magnetic impurities but TIs are not as magnetic impurities break TRS.

In this part of the thesis a minimal instance of a quantum spin pump is proposed and realized. These minimal instances are then interconnected to form a 1D spin pump in the limit of isolated double wells. This spin pump can be interpreted as a dynamical version of the QSHE. The transport properties of the system are analyzed by developing and applying a unique spin-current measurement technique and by direct observation of spin separation. Before introducing the quantum spin pump realizing a dynamical version of the QSHE, topological charge pumping is discussed, which can be interpreted as a dynamical version of the integer QHE.

6.2. Topological charge pumping

The concept of topological charge pumping was discovered by Thouless in the context of the QHE in 1983. He found a quantized transport of charges in 1D systems upon cyclic evolution of the underlying Hamiltonian [95, 198], which is now commonly called a Thouless pump. In his study, he investigated the particle transport in two superimposed 1D periodic potentials that are adiabatically moved with respect to each other. This relative sliding motion induces the periodic variation of the system's Hamiltonian in time. Therefore, the Hamiltonian $\hat{H}(t)$ can be parameterized by a cyclic pump parameter $\phi(t)$. The pump parameter ϕ and the quasi-momentum k along the x-direction are both periodic and span together a closed parameter space. On this parameter space, a generalized Berry curvature $\Omega^n_{k\phi}$ can be defined

$$\Omega^n_{k\phi} = \mathrm{i}\left[\left\langle \partial_k n(k,\phi) \middle| \partial_\phi n(k,\phi) \right\rangle - \left\langle \partial_\phi n(k,\phi) \middle| \partial_k n(k,\phi) \right\rangle\right], \tag{6.1}$$

with $|n(k,\phi)\rangle$ denoting the instantaneous eigenbasis of the 1D Hamiltonian $\hat{H}(\phi)$. This 1D Hamiltonian is related to a 2D system by dimensional reduction [199–201]. Therefore, $\Omega^n_{k\phi}$ is very similar to the Berry curvature (1.15) of the 2D system, in which ϕ takes the role of the quasi-momentum along y. Note that $H(\phi)$ represents a Fourier component of the associated 2D model for every ϕ. Hence, not all states of the 2D model are realized simultaneously.

Pumping refers to the cyclic process of varying the pump parameter such that the Hamiltonian changes adiabatically. The wave function thereby follows the instantaneous eigenstates according to the adiabatic theorem [90] but obtains additional imaginary contributions from other bands. The instantaneous eigenstates of such a periodic Hamiltonian are the Bloch functions $\mathrm{e}^{\mathrm{i}kx}\,|u_n(k,x)\rangle$ with their cell-periodic part $|u_n(k,x)\rangle$. To first order in the rate of change and ignoring global phase factors, the wave function is (Sec. B.1)

$$|\psi_t\rangle = |u_n\rangle - \mathrm{i}\,\hbar \sum_{m\neq n} \frac{|u_m\rangle\,\langle u_m|\partial_t u_n\rangle}{\epsilon_n - \epsilon_m}. \tag{6.2}$$

From this wave function, the expectation value of the crystal-momentum-dependent velocity can be calculated to first order using the quantum version of Hamiltonian mechanics

$$\begin{aligned}\langle v_n(k)\rangle &= \left\langle \frac{\partial \hat{H}(k)}{\partial \hbar k} \right\rangle \\ &= \frac{\partial \epsilon_n}{\hbar\,\partial k} - \mathrm{i} \sum_{m\neq n} \left\{ \frac{\langle u_n|\partial \hat{H}/\partial k|u_m\rangle\,\langle u_m|\partial_t u_n\rangle}{\epsilon_n - \epsilon_m} - \text{h.c.} \right\} \\ &= \frac{\partial \epsilon_n}{\hbar\,\partial k} - \mathrm{i}\big\{\langle \partial_k u_n|\partial_t u_n\rangle - \langle \partial_t u_n|\partial_k u_n\rangle\big\}. \end{aligned} \tag{6.3}$$

The first term is the group velocity and the second term the Berry curvature in momentum–time space. The result can be rewritten to the Berry curvature (6.1), which depends on the pump parameter ϕ by using the rate of change $\dot{\phi}$

$$\langle v_n\rangle = \frac{\partial \epsilon_n}{\hbar\,\partial k} - \Omega^n_{kt} = \frac{\partial \epsilon_n}{\hbar\,\partial k} - \Omega^n_{k\phi}\,\dot{\phi}. \tag{6.4}$$

In summary, a particle acquires a group velocity and an anomalous velocity during the pumping, which depend on the pumping speed and the Berry curvature.

The particle transport during one pump cycle can be calculated by integrating over the occupied crystal momenta and the pump parameter. The resulting displacement only depends on the geometric properties of the pump path but not on the way or speed of pumping. However, the displacement is not quantized unless all crystal-momenta are occupied equally. Then, the integral covers the whole generalized Brillouin zone and the pumped charge is

$$\oiint_{\mathrm{BZ}} \langle v_n\rangle \, \frac{\mathrm{d}k}{2\pi}\,\mathrm{d}\phi = -\frac{1}{2\pi} \oiint_{\mathrm{BZ}} \Omega_{k\phi}\,\mathrm{d}k\,\mathrm{d}\phi = \nu_n \tag{6.5}$$

given by a 2D topological invariant, the Chern number ν_n. Thus, the transport is robust against perturbations [95, 198]. Note that the contribution of the group velocity averages out to zero because the band is reflection symmetric.

To gain a better understanding of the topological nature and the type of pump cycles required for pumping with non-zero Chern number, a tight-binding approximation of two sinusoidal potentials is considered. The period of the potentials are d_l and $d_\mathrm{s} = \alpha d_\mathrm{l}$ with $\alpha \in\,]0,1[$. The resulting Hamiltonian is

$$\hat{H}_\alpha = -\sum_m \frac{1}{2}\Big[J_0 + \delta J_m(\phi)\Big]\Big(\hat{a}^\dagger_{m+1}\hat{a}_m + \text{h.c.}\Big) + \sum_m \frac{1}{2}\Delta_m(\phi)\,\hat{n}_m. \tag{6.6}$$

Here, $J_0/2$ is the tunneling rate between neighboring sites, $\delta J_m/2$ is its site-dependent modulation, and Δ_m is the on-site energy at site m. For small long-lattice depth $V_l^2 \ll 4V_s E_{r,s}$, the modulations of the tunneling and the on-site energy only depend on the long-lattice depth V_l and the relative phase between the two lattices ϕ. In this limit, $\hat{H}_\alpha$ reduces to the generalized 1D Harper equation [86, 202] with

$$\begin{aligned} \delta J_m(\phi) =& \delta J \cos(2\pi\alpha m - \phi), \\ \Delta_m(\phi) =& \Delta \cos(2\pi\alpha(m - 1/2) - \phi). \end{aligned} \tag{6.7}$$

For rational values of $\alpha = p/q$ with $p, q \in \mathbb{N}$, the model has q subbands (Sec. 1.2.2) except for the point $\delta J = \Delta = 0$. A this point, only the short period lattice is present and the gaps close. Note that the Harper equation describes an elliptical pump path around this degeneracy point. For filled subbands, the pumping response is equivalent to the QHE in the Harper–Hofstadter–Hatsugai model with a flux $\alpha\,\Phi_0$ per plaquette [200, 203, 204]. It is a Harper–Hofstadter model with diagonal coupling and has a similar fractal structure as the Hoftadter's butterfly [88]. The pumping process $\dot{\phi}$ in 1D is thereby equivalent to a change in the crystal-momentum along the y-direction $\dot{k}_y$ in 2D and is therefore often referred to as dynamical QHE. This in turn is the same as applying a force or, for charged particles, applying a voltage like in a quantum Hall sample. It is important to stress again that during the pump path the subbands remain always gapped in the same way as the 2D bands are gapped in the Harper–Hofstadter–Hatsugai model. The topological nature and its associated robustness against deformations of the pump path can now be understood and compared to its 2D counterpart. Small deformations of the pump path are equivalent to small deformations of the 2D band. As long as the deformations are small and the pump path does not touch the degeneracy point $\delta J = \Delta = 0$, the bands are gapped. Thus, the topology of the band cannot change and the Chern number remains the same. The pump path in Eq. (6.7) could be shifted in parameter space, e.g. $\Delta_m(\phi) \rightarrow \Delta_m(\phi) + \Delta_{\text{shift}}$. If $\Delta_{\text{shift}} > \Delta$, then the pump path does not include the degeneracy point and the pump process is trivial with zero Chern number [205]. The degeneracy point can therefore be regarded as the source of the magnetic field. Recently, geometric and quantized topological pumps have been realized with ultracold bosonic [204, 206] and fermionic atoms [207]. Moreover, also a dynamical version of the 4D QHE has been implemented by coupling two 1D topological charge pumps in orthogonal directions [208]. This led to the first measurement of the corresponding 2nd Chern number.

6.3. Spin pumping

In analogy to the Thouless pump also spin pumps can be constructed, which can be interpreted as a dynamical version of TIs or QSH systems [209]. They are characterized by a bulk excitation gap and gapless edge excitations. The conceptually easiest realization of such a spin pump uses two independent Thouless pumps; one for each spin. They are constructed in a way that pumping induces spin transported in opposite directions. Note that as the Thouless pumps are independent, the spin S^z components are conserved. Therefore, the system can be interpreted as a dynamical version of the QSHE composed out of two integer quantum Hall (QH) systems and can be described by a spin Chern number $C_{\mathrm{sc}} = \nu_{\uparrow} - \nu_{\downarrow}$. If the Berry curvature is exactly inverted for the two spins, then the system fulfills also TRS and inherits the character of TIs as well.

In electronic systems, however, the electron spin is in general not conserved, e.g. in the presence of spin-orbit coupling. In this situation, the quantized spin transport of the QSHE is no longer protected because spin S^z conservation is violated. However, the system is still topological as long as TRS is not yet broken [209–211] and unconventional topological invariants are required for classification like the $\mathbb{Z}_2$ index [182].

A possible application of spin pumps is to use them as spin current sources, for example for spintronic applications [192]. A range of proposals for spin current generators have been made based on a variety of phenomena. These proposals include spin current generators based on the spin Hall effect [175, 178], periodically modulated interacting quantum wires [212, 213], and TIs [214]. However, only a few experiments have been realized using quantum spin pumps, e.g. in quantum dot structures [215] and by parametrically excited exchange magnons [216].

7. Minimal instance for $\mathbb{Z}_2$ spin pumps

7.1. Spin pumps in a spin-dependent Rice-Mele model

A quantum spin pump that resembles the QSHE in the limit of fully occupied subbands can be implemented with two ultracold atomic species in a species-dependent dynamically controlled optical superlattice. A superlattice can be formed by superimposing a short-period lattices with period d_s and a long-period lattice with $d_\mathrm{l} = 2\, d_\mathrm{s}$ (Sec. 3.1.1). In the tight-binding limit, the resulting description has a two-site unit cell with staggered on-site energies $\pm\Delta/2$ and alternating tunnel couplings $(J \pm \delta J)\,/2$, where δJ is the dimerization parameter. These tight-binding parameters depend on the individual lattice depths and the relative superlattice phase. The discussion is started by only considering a single spin component. The tight-binding model of the superlattice is a special case of the Harper Hamiltonian with $\alpha = 1/2$

$$\hat{H}_\mathrm{RM} = -\sum_m \frac{1}{2}\left[J + (-1)^m\, \delta J\right](\hat{a}^\dagger_{m+1}\hat{a}_m + \mathrm{h.c.}) + \sum_m \frac{1}{2}(-1)^m\, \Delta\, \hat{n}_m, \tag{7.1}$$

which is also called Rice-Mele model [217]. For this model, the pump path is an adiabatic loop in the parameter space (δJ, Δ), e.g. Eq. (6.7). Pumping induces a modulation of the potential such that the species gets transported as long as the degeneracy point ($\delta J = 0$, $\Delta = 0$) is enclosed by the path. The pumped amount of particles per pump cycle is in general not quantized. However, it is geometric and therefore depends on the chosen pump path but not on the pump speed as long as the evolution is adiabatic. To obtain a Thouless pump with quantized transport, subbands need to be fully occupied e.g. the lowest subband. This can be achieved with spinless fermions at half filling, i.e. one particle per two sites of the short lattice, where the Fermi energy lies in the band gap, or with bosons by creating a half-filled Mott insulator.

A spin pump can now be constructed by adding a second species describing the other spin. First assume, that the species do not have any inter-species interactions. Then, their pumping motion is independent and a spin pump can be realized by applying a spin-dependent modulation such that the pump path is run through in the opposite directions for the two spins, which can be achieved by inverting the sign of the energy offset for the two spins $\sigma = \{\uparrow, \downarrow\}$. The resulting Hamiltonian is

$$\hat{H}_{\mathrm{sp}} = -\sum_{m,\sigma} \frac{1}{2} \left[J + (-1)^m \, \delta J_m \right] (\hat{a}^{\dagger}_{m+1,\sigma} \, \hat{a}_{m,\sigma} + \mathrm{h.c.}) + \sum_m (-1)^m \, \frac{\Delta}{2} \, \left(\hat{n}_{m,\uparrow} - \hat{n}_{m,\downarrow} \right) . \qquad (7.2)$$

Here, $\hat{a}^{\dagger}_{m,\sigma}$ is the creation operator and $\hat{n}_{m,\sigma} = \hat{a}^{\dagger}_{m,\sigma}\hat{a}_{m,\sigma}$ the number operator of a spin σ at site m. As a result their Berry curvatures are reversed and the spin transport is oppositely directed. Note that for equal spin mixtures, charge transport is absent. Furthermore, the Hamiltonian conserves charge as well as spin S^z, which is typically what is required for the QSHE. However, the transport is only quantized, if all crystal momenta are populated equally. Moreover, the Hamiltonian is time-reversal symmetric, which also allows for the interpretation of the model as a dynamical version of a TI with spin conservation.

In a second step, assume that the species are coupled by a strong inter-species on-site interaction $U \gg J$. For half filling, tunneling is suppressed and the system can be described by a 1D spin chain

$$\hat{\mathcal{H}} = -\sum_m \frac{1}{4} \left[J_{\mathrm{ex}} + (-1)^m \, \delta J_{\mathrm{ex}} \right] \left(\hat{S}^{+}_m \hat{S}^{-}_{m+1} + \mathrm{h.c.} \right) + \sum_m (-1)^m \, \frac{1}{2} \, \Delta \, \hat{S}^z_m \qquad (7.3)$$

with spin-dependent tilt Δ and alternating exchange coupling $\left(J_{\mathrm{ex}} \pm \delta J_{\mathrm{ex}} \right) / 2$. The exchange coupling is a second order process and is approximately $\left(J \pm \delta J \right)^2 / U$ [4]. The spin operators $\hat{S}^{+}_m = \hat{a}^{\dagger}_{m\uparrow}\hat{a}_{m\downarrow}$ and $\hat{S}^{-}_m = \hat{a}^{\dagger}_{m\downarrow}\hat{a}_{m\uparrow}$ flip the spin at site m and $\hat{S}^{z}_m = \hat{a}^{\dagger}_{m\uparrow}\hat{a}_{m\uparrow} - \hat{a}^{\dagger}_{m\downarrow}\hat{a}_{m\downarrow}$ measures the spin magnetization. For large tilts $\Delta \gg \left(J_{\mathrm{ex}} + \delta J_{\mathrm{ex}} \right) / 2$, the many-body ground state consists of spins locked in an antiferromagnetic order, while for strong exchange coupling $\left(J_{\mathrm{ex}} + \delta J_{\mathrm{ex}} \right) / 2 \gg \Delta$ dimerized entangled pairs are favored. In this interacting 1D spin chain, pumping can be induced equivalently to the non-interacting pump by a variation of δJ_{ex} and Δ. To this end, a pump path in the parameter space (δJ_{ex}, Δ) is realized. However, the criterion for adiabaticity changes. The modulation now needs to be adiabatic compared to the intra-double-well exchange coupling $(J_{\mathrm{ex}} + \delta J_{\mathrm{ex}})/2$. For two bosonic species with intra-species hardcore interactions or two spinless fermionic species, the spin transport is quantized. Note that the spin degree-of-freedom is here represented by the two species. The quantized spin transport is described by a spin Chern number as in the topologically equivalent case of independent spins [182] or by the more generally applicable $\mathbb{Z}_2$ invariant. Such a spin pump can also be interpreted as a dynamical version of the QSHE, where the pump parameter ϕ is an additional dimension in a generalized momentum space [200]. The adiabatic variation of ϕ corresponds to threading of a magnetic flux through a cylinder following Laughlin's interpretation of the integer QHE [201].

7.2. Limit of isolated double wells

The implementation of the non-interacting spin pump Eq. (7.2) requires either non-interacting fermions or bosons with hardcore intra-species and vanishing inter-species interactions. In this regard, the interacting spin pump Eq. (7.3) is simpler as the species can both have strong intra- and inter-species interactions. Nevertheless, both implementations require a dynamically controllable spin-dependent superlattice [218, 219], which is challenging to realize. Therefore, a two-site minimal instance of the spin-dependent Rice-Mele model according to Eq. (7.3) is proposed and realized. This minimal instance can be implemented with a spin-independent superlattice. In the limit of isolates double wells, $\delta J_{\mathrm{ex}} \approx J_{\mathrm{ex}}$, the spin-independent superlattice together with a global spin-dependent gradient locally reproduces the staggered spin-dependent tilts of the interacting spin pump. In Fig. 7.1, the essence of this minimal instance and a sequence to extend it to perform multiple spin-pump cycles is illustrated.

To gain a better understanding of the pumping in the two-site minimal instance, the discussion is restricted to perfectly isolated double wells, $\delta J_{\mathrm{ex}} = J_{\mathrm{ex}}$. This means, that every second link is broken and no tunneling between double wells can occur. It is important to recognize that in the spin-dependent Rice-Mele model Eq. (7.3) the energy offsets between neighboring sites have the same sign in each double well. Therefore, ignoring the energy offsets between sites on broken links, the local tilts can be replaced by a spin-dependent gradient. Hence, the superlattice potential can be chosen spin-independent. Now, each minimal instance is occupied by an up and a down spin in the two-particle ground state for $-\Delta \gg J_{\mathrm{ex}}$ and $J_{\mathrm{ex}} = 0$. The state is $|\uparrow, \downarrow\rangle$, where the spins on the left site are indicated before and the spins on the right site after the comma. The first half pump cycle is performed by adiabatically inverting the energy offset (Fig. 7.1 a), i.e. reversing the gradient in the minimal instance. During this process, the spins exchange their position to $|\downarrow, \uparrow\rangle$ via the intermediate triplet state $(|\uparrow, \downarrow\rangle + |\downarrow, \uparrow\rangle)/\sqrt{2}$ at $\Delta = 0$ (Fig. 7.1 b). To further continue the pump cycle, the minimal instance needs to be shifted by a short lattice period. To this end, the dimerization needs to be flipped. However, simply flipping the dimerization in the realization will not reproduce the correct local tilt in the new minimal instance. Therefore, also the gradient needs to be flipped (Fig. 7.1 c). As all the spins are localized at this stage, the state of the spins remains unchanged. After shifting the minimal instance, pumping can be continued.

To strengthen the intuitive explanation for spin pumping with the minimal instance, an extended model with a global gradient is analyzed. The model with the global gradient is captured by the following Hamiltonian

$$\hat{\mathcal{H}}_{\mathrm{grad}} = -\frac{1}{4}\sum_m \left[J_{\mathrm{ex}} + (-1)^m\,\delta J_{\mathrm{ex}}\right]\left(\hat{S}^+_m \hat{S}^-_{m+1} + \mathrm{h.c.}\right) + \Delta \sum_m \left(m - \frac{1}{2}\right)\hat{S}^z_m. \tag{7.4}$$

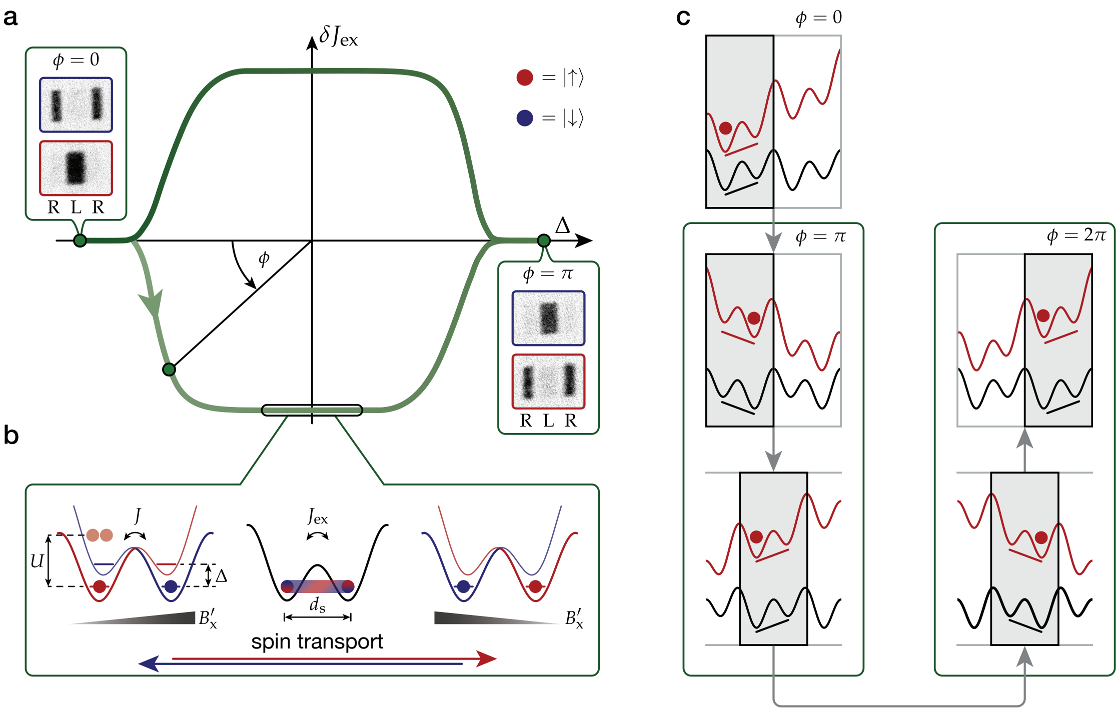

Figure 7.1.: Spin pump cycle and pumping in the minimal instance. **a** Illustration of the spin-pump cycle in the experiment (green) in the parameter space spanned by the spin-dependent tilt Δ the dimerization of the exchange coupling δJ_{ex}. The pump cycle starts on the left at negative Δ and equal exchange coupling on all links. The unit cell is chosen such that the down spin localizes on the right (R) and up spin on the left (L) site. The pump path is parameterized by the angle ϕ, the pump parameter. During the first half pump cycle from $\phi = 0$ to π, $|\uparrow\rangle$ and $|\downarrow\rangle$ spins exchange their position. This exchange of spins is verified by the presented site-resolved band mapping images. **b** Local representation of the minimal instance around $\Delta = 0$. The spin-dependent staggered potential is locally reproduced by a magnetic field gradient. With the red and blue dots, representing up and down spins, the evolution of the two-particle ground state in the double well is illustrated. The bare tunnel coupling on the double well is $(J + \delta J)/2$ and the on-site interaction energy is U. Therefore, the exchange coupling is $J_{ex} \simeq (J + \delta J)^2/U$. During pumping from negative to positive Δ, the localized spin configuration $|\uparrow\downarrow\rangle$ adiabatically changes via the triplet state $(|\uparrow\downarrow\rangle + |\downarrow\uparrow\rangle)/\sqrt{2}$ to the spin configuration $|\downarrow\uparrow\rangle$. Hence, a spin transport appears. **c** Illustration of how the potential with global magnetic gradient (red) can reproduce a potential with local staggered spin-dependent tilts (black) in the limit of isolated double wells. The gray shading marks the isolated double well in scope with a single up spin. Note that the potentials are only shown for this up spin. The pump cycle starts with the top left panel at $\phi = 0$ with the up spin localized to the left site of the double well. The local potentials are the same for the gradient and the staggered model but between the double wells the sign is reversed. However, this is irrelevant as the tunneling is negligibly small. Then, the first half pump cycle is performed and the particle tunnels to the right as shown in **b**. To proceed the pumping, the minimal instance needs to be shifted by a short-period lattice spacing d_s. Therefore, the dimerization is rapidly flipped and the gradient reversed. Again, the local potentials are reproduced by the potential with gradient. Now, the next half pump cycle can be performed followed by another flip of the dimerization and the global gradient to close the pump cycle.

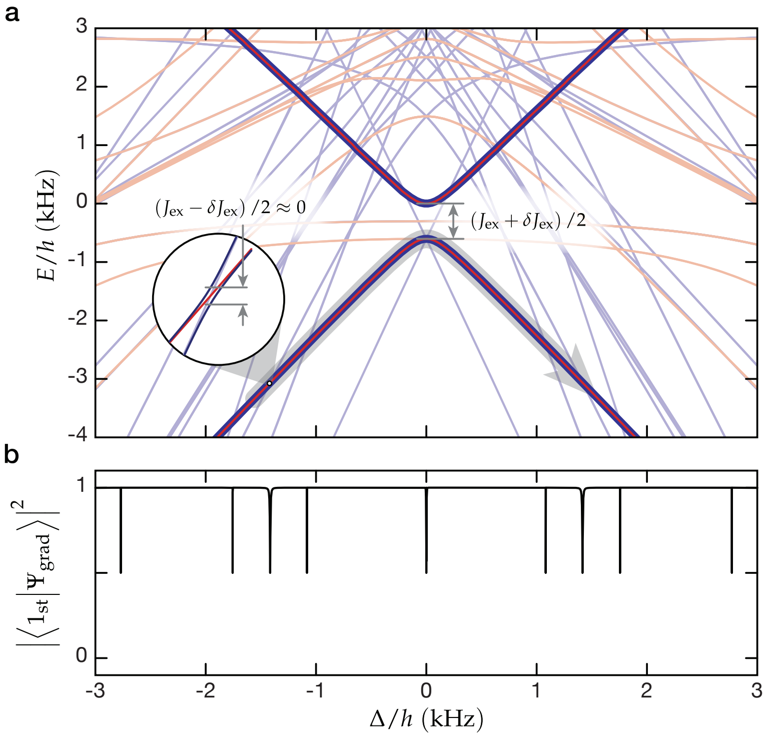

Figure 7.2.: Comparison of the energy spectrum for staggered and gradient model. a A comparison of the energy spectra for two pairs of up and down spins on two double wells is shown for the spin pump with staggered tilts Eq. (7.3) (red) and the spin pump with global gradient Eq. (7.4) (blue). The thicker darker lines represent the ground state of the staggered superlattice $|1_{st}\rangle$ and the corresponding state in the globally tilted lattice $|\Psi_{grad}\rangle$, which is used for pumping in the experiment. **b** The state overlap $|\langle 1_{st}|\Psi_{grad}\rangle|^2$ between these two states is depicted.

It is necessary to start with the ground state of the spin pump with local staggered energy offsets Eq. (7.3), which is the antiferromagnetically ordered state. This state is a highly excited many-body state in the system with a global gradient Eq. (7.4). Nevertheless, this state evolves in the same way in both systems except for a few additional crossings that occur in the energy spectrum of the system with the global gradient. Such an energy spectrum is shown in Fig. 7.2 for two pairs of up and down spins on a chain with two double wells. The energy spectrum is calculated for the experimental parameter set with $J_{ex}/h = 342(2)$ Hz. During the pumping process, the system follows the darker and thicker depicted state. This state is either separated by a large gap from the excited states around $\Delta = 0$ or crosses states with a small gap on the order of the inter-double-well exchange coupling $(J_{ex} - \delta J_{ex})/2$, which can be crossed non-adiabatically. To this end, the pumping needs to be fast compared to $(J_{ex} - \delta J_{ex})/2$ to reach a pure non-adiabatic transfer but remains adiabatic with respect to the intra-double-well exchange coupling $(J_{ex} + \delta J_{ex})/2$. Both limits can be fulfilled simultaneously in an experiment because the inter-double-well exchange coupling can be suppressed exponentially by applying deep lattice potentials and adiabaticity on the double well scale can be reached by a slower ramp speed. To further validate that the antiferromagnetically ordering state at large Δ is mostly identical to the ground state of the model with staggered energy-offsets during pumping, their state overlap is calculated. The result is equal to one everywhere besides at the surrounding of the small gaps. This underlines the similarity of both pumps. In summary, the spin pump with global gradient can be described by the same topological invariant as the model with local tilts in the limit discussed above.

8. Spin-current measurement technique

8.1. Charge and spin currents

8.1.1. Continuity equation

When currents are discussed, the topic is typically narrowed down to the transport of electric charges. However, currents appear in a much broader context and are used for the description of the flow of everything that can actually move, e.g. water, air, charge, and spin. Moreover, this concept can be generalized to the flow of any quantity through a given surface, which is then called flux. A prominent example is the magnetic flux, which is the flow of the magnetic flux density, better known as the magnetic field (Sec. 1.2.1), through a surface.

Our intuition tells us that the flow of extensive quantities need to fulfill a local conservation law. Imagine a small box filled with a quantity. Then, a reduction of this quantity in the box can only occur in two ways: first, the quantity flows away through the surface of the box, or second there is a sink inside the box. Of course, the same holds true for an increase of the quantity, which can either originate from an inflowing net-flux density or a source inside the volume. Mathematically, this local property is captured by the continuity equation. In the integral form the continuity equation reads

$$\frac{\mathrm{d}Q}{\mathrm{d}t} + \oiint\limits_{\partial V} \mathfrak{J}\,\mathrm{d}\mathbf{S} = \mathfrak{S}, \tag{8.1}$$

with $\mathfrak{J}$ the flux density, $Q = \iiint_V \rho_Q \,\mathrm{d}V$ the total amount of the quantity, and $\mathfrak{S}$ the net source rate inside the volume V. For globally conserved quantities, the more restrictive condition of vanishing local sources is often satisfied as well. Hence, the continuity equation reduces to

$$\frac{\mathrm{d}Q}{\mathrm{d}t} = -\oiint\limits_{\partial V} \mathfrak{J}\,\mathrm{d}\mathbf{S}\,. \tag{8.2}$$

In the next section, this classical description will be extended to the flow of conserved quantum particles, whose probability density is described by the expectation value of an operator.

8.1.2. Probability current

In quantum mechanics, the location of a particle can only be described by its probability density. Therefore, the flow of the particle is also a probabilistic quantity and the current becomes a probability current. Assume an operator $\hat{O}$ that describes the density of a conserved quantity, then the probability current density $\mathfrak{J}_O$ is given by the differential form of the continuity equation

$$\frac{\partial \langle \hat{O} \rangle}{\partial t} = -\boldsymbol{\nabla} \cdot \langle \hat{\boldsymbol{\mathfrak{J}}}_O \rangle \,. \tag{8.3}$$

The time-derivative of the expectation value of an operator can be calculated using the Ehrenfest theorem

$$\frac{\mathrm{d}}{\mathrm{d}t} \big\langle \hat{O}(t) \big\rangle = \frac{\mathrm{i}}{\hbar} \big\langle [\hat{H}, \hat{O}(t)] \big\rangle + \Big\langle \frac{\partial \hat{O}}{\partial t} \Big\rangle . \tag{8.4}$$

Note that the operator is typically not explicitly time-dependent and $\big\langle \partial_t \hat{O} \big\rangle = 0$ vanishes. Furthermore, the change from the partial to the total derivative is valid for a stationary evaluation volume.

By discretizing the continuity equation, the probability current operator in the 1D Bose-Hubbard model can by calculated. To this end, the operator $\hat{O} = \hat{n}_i$ is the local number operator at site i and $(\boldsymbol{\nabla} \cdot \langle \boldsymbol{\mathfrak{J}}_O \rangle)_x \to \langle \hat{\mathfrak{J}}_{i+1} \rangle - \langle \hat{\mathfrak{J}}_i \rangle$ the discretized divergence of the current density in 1D along x. Evaluating the expression leads to

$$\begin{aligned}
\frac{\mathrm{d} \langle \hat{n}_i \rangle}{\mathrm{d}t} &= \frac{\mathrm{i}}{\hbar} \big\langle [\hat{H}, \hat{n}_i] \big\rangle = -[\, \langle \hat{\mathfrak{J}}_{i+1} \rangle - \langle \hat{\mathfrak{J}}_i \rangle] \\
&= \frac{\mathrm{i}}{\hbar} \left\langle \left[-J \sum_j \left(\hat{a}_j^\dagger \hat{a}_{j+1} + \text{h.c.} \right), \hat{n}_i \right] \right\rangle \\
&= \left\langle J\, \mathrm{i}\, \hat{a}_i^\dagger \hat{a}_{i+1} + \text{h.c.} \right\rangle - \left\langle J\, \mathrm{i}\, \hat{a}_{i-1}^\dagger \hat{a}_i + \text{h.c.} \right\rangle
\end{aligned} \tag{8.5}$$

and the current operator is identified as

$$\hat{\mathfrak{J}}_{i+1} = -J\, \mathrm{i}\, \hat{a}_i^\dagger \hat{a}_{i+1} + \text{h.c.} \tag{8.6}$$

8.1.3. Definition of a spin current

A rigorous definition of a spin current is rather difficult because in general the spin S^z component is not conserved due to spin-orbit coupling. Therefore, the naive definition via the continuity equation becomes inapplicable. To overcome this limitation, a variety of different spin current definitions have been proposed [177]. The definitions are based on experimental quantities like spin accumulation [220], the subtraction of individual spin currents [214, 221, 222], applying the continuity equation and adding first order spin-mixing terms [223], semi-classical approaches separating non-conserved parts of the spin current due to spin-orbit coupling from conserved parts [224, 225], or by introducing a spin dipole, torque moment, and a change of the spin's wavepacket due to electric fields [226]. Another attempt for the definition of a conserved spin current was made by introducing a torque dipole moment [227], which ensures the Onsager relation. In some situations, however, the spin can be assumed to be conserved [209, 228], and the definition is much simpler. This is indeed the case for the spin pump in the context of the QSHE.

Assume a conserved spin S^z and the Hamiltonian Eq. (7.3), then the definition of the current operator in Eq. (8.5) can be adopted for spin currents

$$\begin{aligned}\frac{\mathrm{d}\langle \hat{S}^z_i\rangle}{\mathrm{d}t} &= \frac{\mathrm{i}}{\hbar}\left\langle [\hat{H}, \hat{S}^z_i]\right\rangle = -[\langle \hat{\jmath}_{i+1}\rangle - \langle \hat{\jmath}_i\rangle] \\ &= \frac{\mathrm{i}}{\hbar}\left\langle\left[-J_{\mathrm{ex}}\sum_j\left(\hat{S}^+_j\hat{S}^-_{j+1} + \mathrm{h.c.}\right), \hat{S}^z_i\right]\right\rangle \\ &= \left\langle J_{\mathrm{ex}}\,\mathrm{i}\,\hat{S}^+_i\hat{S}^-_{i+1} + \mathrm{h.c.}\right\rangle - \left\langle J_{\mathrm{ex}}\,\mathrm{i}\,\hat{S}^+_{i-1}\hat{S}^-_i + \mathrm{h.c.}\right\rangle . \end{aligned} \tag{8.7}$$

The resulting spin current operator on the link $\langle i, i+1\rangle$ is then

$$\hat{\jmath}_{i+1} = -J_{\mathrm{ex}}\,\mathrm{i}\,\hat{S}^+_i\hat{S}^-_{i+1} + \mathrm{h.c.} \tag{8.8}$$

8.2. Spin currents in the minimal instance

8.2.1. Two-site extended Bose-Hubbard model

In Chap. 7, a spin pump of isolated double wells was introduced. Each of the double wells is thereby occupied by a pair of up and down spins and can be interpreted as a minimal instance for this extended spin pump. The minimal instance can be described in the tight-binding limit by a two-site, two-spin Bose-Hubbard Hamiltonian

$$\begin{aligned}\hat{H}_{\mathrm{BH}} = &- J' \sum_{\sigma=\{\uparrow,\downarrow\}}\left(\hat{a}^\dagger_{\mathrm{L},\sigma}\hat{a}_{\mathrm{R},\sigma} + \mathrm{h.c.}\right) - \frac{\Delta}{2}\left(\hat{n}_{\mathrm{L},\downarrow} - \hat{n}_{\mathrm{L},\uparrow} - \hat{n}_{\mathrm{R},\downarrow} + \hat{n}_{\mathrm{R},\uparrow}\right) \\ &+ U\left(\hat{n}_{\mathrm{L},\uparrow}\hat{n}_{\mathrm{L},\downarrow} + \hat{n}_{\mathrm{R},\uparrow}\hat{n}_{\mathrm{R},\downarrow}\right), \end{aligned} \tag{8.9}$$

with $\hat{a}^\dagger_{i,\sigma}$ the creation operator of spin $\sigma \in \{\uparrow,\downarrow\}$ at left (L) or right (R) site $i \in \{\mathrm{L},\mathrm{R}\}$. $\hat{n}_{i,\sigma} = \hat{a}^\dagger_{i,\sigma}\hat{a}_{i,\sigma}$ is the number operator, J' the intra-well tunneling rate, Δ the spin-dependent energy offset between left and right site, and U the on-site interaction energy. As already discussed in the context of the minimal instance for $\mathbb{Z}_2$ LGTs (Sec. 3.1.4), such an interacting two-site model is better captured by the extended Bose-Hubbard model.

There the tunnel matrix element is modified $J = J' + \delta_j$ by density-assisted tunneling $\delta j = g \int w_{\mathrm{L}}^{*2}(r) w_{\mathrm{L}}(r) w_{\mathrm{R}}(r)\, \mathrm{d}r^3$ and correlated- as well as exchange-tunneling processes occur with strength $u_{\mathrm{LR}} = g \int |w_{\mathrm{L}}(r)|^2 |w_{\mathrm{R}}(r)|^2\, \mathrm{d}r^3$. Here, $w_i(r)$ is the Wannier function, $g = 4\pi\hbar^2 a_{\mathrm{s}}/m$ the effective interaction strength, a_{s} the s-wave scattering length and m the mass. Taking these corrections into account is important for an accurate determination of the exchange coupling, especially at large J/U [4, 158]. Including theses terms, the Hamiltonian is

$$\begin{aligned} \hat{H}_{\mathrm{eBH}} = &- J \sum_{\sigma=\{\uparrow,\downarrow\}} \left(\hat{a}^{\dagger}_{\mathrm{L},\sigma} \hat{a}_{\mathrm{R},\sigma} + \mathrm{h.c.} \right) - \frac{\Delta}{2} \left(\hat{n}_{\mathrm{L},\downarrow} - \hat{n}_{\mathrm{L},\uparrow} - \hat{n}_{\mathrm{R},\downarrow} + \hat{n}_{\mathrm{R},\uparrow} \right) \\ &+ U \left(\hat{n}_{\mathrm{L},\uparrow} \hat{n}_{\mathrm{L},\downarrow} + \hat{n}_{\mathrm{R},\uparrow} \hat{n}_{\mathrm{R},\downarrow} \right) + u_{\mathrm{LR}} \left(\hat{n}_{\mathrm{L},\uparrow} \hat{n}_{\mathrm{R},\downarrow} + \hat{n}_{\mathrm{R},\uparrow} \hat{n}_{\mathrm{L},\downarrow} \right) \\ &+ u_{\mathrm{LR}} \left(\hat{a}^{\dagger}_{\mathrm{L},\uparrow} \hat{a}^{\dagger}_{\mathrm{L},\downarrow} \hat{a}_{\mathrm{R},\uparrow} \hat{a}_{\mathrm{R},\downarrow} + \hat{a}^{\dagger}_{\mathrm{L},\uparrow} \hat{a}^{\dagger}_{\mathrm{R},\downarrow} \hat{a}_{\mathrm{R},\uparrow} \hat{a}_{\mathrm{L},\downarrow} + \mathrm{h.c.} \right) . \end{aligned} \tag{8.10}$$

8.2.2. Spin-current operator

In the extended Bose-Hubbard model, the total spin projection S^z is conserved. Therefore, the spin-current operator can be defined following Eq. (8.5)

$$\begin{aligned} \frac{\mathrm{d} \langle \hat{S}^z_{\mathrm{L}} \rangle}{\mathrm{d}t} &= \frac{\mathrm{i}}{\hbar} \left\langle \left[\hat{H}_{\mathrm{eBH}}, \hat{S}^z_{\mathrm{L}} \right] \right\rangle = - \langle \hat{\mathrm{j}}_{\mathrm{L}\to\mathrm{R}} \rangle \\ &= - \left\langle J\, \mathrm{i}\, \hat{a}^{\dagger}_{\mathrm{L},\uparrow} \hat{a}_{\mathrm{R},\uparrow} - J\, \mathrm{i}\, \hat{a}^{\dagger}_{\mathrm{L},\downarrow} \hat{a}_{\mathrm{R},\downarrow} + 2u_{\mathrm{LR}}\, \mathrm{i}\, \hat{a}^{\dagger}_{\mathrm{L},\uparrow} \hat{a}^{\dagger}_{\mathrm{R},\downarrow} \hat{a}_{\mathrm{R},\uparrow} \hat{a}_{\mathrm{L},\downarrow} + \mathrm{h.c.} \right\rangle \end{aligned} \tag{8.11}$$

for the spin projection operator on the left site. Evaluating the equation for $\hat{S}^z_{\mathrm{R}}$ and using that spin currents between two sites need to be equal but oppositely directed, the change of the spin occupations are related

$$\frac{\mathrm{d} \langle \hat{S}^z_{\mathrm{R}} \rangle}{\mathrm{d}t} = - \langle \hat{\mathrm{j}}_{\mathrm{R}\to\mathrm{L}} \rangle = + \langle \hat{\mathrm{j}}_{\mathrm{L}\to\mathrm{R}} \rangle = \frac{\mathrm{d} \langle -\hat{S}^z_{\mathrm{L}} \rangle}{\mathrm{d}t} \tag{8.12}$$

in the two-site model. It is instructive to define the experimentally-practical spin imbalance $\hat{\mathcal{I}}$, which is given by the difference of the site-imbalance $\hat{I}_\sigma$ of the two spins σ

$$\hat{\mathcal{I}} = \frac{1}{2} \left(\hat{I}_{\uparrow} - \hat{I}_{\downarrow} \right) = \frac{1}{2} \left(\hat{n}_{\mathrm{R},\uparrow} - \hat{n}_{\mathrm{L},\uparrow} - \hat{n}_{\mathrm{R},\downarrow} + \hat{n}_{\mathrm{L},\downarrow} \right) = \frac{1}{2} \left(\hat{S}^z_{\mathrm{R}} - \hat{S}^z_{\mathrm{L}} \right) . \tag{8.13}$$

Thus, the spin current between the two sites of a double well can also be related to the change of the spin imbalance

$$\mathrm{j} = \langle \hat{\mathrm{j}}_{\mathrm{L}\to\mathrm{R}} \rangle = \frac{\mathrm{d} \langle \hat{\mathcal{I}} \rangle}{\mathrm{d}t} = \partial_t \mathcal{I} \tag{8.14}$$

The result can be understood as a representation of the integral from of the continuity equation for two sites.

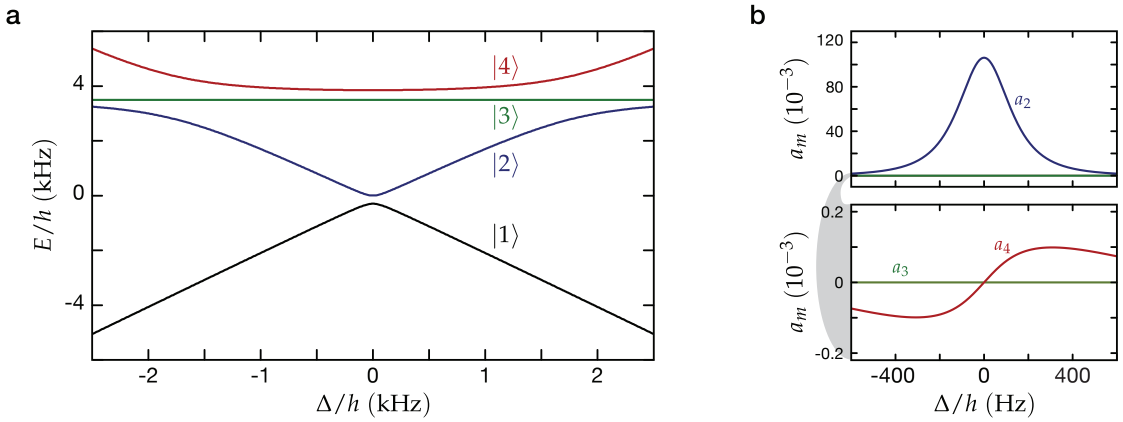

Figure 8.1.: Energy spectrum and admixture-coefficients of the minimal instance. **a** Energy spectrum of the extended Bose-Hubbard model (8.10) for two spins on a double well in dependence on the spin-dependent tilt Δ. For $\Delta \ll |J_{\text{ex}}|$ the ground state is $|1\rangle \approx |\downarrow,\uparrow\rangle$ and for $\Delta \gg |J_{\text{ex}}|$ it is $|\uparrow,\downarrow\rangle$. **b** Magnitude of the admixtures coefficients a_m at different spin-dependent tilt values Δ with rate of change $\dot{\Delta}/h = 82(2)\,\text{kHz/s}$ for experimental parameters with an exchange coupling of $J_{\text{ex}}/h = 342(2)\,\text{Hz}$.

8.2.3. Spin-currents during pumping

To understand the spin-currents during the pumping process, it is helpful to consider the energy spectrum and the evolution of the wave function during the adiabatic change of $\Delta(t)$. The instantaneous eigenstates $|n_t\rangle$ and the corresponding eigenenergies E_n of the two-site extended Bose-Hubbard model (8.10) are defined by the time-independent Schrödinger equation $\hat{H}_{\text{eBH}}\,|n_t\rangle = E_n\,|n_t\rangle$. The energy spectrum E_n is shown in Fig. 8.1 a. The gap between the first and second eigenenergy at $\Delta = 0$ defines the exchange coupling J_{ex}. The ground state is $|1\rangle \approx |\downarrow,\uparrow\rangle$ for positive and $|\uparrow,\downarrow\rangle$ for negative Δ in the limit $|\Delta| \gg J_{\text{ex}}$. In the symmetric configuration at $\Delta = 0$ and for $U \gg J$, it is well approximated by the triplet state $\frac{1}{\sqrt{2}}\big(|\uparrow,\downarrow\rangle + |\downarrow,\uparrow\rangle\big)$. Note that the third eigenstate is independent of Δ.

Starting an adiabatic pumping process at time t_i in the instantaneous eigenstate $|n_{t_i}\rangle$, then the wave function will follow the instantaneous eigenstate $|n_t\rangle$, but it acquires small imaginary contributions $\mathrm{i}\,a_m(t)$ from other eigenstates $|m_t\rangle$, with $m \neq n$. This happens even for a perfectly adiabatic evolution. This admixture occurs only temporarily during the change of the Hamiltonian. In first-order perturbation theory the temporary wave function is

$$|\psi_t\rangle = |n_t\rangle + \mathrm{i}\sum_{m\neq n} a_m(t)\,|m_t\rangle \tag{8.15}$$

with the admixture coefficients

$$a_m(t) = -\frac{\langle m_t|\,\hbar\partial_t\,|n_t\rangle}{E_n(t) - E_m(t)} = -\dot{\Delta}\,\frac{\langle m_t|\,\hbar\partial_\Delta\,|n_t\rangle}{E_n(t) - E_m(t)}. \tag{8.16}$$

A derivation of this wavefunciton following Ref. [89] is presented in Sec. B.1. The coefficients depend on the ramp speed, the energy differences and the variation of the eigenenergies with Δ. For a pump process starting in the ground state, these coefficients are shown in Fig. 8.1 b. The contribution a_2 clearly dominates and other coefficients can be neglected. The reasons are a vanishing or weak dependence of the eigenstates $|3\rangle$ and $|4\rangle$ on Δ as well as a large gap $|E_m - E_1| \sim U \gg J_{\mathrm{ex}}$ for $m > 2$. Therefore, the temporary wave function (8.15) reduces to

$$|\psi_t\rangle \approx |1_t\rangle + \mathrm{i}\,a_2(t)\,|2_t\rangle\,. \tag{8.17}$$

The expectation value of the instantaneous spin-current can be calculated with this temporary wave function and is

$$\mathrm{j}(t) = \left(\langle 1| - \mathrm{i}\,a_2(t)\,\langle 2|\right)\hat{\mathrm{j}}\left(|1\rangle + \mathrm{i}\,a_2(t)\,|2\rangle\right) = 2\,\mathrm{i}\,a_2\,\langle 1|\hat{\mathrm{j}}|2\rangle\,. \tag{8.18}$$

It is directly proportional to the a_2-coefficient and the matrix element between instantaneous eigenstates. Thus, the spin current can be detected by measuring the value of the a_2-coefficient. In the next section, a method to measure the instantaneous spin current is introduced based on the amplitude of spin-imbalance oscillations.

8.3. Measurement method

The spin-current measurement technique is based on a method for detecting particle probability currents on a lattice [68]. In this method, a projection of a current-carrying wave function onto isolated double wells was performed and the subsequent imbalance time-dynamics detected. From the imbalance oscillation amplitude, the probability current can be inferred. Here, instead of particle oscillations, the superexchange oscillations of two spins is detected. Again, the currents can be directly related to the oscillation amplitude.

In the case of the spin pump, the wave function $|\psi_t\rangle$ can be probed by a sudden stop of the pump cycle at time t_{s} (Fig. 8.2). This rapid stop corresponds to a non-adiabatic projection of $|\psi_{t_{\mathrm{s}}}\rangle$ on the static Hamiltonian $\hat{H}_{\mathrm{eBH}}(t_{\mathrm{s}})$. Since $|\psi_{t_{\mathrm{s}}}\rangle$ is in general not an eigenstate of the static Hamiltonian, $|1_{t_{\mathrm{s}}}\rangle$ and $|2_{t_{\mathrm{s}}}\rangle$ acquire a relative phase and the expectation value of the spin-imbalance operator $\mathcal{I}$ oscillates in time

$$\mathcal{I}(t') = A\,\sin\left(\frac{E_2(t_{\mathrm{s}}) - E_1(t_{\mathrm{s}})}{\hbar}\,t'\right) + \mathcal{I}_{\mathrm{s}}. \tag{8.19}$$

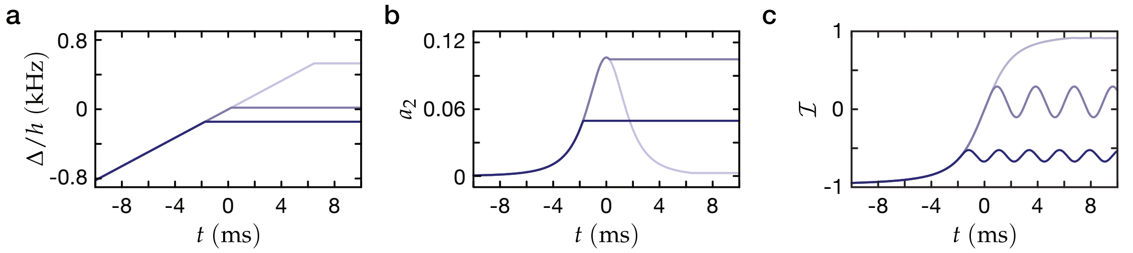

Figure 8.2.: Spin current measurement method. a Pumping is performed by an adiabatic change of Δ with rate $\dot{\Delta}$. The ramp is abruptly stopped at a certain point Δ_s. The graphs show ramps with three different stop values for the experimentally chosen pump rate of $\dot{\Delta} = 82(2)$ kHz/s at $\Delta = 0$. **b** During pumping, the ground-state obtains a small admixture a_2 of the first excited state around $\Delta = 0$. This contribution is responsible for the spin current. **c** The current carrying state is projected on a static Hamiltonian at t_s by abruptly stopping the pump cycle. The admixture from the first excited state leads to spin-imbalance oscillation with an amplitude proportional to a_2. Thus, the oscillation amplitude is also proportional to the instantaneous spin current at t_s. The graph shows a numerical simulation of the spin-imbalance time traces for adiabatic pumping and a perfect projection.

Here, A is the spin-imbalance oscillation acplitude, $\mathcal{I}_\mathrm{s}$ the spin imbalance at time t_s and $t' = t - t_\mathrm{s}$. The oscillation amplitude is directly proportional to the a_2-coefficient

$$A = -2\, a_2(t_\mathrm{s})\, \langle 1_{t_\mathrm{s}} |\, \hat{\mathcal{I}}\, | 2_{t_\mathrm{s}} \rangle \,. \tag{8.20}$$

Thus, the oscillation amplitude is proportional to the spin current according to Eq. (8.18) as the spin current is also proportional to the a_2-coefficient. The proportionality factor between the spin current and the oscillation amplitude can be found by comparing this result to the integral form of the continuity equation (8.14) at time t_s

$$\begin{aligned} \mathrm{j}(t_\mathrm{s}) &= \partial_t \mathcal{I}(t')\big|_{t=t_\mathrm{s}} \\ &= A\, \frac{E_2(t_\mathrm{s}) - E_1(t_\mathrm{s})}{\hbar} \cos\left(\frac{E_2 - E_1}{\hbar}\, t' \right)\bigg|_{t=t_\mathrm{s}} \\ &= A\, \frac{E_2(t_\mathrm{s}) - E_1(t_\mathrm{s})}{\hbar}. \end{aligned} \tag{8.21}$$

9. Experimental setup and calibrations

9.1. Setup

The spin-pump experiment is performed with ultracold ^{87}Rb atoms in a 3D optical lattice. A description of the experimental apparatus can be found in Refs. [143–146]. The chains of isolated double wells are created by a superlattice along the x-direction and deep transverse lattices along y and z to decouple the 1D chains. The two-spin components are implemented by two hyperfine states up $|\uparrow\rangle = |F = 1, m_F = -1\rangle$ and down $|\downarrow\rangle = |F = 1, m_F = +1\rangle$. Note that they have opposite magnetic moments. Thus, the global state-dependent linear potential in Eq. (7.4) can be realized by a magnetic field gradient. During the pumping process, the direction of the magnetic gradient is inverted adiabatically. Furthermore, the dimerization of the superlattice needs to be changed for the sequence with multiple pump cycles (Fig. 7.1). To this end, a second laser is used creating long-period lattice sites shifted in phase by π.

9.2. Experimental sequence

In this section, the experimental sequences for the initial state preparation, the spin current measurement, and multi-cycle pumping are described. Illustrations of these sequences are shown in Fig. 9.1. The experiment starts with ^{87}Rb atoms in the $|F = 1, m_F = -1\rangle$ hyperfine state. They are loaded into a 3D optical lattice of three mutually orthogonal standing waves with wavelengths $\lambda_x = \lambda_y = 767\,\text{nm}$ and $\lambda_z = 844\,\text{nm}$. The lattice parameters are chosen such that the atoms form a Mott insulating state. The atoms are transferred to the hyperfine state $|F = 1, m_F = 0\rangle$ via the intermediate state $|F = 2, m_F = -1\rangle$ with a sequence of microwave-driven adiabatic passages. The microwave pulses are marked by f_{t1} and f_{t2} in Fig. 9.1. Now, two neighboring lattice sites along the x-direction are merged together. They form new isolated lattice sites with twice the period $d_\text{l} = 2d_\text{s}$, where $d_\text{s} = \lambda_x/2$. The merging is achieved by simultaneously increasing the long-period lattice and turning the short-period lattice off. The new lattice sites are mainly occupied by two atoms. They can be transferred from a pair of $|F = 1, m_F = 0\rangle$ atoms to a pair of

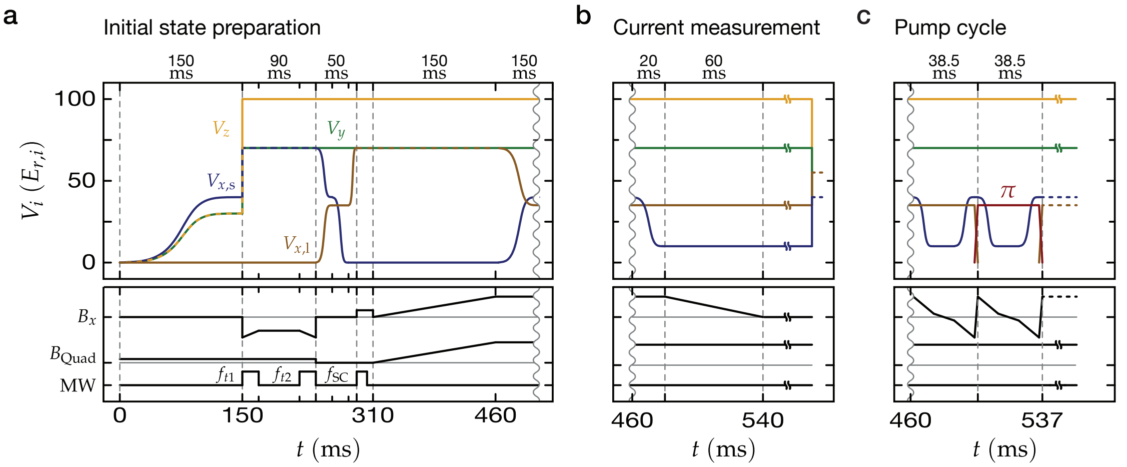

Figure 9.1.: Illustration of the experimental sequences. The course of the lattice potential depths are shown in the upper panels. The lattices with period d_s and d_l along the x-direction (blue and red), d_s along the y-direction (green), and $d_z = \lambda_z/2$ along the z-direction (yellow) are shown in their respective recoil energies. The course of the magnetic quadruple-field strength B_{Quad} and the magnetic bias B_x field along x as well as the microwave pulses (MW) are sketched in the lower panel. **a** Illustration of the initial state preparation sequence. The sequence ends with decoupled sites occupied by atoms in the states $|\uparrow\rangle = |F = 1, m_F = -1\rangle$ and $|\downarrow\rangle = |F = 1, m_F = +1\rangle$ in antiferromagnetic order. **b** Illustration of a current measurement at $\Delta_s = 0$. This part of the sequence directly follows the initial state preparation. Here, a quarter pump cycle is shown. The magnetic gradient ramp, performed by the change of B_x, was abruptly stopped. Then, after a variable hold time the spin imbalance was detected. **c** Illustration of the spin-pump sequence for multiple cycles. This part of the sequence directly follows the initial state preparation. It is used for in-situ and band mapping measurements. Note that after half a pump cycle the dimerization is reversed by swapping to a second laser creating a π-phase-shifted long lattice and therefore isolated double wells shifted by d_s. Simultaneously, the magnetic field gradient is reversed in 2 ms.

$|F = 1, m_F = \pm 1\rangle$ atoms by coherent microwave-mediated spin changing collisions [154]. Thereafter, the lattice sites are occupied by pairs of up and down spins. These spins are now placed on individual short-period lattice sites in an antiferromagnetic order. To this end, a magnetic field gradient is turned on and the long lattice sites are split adiabatically into two decoupled sites by turning on the short period lattice. The final lattice depth $V_s = 40\,E_{r,s}$ is reached in 50 ms. The lattice depth are given in their respective recoil energy $E_{r,i} = h^2/2m_{\mathrm{Rb}}\lambda_i^2$ with m_{Rb} the mass of a Rubidium atom. The magnetic gradient introduces a tilt of $\Delta/h = 2.7(2)$ kHz between neighboring sites during the splitting. This leads to the antiferromagnetic ordering of the spins. Note that the lattice sites are decoupled with $J_{\mathrm{ex}} \approx 0$. After this initial state preparation, pumping is performed.

The current measurement technique is only applied to the first half of the pump cycle. The sequence starts by adiabatically coupling every other lattice site by decreasing the short-period lattice depth V_s in the presence of the magnetic gradient field. Then, pumping is induced by reversing the magnetic gradient. To this end, the magnetic bias field B_x is changed with a constant rate. For the current measurement, pumping is abruptly stopped, i.e. B_x is suddenly kept constant at a certain final value of the magnetic tilt Δ_s. Depending on the strength of the instantaneous spin current, a spin-imbalance oscillation occurs. This time-dependent oscillation can be measured by rapidly freezing the dynamics with an increased short-period lattice depth after a variable holdtime t'. Then, a site-resolved band mapping was performed in combination with a Stern-Gerlach field. The spin components separate spatially during time-of-flight and the four site occupations $n_{\mathrm{L}\downarrow}$, $n_{\mathrm{L}\uparrow}$, $n_{\mathrm{R}\downarrow}$, and $n_{\mathrm{R}\uparrow}$ can be simultaneously extracted from each absorption image.

The experimental sequence to measure the spin separation after multiple pump cycles also starts by adiabatically coupling every other lattice site. Therefore, the short-period lattice depth V_s is decreased in the presence of a magnetic gradient field. Pumping is performed by adiabatically inverting the spin-dependent gradient. To this end, the bias field B_x is changed. After half a pump cycle, the spin-dependent gradient has been inverted and the motion of the particles is frozen again through a deep short-period lattice depth. In this configuration $J_\mathrm{ex} \approx 0$ and no tunneling can occur. To continue the pump cycle, the dimerization is flipped by swapping to a second long-period lattice laser, which creates a π-shifted long-period lattice, i.e. a long-period lattice that is shifted by one site of the short lattice. Simultaneously, also the magnetic bias field is set back to its initial value to reverse the magnetic field gradient in 2 ms. The reason for this is explained in Fig. 7.1. This half pump cycle can now be repeated multiple times. Before in-situ imaging, atoms initially in the $|F = 1, m_F = 0\rangle$ state are removed, which correspond to atoms on singly-occupied double wells during the preparation sequence. Therefore, simultaneously a microwave field on the $|F = 1, m_F = 0\rangle \rightarrow |F = 2, m_F = 0\rangle$ transition and a resonant imaging light pulse to remove the atoms in the $F = 2$ manifold was applied. Subsequently, one of the spin states is selected and transferred to the $|F = 2, m_F = 0\rangle$ state by a microwave-driven adiabatic passage and imaged by absorption imaging.

9.3. Calibrations

The tunnel coupling J' between double-well sites can be calibrated by measuring single-particle imbalance oscillations. To this end, an $n = 1$-Mott insulator state in the long-period lattice is prepared. Each long-period lattice site is then split in two short-period lattice sites in the presence of an energy offset $\Delta \gg J'$ between neighboring sites. During the splitting, the particle adiabatically follows the ground state and localizes to the energetically lower-lying site. The resulting lattice sites are decoupled and $J \approx 0$. Now, the energy offset is nonadiabatically removed to reach $\Delta = 0$. To start the imbalance dynamics, the sites are coupled by ramping down the short-period lattice nonadiabatically in 200 μs to the lattice depth at which J' needs to be calibrated. The localized particle is not in an eigenstate of a symmetric double well. It is in an equal superposition of the ground $|1\rangle$ and first excited state $|2\rangle$. Thus, the imbalance oscillates in time. This time-dependent particle imbalance is measured by site-resolved band mapping and its oscillation frequency f_{bare} is defined by the band gap. Therefore, the tunnel coupling can be calculated $J' = h\, f_{\mathrm{bare}}/2$.

The calibration of the on-site interaction energy U in this part is performed similar to the calibration in Sec. 3.1.5. In both calibrations, the superexchange oscillation frequency is used to numerically calculate U for a known bare-tunnel coupling J' from the extended Bose-Hubbard model. The difference is that here, it is sufficient to consider U at $\Delta = 0$ while in the minimal instance for $\mathbb{Z}_2$ LGTs, a calibration of U was required at $\Delta \approx U$. In consequence, the spin states $|F = 1, m_F = \pm 1\rangle$ can be used here. Initially, they are localized on the left and right site of the double well in the presence of a large spin-dependent tilt Δ (Sec. 9.2). Then, the magnetic fields, except for a small bias field to maintain the quantization axis, are switched off to non-adiabatically remove the tilt while $J_{\mathrm{ex}} \approx 0$. In a next step, the sites are coupled by decreasing the short-period lattice within 200 μs to the final value, at which U needs to be calibrated. The localized state is not an eigenstate of the symmetric double well and therefore superexchange oscillations occur [4].Luo The exchange coupling J_{ex} can be calculated using the measured oscillation frequency, by solving the extended Bose-Hubbard model numerically.

The magnetic gradient field, responsible for the spin-dependent gradient potential, consists of a two contributions. The first contribution stems from a pair of coils in anti-Helmholtz configuration in z-direction. The resulting quadrupole field is

$$\mathbf{B}_{\mathrm{quad}} = B_{\mathrm{quad}} \left(x\, \mathbf{e}_x + y\, \mathbf{e}_y - 2z\, \mathbf{e}_z \right), \tag{9.1}$$

with $\mathbf{e}_i$ the unit vector in the ith direction. The second contribution is an homogeneous bias field $B_x\, \mathbf{e}_x$ from a pair of coils in Helmholtz configuration oriented in the x-direction. Assume that the atom cloud is roughly in the center at $x \approx 0$, then the resulting total magnetic field is

$$B = \sqrt{(B_{\mathrm{quad}} x + B_x)^2 + B_{\mathrm{ofs}}^2(y, z)}. \tag{9.2}$$

For small $B_x \ll B_{\mathrm{ofs}}$, the magnetic gradient $B' = \partial_x B$. depends linearly on B_x. To correctly interpret the results of the current measurement method, an accurate knowledge of the spin-dependent double-well tilt induced by the magnetic gradient is essential. Therefore, a laser-assisted tunneling spectroscopy was performed for calibration. The method uses laser beams, which interfere under an angle of 90°. The result is a lattice oriented at 45° to the physical lattice. When a frequency difference of $\delta\omega$ between the beams is applied,

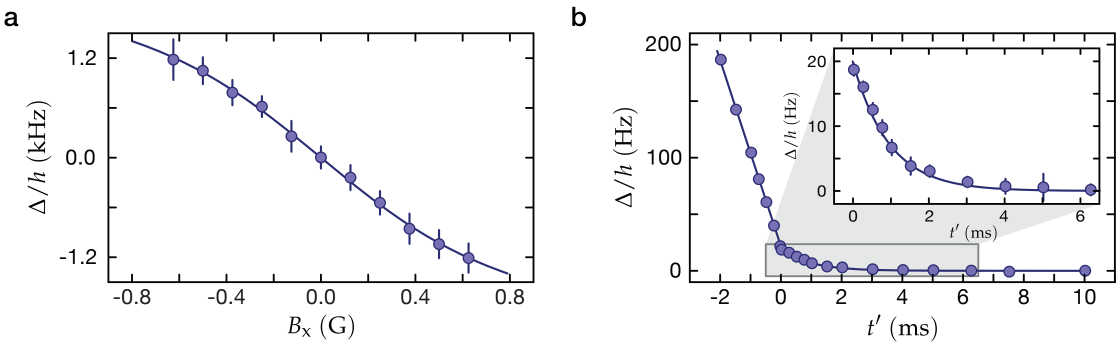

Figure 9.2.: Calibrations of the magnetic gradient. **a** Magnetic tilt calibration in a tilted double well using laser-assisted tunneling spectroscopy. The calibration is performed for various bias fields B_x. The magnetic tilt Δ was calculated from the measured resonance frequency f_res by subtracting the double-well tilt $2\Delta = h f_\mathrm{res} - \delta_0$. The data points and error bars are average and standard deviation of a differential measurement with four repetitions per hyperfine state $|F = 2, m_F = \pm 2\rangle$. **b** The residual exponential decay of Δ after the ramp stop at $t' = t - t_\mathrm{s}$ was calibrated by microwave spectroscopy on the $|F = 1, m_F = -1\rangle \rightarrow |F = 2, m_F = -2\rangle$ transition. To this end, the gradient ramp was stopped at $\Delta_\mathrm{s} = 0$ and the magnetic field was measured. Before the stop at t_s, the magnetic field changes linearly and afterwards an exponential decay is clearly visible. The decay constant $\tau_\mathrm{d} = 1.05(5)$ ms and the value Δ_d can be determined by an exponential fit to the data for $t' > 0$ and a linear fit to the data for $t' < 0$. Note that the value Δ_d depends on the double-well site distance.

then the lattice moves and modulates the on-site energy of the underlying lattice structure. The calibration starts with a single $|F = 2, m_F = \pm 2\rangle$-particle in the ground state of a tilted double-well potential with $\delta_0/h = 4.91(2)$ kHz. In the presence of the gradient, the magnetic tilt $\pm 2\Delta$ adds to the double-well tilt δ_0. At the resonance frequency $\hbar\,\delta\omega = \pm 2\Delta + \delta_0$, the lattice modulation induces tunneling. Several spectroscopy scans for different magnetic field values B_x were performed. The result is shown in Fig. 9.2 a. For large B_x a deviation from the linear behavior is visible, which can be captured by fitting the magnetic field distribution of a quadrupole field

$$\Delta \propto \frac{B_x B_\mathrm{quad}}{\sqrt{B_x^2 + B_\mathrm{ofs}^2}}, \tag{9.3}$$

where both B_quad and B_ofs are fit variables.

For the current measurement, the magnetic gradient ramp needs to be stopped abruptly at a certain value Δ_s. Experimentally, it was found that an instantaneous stop on experimental time scales is not possible. After the stop, a small residual gradient remains that slowly decays during the current measurement. Characterizing the magnitude of the residual gradient Δ_d at t_s as well as the decay time τ_d is crucial for a correct interpretation of the current measurement. The characterization is achieved by measuring the total magnetic field value with microwave spectroscopy. It starts with a single spin in the $|F = 1, m_F = -1\rangle$ hyperfine state and in the ground state of a double well with a strong magnetic tilt. Then, the gradient is reduced with the identical rate as for the current measurement and stopped at $\Delta_\mathrm{s} = 0$. However, pumping was inhibited by decoupling the lattice sites during this process. Now, microwave spectroscopy is performed on the $|F = 1, m_F = -1\rangle \rightarrow |F = 2, m_F = -2\rangle$ transition with a pulse width of 44 µs to determine the residual strength of the magnetic bias field. The spectroscopy is performed for various times around t_s. The gradients $\Delta(t')$ extracted from the residual magnetic bias field are shown in Fig. 9.2 b. After the stop at times $t' > 0$ a clear exponential decay $\Delta_\mathrm{d}\, e^{-t'/\tau_\mathrm{d}}$ is visible. The decay constant is fitted $\tau_\mathrm{d} = 1.05(5)\,\mathrm{ms}$. For times $t' < 0$, a linear dependence of the gradient on time is shown. A comparison of this slope with the gradient calibration from Fig. 9.2 a allows to quantify the amplitude to $\Delta_\mathrm{d}/h = 24.3(6)\,\mathrm{Hz}$ for sites separated by d_s. This corresponds to a tilt in the superlattice for the experimental parameters of $\Delta_\mathrm{d}/h = 19.8(5)\,\mathrm{Hz}$ at $J_\mathrm{ex}/h = 342(2)\,\mathrm{Hz}$ and $\Delta_\mathrm{d}/h = 19.4(5)\,\mathrm{Hz}$ at $J_\mathrm{ex}/h = 467(3)\,\mathrm{Hz}$. The difference originates mainly from the slightly different distance between the sites depending on the double-well parameters.

The site-resolved band mapping technique has a reduced detection efficiency if two distinguishable particles share the same double well. This reduction originates from a dephasing during singlet–triplet oscillations between particles in the first and the third Bloch band of the long-period lattice as will be briefly discussed here. In the site-resolved band mapping technique, particles from one of the double-well sites will be transferred to the first Bloch band, while particles from the other site will be transferred to the third band of the long-period lattice. During this transfer and the hold time prior to the band mapping, singlet–triplet oscillations occur [4, 5]. Note that the hold time before the band mapping needs to be matched with the singlet–triplet oscillation frequency, such that the correct value for the spin imbalance is detected. However, the detected imbalance is reduced most likely due to dephasing during the merging ramps. The detection efficiency can be calibrated and the measured imbalances can then be rescaled by a constant calibration factor. The calibration measurement compares the two-spin site-resolved band mapping with a single-spin band mapping, where shortly before the merging one of the spin components is removed by an adiabatic spin transfer and a subsequent resonant light pulse.

10. Measurements and numerical analysis

10.1. Measurements of spin separation

A first direct evidence for spin transport in the spin pumping scheme was gained from a measurement of spin separation. To this end, the center-of-mass transport of individual spin components is determined from spin-selective in-situ images. The experiment is initialized by a state prepared according to the preparation sequence described in Sec. 9.2. This state has antiferromagnetically ordered spins. The pumping sequence starts by decreasing every other barrier. During this process, neighboring spins are transferred to the ground states of double wells and up and down spins stay localized on the left and right side because a large magnetic gradient $\Delta \gg J_{\mathrm{ex}}$ is present. This state will be shortly denoted as $|\uparrow, \downarrow\rangle$. Then, the first half pump cycle is performed by changing the sign of the magnetic gradient adiabatically compared to the exchange coupling J_{ex}. The wave function follows the instantaneous eigenstate and the two spins exchange their positions via the delocalized triplet state $(|\uparrow\downarrow\rangle + |\downarrow\uparrow\rangle)/\sqrt{2}$ at $\Delta = 0$. To proceed the cycle, the minimal instance needs to be shifted. To this end, individual sites are decoupled by a deep short-lattice potential, the dimerization is flipped, and the magnetic gradient is reversed (Fig. 7.1 c). This process can be interpreted as a projection on double wells shifted by one lattice site. The wave function, however, remains unchanged during this sudden switch because the spins are localized to individual sites. Therefore, the spins can be transferred to the ground state of the new shifted double wells by coupling the double-well sites. Now, the second half of the pump cycle can be performed. After a full cycle, the two spin components have each moved by $2\,d_s$ in opposite directions; therefore the total particle current vanishes as the contributions from the two spin components exactly cancel each other. Thus, pumping leads to a spin transport without inducing a particle current. A measurement result of the spins' center-of-mass position from in-situ absorption images is shown in Fig. 10.1. The spins clearly separate as a function of the pump parameter ϕ. However, deviations from the ideal spin transport are found.

To gain more insights into the deviations observed in the spin-separation data, a measurement of the static spin imbalance $\mathcal{I}_{\mathrm{s}}$ was conducted. The result is shown in Fig. 10.2. Therein, the pump parameter ϕ is defined as the angle of the pump path in the normalized

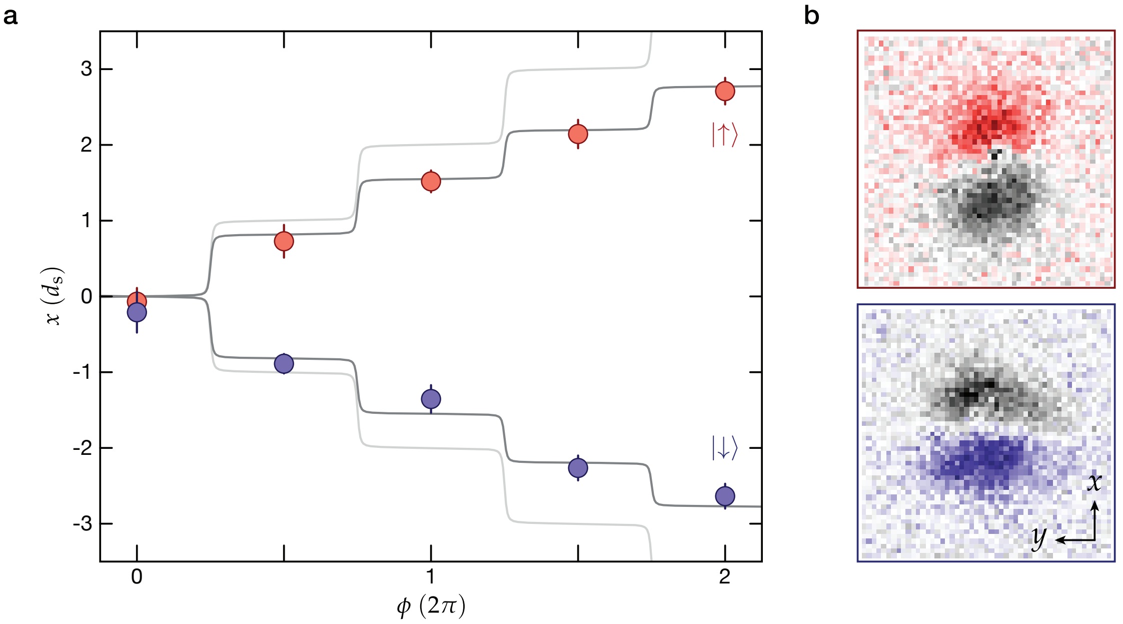

Figure 10.1.: Spin separation. The data points show the center-of-mass position of up (red) and down (blue) spins as a function of the pump parameter ϕ. The data points and error bars are the average and the error of the mean of ten data sets. A data set consists of ten pairs of a spin-selectively imaged atom cloud. Each pair contains an image of the atom cloud from the pumping sequence and an image from a reference sequence with the same length but constant pump parameter $\phi = 0$. The solid lines depict the calculated transport of a localized spin. The ideal pumping motion is shown in light gray and the pumping motion taking into account a reduced ground state occupation and a finite pump efficiency in dark gray. The pumping efficiency is independently calibrated by band mapping. **b** The images are the difference of in-situ absorption images between a pumping and the corresponding reference data set for both spins.

parameter space $(\delta J_{\text{ex}}/\delta J_{\text{ex,max}}, \Delta/\Delta_{\text{max}})$. Note that the spin imbalance is taken with respect to a fixed double well position. At $\phi = 0$, the spin imbalance is negative and the state is predominantly $|\uparrow\downarrow\rangle$. During the first half pump cycle, the spins exchange their position to $|\downarrow\uparrow\rangle$ and the spin imbalance becomes positive. Further half pump cycles are appended after flips of the dimerization. Each time, the spin imbalance is inverted. In Fig. 10.2, also deviations to the ideally expected evolution of the spin imbalance are visible. First, the absolute value of the initial spin imbalance is not exactly one, which can be explained by a small occupation of spins in the first excited state after the initial state preparation. The extracted ground state occupation is $n_1^{(0)} = 0.94$. Second, the transfer does not perfectly invert the spin imbalance. This imperfection is mainly attributed to nonadiabatic transfer to higher bands, during the pumping process. Applying slower ramps to better maintain adiabaticity is experimentally challenging, as other heating sources like technical noise on the lattice beams start to become significant. A pump efficiency $\beta_i = (\mathcal{I}_{i-1} - \mathcal{I}_i)/2\mathcal{I}_{i-1}$,

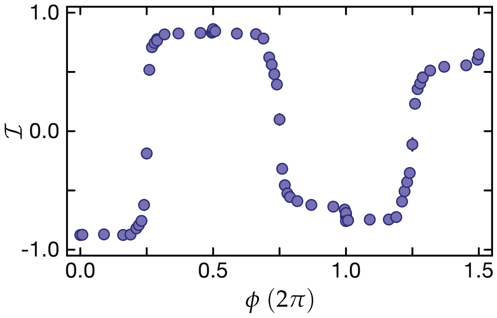

Figure 10.2.: Static spin imbalance $\mathcal{I}$ during the pump cycle. The static spin imbalance for multiple pump cycles is measured using the same sequence as for the spin separation measurement but replacing the in-situ imaging by a spin-resolved band-mapping. The pump parameter ϕ is defined as the angle of the pump path in normalized parameter space $(\delta J_{\mathrm{ex}}/\delta J_{\mathrm{ex,max}}, \Delta/\Delta_{\mathrm{max}})$. The data points are an average of five repetitions and the error bars show the error of the mean.

with $\mathcal{I}_i$ the spin imbalance after the ith half pump cycle, can be extracted from the data and is $\beta_{1\ldots4} = \{0.97, 0.91, 0.96, 0.90\}$. It describes how much ground state occupation stays in the ground state after half a pump cycle. Note that at $\phi = 2\pi$, there is a small step in $\mathcal{I}$. The step mainly originates from singly occupied sites created at the edge of the atom cloud during pumping.

Using the calibrated initial state occupation and pump efficiency, the expected motion of a localized spin can be calculated. The step height of each step i is thereby

$$s_i = \beta_i \Big(2 n_{0,\mathrm{gs}} \prod_{j=0}^{i-1} \beta_j - 1 \Big) \tag{10.1}$$

with $n_{0,\mathrm{gs}} = 0.94$ and $\beta_0 = 1$. The total displacement after multiple half pump cycles is then

$$x = \sum_{j=1} s_j. \tag{10.2}$$

This fit-free result is shown in Fig. 10.1 as dark gray curve and is in good agreement with the in-situ spin-separation measurement.

10.2. Measurements of spin currents

After first detecting spin separation in response to spin pumping, instantaneous spin currents are measured in a second step. To this end, the spin-current measurement method introduced in Sec. 8.3 is used. The pump cycle is thereby interrupted abruptly and the

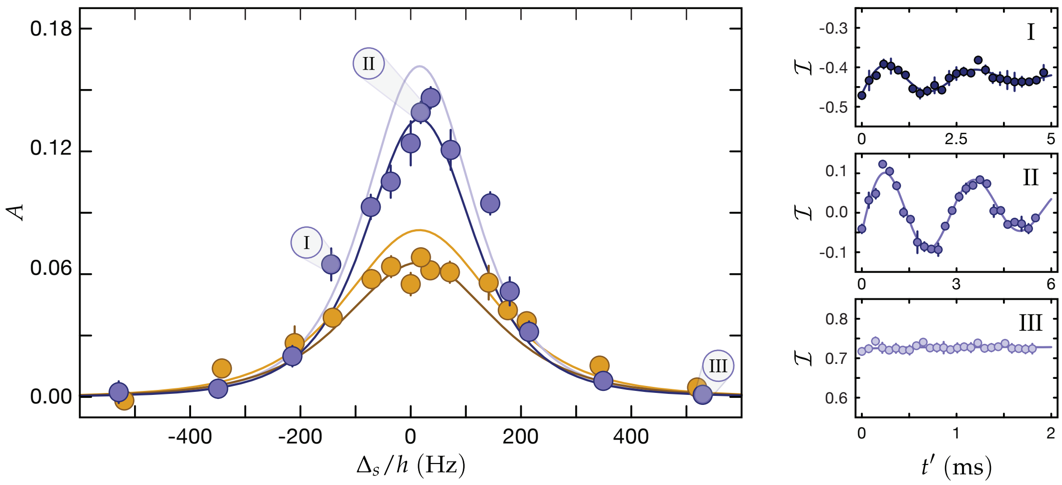

Figure 10.3.: Spin-current measurement. A spin current measurement is performed according the method illustrated in Fig. 8.2. To this end, pumping is performed at a speed of $\dot{\Delta} = 82(2)$ kHz/s at $\Delta = 0$ and abruptly interrupted. The projection leads to a spin-imbalance oscillation with an amplitude A proportional to the spin current. The oscillation amplitude is shown for two data sets with different exchange coupling $J_{\text{ex}}/h = 342(2)$ Hz (blue) and $J_{\text{ex}}/h = 467(3)$ Hz (orange). The amplitude A is obtained from a fit of Eq. (10.3) to spin-imbalance time traces. The data points are the fit values and the error bars the fit uncertainties. Three exemplary time traces are shown in the panels on the right hand side. They correspond to $\Delta_s/h = -144(7)$ Hz (I, dark blue), $\Delta_s/h = 18(5)$Hz (II, blue), and $\Delta_s/h = 530(30)$ Hz (III, light blue). These traces consist of 26 time points and are averaged five times. The numerical model shown in the main plot considers a reduced detection efficiency of the oscillation amplitude due to a residual exponential decay of Δ (light solid line). The dark solid lines additionally consider a finite ground state occupation of 97(1) % and pump efficiency of 89(1) %. These efficiencies are both measured separately by band mapping.

subsequent spin-imbalance oscillations are analyzed. Experimentally, this is done by stopping the gradient ramp suddenly at $\Delta_s = \Delta(t_s)$. Then, a time trace of the resulting superexchange oscillations were recorded by a simultaneous measurement of the spin-dependent site occupations $n_{L\uparrow}$, $n_{L\downarrow}$, $n_{R\uparrow}$, and $n_{R\downarrow}$ taking spin- and site-resolved band mapping images [4, 147]. The resulting time trace was fitted by the function

$$\mathcal{I}_{\text{fit}}\left(t'\right) = A\, e^{-t'/\tau_{\text{ex}}} \sin\left(\omega_{\text{ex}} t' + \theta\right) + \mathcal{I}_s + \mathcal{I}_d\, e^{-t'/\tau_d} \tag{10.3}$$

with $t' = t - t_s$ and $\theta \approx 0$. This small phase shift θ accounts for a finite freezing ramp speed. The fit function considers two additional effects to the ideal time evolution. First, a finite lifetime of the imbalance oscillations is taken into account. The decay is assumed to be exponential with a time constant τ_{ex} and accounts for dephasing between the oscillations on different double wells. This decay constant τ_{ex} and the oscillation frequency $\omega_{\text{ex}} \simeq (E_2 - E_1)/\hbar$ were separately determined for each Δ_s by independent superexchange oscillation measurements. Second, an additional decaying imbalance offset $\mathcal{I}_\mathrm{d}$ is taken into account. This imbalance decay with $\tau_\mathrm{d} = 1.05(5)\,\mathrm{ms}$ is caused by an exponential relaxation of a small residual magnetic field gradient inducing an energy-offset between neighboring sites of $-24.3(6)\,\mathrm{Hz}/d_s$ after the abrupt stop (Sec. 9.3). In Fig. 10.3 the fitted oscillation amplitudes are summarized for two different exchange couplings together with exemplary spin-imbalance time traces. It is clearly visible that the spin current is peaked around $\Delta = 0$, where the ground state is delocalized and spins exchange their position. For large gradients, the eigenstates are independent of Δ and the spin current vanishes. Note that the spin current has its maximum not exactly at $\Delta = 0$. The maximum is slightly shifted towards higher values due to the residual gradient Δ_d. The shape of the peak and therefore also the instantaneous spin current strongly depends on the exchange coupling J_ex. The wavefunction delocalizes more for larger J_ex and it depends less on Δ. Therefore, the peak width increases while the maximum amplitude decreases. However, unlike the instantaneous current, the transported spin during one pump cycle is independent of the pump parameters. The transported spin can be extracted from the integrated spin current or from a comparison of the measured oscillation amplitudes and a model. To make a meaningful comparison, the detection efficiency needs to be included. The light colored solid lines in Fig. 10.3 represent perfect transport but reduced detection efficiency. The deviation between theory taking into account the detection efficiency of the measurement can be estimated fitting the model to the data by rescaling it with a global amplitude. The resulting factor is 0.84(6), which can be interpreted as the reduction of the integrated measured current due to a finite pumping efficiency compared to the ideal transported spin polarization. The dark colored solid lines include in addition to the detection efficiency also the finite pump efficiency seen in the spin separation measurement, which is calibrated via the static spin-imbalance. The model has no fit parameter and agrees well with the measured data. To quantify the deviations, the model is fitted to the measured spin-oscillation amplitudes by rescaling its amplitude with a global factor. This leads to fit values of 1.05(8) for $J_\mathrm{ex}/h = 342(2)\,\mathrm{Hz}$ and 1.06(8) for $J_\mathrm{ex}/h = 467(3)\,\mathrm{Hz}$. In the next paragraph, the model including the detection and pump efficiency are discussed in more detail.

The ideal spin-oscillation amplitude for a perfect projection of the pump's wave function on the static double well can be calculated from Eq. (8.20). The result is shown in Fig. 10.4 as green solid lines and is contrasted with the amplitudes including corrections discussed in the following. This ideal projection is only reached for an instantaneous stop of the gradient ramp, which means that Δ_s is static right after t_s. However, in experiments the stop is smoothened by a decaying residual magnetic gradient, which in fact reduces the measured oscillation amplitude. This effect can be calculated numerically by solving the time-dependent Schrödinger equation for a two-spin two-site extended Bose-Hubbard model including the residual gradient. The assumptions are an initial state after adia-

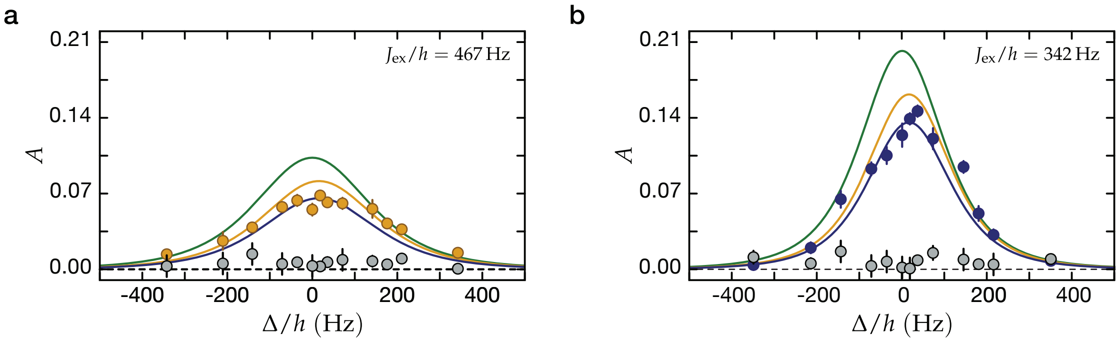

Figure 10.4.: Comparison of models for the spin current measurement. Δ is ramped with a rate of $\dot{\Delta} = 82(2)\,\mathrm{kHz/s}$ at $\Delta = 0$ and the ramp is stopped abruptly at different points in the cycle Δ_s The measured spin-imbalance oscillation amplitude of the data sets **a** $J_\mathrm{ex}/h = 467(3)\,\mathrm{Hz}$ (orange) and **b** $J_\mathrm{ex}/h = 342(2)\,\mathrm{Hz}$ (blue) from Fig. 10.3 are shown together with different models. The ideally expected oscillation amplitude for perfect pumping and detection is the green solid line. The model shown in orange takes into account a reduced detection efficiency due to a residual exponential decay of the magnetic field gradient after the stop of the gradient ramp. The model shown in blue additionally considers the detection efficiency also a finite ground state occupation of $97(1)\,\%$ and a pump efficiency of $89(1)\,\%$. Moreover, the particle current is evaluated from the same source data (gray) by analyzing the particle imbalance oscillations between the left and right side of the double well.

batic evolution according to Eq. (8.17) at a gradient of $\Delta_\mathrm{s} + \Delta_\mathrm{d}$ and a time-dependent Hamiltonian $\hat{H}_\mathrm{eBH}(\Delta_\mathrm{d} e^{-t'/\tau_\mathrm{d}} + \Delta_\mathrm{s})$. From the time-evolved wave function, the expectation value of the spin imbalance $\mathcal{I}(t')$ was calculated. The spin-oscillation amplitude is then extracted from the imbalance time trace by a fit to Eq. (10.3) as for the experimental data. The simulated results are shown in 10.4 as orange solid lines.

In a next step, the effect of finite excited state occupation and finite pumping efficiency on the detected current is considered. As discussed before, the preparation of a spin chain, in which all double wells occupy the ground state is experimentally extremely difficult. Thus, a few double wells will be in excited states, which lead to a reduced spin transport. This reduction can be well modeled assuming only double wells in the ground and first excited state. Both band occupations can be extracted from the initial spin imbalance

$$n_{0,\mathrm{gs}} = \frac{\mathcal{I}_\mathrm{ideal,gs} + \mathcal{I}_0}{2\mathcal{I}_\mathrm{ideal,gs}}, \quad \text{and} \quad n_{0,\mathrm{es}} = \frac{\mathcal{I}_\mathrm{ideal,es} + \mathcal{I}_0}{2\mathcal{I}_\mathrm{ideal,es}} = \frac{\mathcal{I}_\mathrm{ideal,gs} - \mathcal{I}_0}{2\mathcal{I}_\mathrm{ideal,gs}}, \tag{10.4}$$

when the ideal spin imbalance for ground and excited states are considered to be negative equal $\mathcal{I}_\mathrm{ideal,es} = -\mathcal{I}_\mathrm{ideal,gs}$. The transport is captured by the integrated spin current $\bar{\jmath} = \int_{t_\mathrm{i}}^{t_\mathrm{f}} \jmath(t)\,\mathrm{d}t$ of both states weighted by the initial band occupation and the pump efficiency. The spin currents for the ground and first excited band are oppositely directed and therefore also the integrated spin currents $\bar{\jmath}_\mathrm{gs,ideal} = -\bar{\jmath}_{es,\mathrm{ideal}}$ are oppositely directed. In

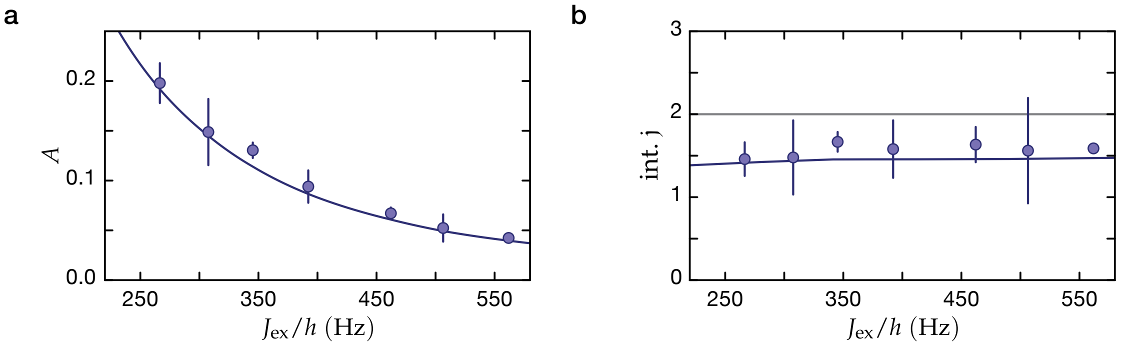

Figure 10.5.: Spin imbalance oscillation amplitude A at $\Delta_s = 0$ as a function of J_{ex}. a The data points and error bars represent the average and standard deviation of fitted spin-imbalance oscillation amplitudes for three measured time traces. The numerical model (blue line) considers a reduced detection efficiency, a measured initial state occupancy, and finite pump efficiency (see. Fig. 10.4). **b** As indicated by the data in Fig. 10.3, a global scaling factor for each exchange coupling is sufficient to estimate the integrated spin current per pump cycle. Therefore, an estimate of the integrated spin current is shown and compared to the ideal integrated spin current of two (gray line).

addition, the pump efficiencies for the two states are assumed to be equal $\beta_{1,\mathrm{gs}} = \beta_{1,\mathrm{es}}$. Then, the integrated spin current is

$$\begin{aligned} \bar{\mathrm{j}} &= n_{0,\mathrm{gs}}\,\beta_{\mathrm{gs}}\,\bar{\mathrm{j}}_{\mathrm{ideal,gs}} + n_{0,\mathrm{es}}\,\beta_{\mathrm{es}}\,\bar{\mathrm{j}}_{\mathrm{ideal,es}} \\ &= \left(n_{0,\mathrm{gs}} - n_{0,\mathrm{es}}\right)\beta_{1,\mathrm{gs}}\,\bar{\mathrm{j}}_{\mathrm{ideal,es}} \\ &= \mathcal{I}_0 - \mathcal{I}_1, \end{aligned} \tag{10.5}$$

where $\mathcal{I}_0$ is the initial and $\mathcal{I}_1$ the final spin imbalance of the first pump cycle. The expected reduction of the integrated spin current can be approximately incorporated in the data analysis by rescaling the spin current $\mathrm{j}(t)$ with a global factor or equivalently rescaling the spin-oscillation amplitude. The rescaling corresponds to pumping with perfect pump efficiency and an effective average state occupation. The blue line in Fig. 10.4 shows the spin-oscillation amplitude taking into account the detection efficiency, the initial ground state occupation, and the pump efficiency. Note that the model does not contain any fit parameters.

In a last set of experiments, the dependence of the maximum current on the exchange coupling is studied. And in this context also the total integrated current and therefore the transported spin is estimated. To this end, the spin-oscillation amplitude for various J_{ex} at $\Delta_s = 0$ was recorded with the current measurement method. The result is shown in Fig. 10.5 a. For larger exchange couplings the maximum oscillation amplitude decreases as the wave functions are more delocalized over the pump cycle and therefore the flow of the current is distributed over a larger gradient range. The model introduced before, which includes the current measurement's detection and finite pump efficiency, is in agreement with the measured data (solid blue line). Furthermore, the integrated spin current can be estimated from this measurement using the assumption made already before that rescaling of the model by a global factor captures the corrections and therefore the reduction of the transported spin. This assumption is well supported by the two data sets in Fig. 10.3. Therefore, the integrated spin current can be extracted by rescaling the ideal amplitude. The result is shown in Fig. 10.5 b. The integrated spin current is found to be constant for all exchange couplings. In conclusion, this shows that even though the shape and amplitude of the instantaneous spin currents change, the transported spin is only defined by the pump path's topology and not by the specific tunneling parameters.

10.3. Conclusions

In this second part, the implementation of a spin pump based on a chain of two-site minimal instances was demonstrated. This spin pump can be interpreted as a dynamical version of the QSHE in the limit, where processes on the minimal instance are adiabatic and processes between individual minimal instances are purely-nonadiabatic. The instantaneous spin currents resulting from this spin pump were analyzed by a newly introduced detection method. The method relates the instantaneous spin current in the system to the spin-imbalance oscillation amplitude on double wells after projecting the system on these double wells. A comparison of the resulting spin-imbalance oscillation amplitudes with an adiabatic model demonstrates that the integrated spin current is independent of the specific pump parameters. This supports both the underlying topological nature of the pump path and especially also the applicability of the spin-current measurement technique. It is important to emphasize, that the spin-current measurement technique can be applied to more general situations. Furthermore, combining this technique with single-site resolution would allow for the detection of e.g. local spin currents and edge excitations in finite systems [229]. Moreover, systems described by the nontrivial $\mathbb{Z}_2$-invariant can be realized with time-reversal invariant spin orbit interactions [209, 211]. When TRS is broken but spin conservation remains, then the topological properties of the QSH system persist and a description with spin-Chern numbers is possible [211]. Furthermore, a topological, interaction-driven quantum motor [230, 231] can be accomplished by only pumping one component while the other is coupled by interactions. For spin pumps with highly degenerate many-body ground states, fractional transport is predicted [232].

Part III.

Appendix

A. Effective Hamiltonian of the $\mathbb{Z}_2$ double well

A.1. Floquet expansion

The derivations of the effective Hamiltonian in these sections directly follow the presentation in the Supplementary Material of Ref. [17]. The time-dependent double-well model Eq. (2.24) realizes in the high frequency limit a minimal instance for $\mathbb{Z}_2$ LGTs. The model can be expressed by the four basis states representing the four possible site occupations of the a- and f-particles: $|\mathrm{LL}\rangle = |a,0\rangle \otimes |f,0\rangle$, $|\mathrm{LR}\rangle = |a,0\rangle \otimes |0,f\rangle$, $|\mathrm{RL}\rangle = |0,a\rangle \otimes |f,0\rangle$, and $|\mathrm{RR}\rangle = |0,a\rangle \otimes |0,f\rangle$, where the labels a and f before or after the comma mark the particle occupation on the left and right site. The resulting Hamiltonian is

$$\begin{aligned}\hat{H}(t) = &- J\left(|\mathrm{RL}\rangle\langle\mathrm{LL}| + |\mathrm{RR}\rangle\langle\mathrm{LR}| + |\mathrm{RR}\rangle\langle\mathrm{RL}| + |\mathrm{LR}\rangle\langle\mathrm{LL}| + \mathrm{h.c.}\right)\\ &+ U\left(2\,|\mathrm{LL}\rangle\langle\mathrm{LL}| + |\mathrm{RL}\rangle\langle\mathrm{RL}| + |\mathrm{RR}\rangle\langle\mathrm{RR}|\right)\\ &+ A\cos(\omega t + \phi)\left(2\,|\mathrm{LL}\rangle\langle\mathrm{LL}| + |\mathrm{LR}\rangle\langle\mathrm{LR}| + |\mathrm{RL}\rangle\langle\mathrm{RL}|\right),\end{aligned} \tag{A.1}$$

with J the tunneling rate of both a- and f-particles and U the intra-species interaction energy. Note that the term proportional to U includes the a–f particle interaction as well as a species-dependent energy offset $\Delta_f = U$ between the two sites.

This time-dependent Hamiltonian can be expanded in a series of time-independent terms in powers of $1/\omega$ according to Floquet theory. In the high-frequency limit, this series can be truncated to lowest order. In the following, the effective Hamiltonian $\hat{H}_F$ is derived as described in Ref. [69, 101] up to first order. To this end, a transformation $|\psi\rangle \to |\psi'\rangle = \hat{R}(t)\,|\psi\rangle$ is found, which transforms the time-dependent Hamiltonian $\hat{H}$ to a new Hamiltonian without divergent terms in the high-frequency limit. This Hamiltonian is then expressed in a Fourier-series with time-independent components $\hat{\mathcal{H}}^{(k)}$

$$\hat{\mathcal{H}}(t) = \hat{R}\hat{H}(t)\hat{R}^\dagger - \mathrm{i}\hat{R}\partial_t\hat{R}^\dagger = \sum_{k\in\mathbb{Z}} \hat{\mathcal{H}}^{(k)}\mathrm{e}^{\mathrm{i}k\omega t}. \tag{A.2}$$

For Eq. (A.1), an appropriate transformation is

$$\begin{aligned}\hat{R}(t) = \exp\Big\{ &+\mathrm{i}\omega t \big(2 \left|\mathrm{LL}\right\rangle \left\langle\mathrm{LL}\right| + \left|\mathrm{RL}\right\rangle \left\langle\mathrm{RL}\right| + \left|\mathrm{RR}\right\rangle \left\langle\mathrm{RR}\right|\big) \\ &+ \frac{\mathrm{i}A}{\hbar\omega} \sin(\omega t + \phi) \big(2 \left|\mathrm{LL}\right\rangle \left\langle\mathrm{LL}\right| + \left|\mathrm{LR}\right\rangle \left\langle\mathrm{LR}\right| + \left|\mathrm{RL}\right\rangle \left\langle\mathrm{RL}\right|\big) \Big\}.\end{aligned} \tag{A.3}$$

With this transformation, the Fourier components are

$$\begin{aligned}\hat{\mathcal{H}}^{(k)} = &- J \Big\{ \mathcal{J}_{-k-1}(\chi) \left|\mathrm{RL}\right\rangle \left\langle\mathrm{LL}\right| \mathrm{e}^{\mathrm{i}(k+1)\phi} + \mathcal{J}_{k-1}(\chi) \left|\mathrm{LL}\right\rangle \left\langle\mathrm{RL}\right| \mathrm{e}^{\mathrm{i}(k-1)\phi} \\ &+ \mathcal{J}_{-k+1}(\chi) \left|\mathrm{RR}\right\rangle \left\langle\mathrm{LR}\right| \mathrm{e}^{\mathrm{i}(k-1)\phi} + \mathcal{J}_{k+1}(\chi) \left|\mathrm{LR}\right\rangle \left\langle\mathrm{RR}\right| \mathrm{e}^{\mathrm{i}(k+1)\phi} \\ &+ \mathcal{J}_{-k}(\chi) \left|\mathrm{RR}\right\rangle \left\langle\mathrm{RL}\right| \mathrm{e}^{\mathrm{i}k\phi} + \mathcal{J}_{k}(\chi) \left|\mathrm{RL}\right\rangle \left\langle\mathrm{RR}\right| \mathrm{e}^{\mathrm{i}k\phi} \\ &+ \mathcal{J}_{-k-2}(\chi) \left|\mathrm{LR}\right\rangle \left\langle\mathrm{LL}\right| \mathrm{e}^{\mathrm{i}(k+2)\phi} + \mathcal{J}_{+k-2}(\chi) \left|\mathrm{LL}\right\rangle \left\langle\mathrm{LR}\right| \mathrm{e}^{\mathrm{i}(k-2)\phi} \Big\} \\ &+ (U - \hbar\omega)\delta_{k0} \Big\{ 2 \left|\mathrm{LL}\right\rangle \left\langle\mathrm{LL}\right| + \left|\mathrm{RL}\right\rangle \left\langle\mathrm{RL}\right| + \left|\mathrm{RR}\right\rangle \left\langle\mathrm{RR}\right| \Big\},\end{aligned} \tag{A.4}$$

where $\mathcal{J}_\nu(\chi)$ is the νth Bessel function of the first kind with the dimensionless driving strength $\chi = A/\hbar\omega$ and δ_{ij} is the Kronecker delta.

Note that in the finite-frequency regime the resonant driving frequency for a tilted double well with the energy difference U is not exactly $\hbar\omega = U$; it is given by the energy gap, $\hbar\omega = \sqrt{U^2 + 4J^2} \neq U$. In the high-frequency limit $U \gg J$, however, $\hbar\omega \simeq U$.

The lowest orders of the Floquet Hamiltonian can now be calculated with the components $\hat{\mathcal{H}}^{(k)}$ from Eq. (A.4). They are

$$\hat{H}_\mathrm{F} = \hat{\mathcal{H}}^{(0)} + \frac{1}{\hbar\omega} \sum_{k>0} \frac{1}{k} \left[\hat{\mathcal{H}}^{(+k)}, \hat{\mathcal{H}}^{(-k)} \right] + \mathcal{O}\left(\frac{1}{\omega^2}\right). \tag{A.5}$$

A.2. Floquet model in the infinite-frequency limit

In the infinite frequency limit $U/J \to \infty$, resonant driving is at $\hbar\omega \simeq U$ and the diagonal contributions in Eq. (A.4) vanish. Furthermore, the Floquet Hamiltonian (A.5) can be restricted to the lowest order

$$\begin{aligned}\hat{H}^0_\mathrm{F} = &- J \big\{ \mathcal{J}_1(\chi) \left|\mathrm{RL}\right\rangle \left\langle\mathrm{LL}\right| \mathrm{e}^{\mathrm{i}(\pi+\phi)} + \mathcal{J}_1(\chi) \left|\mathrm{RR}\right\rangle \left\langle\mathrm{LR}\right| \mathrm{e}^{-\mathrm{i}\phi} \\ &+ \mathcal{J}_0(\chi) \left|\mathrm{RR}\right\rangle \left\langle\mathrm{RL}\right| + \mathcal{J}_2(\chi) \left|\mathrm{LR}\right\rangle \left\langle\mathrm{LL}\right| \mathrm{e}^{2\phi} + \mathrm{h.c.} \big\}.\end{aligned} \tag{A.6}$$

In the following, $\hat{H}^0_\mathrm{F}$ will be referred to as zeroth-order Floquet Hamiltonian. Here, the a-particle tunneling is described by $\left|\mathrm{RL}\right\rangle \left\langle\mathrm{LL}\right|$ and $\left|\mathrm{RR}\right\rangle \left\langle\mathrm{LR}\right|$ and the f-particle tunneling by $\left|\mathrm{RR}\right\rangle \left\langle\mathrm{RL}\right|$ and $\left|\mathrm{LR}\right\rangle \left\langle\mathrm{LL}\right|$. Note that the tunnel coupling for the a-particles is renormalized by the first-order Bessel function of the first kind $\mathcal{J}_1(\chi)$ and the f-particle tunneling by the zeroth- $\mathcal{J}_0(\chi)$ and second-order Bessel functions $\mathcal{J}_2(\chi)$ depending on the a-particle's position. Furthermore, for $\phi = 0$, tunneling of the a-particle receives a phase of either zero or π depending on the f-particle's position while tunneling of the f-particle is real-valued.

A.3. Floquet model including first-order correction for finite-frequency drive

In a next step, the first-order terms of the Floquet expansion are calculated. To simplify the analysis, only stroboscopic time points $n\,T$ with $T = 2\pi/\omega$ and $n \in \mathbb{N}$ are considered and the driving phase is set to $\phi = 0$. However, a small deviation from the ideal driving frequency is taken into account. Following the definition in Eq. (A.5) and using the Fourier components Eq. (A.4), the first-order term of the Floquet expansion can be calculated to

$$\begin{aligned}
\hat{H}_{\mathrm{F}} =& \hat{\mathcal{H}}^{(0)} + \frac{J^2}{\hbar\omega}\sum_{k>0}\frac{1}{k}\Big\{ |\mathrm{RL}\rangle\,\langle\mathrm{LR}|\,\big[\mathcal{J}_{-k-1}(\chi)\,\mathcal{J}_{-k-2}(\chi) + \mathcal{J}_{k}(\chi)\,\mathcal{J}_{k+1}(\chi) \\
&\qquad\qquad - \mathcal{J}_{k-1}(\chi)\,\mathcal{J}_{k-2}(\chi) - \mathcal{J}_{-k}(\chi)\,\mathcal{J}_{-k+1}(\chi)\big] + \text{h.c.} \\
&\qquad + |\mathrm{RR}\rangle\,\langle\mathrm{LL}|\,\big[\mathcal{J}_{-k+1}(\chi)\,\mathcal{J}_{k-2}(\chi) + \mathcal{J}_{-k}(\chi)\,\mathcal{J}_{k-1}(\chi) \\
&\qquad\qquad - \mathcal{J}_{k+1}(\chi)\,\mathcal{J}_{-k-2}(\chi) - \mathcal{J}_{+k}(\chi)\,\mathcal{J}_{-k-1}(\chi)\big] + \text{h.c.}\Big\} \\
&+ \frac{J^2}{\hbar\omega}\sum_{k>0}\frac{1}{k}\Big\{ \big(|\mathrm{LL}\rangle\,\langle\mathrm{LL}| - |\mathrm{LR}\rangle\,\langle\mathrm{LR}|\big)\big[\mathcal{J}_{k-1}(\chi)^2 + \mathcal{J}_{k-2}(\chi)^2 \\
&\qquad\qquad - \mathcal{J}_{-k-1}(\chi)^2 - \mathcal{J}_{-k-2}(\chi)^2\big] \\
&\qquad + \big(|\mathrm{RR}\rangle\,\langle\mathrm{RR}| - |\mathrm{RL}\rangle\,\langle\mathrm{RL}|\big)\big[\mathcal{J}_{-k+1}(\chi)^2 + \mathcal{J}_{-k}(\chi)^2 \\
&\qquad\qquad - \mathcal{J}_{k+1}(\chi)^2 - \mathcal{J}_{k}(\chi)^2\big]\Big\} \\
=& \hat{\mathcal{H}}^{(0)} + \hat{H}^{(1)}_{\mathrm{pair-hopping}} + \hat{H}^{(1)}_{\mathrm{detuning}}.
\end{aligned} \tag{A.7}$$

The resulting first-order term has two contributions: a pair-tunneling term $\hat{H}^{(1)}_{\mathrm{pair-hopping}}$, where both particles tunnel, and a detuning term $\hat{H}^{(1)}_{\mathrm{detuning}}$ that describes the deviation from the exact resonance condition. Note that the diagonal terms in $\hat{\mathcal{H}}^0$ become nonzero.

For a calculation of the time evolution with higher-order terms, the time evolution operator $\hat{U}$ gets modified. The modification depends in general on the transformation $\hat{R}$ and the kick operator $\hat{K}$ [69]. However, if the time-evolution is only evaluated at stroboscopic times the time-evolution operator simplifies to

$$\hat{U}(0 \to nT) = e^{-\mathrm{i}\hat{K}} e^{-\mathrm{i}\hat{H}_{\mathrm{F}} nT/\hbar} e^{\mathrm{i}\hat{K}} \tag{A.8}$$

and only depends on the stroboscopic kick operator

$$\hat{K} = \frac{1}{\mathrm{i}\hbar\omega} \sum_{k>0} \frac{1}{k} \left(\hat{\mathcal{H}}^{(+k)} - \hat{\mathcal{H}}^{(-k)} \right) + \mathcal{O}\left(\frac{1}{\omega^2} \right) . \tag{A.9}$$

B. Spin currents

B.1. Derivation of the coefficients for the temporary wave function

Following reference [89], a derivation of the time-dependent wave function $|\psi(t)\rangle$ according to an adiabatically varying Hamiltonian is presented. Assume therefore that the Hamiltonian $\mathcal{H}[\Delta(t)]$ depends on a parameter Δ, which varies slowly in time. It is constructive to expand $|\psi(t)\rangle$ in the instantaneous eigenstates $|n(t)\rangle$ of the Hamiltonian $\mathcal{H}$

$$|\psi(t)\rangle = \sum_n \exp\left(-\frac{\mathrm{i}}{\hbar}\int_{t_0}^{t} \mathrm{d}t' E_n(t')\right) \alpha_n(t)\, |n(t)\rangle\,. \tag{B.1}$$

The wave function $|\psi(t)\rangle$ has to fulfill the time-dependent Schrödinger equation. This leads to a set of coupled differential equations

$$\partial_t \alpha_n(t) = -\sum_m \alpha_m(t)\, \langle n(t)|\, \partial_t\, |m(t)\rangle \exp\left(-\frac{\mathrm{i}}{\hbar}\int_{t_0}^{t} \mathrm{d}t' \left[E_m(t') - E_n(t')\right]\right) \tag{B.2}$$

for the α-coefficients of the expansion Eq. (B.1). A suitable phase choice can be made by enforcing the parallel transport condition $\langle n(t)|\, \partial_t\, |n(t)\rangle = 0$. Starting initially from the eigenstate $|n\rangle$, which means for the coefficients $\alpha_n(0) = 1$, the equations can be simplified by considering only terms in first order of the rate of change. This assumption effectively neglects back coupling $\alpha_{m\neq n}(t) = 0$ for all times. Thus, $\partial_t \alpha_n(t) = 0$, but for $m \neq n$, the coefficients can be finite

$$\partial_t \alpha_m(t) = -\,\langle m(t)|\, \partial_t\, |n(t)\rangle \exp\left(-\frac{\mathrm{i}}{\hbar}\int_{t_0}^{t} \mathrm{d}t' \left[E_n(t') - E_m(t')\right]\right). \tag{B.3}$$

Integrating this equation by parts is possible since the exponential factor oscillates fast and the coefficients vary slowly. The result is

$$\alpha_m(t) = -\mathrm{i}\hbar \frac{\langle m(t)|\, \partial_t\, |n(t)\rangle}{E_n - E_m} \exp\left(-\frac{\mathrm{i}}{\hbar}\int_{t_0}^{t} \mathrm{d}t' \left[E_n(t') - E_m(t')\right]\right). \tag{B.4}$$

Together with the coefficients in Eq. (B.1), the time-dependent wave function is approximately

$$|\psi(t)\rangle = \left\{ |n\rangle - \mathrm{i}\hbar \sum_{m\neq n} |m\rangle \frac{\langle m|\, \partial_t \,|n\rangle}{E_n - E_m} \right\} \exp\left(-\frac{\mathrm{i}}{\hbar} \int_{t_0}^{t} \mathrm{d}t' E_n(t') \right). \tag{B.5}$$

In the final step, the unimportant global phase factor is dropped and the following short form introduced

$$|\psi\rangle = |n\rangle + \mathrm{i} \sum_{m\neq n} a_m \,|m\rangle \tag{B.6}$$

with the a-coefficients

$$a_m = -\frac{\langle m|\, \hbar\partial_t \,|n\rangle}{E_n - E_m} = -\dot{\Delta} \frac{\langle m|\, \hbar\partial_\Delta \,|n\rangle}{E_n - E_m}. \tag{B.7}$$

B.2. Operator expectation value after stop of the adiabatic evolution

In the context of the spin-current measurement, the time-dependent evolution of the expectation value of the spin-imbalance operator needs to be analyzed after the non-adiabatic stop of the Hamiltonian's variation. To this end, the expectation value of a general operator $\mathcal{M}$ is considered with respect to the time-dependent wave function Eq. (B.6). Note that after stopping the time dependence of the Hamiltonian, the instantaneous eigenstates stay the same. In the static Hamiltonian they evolve according to

$$|n_t\rangle\,(t) = \mathrm{e}^{-\frac{\mathrm{i}}{\hbar} E_n t}\, |n\rangle \tag{B.8}$$

with E_n the eigenenergy of the the eigenstate $|n\rangle$. The expectation value of the operator $\mathcal{M}$ is then

$$\begin{aligned} \langle \mathcal{M}(t) \rangle &= \left(\langle n|\, e^{+\frac{\mathrm{i}}{\hbar} E_n t} - \mathrm{i} \sum_{m\neq n} a_m \,\langle m|\, e^{+\frac{\mathrm{i}}{\hbar} E_m t} \right) \mathcal{M} \left(e^{-\frac{\mathrm{i}}{\hbar} E_n t}\, |n\rangle + \mathrm{i} \sum_{m'\neq n} a_{m'} e^{-\frac{\mathrm{i}}{\hbar} E_m t}\, |m'\rangle \right) \\ &= \langle n|\, \mathcal{M} \,|n\rangle + \sum_{m,m'\neq n} a_m a_{m'} e^{+\frac{\mathrm{i}}{\hbar}(E_m - E_{m'})t}\, \langle m|\, \mathcal{M} \,|m'\rangle \\ &\quad + \mathrm{i} \left(\sum_{m\neq n} a_m e^{+\frac{\mathrm{i}}{\hbar}(E_n - E_m)t}\, \langle n|\, \mathcal{M} \,|m\rangle - \sum_{m\neq n} a_m e^{-\frac{\mathrm{i}}{\hbar}(E_n - E_m)t}\, \langle m|\, \mathcal{M} \,|n\rangle \right). \end{aligned} \tag{B.9}$$

To simplify the result, only the first two eigenstates are considered. The initial state is $|n\rangle \equiv |1\rangle$ and the first excited state is $|2\rangle$. Both eigenstates are chosen real. Furthermore, only operators with real matrix elements $\langle 1|\, \mathcal{M} \,|2\rangle \in \mathbb{R}$ are considered, e.g. the spin-imbalance operator. The the result reduces to

$$\langle \mathcal{M}(t) \rangle = 2\, a_2 \,\langle 1|\, \mathcal{M} \,|2\rangle \sin\left(\frac{E_2 - E_1}{\hbar} t \right) = A_2^{(\mathcal{M})} \sin\left(\frac{E_2 - E_1}{\hbar} t \right). \tag{B.10}$$

Acronyms

BEC Bose-Einstein condensate.

cQED compact quantum electrodynamics.

DMRG density matrix renormalization group.

LGT lattice gauge theory.

QCD quantum chromodynamics.
QH quantum Hall.
QHE quantum Hall effect.
QSH system quantum spin Hall system.
QSHE quantum spin Hall effect.

RVB resonating valence-bond.

SCC spin-changing collisions.

TI topological insulator.
TRS time-reversal symmetry.

Bibliography

[1] I. Bloch, J. Dalibard, and S. Nascimbène. “Quantum simulations with ultracold quantum gases”. *Nat. Phys.* 8.4 (2012), pp. 267–276 (cit. on pp. 1, 7).

[2] C. Gross and I. Bloch. “Quantum simulations with ultracold atoms in optical lattices”. *Science* 357.6355 (2017), pp. 995–1001 (cit. on pp. 1, 7).

[3] A. N. Wenz, G. Zürn, S. Murmann, I. Brouzos, T. Lompe, and S. Jochim. “From Few to Many: Observing the Formation of a Fermi Sea One Atom at a Time”. *Science* 342.6157 (2013), pp. 457–460 (cit. on p. 1).

[4] S. Trotzky, P. Cheinet, S. Fölling, M. Feld, U. Schnorrberger, A. M. Rey, A. Polkovnikov, E. A. Demler, M. D. Lukin, and I. Bloch. “Time-Resolved Observation and Control of Superexchange Interactions with Ultracold Atoms in Optical Lattices”. *Science* 319.5861 (2008), pp. 295–299 (cit. on pp. 1, 37, 48, 82, 90, 98, 100, 104).

[5] M. Anderlini, P. J. Lee, B. L. Brown, J. Sebby-Strabley, W. D. Phillips, and J. V. Porto. “Controlled exchange interaction between pairs of neutral atoms in an optical lattice”. *Nature* 448.7152 (2007), pp. 452–456 (cit. on pp. 1, 100).

[6] S. Fölling, S. Trotzky, P. Cheinet, M. Feld, R. Saers, A. Widera, T. Müller, and I. Bloch. “Direct observation of second-order atom tunnelling”. *Nature* 448.7157 (2007), pp. 1029–1032 (cit. on pp. 1, 36–38, 48).

[7] A. M. Kaufman, B. J. Lester, C. M. Reynolds, M. L. Wall, M. Foss-Feig, K. R. A. Hazzard, A. M. Rey, and C. A. Regal. “Two-particle quantum interference in tunnel-coupled optical tweezers”. *Science* 345.6194 (2014), pp. 306–309 (cit. on p. 1).

[8] S. Murmann, A. Bergschneider, V. M. Klinkhamer, G. Zürn, T. Lompe, and S. Jochim. “Two Fermions in a Double Well: Exploring a Fundamental Building Block of the Hubbard Model”. *Phys. Rev. Lett.* 114 (8 2015), p. 080402 (cit. on p. 1).

[9] A. Kaufman and C. Regal. “Electron Model Captured by Atom Pair”. *Physics* 8 (2015), p. 16 (cit. on p. 1).

[10] S. Nascimbène, Y.-A. Chen, M. Atala, M. Aidelsburger, S. Trotzky, B. Paredes, and I. Bloch. “Experimental Realization of Plaquette Resonating Valence-Bond States with Ultracold Atoms in Optical Superlattices”. *Phys. Rev. Lett.* 108 (20 2012), p. 205301 (cit. on p. 1).

[11] H.-N. Dai, B. Yang, A. Reingruber, H. Sun, X.-F. Xu, Y.-A. Chen, Z.-S. Yuan, and J.-W. Pan. "Four-body ring-exchange interactions and anyonic statistics within a minimal toric-code Hamiltonian". *Nat. Phys.* 13.12 (2017), p. 1195 (cit. on pp. 2, 71).

[12] R. B. Laughlin. "Anomalous Quantum Hall Effect: An Incompressible Quantum Fluid with Fractionally Charged Excitations". *Phys. Rev. Lett.* 50 (18 1983), pp. 1395–1398 (cit. on p. 2).

[13] B. Paredes and I. Bloch. "Minimum instances of topological matter in an optical plaquette". *Phys. Rev. A* 77 (2 2008), p. 023603 (cit. on p. 2).

[14] M. Aidelsburger, M. Atala, S. Nascimbène, S. Trotzky, Y.-A. Chen, and I. Bloch. "Experimental Realization of Strong Effective Magnetic Fields in an Optical Lattice". *Phys. Rev. Lett.* 107.25 (2011), p. 255301 (cit. on pp. 2, 7).

[15] P. Schauß, M. Cheneau, M. Endres, T. Fukuhara, S. Hild, A. Omran, T. Pohl, C. Gross, S. Kuhr, and I. Bloch. "Observation of spatially ordered structures in a two-dimensional Rydberg gas". *Nature* 491.7422 (2012), pp. 87–91 (cit. on p. 2).

[16] J. Li, M.-T. Zhou, B. Jing, X.-J. Wang, S.-J. Yang, X. Jiang, K. Mølmer, X.-H. Bao, and J.-W. Pan. "Hong-Ou-Mandel Interference between Two Deterministic Collective Excitations in an Atomic Ensemble". *Phys. Rev. Lett.* 117 (18 2016), p. 180501 (cit. on p. 2).

[17] C. Schweizer, F. Grusdt, M. Berngruber, L. Barbiero, E. Demler, N. Goldman, I. Bloch, and M. Aidelsburger. "Floquet approach to $\mathbb{Z}_2$ lattice gauge theories with ultracold atoms in optical lattices". *Nat. Phys.* (2019) (cit. on pp. 2, 7, 15, 65, 68, 111).

[18] C. Schweizer, M. Lohse, R. Citro, and I. Bloch. "Spin Pumping and Measurement of Spin Currents in Optical Superlattices". *Phys. Rev. Lett.* 117 (17 2016), p. 170405 (cit. on p. 2).

[19] M. Levin and X.-G. Wen. "Colloquium: Photons and electrons as emergent phenomena". *Rev. Mod. Phys.* 77.3 (2005), pp. 871–879 (cit. on pp. 5, 6).

[20] A. Salam. "Gauge unification of fundamental forces". *Rev. Mod. Phys.* 52 (3 1980), pp. 525–538 (cit. on p. 5).

[21] S. Aoki et al. "Review of lattice results concerning low-energy particle physics". *Eur. Phys. J. C* 77.2 (2017), p. 112 (cit. on p. 5).

[22] F. J. Wegner. "Duality in Generalized Ising Models and Phase Transitions without Local Order Parameters". *J. Math. Phys.* 12.10 (1971), pp. 2259–2272 (cit. on pp. 6, 16, 20).

[23] M. E. Peskin. "Mandelstam-'t Hooft duality in Abelian lattice models". *Ann. Phys.* 113.1 (1978), pp. 122–152 (cit. on p. 6).

[24] C. Dasgupta and B. I. Halperin. "Phase Transition in a Lattice Model of Superconductivity". *Phys. Rev. Lett.* 47 (21 1981), pp. 1556–1560 (cit. on p. 6).

[25] M. P. A. Fisher and D. H. Lee. "Correspondence between two-dimensional bosons and a bulk superconductor in a magnetic field". *Phys. Rev. B* 39 (4 1989), pp. 2756–2759 (cit. on p. 6).

[26] N. Read and S. Sachdev. "Valence-bond and spin-Peierls ground states of low-dimensional quantum antiferromagnets". *Phys. Rev. Lett.* 62 (14 1989), pp. 1694–1697 (cit. on p. 6).

[27] N. Read and S. Sachdev. "Some features of the phase diagram of the square lattice SU(N) antiferromagnet". *Nucl. Phys. B* 316.3 (1989), pp. 609–640 (cit. on p. 6).

[28] N. Read and S. Sachdev. "Spin-Peierls, valence-bond solid, and Néel ground states of low-dimensional quantum antiferromagnets". *Phys. Rev. B* 42 (7 1990), pp. 4568–4589 (cit. on p. 6).

[29] S. A. Kivelson, D. S. Rokhsar, and J. P. Sethna. "Topology of the resonating valence-bond state: Solitons and high-T_c superconductivity". *Phys. Rev. B* 35 (16 1987), pp. 8865–8868 (cit. on p. 6).

[30] R. Moessner, S. L. Sondhi, and E. Fradkin. "Short-ranged resonating valence bond physics, quantum dimer models, and Ising gauge theories". *Phys. Rev. B* 65 (2 2001), p. 024504 (cit. on p. 6).

[31] G. Baskaran and P. W. Anderson. "Gauge theory of high-temperature superconductors and strongly correlated Fermi systems". *Phys. Rev. B* 37 (1 1988), pp. 580–583 (cit. on p. 6).

[32] I. Affleck and J. B. Marston. "Large-n limit of the Heisenberg-Hubbard model: Implications for high-T_c superconductors". *Phys. Rev. B* 37 (7 1988), pp. 3774–3777 (cit. on p. 6).

[33] I. Affleck, Z. Zou, T. Hsu, and P. W. Anderson. "SU(2) gauge symmetry of the large-U limit of the Hubbard model". *Phys. Rev. B* 38 (1 1988), pp. 745–747 (cit. on p. 6).

[34] P. A. Lee, N. Nagaosa, and X.-G. Wen. "Doping a Mott Insulator: Physics of High Temperature Superconductivity". *Rev. Mod. Phys.* 78.1 (2006), pp. 17–85 (cit. on pp. 6, 19).

[35] T. Senthil and M. P. A. Fisher. "$\mathbb{Z}_2$ gauge theory of electron fractionalization in strongly correlated systems". *Phys. Rev. B* 62 (12 2000), pp. 7850–7881 (cit. on pp. 6, 19).

[36] L. Balents. "Spin liquids in frustrated magnets". *Nature* 464.7286 (2010), p. 199 (cit. on pp. 6, 19).

[37] N. Read and S. Sachdev. "Large-N expansion for frustrated quantum antiferromagnets". *Phys. Rev. Lett.* 66 (13 1991), pp. 1773–1776 (cit. on pp. 6, 19).

[38] R. A. Jalabert and S. Sachdev. "Spontaneous alignment of frustrated bonds in an anisotropic, three-dimensional Ising model". *Phys. Rev. B* 44 (2 1991), pp. 686–690 (cit. on p. 6).

[39] M. Hermele, M. P. A. Fisher, and L. Balents. "Pyrochlore photons: The $U(1)$ spin liquid in a $S = \frac{1}{2}$ three-dimensional frustrated magnet". *Phys. Rev. B* 69 (6 2004), p. 064404 (cit. on p. 6).

[40] X. G. Wen. "Non-Abelian statistics in the fractional quantum Hall states". *Phys. Rev. Lett.* 66 (6 1991), pp. 802–805 (cit. on pp. 6, 19).

[41] X.-G. Wen. "Projective construction of non-Abelian quantum Hall liquids". *Phys. Rev. B* 60 (12 1999), pp. 8827–8838 (cit. on p. 6).

[42] I. Ichinose and T. Matsui. "Lattice gauge theory for condensed matter physics: Ferromagnetic superconductivity as its example". *Mod. Phys. Lett. B* 28.22 (2014), p. 1430012 (cit. on p. 6).

[43] J. K. Jain. *Composite Fermions*. Cambridge University Press, 2007 (cit. on p. 6).

[44] X.-G. Wen. *Quantum Field Theory of Many-body Systems*. Oxford University Press, 2004 (cit. on pp. 6, 14, 19).

[45] N. Metropolis, A. W. Rosenbluth, M. N. Rosenbluth, A. H. Teller, and E. Teller. "Equation of state calculations by fast computing machines". *J. Chem. Phys.* 21.6 (1953), pp. 1087–1092 (cit. on p. 6).

[46] M. Troyer and U.-J. Wiese. "Computational Complexity and Fundamental Limitations to Fermionic Quantum Monte Carlo Simulations". *Phys. Rev. Lett.* 94.17 (2005), p. 170201 (cit. on p. 6).

[47] M. G. Alford, A. Schmitt, K. Rajagopal, and T. Schäfer. "Color superconductivity in dense quark matter". *Rev. Mod. Phys.* 80.4 (2008), pp. 1455–1515 (cit. on p. 6).

[48] S. Gazit, M. Randeria, and A. Vishwanath. "Emergent Dirac fermions and broken symmetries in confined and deconfined phases of $\mathbb{Z}_2$ gauge theories". *Nat. Phys.* 13.5 (2017), pp. 484–490 (cit. on pp. 6, 20, 21).

[49] M.-C. Bañuls, K. Cichy, J. I. Cirac, K. Jansen, S. Kühn, and H. Saito. "Towards overcoming the Monte Carlo sign problem with tensor networks". *EPJ Web Conf.* 137 (2017), p. 04001 (cit. on p. 6).

[50] M. Dalmonte and S. Montangero. "Lattice gauge theory simulations in the quantum information era". *Contemp. Phys.* 57.3 (2016), pp. 388–412 (cit. on pp. 6, 15).

[51] R. Blatt and C. F. Roos. "Quantum simulations with trapped ions". *Nat. Phys.* 8.4 (2012), pp. 277–284 (cit. on p. 7).

[52] A. Aspuru-Guzik and P. Walther. "Photonic quantum simulators". *Nat. Phys.* 8.4 (2012), p. 285 (cit. on p. 7).

[53] M. Saffman. "Quantum computing with atomic qubits and Rydberg interactions: progress and challenges". *J. Phys. B.-At. Mol. Opt.* 49.20 (2016), p. 202001 (cit. on p. 7).

[54] S. Schmidt and J. Koch. "Circuit QED lattices: Towards quantum simulation with superconducting circuits". *Ann. Phys. (Berlin)* 525.6 (2013), pp. 395–412 (cit. on p. 7).

[55] G. Romero, E. Solano, and L. Lamata. "Quantum Simulations with Circuit Quantum Electrodynamics". 2017, pp. 153–180 (cit. on p. 7).

[56] E. Zohar, J. I. Cirac, and B. Reznik. "Quantum simulations of lattice gauge theories using ultracold atoms in optical lattices". *Rep. Prog. Phys.* 79.1 (2015), p. 014401 (cit. on pp. 7, 16–19, 25).

[57] M. Mathur and T. P. Sreeraj. "Lattice gauge theories and spin models". *Phys. Rev. D* 94.8 (2016), p. 085029 (cit. on p. 7).

[58] M. Falcioni, E. Marinari, M. L. Paciello, G. Parisi, and B. Taglienti. "Phase transition analysis in $\mathbb{Z}_2$ and $U(1)$ lattice gauge theories". *Phys. Lett. B* 105.1 (1981), pp. 51–54 (cit. on p. 7).

[59] E. Zohar, A. Farace, B. Reznik, and J. I. Cirac. "Digital Quantum Simulation of $\mathbb{Z}_2$ Lattice Gauge Theories with Dynamical Fermionic Matter". *Phys. Rev. Lett.* 118.7 (2017), p. 070501 (cit. on p. 7).

[60] D. Horn, M. Weinstein, and S. Yankielowicz. "Hamiltonian approach to $Z(N)$ lattice gauge theories". *Phys. Rev. D* 19 (12 1979), pp. 3715–3731 (cit. on pp. 7, 19).

[61] R. Shankar. *Quantum Field Theory and Condensed Matter: An Introduction*. Cambridge University Press, 2017 (cit. on p. 7).

[62] L. Barbiero, C. Schweizer, M. Aidelsburger, E. Demler, N. Goldman, and F. Grusdt. "Coupling ultracold matter to dynamical gauge fields in optical lattices: From flux-attachment to $\mathbb{Z}_2$ lattice gauge theories". *arXiv* 1810.02777 (2018) (cit. on pp. 7, 15, 28, 65, 68, 69, 71, 72).

[63] A. R. Kolovsky. "Creating artificial magnetic fields for cold atoms by photon-assisted tunneling". *Europhys. Lett.* 93.2 (2011), p. 20003 (cit. on pp. 7, 13).

[64] A. Bermudez, T. Schaetz, and D. Porras. "Photon-assisted-tunneling toolbox for quantum simulations in ion traps". *New J. Phys.* 14.5 (2012), p. 053049 (cit. on p. 7).

[65] M. Aidelsburger, M. Atala, M. Lohse, J. T. Barreiro, B. Paredes, and I. Bloch. "Realization of the Hofstadter Hamiltonian with Ultracold Atoms in Optical Lattices". *Phys. Rev. Lett.* 111 (18 2013), p. 185301 (cit. on pp. 7, 13).

[66] H. Miyake, G. A. Siviloglou, C. J. Kennedy, W. C. Burton, and W. Ketterle. "Realizing the Harper Hamiltonian with Laser-Assisted Tunneling in Optical Lattices". *Phys. Rev. Lett.* 111.18 (2013), p. 185302 (cit. on pp. 7, 13).

[67] C. V. Parker, L.-C. Ha, and C. Chin. "Direct observation of effective ferromagnetic domains of cold atoms in a shaken optical lattice". *Nat. Phys.* 9.12 (2013), pp. 769–774 (cit. on p. 7).

[68] M. Atala, M. Aidelsburger, M. Lohse, J. T. Barreiro, B. Paredes, and I. Bloch. "Observation of chiral currents with ultracold atoms in bosonic ladders". *Nat. Phys.* 10.7 (2014), pp. 13–15 (cit. on pp. 7, 92).

[69] N. Goldman, J. Dalibard, M. Aidelsburger, and N. R. Cooper. "Periodically driven quantum matter: The case of resonant modulations". *Phys. Rev. A* 91 (3 2015), p. 033632 (cit. on pp. 7, 13, 28, 29, 69, 111, 113).

[70] M. E. Tai, A. Lukin, M. Rispoli, R. Schittko, T. Menke, D. Borgnia, P. M. Preiss, F. Grusdt, A. M. Kaufman, and M. Greiner. "Microscopy of the interacting Harper–Hofstadter model in the few-body limit". *Nature* 546 (2017), pp. 519–523 (cit. on pp. 7, 14).

[71] M. Tarnowski, F. N. Ünal, N. Fläschner, B. S. Rem, A. Eckardt, K. Sengstock, and C. Weitenberg. "Measuring topology from dynamics by obtaining the Chern number from a linking number". *Nat. Commun.* 10 (2019), p. 1728 (cit. on p. 7).

[72] R. Ma, M. E. Tai, P. M. Preiss, W. S. Bakr, J. Simon, and M. Greiner. "Photon-Assisted Tunneling in a Biased Strongly Correlated Bose Gas". *Phys. Rev. Lett.* 107.9 (2011), p. 095301 (cit. on pp. 7, 28).

[73] Y.-A. Chen, S. Nascimbène, M. Aidelsburger, M. Atala, S. Trotzky, and I. Bloch. "Controlling Correlated Tunneling and Superexchange Interactions with ac-Driven Optical Lattices". *Phys. Rev. Lett.* 107 (21 2011), p. 210405 (cit. on pp. 7, 28).

[74] F. Meinert, M. J. Mark, K. Lauber, A. J. Daley, and H.-C. Nägerl. "Floquet Engineering of Correlated Tunneling in the Bose-Hubbard Model with Ultracold Atoms". *Phys. Rev. Lett.* 116 (20 2016), p. 205301 (cit. on pp. 7, 28, 38).

[75] C. Sträter, S. C. L. Srivastava, and A. Eckardt. "Floquet Realization and Signatures of One-Dimensional Anyons in an Optical Lattice". *Phys. Rev. Lett.* 117.20 (2016), p. 162 (cit. on pp. 7, 28).

[76] R. Desbuquois, M. Messer, F. Görg, K. Sandholzer, G. Jotzu, and T. Esslinger. "Controlling the Floquet state population and observing micromotion in a periodically driven two-body quantum system". *Phys. Rev. A* 96.5 (2017), p. 053602 (cit. on pp. 7, 28).

[77] F. Görg, M. Messer, K. Sandholzer, G. Jotzu, R. Desbuquois, and T. Esslinger. "Enhancement and sign change of magnetic correlations in a driven quantum many-body system". *Nature* 553.7689 (2018), pp. 481–485 (cit. on pp. 7, 28).

[78] F. Görg, K. Sandholzer, J. Minguzzi, R. Desbuquois, M. Messer, and T. Esslinger. "Realization of density-dependent Peierls phases to engineer quantized gauge fields coupled to ultracold matter". *Nature Physics* (2019), pp. 1–7 (cit. on pp. 7, 15, 28, 69).

[79] J. C. Maxwell. *The scientific papers of James Clerk Maxwell*. Ed. by W. D. Nieven. Cambridge University Press, 1890 (cit. on p. 8).

[80] C. N. Yang. "The conceptual origins of Maxwell's equations and gauge theory". *Phys. Today* 67.11 (2014), p. 45 (cit. on p. 8).

[81] L. O'Raifeartaigh and N. Straumann. "Gauge theory: Historical origins and some modern developments". *Rev. Mod. Phys.* 72.1 (2000), p. 1 (cit. on p. 8).

[82] R. P. Feynman, R. B. Leighton, and M. Sands. *The Feynman lectures on physics, Vol. II: Mainly Electromagnetism and Matter*. Vol. 2. Basic books, 2011 (cit. on pp. 8, 9).

[83] Y. Aharonov and D. Bohm. "Significance of Electromagnetic Potentials in the Quantum Theory". *Phys. Rev.* 115 (3 1959), pp. 485–491 (cit. on p. 9).

[84] W. C. Chew. "Electromagnetic theory on a lattice". *J. Appl. Phys.* 75.10 (1994), pp. 4843–4850 (cit. on p. 9).

[85] M. Aidelsburger, S. Nascimbène, and N. Goldman. "Artificial gauge fields in materials and engineered systems". *C. R. Phys.* 19.6 (2018), pp. 394–432 (cit. on pp. 10, 11, 13).

[86] P. G. Harper. "Single Band Motion of Conduction Electrons in a Uniform Magnetic Field". *Proc. Phys. Soc. A* 68.10 (1955), pp. 874–878 (cit. on pp. 11, 79).

[87] M. Y. Azbel. "Energy spectrum of a conduction electron in a magnetic field". *JETP* 19.3 (1964), pp. 634–645 (cit. on p. 11).

[88] D. R. Hofstadter. "Energy levels and wave functions of Bloch electrons in rational and irrational magnetic fields". *Phys. Rev. B* 14 (6 1976), pp. 2239–2249 (cit. on pp. 11, 79).

[89] D. Xiao, M.-C. Chang, and Q. Niu. "Berry phase effects on electronic properties". *Rev. Mod. Phys.* 82 (3 2010), pp. 1959–2007 (cit. on pp. 11, 12, 75, 92, 115).

[90] T. Kato. "On the Adiabatic Theorem of Quantum Mechanics". *J. Phys. Soc. Japan* 5.6 (1950), pp. 435–439 (cit. on pp. 11, 77).

[91] M. V. Berry. "Quantal phase factors accompanying adiabatic changes". *Proc. R. Soc. A* 392.1802 (1984), pp. 45–57 (cit. on pp. 12, 75).

[92] D. J. Thouless, M. Kohmoto, M. P. Nightingale, and M. den Nijs. "Quantized Hall Conductance in a Two-Dimensional Periodic Potential". *Phys. Rev. Lett.* 49 (6 1982), pp. 405–408 (cit. on pp. 12, 76).

[93] B. Riemann. *Theorie der Abel'schen Functionen*. Georg Reimer Berlin, 1857 (cit. on p. 12).

[94] F. E. P. Hirzebruch and M. Kreck. *On the Concept of Genus in Topology and Complex Analysis*. 2009 (cit. on p. 12).

[95] Q. Niu and D. J. Thouless. "Quantised adiabatic charge transport in the presence of substrate disorder and many-body interaction". *J. Phys. A* 17.12 (1984), p. 2453 (cit. on pp. 13, 77, 78).

[96] Q. Niu, D. J. Thouless, and Y.-S. Wu. "Quantized Hall conductance as a topological invariant". *Phys. Rev. B* 31 (6 1985), pp. 3372–3377 (cit. on p. 13).

[97] J. E. Avron and R. Seiler. "Quantization of the Hall Conductance for General, Multiparticle Schrödinger Hamiltonians". *Phys. Rev. Lett.* 54 (4 1985), pp. 259–262 (cit. on p. 13).

[98] D. Jaksch and P. Zoller. "Creation of effective magnetic fields in optical lattices: The Hofstadter butterfly for cold neutral atoms". *New J. Phys.* 5 (2003), pp. 56–56 (cit. on p. 13).

[99] M. Bukov, L. D'Alessio, and A. Polkovnikov. "Universal high-frequency behavior of periodically driven systems: From dynamical stabilization to Floquet engineering". *Adv. Phys.* 64.2 (2015), pp. 139–226 (cit. on pp. 13, 28, 72).

[100] T. Oka and S. Kitamura. "Floquet Engineering of Quantum Materials". *Annu. Rev. Condens. Matter Phys.* 10.1 (2019), pp. 387–408 (cit. on p. 13).

[101] N. Goldman and J. Dalibard. "Periodically Driven Quantum Systems: Effective Hamiltonians and Engineered Gauge Fields". *Phys. Rev. X* 4 (3 2014), p. 031027 (cit. on pp. 13, 28, 29, 49, 72, 111).

[102] N. Goldman, G. Juzeliūnas, P. Öhberg, and I. B. Spielman. "Light-induced gauge fields for ultracold atoms". *Rep. Prog. Phys.* 77.12 (2014), p. 126401 (cit. on p. 13).

[103] K. v. Klitzing, G. Dorda, and M. Pepper. "New Method for High-Accuracy Determination of the Fine-Structure Constant Based on Quantized Hall Resistance". *Phys. Rev. Lett.* 45 (6 1980), pp. 494–497 (cit. on pp. 14, 76).

[104] D. C. Tsui, H. L. Stormer, and A. C. Gossard. "Two-Dimensional Magnetotransport in the Extreme Quantum Limit". *Phys. Rev. Lett.* 48 (22 1982), pp. 1559–1562 (cit. on p. 14).

[105] M. Aidelsburger, M. Lohse, C. Schweizer, M. Atala, J. T. Barreiro, S. Nascimbène, N. R. Cooper, I. Bloch, and N. Goldman. "Measuring the Chern number of Hofstadter bands with ultracold bosonic atoms". *Nat. Phys.* 11.2 (2015), pp. 162–166 (cit. on p. 14).

[106] R. N. Palmer and D. Jaksch. "High-Field Fractional Quantum Hall Effect in Optical Lattices". *Phys. Rev. Lett.* 96 (18 2006), p. 180407 (cit. on p. 14).

[107] M. Hafezi, A. S. Sørensen, E. Demler, and M. D. Lukin. "Fractional quantum Hall effect in optical lattices". *Phys. Rev. A* 76 (2 2007), p. 023613 (cit. on p. 14).

[108] F. Grusdt, N. Y. Yao, D. Abanin, M. Fleischhauer, and E. Demler. "Interferometric measurements of many-body topological invariants using mobile impurities". *Nat. Commun.* 7 (2016), p. 11994 (cit. on p. 14).

[109] C. Repellin and N. Goldman. "Detecting Fractional Chern Insulators through Circular Dichroism". *Phys. Rev. Lett.* 122 (16 2019), p. 166801 (cit. on p. 14).

[110] B. Douçot, L. B. Ioffe, and J. Vidal. "Discrete non-Abelian gauge theories in Josephson-junction arrays and quantum computation". *Phys. Rev. B* 69 (21 2004), p. 214501 (cit. on p. 15).

[111] D. Marcos, P. Rabl, E. Rico, and P. Zoller. "Superconducting Circuits for Quantum Simulation of Dynamical Gauge Fields". *Phys. Rev. Lett.* 111 (11 2013), p. 110504 (cit. on p. 15).

[112] H. Weimer, M. Müller, I. Lesanovsky, P. Zoller, and H. P. Büchler. "A Rydberg quantum simulator". *Nat. Phys.* 6.5 (2010), pp. 382–388 (cit. on p. 15).

[113] L. Tagliacozzo, A. Celi, A. Zamora, and M. Lewenstein. "Optical Abelian lattice gauge theories". *Ann. Phys. (New York)* 330 (2013), pp. 160–191 (cit. on p. 15).

[114] J. Zhang, J. Unmuth-Yockey, J. Zeiher, A. Bazavov, S.-W. Tsai, and Y. Meurice. "Quantum Simulation of the Universal Features of the Polyakov Loop". *Phys. Rev. Lett.* 121 (22 2018), p. 223201 (cit. on p. 15).

[115] B. Buyens, F. Verstraete, and K. Van Acoleyen. "Hamiltonian simulation of the Schwinger model at finite temperature". *Phys. Rev. D* 94.8 (2016), p. 085018 (cit. on p. 15).

[116] U.-J. Wiese. "Ultracold quantum gases and lattice systems: Quantum simulation of lattice gauge theories". *Ann. Phys. (Berlin)* 525.10-11 (2013), pp. 777–796 (cit. on p. 15).

[117] E. Zohar, J. I. Cirac, and B. Reznik. "Quantum simulations of gauge theories with ultracold atoms: Local gauge invariance from angular-momentum conservation". *Phys. Rev. A* 88 (2 2013), p. 023617 (cit. on p. 15).

[118] U.-J. Wiese. “Towards quantum simulating QCD”. *Nucl. Phys. A* 931 (2014), pp. 246–256 (cit. on p. 15).

[119] S. Notarnicola, E. Ercolessi, P. Facchi, G. Marmo, S. Pascazio, and F. V. Pepe. “Discrete Abelian gauge theories for quantum simulations of QED”. *J. Phys. A Math. Theor.* 48.30 (2015), 30FT01 (cit. on p. 15).

[120] V. Kasper, F. Hebenstreit, M. Oberthaler, and J. Berges. “Schwinger pair production with ultracold atoms”. *Physics Letters B* 760 (2016), pp. 742–746 (cit. on p. 15).

[121] V. Kasper, F. Hebenstreit, F. Jendrzejewski, M. K. Oberthaler, and J. Berges. “Implementing quantum electrodynamics with ultracold atomic systems”. *New J. Phys.* 19.2 (2017), p. 023030 (cit. on p. 15).

[122] Y. Kuno, S. Sakane, K. Kasamatsu, I. Ichinose, and T. Matsui. “Quantum simulation of $(1+1)$-dimensional $U(1)$ gauge-Higgs model on a lattice by cold Bose gases”. *Phys. Rev. D* 95 (9 2017), p. 094507 (cit. on p. 15).

[123] N. Klco, E. F. Dumitrescu, A. J. McCaskey, T. D. Morris, R. C. Pooser, M. Sanz, E. Solano, P. Lougovski, and M. J. Savage. “Quantum-classical computation of Schwinger model dynamics using quantum computers”. *Phys. Rev. A* 98 (3 2018), p. 032331 (cit. on p. 15).

[124] E. A. Martinez, C. A. Muschik, P. Schindler, D. Nigg, A. Erhard, M. Heyl, P. Hauke, M. Dalmonte, T. Monz, P. Zoller, and R. Blatt. “Real-time dynamics of lattice gauge theories with a few-qubit quantum computer”. *Nature* 534.7608 (2016), pp. 516–519 (cit. on p. 15).

[125] M. J. Edmonds, M. Valiente, Juzeliūnas, L. Santos, and P. Öhberg. “Simulating an Interacting Gauge Theory with Ultracold Bose Gases”. *Phys. Rev. Lett.* 110 (8 2013), p. 085301 (cit. on p. 15).

[126] L. W. Clark, B. M. Anderson, L. Feng, A. Gaj, K. Levin, and C. Chin. “Observation of Density-Dependent Gauge Fields in a Bose-Einstein Condensate Based on Micromotion Control in a Shaken Two-Dimensional Lattice”. *Phys. Rev. Lett.* 121 (3 2018), p. 030402 (cit. on p. 15).

[127] K. G. Wilson. “Confinement of quarks”. *Phys. Rev. D* 10.8 (1974), pp. 2445–2459 (cit. on p. 16).

[128] A. M. Polyakov. “Interaction of goldstone particles in two dimensions. Applications to ferromagnets and massive Yang-Mills fields”. *Phys. Lett. B* 59.1 (1975), pp. 79–81 (cit. on p. 16).

[129] A. M. Polyakov. “Compact gauge fields and the infrared catastrophe”. *Phys. Lett. B* 59.1 (1975), pp. 82–84 (cit. on p. 16).

[130] J. B. Kogut. “An introduction to lattice gauge theory and spin systems”. *Rev. Mod. Phys.* 51.4 (1979), p. 659 (cit. on pp. 16–19).

[131] G. ’t Hooft. “On the phase transition towards permanent quark confinement”. *Nucl. Phys. B* 138.1 (1978), pp. 1–25 (cit. on p. 19).

[132] J. B. Kogut. “The lattice gauge theory approach to quantum chromodynamics”. *Rev. Mod. Phys.* 55.3 (1983), pp. 775–836 (cit. on p. 19).

[133] G. ’t Hooft. “Confinement of quarks”. *Nucl. Phys. A* 721 (2003), pp. C3–C19 (cit. on p. 19).

[134] C. Prosko, S.-P. Lee, and J. Maciejko. “Simple $\mathbb{Z}_2$ lattice gauge theories at finite fermion density”. *Phys. Rev. B* 96.20 (2017), p. 205104 (cit. on pp. 19, 20, 25).

[135] E. Pavarini, P. Coleman, and E. Koch. *Many-Body Physics: From Kondo to Hubbard*. Tech. rep. Theoretische Nanoelektronik, 2015 (cit. on p. 19).

[136] H. Ju and L. Balents. “Finite-size effects in the $\mathbb{Z}_2$ spin liquid on the Kagome lattice”. *Phys. Rev. B* 87.19 (2013), p. 195109 (cit. on p. 19).

[137] Y. Huh, M. Punk, and S. Sachdev. “Vison states and confinement transitions of $\mathbb{Z}_2$ spin liquids on the Kagome lattice”. *Phys. Rev. B* 84 (9 2011), p. 094419 (cit. on p. 20).

[138] Y. Wan and O. Tchernyshyov. “Phenomenological $\mathbb{Z}_2$ lattice gauge theory of the spin-liquid state of the Kagome Heisenberg antiferromagnet”. *Phys. Rev. B* 87 (10 2013), p. 104408 (cit. on p. 20).

[139] D. González-Cuadra, A. Dauphin, P. R. Grzybowski, P. Wójcik, M. Lewenstein, and A. Bermudez. “Symmetry-breaking topological insulators in the $\mathbb{Z}_2$ Bose-Hubbard model”. *Phys. Rev. B* 99 (4 2019), p. 045139 (cit. on p. 20).

[140] A. Y. Kitaev. “Fault-tolerant quantum computation by anyons”. *Ann. Phys. (New York)* 303 (2003), pp. 2–30 (cit. on p. 20).

[141] E. Fradkin and S. H. Shenker. “Phase diagrams of lattice gauge theories with Higgs fields”. *Phys. Rev. D* 19.12 (1979), pp. 3682–3697 (cit. on p. 20).

[142] A. Eckardt. “Colloquium: Atomic quantum gases in periodically driven optical lattices”. *Rev. Mod. Phys.* 89.1 (2017), p. 311 (cit. on pp. 28, 72).

[143] M. Aidelsburger. “Ultracold atoms in periodically driven optical lattices”. MA thesis. München: Ludwig-Maximilians-Universität, 2011 (cit. on pp. 35, 95).

[144] M. Atala. “Measuring Topological Invariants and Chiral Meissner Currents with Ultracold Bosonic Atoms”. PhD thesis. München: Ludwig-Maximilians-Universität, 2011 (cit. on pp. 35, 95).

[145] M. Aidelsburger. “Artificial gauge fields with ultracold atoms in optical lattices”. PhD thesis. München: Ludwig-Maximilians-Universität, 2015 (cit. on pp. 35, 95).

[146] M. Lohse. "Topological Charge Pumping with Ultracold Bosonic Atoms in Optical Superlattices". PhD thesis. München: Ludwig-Maximilians-Universität, 2018 (cit. on pp. 35, 95).

[147] J. Sebby-Strabley, M. Anderlini, P. S. Jessen, and J. V. Porto. "Lattice of double wells for manipulating pairs of cold atoms". *Phys. Rev. A* 73.3 (2006), p. 033605 (cit. on pp. 36–38, 48, 104).

[148] B. J. Keay, S. Zeuner, S. J. Allen, K. D. Maranowski, A. C. Gossard, U. Bhattacharya, and M. J. W. Rodwell. "Dynamic Localization, Absolute Negative Conductance, and Stimulated, Multiphoton Emission in Sequential Resonant Tunneling Semiconductor Superlattices". *Phys. Rev. Lett.* 75.22 (1995), pp. 4102–4105 (cit. on p. 38).

[149] H. Lignier, C. Sias, D. Ciampini, Y. Singh, A. Zenesini, O. Morsch, and E. Arimondo. "Dynamical Control of Matter–Wave Tunneling in Periodic Potentials". *Phys. Rev. Lett.* 99 (22 2007), p. 220403 (cit. on p. 38).

[150] C. Sias, H. Lignier, Y. Singh, A. Zenesini, D. Ciampini, O. Morsch, and E. Arimondo. "Observation of Photon-Assisted Tunneling in Optical Lattices". *Phys. Rev. Lett.* 100.4 (2008), p. 63 (cit. on p. 38).

[151] E. Kierig, U. Schnorrberger, A. Schietinger, J. Tomkovic, and M. K. Oberthaler. "Single-Particle Tunneling in Strongly Driven Double-Well Potentials". *Phys. Rev. Lett.* 100.19 (2008), p. 190405 (cit. on p. 38).

[152] C. E. Creffield, F. Sols, D. Ciampini, O. Morsch, and E. Arimondo. "Expansion of matter waves in static and driven periodic potentials". *Phys. Rev. A* 82 (3 2010), p. 035601 (cit. on p. 38).

[153] S. Mukherjee, A. Spracklen, D. Choudhury, N. Goldman, P. Öhberg, E. Andersson, and R. R. Thomson. "Modulation-assisted tunneling in laser-fabricated photonic Wannier-Stark ladders". *New J. Phys.* 17.11 (2015), p. 115002 (cit. on p. 38).

[154] A. Widera, F. Gerbier, S. Fölling, T. Gericke, O. Mandel, and I. Bloch. "Coherent Collisional Spin Dynamics in Optical Lattices". *Phys. Rev. Lett.* 95 (19 2005), p. 190405 (cit. on pp. 38, 47, 96).

[155] C. J. Myatt, E. A. Burt, R. W. Ghrist, E. A. Cornell, and C. E. Wieman. "Production of Two Overlapping Bose-Einstein Condensates by Sympathetic Cooling". *Phys. Rev. Lett.* 78 (4 1997), pp. 586–589 (cit. on p. 38).

[156] H. Schmaljohann, M. Erhard, J. Kronjäger, M. Kottke, S. van Staa, L. Cacciapuoti, J. J. Arlt, K. Bongs, and K. Sengstock. "Dynamics of $F = 2$ Spinor Bose-Einstein Condensates". *Phys. Rev. Lett.* 92 (4 2004), p. 040402 (cit. on p. 38).

[157] H. A. Gersch and G. C. Knollman. "Quantum Cell Model for Bosons". *Phys. Rev.* 129 (2 1963), pp. 959–967 (cit. on pp. 40, 61).

[158] V. W. Scarola and S. Das Sarma. “Quantum Phases of the Extended Bose-Hubbard Hamiltonian: Possibility of a Supersolid State of Cold Atoms in Optical Lattices”. *Phys. Rev. Lett.* 95 (3 2005), p. 033003 (cit. on pp. 40, 55, 62, 72, 90).

[159] U. Bissbort. “Dynamical Effects and Disorder in Ultracold Bosonic Matter”. PhD thesis. Frankfurt am Main: Johann Wolfgang Goethe-Universität, 2012 (cit. on p. 41).

[160] N. Navon, A. L. Gaunt, R. P. Smith, and Z. Hadzibabic. “Critical dynamics of spontaneous symmetry breaking in a homogeneous Bose gas”. *Science* 347.6218 (2015), pp. 167–170 (cit. on p. 55).

[161] L. Chomaz, L. Corman, T. Bienaimé, R. Desbuquois, C. Weitenberg, S. Nascimbene, J. Beugnon, and J. Dalibard. “Emergence of coherence via transverse condensation in a uniform quasi-two-dimensional Bose gas”. *Nat. Commun.* 6 (2015), p. 6162 (cit. on p. 55).

[162] D. Banerjee, M. Bögli, M. Dalmonte, E. Rico, P. Stebler, U.-J. Wiese, and P. Zoller. “Atomic Quantum Simulation of $U(N)$ and $\mathrm{SU}(N)$ Non-Abelian Lattice Gauge Theories”. *Phys. Rev. Lett.* 110 (12 2013), p. 125303 (cit. on pp. 60, 72).

[163] S. Kühn, J. I. Cirac, and M.-C. Bañuls. “Quantum simulation of the Schwinger model: A study of feasibility”. *Phys. Rev. A* 90 (4 2014), p. 042305 (cit. on pp. 60, 72).

[164] I. H. Deutsch and P. S. Jessen. “Quantum-state control in optical lattices”. *Phys. Rev. A* 57 (3 1998), pp. 1972–1986 (cit. on pp. 70, 71).

[165] M. I. Dyakonov and V. I. Perel. “Possibility of orienting electron spins with current”. *J. Exp. Theor. Phys.* 13 (1971), p. 467 (cit. on p. 75).

[166] M. I. Dyakonov and V. I. Perel. “Current-induced spin orientation of electrons in semiconductors”. *Phys. Lett. A* 35.6 (1971), pp. 459–460 (cit. on p. 75).

[167] E. H. Hall. “On a New Action of the Magnet on Electric Currents”. *Am. J. Math.* 2.3 (1879), pp. 287–292 (cit. on p. 75).

[168] N. F. Mott and H. S. W. Massey. *The theory of atomic collisions*. Vol. 35. Clarendon Press Oxford, 1965 (cit. on p. 75).

[169] B. A. Bernevig and S.-C. Zhang. “Quantum Spin Hall Effect”. *Phys. Rev. Lett.* 96 (10 2006), p. 106802 (cit. on pp. 75, 76).

[170] A. A. Bakun, B. P. Zakharchenya, A. A. Rogachev, M. N. Tkachuk, and V. G. Fleisher. “Observation of a surface photocurrent caused by optical orientation of electrons in a semiconductor”. *JETP Lett.* 40.11 (1984) (cit. on p. 75).

[171] N. Nagaosa, J. Sinova, S. Onoda, A. H. MacDonald, and N. P. Ong. “Anomalous Hall effect”. *Rev. Mod. Phys.* 82 (2 2010), pp. 1539–1592 (cit. on pp. 75, 76).

[172] A. Kundt. “Das Hall’sche Phänomen in Eisen, Kobalt und Nickel”. *Ann. Phys.* 285.6 (1893), pp. 257–271 (cit. on p. 75).

[173] J. E. Hirsch. “Spin Hall Effect”. *Phys. Rev. Lett.* 83 (9 1999), pp. 1834–1837 (cit. on p. 75).

[174] R. Karplus and J. M. Luttinger. “Hall effect in ferromagnetics”. *Phys. Rev.* 95.5 (1954), p. 1154 (cit. on p. 75).

[175] S. Murakami, N. Nagaosa, and S.-C. Zhang. “Dissipationless Quantum Spin Current at Room Temperature”. *Science* 301.5638 (2003), pp. 1348–1351 (cit. on pp. 76, 80).

[176] J. Sinova, D. Culcer, Q. Niu, N. A. Sinitsyn, T. Jungwirth, and A. H. MacDonald. “Universal Intrinsic Spin Hall Effect”. *Phys. Rev. Lett.* 92 (12 2004), p. 126603 (cit. on p. 76).

[177] S. Murakami. “Intrinsic Spin Hall Effect”. *Advances in Solid State Physics*. Ed. by B. Kramer. Berlin, Heidelberg: Springer Berlin Heidelberg, 2006, pp. 197–209 (cit. on pp. 76, 88).

[178] Y. K. Kato, R. C. Myers, A. C. Gossard, and D. D. Awschalom. “Observation of the Spin Hall Effect in Semiconductors”. *Science* 306.5703 (2004), pp. 1910–1913 (cit. on pp. 76, 80).

[179] J. Wunderlich, B. Kaestner, J. Sinova, and T. Jungwirth. “Experimental Observation of the Spin-Hall Effect in a Two-Dimensional Spin-Orbit Coupled Semiconductor System”. *Phys. Rev. Lett.* 94 (4 2005), p. 047204 (cit. on p. 76).

[180] F. D. M. Haldane. “Model for a Quantum Hall Effect without Landau Levels: Condensed-Matter Realization of the "Parity Anomaly"”. *Phys. Rev. Lett.* 61 (18 1988), pp. 2015–2018 (cit. on p. 76).

[181] C. L. Kane and E. J. Mele. “$\mathbb{Z}_2$ Topological Order and the Quantum Spin Hall Effect”. *Phys. Rev. Lett.* 95 (14 2005), p. 146802 (cit. on p. 76).

[182] C. L. Kane and E. J. Mele. “Quantum Spin Hall Effect in Graphene”. *Phys. Rev. Lett.* 95 (22 2005), p. 226801 (cit. on pp. 76, 80, 82).

[183] X.-L. Qi and S.-C. Zhang. “The quantum spin Hall effect and topological insulators”. *Phys. Today* (2010) (cit. on p. 76).

[184] M. König, S. Wiedmann, C. Brüne, A. Roth, H. Buhmann, L. W. Molenkamp, X.-L. Qi, and S.-C. Zhang. “Quantum Spin Hall Insulator State in HgTe Quantum Wells”. *Science* 318.5851 (2007), pp. 766–770 (cit. on p. 76).

[185] Y. Ando. “Topological Insulator Materials”. *J. Phys. Soc. Japan* 82.10 (2013), p. 102001 (cit. on p. 76).

[186] L. Fu and C. L. Kane. "Topological insulators with inversion symmetry". *Phys. Rev. B* 76 (4 2007), p. 045302 (cit. on p. 76).

[187] D. Hsieh, D. Qian, L. Wray, Y. Xia, Y. S. Hor, R. J. Cava, and M. Z. Hasan. "A topological Dirac insulator in a quantum spin Hall phase". *Nature* 452.7190 (2008), p. 970 (cit. on p. 76).

[188] H. Zhang, C.-X. Liu, X.-L. Qi, X. Dai, Z. Fang, and S.-C. Zhang. "Topological insulators in Bi_2Se_3, Bi_2Te_3 and Sb_2Te_3 with a single Dirac cone on the surface". *Nat. Phys.* 5.6 (2009), pp. 438–442 (cit. on p. 76).

[189] Y. Xia, D. Qian, D. Hsieh, L. Wray, A. Pal, H. Lin, A. Bansil, D. Grauer, Y. S. Hor, R. J. Cava, and M. Z. Hasan. "Observation of a large-gap topological-insulator class with a single Dirac cone on the surface". *Nat. Phys.* 5.6 (2009), pp. 398–402 (cit. on p. 76).

[190] D. Hsieh, Y. Xia, L. Wray, D. Qian, A. Pal, J. H. Dil, J. Osterwalder, F. Meier, G. Bihlmayer, C. L. Kane, Y. S. Hor, R. J. Cava, and M. Z. Hasan. "Observation of Unconventional Quantum Spin Textures in Topological Insulators". *Science* 323.5916 (2009), pp. 919–922 (cit. on p. 76).

[191] Y. L. Chen, J. G. Analytis, J.-H. Chu, Z. K. Liu, S.-K. Mo, X. L. Qi, H. J. Zhang, D. H. Lu, X. Dai, Z. Fang, S. C. Zhang, I. R. Fisher, Z. Hussain, and Z.-X. Shen. "Experimental Realization of a Three-Dimensional Topological Insulator, Bi_2Te_3". *Science* 325.5937 (2009), pp. 178–181 (cit. on p. 76).

[192] G. A. Prinz. "Magnetoelectronics". *Science* 282.5394 (1998), pp. 1660–1663 (cit. on pp. 76, 80).

[193] S. D. Sarma, J. Fabian, X. Hu, and I. Žutić. "Spin electronics and spin computation". *Solid State Commun.* 119.4 (2001), pp. 207–215 (cit. on p. 76).

[194] I. Žutić, J. Fabian, and S. Das Sarma. "Spintronics: Fundamentals and applications". *Rev. Mod. Phys.* 76 (2 2004), pp. 323–410 (cit. on p. 76).

[195] M. C. Rechtsman, J. M. Zeuner, Y. Plotnik, Y. Lumer, D. Podolsky, F. Dreisow, S. Nolte, M. Segev, and A. Szameit. "Photonic Floquet topological insulators". *Nature* 496.7444 (2013), p. 196 (cit. on p. 76).

[196] Y. Yang, Z. Xu, L. Sheng, B. Wang, D. Y. Xing, and D. N. Sheng. "Time-Reversal-Symmetry-Broken Quantum Spin Hall Effect". *Phys. Rev. Lett.* 107 (6 2011), p. 066602 (cit. on p. 76).

[197] W. Luo, D. Shao, M.-X. Deng, W. Deng, and L. Sheng. "Time-reversal-breaking induced quantum spin Hall effect". *Sci. Rep.* 7 (2017), p. 43049 (cit. on p. 76).

[198] D. J. Thouless. "Quantization of particle transport". *Phys. Rev. B* 27 (10 1983), pp. 6083–6087 (cit. on pp. 77, 78).

[199] X.-L. Qi, T. L. Hughes, and S.-C. Zhang. "Topological field theory of time-reversal invariant insulators". *Phys. Rev. B* 78 (19 2008), p. 195424 (cit. on p. 77).

[200] Y. E. Kraus, Y. Lahini, Z. Ringel, M. Verbin, and O. Zilberberg. "Topological States and Adiabatic Pumping in Quasicrystals". *Phys. Rev. Lett.* 109 (10 2012), p. 106402 (cit. on pp. 77, 79, 82).

[201] R. B. Laughlin. "Quantized Hall conductivity in two dimensions". *Phys. Rev. B* 23 (10 1981), pp. 5632–5633 (cit. on pp. 77, 82).

[202] G. Roux, T. Barthel, I. P. McCulloch, C. Kollath, U. Schollwöck, and T. Giamarchi. "Quasiperiodic Bose-Hubbard model and localization in one-dimensional cold atomic gases". *Phys. Rev. A* 78 (2 2008), p. 023628 (cit. on p. 79).

[203] Y. Hatsugai and M. Kohmoto. "Energy spectrum and the quantum Hall effect on the square lattice with next-nearest-neighbor hopping". *Phys. Rev. B* 42 (13 1990), pp. 8282–8294 (cit. on p. 79).

[204] M. Lohse, C. Schweizer, O. Zilberberg, M. Aidelsburger, and I. Bloch. "A Thouless quantum pump with ultracold bosonic atoms in an optical superlattice". *Nat. Phys.* 12.4 (2016), pp. 350–354 (cit. on p. 79).

[205] A. Hayward, C. Schweizer, M. Lohse, M. Aidelsburger, and F. Heidrich-Meisner. "Topological charge pumping in the interacting bosonic Rice-Mele model". *Phys. Rev. B* 98 (24 2018), p. 245148 (cit. on p. 79).

[206] H.-I. Lu, M. Schemmer, L. M. Aycock, D. Genkina, S. Sugawa, and I. B. Spielman. "Geometrical Pumping with a Bose-Einstein Condensate". *Phys. Rev. Lett.* 116 (20 2016), p. 200402 (cit. on p. 79).

[207] S. Nakajima, T. Tomita, S. Taie, T. Ichinose, H. Ozawa, L. Wang, M. Troyer, and Y. Takahashi. "Topological Thouless pumping of ultracold fermions". *Nat. Phys.* 12.4 (2016), pp. 296–300 (cit. on p. 79).

[208] M. Lohse, C. Schweizer, H. M. Price, O. Zilberberg, and I. Bloch. "Exploring 4D quantum Hall physics with a 2D topological charge pump". *Nature* 553.7686 (2018), p. 55 (cit. on p. 79).

[209] R. Shindou. "Quantum Spin Pump in $S = 1/2$ Antiferromagnetic Chains —Holonomy of Phase Operators in sine-Gordon theory—". *J. Phys. Soc. Japan* 74.4 (2005), pp. 1214–1223 (cit. on pp. 79, 80, 89, 108).

[210] L. Fu and C. L. Kane. "Time reversal polarization and a $\mathbb{Z}_2$ adiabatic spin pump". *Phys. Rev. B* 74 (19 2006), p. 195312 (cit. on p. 80).

[211] C. Q. Zhou, Y. F. Zhang, L. Sheng, R. Shen, D. N. Sheng, and D. Y. Xing. "Proposal for a topological spin Chern pump". *Phys. Rev. B* 90 (8 2014), p. 085133 (cit. on pp. 80, 108).

[212] P. Sharma and C. Chamon. “Quantum Pump for Spin and Charge Transport in a Luttinger Liquid”. *Phys. Rev. Lett.* 87 (9 2001), p. 096401 (cit. on p. 80).

[213] R. Citro, N. Andrei, and Q. Niu. “Pumping in an interacting quantum wire”. *Phys. Rev. B* 68 (16 2003), p. 165312 (cit. on p. 80).

[214] R. Citro, F. Romeo, and N. Andrei. “Electrically controlled pumping of spin currents in topological insulators”. *Phys. Rev. B* 84 (16 2011), p. 161301 (cit. on pp. 80, 89).

[215] S. K. Watson, R. M. Potok, C. M. Marcus, and V. Umansky. “Experimental Realization of a Quantum Spin Pump”. *Phys. Rev. Lett.* 91 (25 2003), p. 258301 (cit. on p. 80).

[216] C. W. Sandweg, Y. Kajiwara, A. V. Chumak, A. A. Serga, V. I. Vasyuchka, M. B. Jungfleisch, E. Saitoh, and B. Hillebrands. “Spin Pumping by Parametrically Excited Exchange Magnons”. *Phys. Rev. Lett.* 106 (21 2011), p. 216601 (cit. on p. 80).

[217] M. J. Rice and E. J. Mele. “Elementary Excitations of a Linearly Conjugated Diatomic Polymer”. *Phys. Rev. Lett.* 49 (19 1982), pp. 1455–1459 (cit. on p. 81).

[218] P. J. Lee, M. Anderlini, B. L. Brown, J. Sebby-Strabley, W. D. Phillips, and J. V. Porto. “Sublattice Addressing and Spin-Dependent Motion of Atoms in a Double-Well Lattice”. *Phys. Rev. Lett.* 99 (2 2007), p. 020402 (cit. on p. 83).

[219] H.-N. Dai, B. Yang, A. Reingruber, X.-F. Xu, X. Jiang, Y.-A. Chen, Z.-S. Yuan, and J.-W. Pan. “Generation and detection of atomic spin entanglement in optical lattices”. *Nat. Phys.* 12.8 (2016), pp. 783–787 (cit. on p. 83).

[220] S. A. Crooker, M. Furis, X. Lou, C. Adelmann, D. L. Smith, C. J. Palmstrøm, and P. A. Crowell. “Imaging spin transport in lateral ferromagnet/semiconductor structures”. *Science* 309.5744 (2005), pp. 2191–2195 (cit. on p. 88).

[221] S. O. Valenzuela and M. Tinkham. “Electrical detection of spin currents: The spin-current induced Hall effect”. *J. Appl. Phys.* 101.9 (2007), 09B103 (cit. on p. 89).

[222] M. C. Beeler, R. A. Williams, K. Jimenez-Garcia, L. J. LeBlanc, A. R. Perry, and I. B. Spielman. “The spin Hall effect in a quantum gas”. *Nature* 498.7453 (2013), p. 201 (cit. on p. 89).

[223] S. Maekawa, H. Adachi, K.-i. Uchida, J. Ieda, and E. Saitoh. “Spin Current: Experimental and Theoretical Aspects”. *J. Phys. Soc. Japan* 82.10 (2013), p. 102002 (cit. on p. 89).

[224] S. Murakami, N. Nagosa, and S.-C. Zhang. “$SU(2)$ non-Abelian holonomy and dissipationless spin current in semiconductors”. *Phys. Rev. B* 69 (23 2004), p. 235206 (cit. on p. 89).

[225] S. Murakami, N. Nagaosa, and S.-C. Zhang. “Spin-Hall Insulator”. *Phys. Rev. Lett.* 93 (15 2004), p. 156804 (cit. on p. 89).

[226] D. Culcer, J. Sinova, N. A. Sinitsyn, T. Jungwirth, A. H. MacDonald, and Q. Niu. "Semiclassical Spin Transport in Spin-Orbit-Coupled Bands". *Phys. Rev. Lett.* 93 (4 2004), p. 046602 (cit. on p. 89).

[227] J. Shi, P. Zhang, D. Xiao, and Q. Niu. "Proper Definition of Spin Current in Spin-Orbit Coupled Systems". *Phys. Rev. Lett.* 96 (7 2006), p. 076604 (cit. on p. 89).

[228] M. Governale, F. Taddei, and R. Fazio. "Pumping spin with electrical fields". *Phys. Rev. B* 68 (15 2003), p. 155324 (cit. on p. 89).

[229] Y. Hatsugai and T. Fukui. "Bulk-edge correspondence in topological pumping". *Phys. Rev. B* 94 (4 2016), p. 041102 (cit. on p. 108).

[230] F. Zhou. "Topological spin pumps: The effect of spin rotation on quantum pumps". *Phys. Rev. B* 70 (12 2004), p. 125321 (cit. on p. 108).

[231] R. Bustos-Marún, G. Refael, and F. von Oppen. "Adiabatic Quantum Motors". *Phys. Rev. Lett.* 111 (6 2013), p. 060802 (cit. on p. 108).

[232] D. Meidan, T. Micklitz, and P. W. Brouwer. "Topological classification of interaction-driven spin pumps". *Phys. Rev. B* 84 (7 2011), p. 075325 (cit. on p. 108).

Acknowledgement

Here, I want to take the opportunity to say thanks to the amazing people I had the chance to work with. Without them, many things would have been impossible. First, thanks to Immanuel Bloch for giving me the chance to work in his group, for acting as the supervisor of this thesis, and for keeping the incredibly productive atmosphere alive. Moreover, I want to thank him for trusting us, the *MunichBosonTeam*, letting us work independently, and giving us time to develop and experiment with our own ideas.

A big thanks goes to everyone in the *MunichBosonTeam*: Michael Lohse, Monika Aidelsburger, Moritz Berngruber, Marcos Atala, and Julio Barreiro. It was a great pleasure. Especially, I want to thank Michael, with whom I shared the lab for many years. He is an incredible physicist with a very sharp mind and I am pleased he shared his physical insights with me. I really enjoyed our harmonic atmosphere and I am very grateful for this time. I also do not want to miss to thank Monika for the many wonderful conversations, for her being very motivating and extraordinary supportive.

I want to thank our theory friends, Luca Barbiero, Roberta Citro, Eugene Demler, Nathan Goldman, Fabian Grusdt, Andrew Hayward, Fabian Heidrich-Meissner, Hannah Price, and Oded Zilberberg, for sharing their physical perspective with me and their abundance of patience during times of slow progress at the experiment. I am especially grateful to Fabian proposing and accompanying me with the $\mathbb{Z}_2$ LGT project together with Nathan.

Thanks to all members of the Bloch group during my PhD time for their help, stimulating discussions, and relaxing table talks during the lunch breaks. They created a very enjoyable and productive atmosphere. I like to thank Ildiko Kecskesi for her help resolving administrative issues very smoothly.

I also want to thank Michael Knap for being the second referee for my thesis, and Alexander Högele and Dieter Braun for being part of my thesis defense committee.

Thanks to Monika and Michael for their fast proof-reading, which made the thesis more accurate and improved the presentation. Also, thanks to Anna-Lena Cost and Isabel Hoppe for their spelling, grammar and beneficial language comments.

Special thanks go to my family and friends for their continuous support and last but not least to Anna-Lena for always being there for me.